Ionic Liquids in Dye Sensitized Solar Cells

Theoretical Assessment of Properties and Applications

Dissertation

zur

Erlangung des Doktorgrades (Dr. rer. nat.)

der

Mathematisch-Naturwissenschaftlichen Fakultät

der

Rheinischen Friedrich-Wilhelms-Universtät Bonn.

Vorgelegt von

Henry Weber

aus

Zwenkau

Bonn, Juli 2016

Angefertigt mit Genehmigung der Mathematisch-Naturwissenschaftlichen Fakultät
der Rheinischen Friedrich-Wilhelms-Universität Bonn

1. Gutachter:	Prof. Dr. Barbara Kirchner
2. Gutachter:	Prof. Dr. Thomas Bredow
Tag der Promotion:	25.10.2016
Erscheinungsjahr:	2016

"*We have a choice. We can either be the last generation that doesn't understand this problem, or the first generation to solve the problems. I want to be the first generation to solve the problems.*"

– Sadiq Khan, mayor of London.

Abstract

Dye-sensitized solar cells have the potential to play a major role in the future of the global energy economy. Unfortunately, they still lack the consistency and durability to be truly competitive from a commercial point of view. The use of ionic liquids may hold a solution to most of the current drawbacks; thus, the implications of their use in dye-sensitized solar cells are approached by means of quantum chemical calculations and computational modeling.

The pure bulk phase of three promising cyano-based ionic liquids was investigated by *ab initio* molecular dynamics studies. Differences in cation–cation structuring was revealed despite the fact that all liquids bear the same cation, which might be correlated to macroscopic properties such as viscosity. The semiconductor–electrolyte interface is of special interest, as many processes occur here in a complete device. Characterization of this system was attempted on different pathways: First, the adsorption behavior was investigated in detail for selected cyano-based ILs in order to understand specific interactions. Second, a polarizable molecular dynamics force field was parametrized to study the extended TiO_2–ionic liquid interface, focusing on cooperative and bulk phase effects. Third, a great variety of ionic liquids were classified in their ability to shift the energy levels of the semiconductor TiO_2. Furthermore, influences of the ionic liquid electrolyte on the sensitizing dye were studied. Directed coordination plays a role, and a universal redshift of adsorption spectra upon solvation with respect to the gas phase is apparent.

Beneficial effects of ionic liquid application can be fine-tuning of semiconductor energy levels or spectroscopic properties of the dye, they can build blocking layers on the surface to prevent unfavored recombination reactions, or can enhance dye regeneration by favorably interacting with the redox mediator. Ultimately, the choice of the ionic liquid decides. Choosing the "right" ionic liquid can certainly have beneficial effects on the dye-sensitized solar cell, whereas choosing the "wrong" ionic liquid will result in inferior properties. By illuminating the fundamental processes involved, the results presented herein shall guide the choice of the ionic liquid electrolyte in future applications.

Contents

1 Introduction

As mankind develops, so does its inevitable demand for energy. With regard to limited resources such as gas, coal, and oil, the necessity of developing and harvesting sustainable, renewable energy sources is greater than ever before. Fortunately, this urgent demand incentivizes scientists all over the world to explore, develop, and refine new and present technologies. The most prominent solutions to sustainable energy involve the use of water, wind, tides, biomass, geothermal heat, and the sun as renewable energy sources.[1] While the sun is not strictly a renewable energy sorce for the matter of physics, it is a huge power plant that is working without any problems, and current estimations indicate that the sun could provide approximately 2850 times the current global energy needs,[1] so we would be smart to use this opportunity.

Solar energy can be harvested to generate electricity via solar photovoltaics (PV) or by concentrating solar power panels. The latter technology provides electricity by focusing solar irradiation to heat an external medium, which can be a solid, liquid, or gas, and which is then used to generate electricity. Concentrating solar power panels are scalable to large applications in the megawatt regime, and commercial plants already exist in countries including the United States or Spain.[1]

PV technologies to directly convert sunlight into electricity are vast, and Figure 1.1 gives an overview of progression and very recent state-of-the-art PV technologies, which will be discussed in the following. The general working principle is to use the incident radiation to generate an electron–hole pair, which is then separated. The electron is moved to the working electrode and used as electric current before the recombination of hole and electron is allowed at the counter electrode (CE). PV technologies can be divided roughly into three categories:

(i) The first generation of solar cells is based on mono- and polycrystalline silicon. The PV module consists of an *n*-type layer, a *p*-type layer and the *pn*-junction. These cells dominate the market with high durabilities and very good efficiencies of up to 24.4 %,[2] albeit with one significant shortcoming: the price. In order to achieve the high purity required, the crystalline silicon must be manufactured stepwise via very expensive, energy demanding procedures. Over the past decades, the PV industry has benefited massively from the electronic industry, which required silicon in an even higher purity grade than for PV applications. The surplus from the electronic industry was more than sufficient for the initially low demands of the PV industry. Unfortunately, the amount of material needed in the PV manufacturing is rising, in contrast to the microelectronic industry,

where miniaturization and new technologies lower the amount of silicon needed. Simultaneously, the silicon price keeps increasing, which renders this first generation of solar cells too expensive to compete with traditional fossil fuels or other renewable energy sources.

(ii) The second generation of solar cells began to emerge in the late 1970's using amorphous Si.[3] The high light absorption of amorphous Si enabled thin-film technologies, and the lower cost of the raw material sparked the interest in these technologies. Unfortunately, amorphous Si solar cells suffer from the Staebler–Wronski degradation effect, which causes a decrease of up to 50 % in cell efficiency under illumination.[4] Succeeding technologies involve CdTe systems,[5] CIGS (copper indium gallium diselenide),[6] and GaAs systems.[7] Although displaying promising laboratory and module efficiencies, common drawbacks are either low abundance of the required materials (*e.g.*, In, Te) or high inherent toxicity of the involved elements (*e.g.*, Cd, Te, As).

(iii) The third generation of solar cells can be summarized as cells that aim to overcome the Shockley–Queisar limit of $\eta = 31$ % efficiency of a single-junction. These multijunction cells are constructed by combining materials with different band gaps. A prominent and very advanced example in this category is the triple junction InGaP/GaAs/InGaAs cell with a reported efficiency of $\eta = 37.9$ % in 2013.[8] Using concentrated sunlight, the performance can be pushed even further, as impressively demonstrated by the Fraunhofer institute reporting an efficiency of $\eta = 46.0$ % recently.[9]

All technologies discussed so far are based on inorganic materials. Apart from that, organic photovoltaics (OPV) have emerged as a cheap alternative.[11] The working principle of organic solar cells has many similarities to that of conventional silicon-based solar cells. In order to work correctly, the incident photon must create an electron–hole pair in the active layer of the OPV. In contrast to the inorganic version, in which charge diffusion of generated electrons in the continuous conduction band occurs, the excited electron, located in the lowest unoccupied molecular orbital (LUMO), is more tightly bound to the organic molecule, leaving an electron deficiency in the highest molecular orbital (HOMO). This bound electron–hole pair is called an exciton. Without external influence, this pair would then quickly recombine to reform the initial state. Therefore, the active layer contains acceptor molecules which can receive the excited electron. If the driving force of this charge transport is larger than the binding energy of the exciton in the donor, the electron–hole pair dissociates, and the electron can diffuse to the working electrode to be used as electricity. With the appropriate choice of all components, record efficiencies of $\eta = 11.5$ % have been reported.[12]

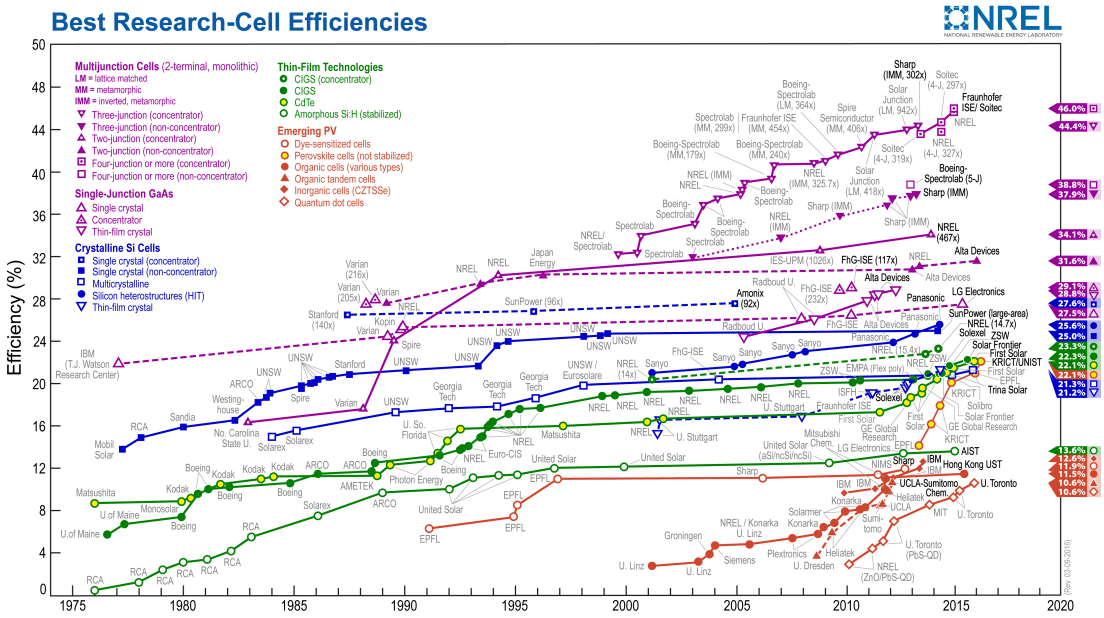

Figure 1.1: Summary of progression and current status of various photovoltaics. This plot is courtesy of the National Renewable Energy Laboratory, Golden, CO.[10] For enlarged version, see Figure A.1 on page 144.

1.1 Dye-Sensitized Solar Cell

For a semiconductor like Si or GaAs, the quantity that qualifies this material to be used in PV technologies is the bandgap, which has to coincide energetically with visible light in order to harvest it efficiently. Cheap, stable, and easily available semiconductors like TiO_2 or ZnO have a large bandgap in the ultraviolet (UV) region of light (*e.g.*, 3.2 eV for TiO_2 anatase), rendering them inefficient for the capture of sunlight. But what if that bandgap could be changed? By adsorbing an appropriate dye on the surface of the semiconductor, the spectral absorption range is extended, effectively sensitizing the semiconductor to absorb visible light. This is the basic working idea behind the technology of dye-sensitized solar cells (DSCs).

Technically, DSCs consist of hybrid materials and are categorized as second generation solar cells with the potential of becoming a third generation. The common DSC is built up by two transparent conducting oxides—the working and counter electrode. The working electrode is covered with the sensitized semiconductor, whereas the counter electrode is covered with a catalyst. These two systems are sandwiched together, and the space in between is filled with an electrolyte, most notably containing the redox pair. This standard setup of a DSC is illustrated in Figure 1.2.

The working principle of the DSC is depicted in Figure 1.3. To start the cycle, the dye molecule $\mathbf{D}^0$ absorbs an incident photon (k_1), generating an excited dye molecule $\mathbf{D}^*$. Normally, relaxation of the excited dye would occur (k_{-1}), but as the dye is covalently bound to the semiconductor, a very fast dissociation of charges occurs, and

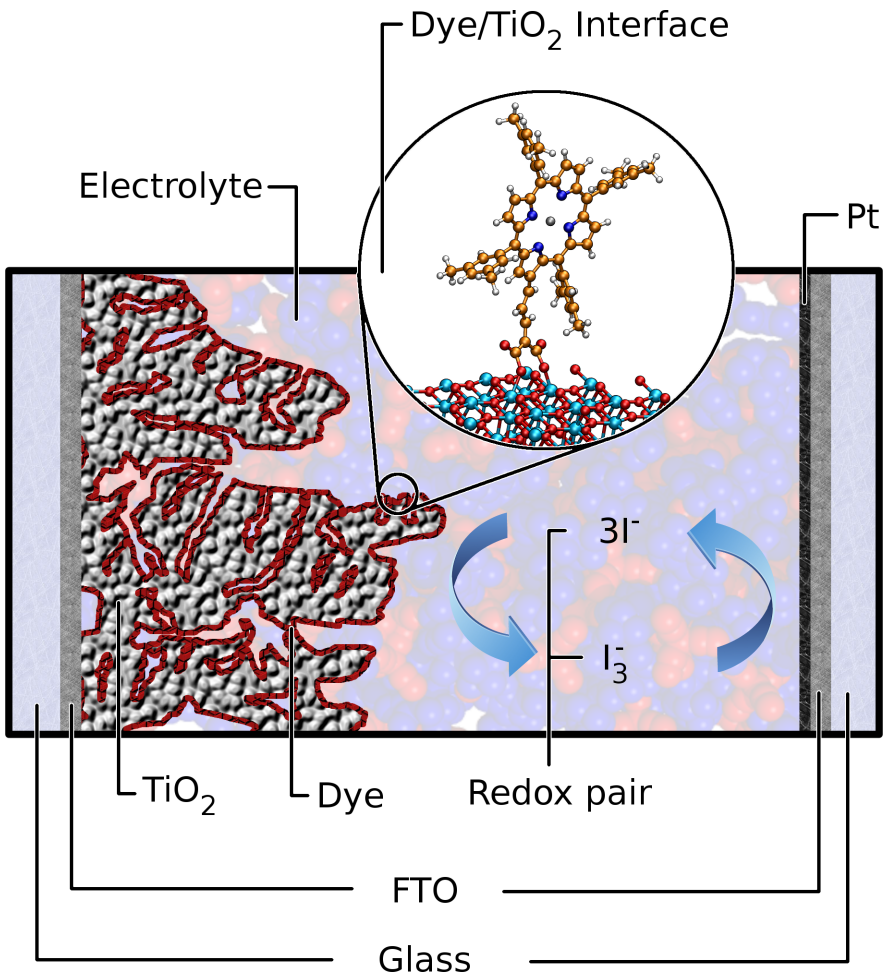

Figure 1.2: Setup of an exemplary DSC device with all essential components. The semiconductor TiO_2 is covered by the dye, the glass is coated with fluorine-doped tin-oxide (FTO) to be electrically conductive, and the counter electrode is loaded with a platinum catalyst. The dye shown in the magnified area is **GD2**.

the electron is injected into the conduction band (CB) of the semiconductor (k_2). This process is driven kinetically rather than thermodynamically. Clearly, the most energy could be gained by relaxation of **D*** to the initial ground state, but instead, electron injection occurs because this process is much faster and occurs in the femtosecond regime, whereas relaxation usually occurs in the picosecond regime. This circumstance leads to a relative injection rate near unity and is one of the reasons why DSCs are working at all. The injected electron hops through the semiconductor particles until it eventually reaches the working electrode (k_3). The remaining oxidized dye $\mathbf{D}^+$ is swiftly reduced by the redox pair $\mathbf{R}/\mathbf{R}^+$ present in the electrolyte (k_4). After diffusion (k_5), the oxidized redox species $\mathbf{R}^+$ recombines with an electron at the CE, regenerating the reduced redox component **R**, which closes the cycle. This sequence is disturbed by unwanted deactivation processes, depicted in red in Figure 1.3. Radiative or non-radiative relaxation of the excited dye without electron injection (k_{-1}), and

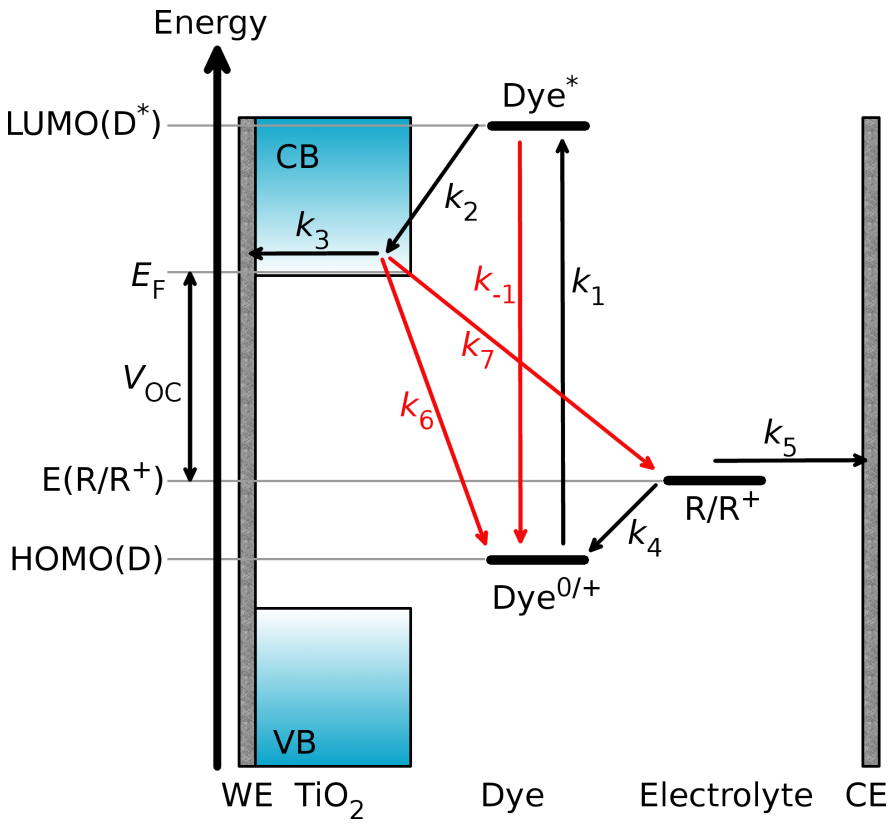

Figure 1.3: The graphic shows the general working principle of a DSC with the respective energy levels of the components. The black arrows indicate fundamental steps of a working DSC: k_1: Photoexcitation of the dye from the ground state $\mathbf{D}^0$ to the excited state $\mathbf{D^*}$. k_2: Injection of the electron into the conduction band of the semiconductor. k_3: Transport of the injected electron to the conducting material of the working electrode (WE). k_4: Regeneration of the oxidized dye $\mathbf{D}^+$ by the redox pair $\mathbf{R}/\mathbf{R}^+$. k_5: Diffusion of the oxidized redox species $\mathbf{R}^+$ to the counter electrode (CE). Important competing processes are shown in red: k_{-1}: Radiative or non-radiative deactivation of $\mathbf{D^*}$. k_6: Recombination of injected electrons with $\mathbf{D}^+$. k_7: Recombination of injected electrons with $\mathbf{R}^+$. Further shown is the open-circuit voltage V_{OC} as the difference of titania's Fermi energy E_{F} and the redox potential $E(\mathbf{R}/\mathbf{R}^+)$ of the redox pair.

recombination of conduction band electrons with the oxidized dye (k_6), the redox pair, or other electrolyte components (k_7) are the most prominent side reactions.

For this complex setup to work, the correct materials for the different tasks have to be chosen with care, and optimization is an ongoing process. The alignment of the energy levels involved is of special importance, which is also depicted in Figure 1.3. The sequence $E_{\mathrm{HOMO}}(\mathbf{D}^{0/+}) < E(\mathbf{R}/\mathbf{R}^+) < E_{\mathrm{F}} < E_{\mathrm{LUMO}}(\mathbf{D^*})$ is mandatory. The difference of $E_{\mathrm{HOMO}}(\mathbf{D}^{0/+})$ and $E(\mathbf{R}/\mathbf{R}^+)$ defines the dye regeneration overpotential, the difference of $E(\mathbf{R}/\mathbf{R}^+)$ and E_{F} the maximum attainable open-circuit voltage V_{OC}, and the difference of E_{F} and $E_{\mathrm{LUMO}}(\mathbf{D^*})$ gives the electron injection overpotential, which will significantly influence the short-circuit current I_{SC}. The parameters V_{OC} and I_{SC} are very essential parameters of any solar cell: V_{OC} is the maximum voltage the solar cell can achieve, which is consequently measured at open-circuit conditions.

I_{SC} is the maximum current which can be obtained from the operating solar cell, which is maximal at short-circuit conditions. I_{SC} is dependent on the number of incident photons converted to sunlight, and therefore dependent on the solar cell area. To remove this dependence, the short-circuit current density J_{SC}, which is current per area, is usually given instead. Additionally, the number of incident photons is dependent on the light intensity, and standardized measurements are performed at 1000 Wm^{-2} by default. Furthermore, as I_{SC} also depends on the spectral distribution of incident photons, measurements are generally performed under a simulated sunlight spectrum, air mass (AM) 1.5 G, which is equivalent to sunlight that traveled through 1.5 times the earth's atmosphere thickness. The "G" means global radiation, which equals an intensity of 964 Wm^{-2} and justifies the standard operating conditions of 1000 Wm^{-2}. The efficiency η of a solar cell is then given by the equation

$$\eta = \frac{J_{SC} V_{OC} FF}{P_{in}} \tag{1.1.1}$$

with the fill factor FF and the intensity of incident light P_{in}. The fill factor is the ratio of the maximum power P_{max} obtained from the cell and the product of V_{OC} and J_{SC}, *i.e.:*

$$FF = \frac{P_{max}}{J_{SC} V_{OC}}. \tag{1.1.2}$$

In the following, materials used to build real DSC devices are discussed, and the physical processes involved in the given subsystems of the DSC are explained.

1.1.1 Semiconductor

The role of the semiconductor is to accept the excited electron and to transport it to the working electrode. Additionally, it is the physical matrix on which the dye is adsorbed. Typically, TiO_2 is employed for this matter. It is photochemically and thermally very stable, cheap, readily available, well understood, non-toxic, and already widely used in different applications throughout all sectors of industry. In DSCs, it is usually applied in the form of anatase nanoparticles. On the one hand, anatase is the favored modification, because it has a larger bandgap than rutile (3.2 eV compared to 3.0 eV for rutile), and is the most stable modification for TiO_2 nanoparticles. The large bandgap may at first seem to be disadvantageous, because the sole reason for the sensitization is to make TiO_2 absorbant in the visible spectrum. Yet the higher band gap is linked to a higher conduction band edge energy (E_{CB}) leading to a favorable higher Fermi energy E_F and open-circuit voltage V_{OC} of the DSC. The nanostructuring of TiO_2 is required to ensure sufficient light absorption. The dye sensitizer can only be adsorbed as a monolayer and therfore, a high surface area of TiO_2 is needed to reach a sufficient density of dye molecules. In fact, the breakthrough of the DSC

technology in 1991 was attributed to the use of mesoporous TiO_2 nanoparticles instead of a flat, crystalline surface, increasing the intrinsic surface area 1000-fold.[13] The TiO_2 nanoparticles are commonly in the range of 20 nm in diameter, and are deposited in a layer of approximately 10 μm thickness. Although thicker layers would be aspired due to higher absorption rate of light, the diffusion length of electrons in the TiO_2 layer limits the maximum thickness. The electron diffusion length L, typically in the order of 5 μm $< L <$ 20 μm,[14] should be larger than the nanoparticle layer thickness. Alternative approaches incorporating nanotubes, nanorods, nanowires and others have been shown to work as well. For example, a very high electron diffusion length in the order of 100 μm was measured in a TiO_2-nanotube DSC.[15]

The main driving force for electron diffusion in the mesoporous TiO_2 film is the concentration gradient between the dye-covered surface and the conducting material (*e.g.*, fluorine-doped tin oxide (FTO)).[16–18] The negative charge built by the injected electrons in the conduction band is compensated by adsorbed cations on the surface of TiO_2, which is the reason for significant cation effects on the electron's effective diffusion length.[19] During diffusion through the semiconductor, the electron is likely to be captured temporarily or permanently in trap states. Deep trap states approximately 0.5 eV below the conduction band edge are most probably associated with surface defects such as an oxygen vacancy of anatase.[20] Consequently, electrons trapped in these deep states are unlikely to contribute to the electron transport.[21] On the contrary, shallow trap states contribute to the electron transport. Examples for shallow trap states are crystal defects in the TiO_2 bulk, or at the TiO_2/electrolyte interface as a consequence of Coulombic trapping via adsorbed cations.[22–24] Additionally, the geometry of the TiO_2 film is of importance. Due to the random nature of diffusion, a porous network with many dead ends (*i.e.*, particles with only one neighbor) leads to a slower overall electron transport. Therefore, a critical maximum porosity of 76 % was found to ensure efficient electron transport.[25]

Apart from trapping, recombination of the electron will lead to a decrease of electron transport and can occur via two main routes: (i) with the oxidized dye molecules (k_6) and (ii) with suitable components of the electrolyte mixture (k_7). Recombination of conduction band electrons and oxidized dye molecules will obviously compete with the dye regeneration (k_4) provided by the redox pair in the electrolyte. Unfortunately, reports on the exact kinetics of this pathway are inconsistent. For the most part, reported kinetics are in accordance with the Marcus inverted region, which means that an increase in driving force of the recombination will lead to a decrease in the respective transfer rate constant, and the transfer is thermally activated.[26,27] On the contrary, other studies suggest that either the kinetics is hardly affected by changes of the driving force,[28,29] or that the kinetics can even be in the Marcus normal region.[30] These findings suggest that the electron–oxidized dye recombination is a highly complex mechanism, which depends heavily on multiple factors, including, but not limited to,

the choice of materials, TiO_2 nanoparticle size, and temperature.

1.1.2 Dye

At the very heart of a DSC, there must be a dye, or sensitizer. The key role of this component is to transform the light-insensitive semiconductor into a material that absorbs as much light as possible. This is achieved by adsorption of suitable dyes on the semiconductor's surface, effectively adding energetically higher-lying occupied states in the empty band gap region. This is far from trivial, and in order to achieve stable high performances, the dye has to meet certain requirements:[31]

(i) The dye should absorb all incident light up to $\lambda = 950$ nm.

(ii) The dye should stably adsorb both chemically and thermally on the semiconductor's surface. This is usually ensured by carboxylate, phosphate, or sulfate anchoring groups.

(iii) The dye's LUMO should energetically match the semiconductor's conduction band edge to ensure efficient electron transfer.

(iv) The dye's HOMO has to be energetically lower than the redox pair's HOMO to guarantee efficient dye regeneration.

(v) The dye's excited and oxidized state should sustain at least 10^8 turnovers without significant degradation, translating to approximately 20 years of outdoor application.

An excellent example of an engineered dye that meets all of the above mentioned requirements is the black dye, or **N749**,[32] depicted in Fig 1.4. The ruthenium based dye shows broad absorption of light up to $\lambda = 920$ nm, which is almost perfect. Absorption of light in the wavelength region above 950 nm is believed to only minimally improve the performance, because the real sunlight spectrum after passing through the earth's atmosphere has a very low intensity around 950 nm, and decreases for wavelengths in the infrared region due to absorption by water and CO_2 in our atmosphere. The large terpyridyl ligand carries carboxylate groups, which tightly adsorb on a TiO_2 surface via covalent bonds between the surface's titanium atoms and the dye's oxygen atoms. The dye's energy levels also meet the aforementioned requirements. It is important to note that the dye's LUMO is mostly located on the ligand adsorbed on TiO_2, meaning that the metal-to-ligand charge transfer (MLCT) in **N749** locates the excited electron near the surface, offering an efficient injection into the conduction band. Moreover, the dye is chemically and thermally very stable, making it suitable for highly durable DSCs. Certified efficiencies of DSCs sensitized with **N749** of up to 10.4 % have been reported.[35] Though showing very promising efficiencies, high cost, limited availability of noble and transition metals such as Ru or Os, and potential toxicity collide with

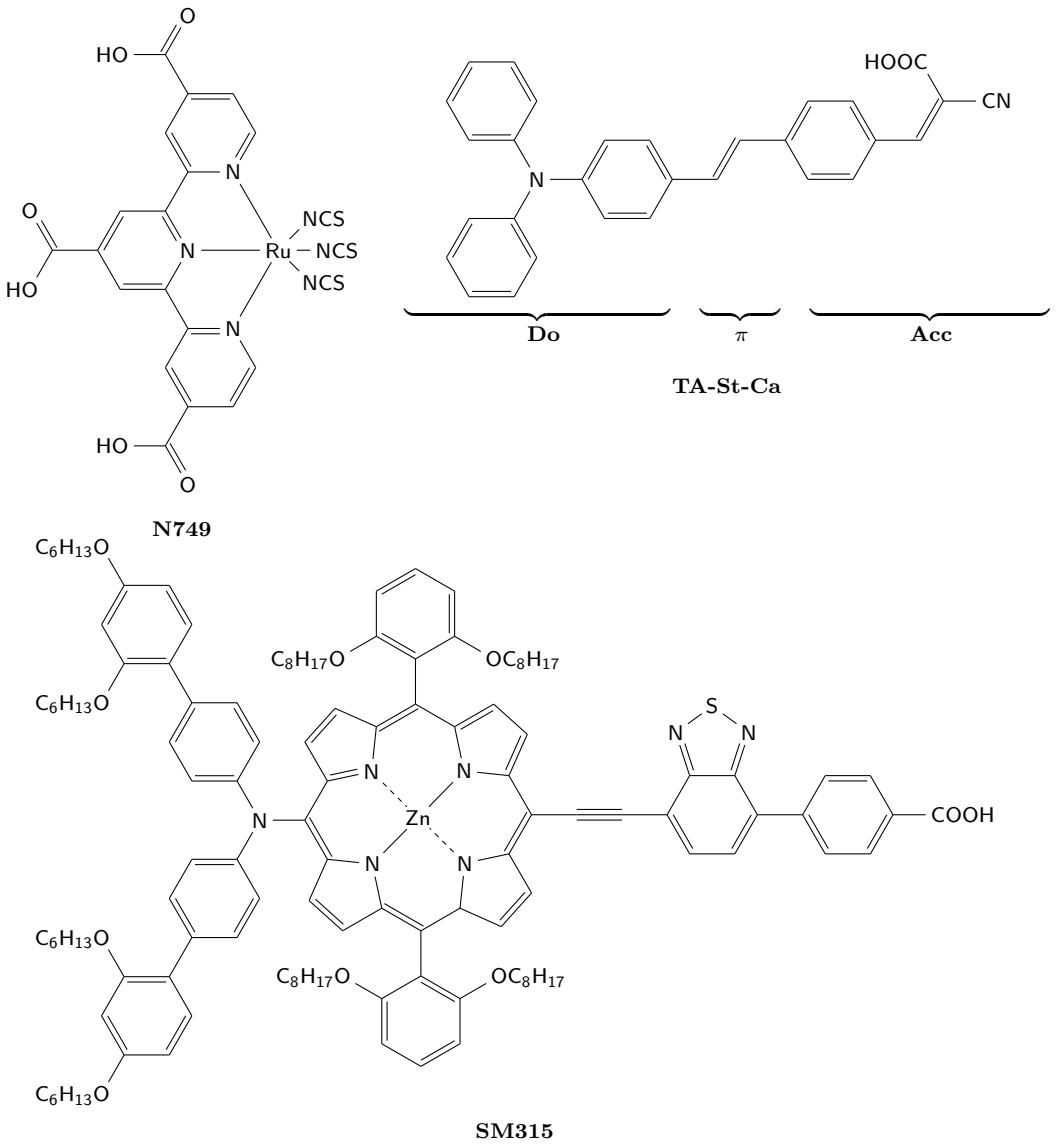

Figure 1.4: Chemical structure of the dyes **N749**,[32] **TA-St-Ca**,[33] and **SM315**.[34] **Do** is the donor unit, **Acc** the acceptor unit, and π the π-bridge. The dye **N749** often refers to the deprotonated form, usually including the tetrabutylammonium cation.

the initial purpose of the DSC being a low-cost, environmentally-friendly alternative to inorganic solar cells. Consequently, the trend to design and utilize metal-free organic dyes emerged, potentially combining low cost and low toxicity or even biodegradability.

Inspired by nature, first attempts in this regard revolved around porphyrin-based sensitizers, mimicking nature's light harvesting workhorse—chlorophyll. Initial efficiencies reported at $\eta = 2.6\,\%$ in 1993[36] were low compared to the best working ruthenium sensitizers at that time. Further testing and development of porphyrin sensitized solar cells led to efficiencies around 7 % in 2007,[37] but organic dyes still could not compete with the established Ru-dyes. In order to make organic dyes truly competitive, a rational design concept was needed to guide further research. In 2007, Hwang *et al.* reported

record efficiencies of 9.1 % and presented the organic dye **TA-St-Ca** (Figure 1.4) of the general form **Do**–π–**Acc**–TiO_2, with the donor **Do**, an electron rich group where most of the molecule's HOMO electron density is located, the acceptor **Acc**, where most of the dye's LUMO is located, and a π-bridge linking **Do** and **Acc**.[33] With this design, efficient electron injection is ensured due to the LUMO being near the TiO_2's surface, and recombination of injected electrons with the oxidized dye is suppressed because the HOMO is far away from the surface. Simultaneously, dye regeneration is improved because the donor part of the dye reaches far into the electrolyte of the dye. This concise design strategy was a major breakthrough for the metal-free dyes, and many dyes evolved with this underlying concept. Today, hundreds of different porphyrin dyes have been synthesized and tested, due to the huge design capabilities of porphyrin through functionalization, linking to other chromophores, or fusing of multiple porphyrins.[38] Ultimately, the porphyrin-based dye **SM315** (see Figure 1.4) of the general **Do**–π–**Acc** form was presented in 2014, showing efficiencies of 13 % under full sun illumination, and even outperforming the best Ru-based dyes.[34]

Apart from porphyrin, a number of natural and synthetic substances provide the body for dyes suitable for sensitization of DSCs, of which some have already been employed, including cyanine,[39,40] merocyanine,[40,41] phthalocyanine,[42] indoline,[43] coumarin,[44] eosin,[45] perylene,[46] anthraquinone,[47] squarine,[48–50] or triarylamine[39,51–53] (as in **TA-St-Ca**[33]).

While further functionalization and exploration might lead to better dyes, another feasible approach may be co-sensitization, which means sensitization with two or more dyes. By combining dyes with complementary light absorption characteristics, the overall sensitivity can be enhanced, increasing the photon-to-current efficiency over the whole spectral range. For a long time, the approach of co-sensitization was not fruitful, because of internal problems such as quenching of excited states and electron transfer between the adsorbed dyes.[54] Quenching of excited states between the adsorbed dyes is especially strong for high surface concentrations. Thus, low dye loadings would be preferred, which obviously competes with the amount of light absorbed. In order to harvest enough light even for low dye concentrations, a very high molar extinction coefficient is required. Transition metal dyes with MLCT as the paramount photon absorption reaction typically have low extinction coefficients, but organic dyes often have much higher molar extinction coefficients, and are therefore more suitable for co-sensitization. Consequently, the first promising co-sensitized DSC containing a porphyrin dye (**YD2**) and an indoline dye (**D2015**[55]) was reported in 2010.[56] The presented cell showed enhanced performance of $\eta = 6.9$ %, compared to efficiencies of individual sensitization, $\eta = 5.6 - 5.7$ %. Although far from perfect, the principle has been shown to work. In the end of 2011, a *Science* article by Grätzel and coworkers appeared, reporting unprecedented $\eta = 12.3$ % under full sun illumination for a DSC co-sensitized by **YD2-o-C8** and **Y123**, and 13.1 % under 50 % sun illumination.[57]

Interestingly, this DSC used a $Co^{II/III}$ redox couple. The influence of the redox couple will be discussed in the next paragraph.

1.1.3 Redox Mediator

The crucial task of the redox pair $\mathbf{R}/\mathbf{R}^+$ is the regeneration of the oxidized dye $\mathbf{D}^+$. This simple redox reaction is best described by the equation:[58]

$$\mathbf{D}^+ + \mathbf{R} \xrightarrow{k_4} \mathbf{D} + \mathbf{R}^+, \tag{1.1.3}$$

using k_4 from Figure 1.3. From an energetic point of view, the redox potential of the redox pair $\mathbf{R}/\mathbf{R}^+$ must be more negative than the redox potential of the dye pair $\mathbf{D}/\mathbf{D}^+$. This necessity directly limits the maximum V_{OC}, and the difference between $E(\mathbf{R}/\mathbf{R}^+)$ and $E(\mathbf{D}/\mathbf{D}^+)$, called dye regeneration overpotential, is effectively lost as usable energy. Logically, the dye regeneration overpotential should be minimal to achieve high device performance, but it is required to be large enough to ensure efficient dye regeneration.

Over the course of the last two decades, the I^-/I_3^- redox pair emerged as the standard choice for several reasons. Considering Figure 1.3, it has positive effects on k_3, k_4, k_5, and k_7. The standard dyes for DSCs have been the ruthenium dyes **N719** and **N749**, and they work perfectly with the I^-/I_3^- redox couple regenerating the dyes with near unity efficiency (k_4 favored against k_{-1} and k_6).[59] This is rather surprising, considering the complicated mechanism of this redox reaction, which most likely occurs in the following fashion:[59]

$$\mathbf{D}^+ + I^- \longrightarrow (\mathbf{D}\cdots I) \tag{1.1.4}$$

$$(\mathbf{D}\cdots I) + I^- \longrightarrow (\mathbf{D}\cdots I_2^{-\bullet}) \tag{1.1.5}$$

$$(\mathbf{D}\cdots I_2^{-\bullet}) \longrightarrow \mathbf{D} + I_2^{-\bullet} \tag{1.1.6}$$

$$2\,I_2^{-\bullet} \longrightarrow I_3^- + I^- \tag{1.1.7}$$

Formation of the dye–iodide complex $(\mathbf{D}\cdots I)$ in step (1.1.4) instead of the free radical $I^\bullet$ is energetically more favorable, because the standard electrode potential of the iodine pair is $U^0(I^\bullet/I^-) = +1.33$ V, which is higher than $U^0(\mathbf{D}/\mathbf{D}^+)$ of most dye redox pairs. After addition of another I^-, the complex dissociates into the regenerated dye and an $I_2^{-\bullet}$ radical anion, whose formation in the process was proven spectroscopically.[60] Disproportionation of $I_2^{-\bullet}$ then leaves the oxidized species I_3^- and regenerates the second I^-. Fortunately, the complicated redox reaction nature of I^-/I_3^- results in a very slow electron transfer of injected electrons to I_3^- (k_7 in Figure 1.3),[61,62] allowing large electron diffusion lengths (favorable for path k_3) and charge collection efficiencies at the conduction material near unity.[63] Additionally, high diffusion coefficients are obtained for the relatively small sized I^- and I_3^- ions (path k_5), which are required for an efficient

redox pair regeneration. The mobility of I^-/I_3^- is high even in viscous liquids most probably due to a Grotthus-type mechanism.[64,65] Apart from that, iodide is highly soluble in most common solvents and very stable with respect to thermal degradation or decomposition.

Unfortunately, the I^-/I_3^- redox pair also has some drawbacks. The regeneration mechanism implicates that $I^-/I_2^{-\bullet}$ is the actual redox pair in the process. The estimated potential loss of $\approx 430\,\mathrm{mV}$ between the redox potentials of $I^-/I_2^{-\bullet}$ and I^-/I_3^- necessitates a large dye regeneration overpotential when the I^-/I_3^- pair is used.[66] This directly limits the maximum V_{OC} to $\approx 0.8\,\mathrm{V}$, which is one of the biggest drawbacks when using this redox pair.[67] Additionally, many modern dyes, which are believed to be superior to the common ruthenium dyes are observed to perform worse because of the incompatibility with the I^-/I_3^- redox pair, inherently limiting the progress and advance in DSC research.[27,68–70]

The search for alternative redox pairs revealed a variety of approaches. Very similar redox pairs such as Br^-/Br_3^-,[45,71] $SCN^-/(SCN)_3^-$,[72,73] or $SeCN^-/(SeCN)_3^-$ [72–74] were tested with mixed success. Transition metal based organometallic compounds quickly became the center of interest because of their simple one-electron transfer redox mechanism. For example, ferrocene was utilized, but mainly to study the nature of recombination pathways in a DSC, because the high recombination of injected electrons with ferrocene (path k_7) extremely decreases the device performance.[75] Although a blocking layer was shown to decrease the undesired back transfer of electrons,[75] only little attention was paid to the ferrocene redox couple on the whole. Nickel- or copper-containing redox couples were employed in DSCs. Notably, $Ni^{III/IV}$-bis(dicarbollide) showed promising results due to fast regeneration of the dye and a low corrosive behavior.[76] Whereas a very similar copper–phenanthroline complex showed similar positive properties, a low driving force of dye regeneration rendered this system inferior.[77]

To date, the most promising alternative to the well established I^-/I_3^- involves organometallic cobalt polypyridyl complexes, which were used successfully in different approaches.[57,78–82] The best performing porphyrin DSC achieving efficiencies of up to 13 % utilized the tris(2,2'-bipyridyl)$cobalt^{II/III}$ redox couple.[34] The success of the Co redox shuttle is mainly attributed to the simple outer-sphere electron transfer mechanism, which allows for a simple redox mechanism consistent with Marcus theory, and no specific binding site at the dye is required. While showing an efficient dye regeneration, the relatively large reorganization energy of the redox pair results in slow recombination with conduction band electrons, which is clearly superior to the other outer-sphere redox couples based on Fe, Ni, and Cu.[78] Furthermore, functionalization of the ligands is capable of tuning the energetics. By adjustment of the energy levels of redox pair and employed dye, the loss due to the dye regeneration overpotential can be minimized. This allows for very high values of V_{OC} up to 1 V,[34] and consequently, very high efficiencies. One drawback of the Co redox systems are the rather bulky

polypyridyl ligands, leading to decreased diffusion constants, and ultimately to mass transport limitations in some cases.[83,84]

Ondersma *et al.* predicted in a recent article that the redox shuttle will play the key role in increasing DSC device efficiencies.[67] The authors reported a model route to achieve efficiencies of up to 20 % with DSCs by mainly focusing on the redox potential and reorganization energy of the redox pair. Additionally, the recombination reactions of conduction band electrons with the redox pair were determined as crucial. The reduction of this pathway either by decreasing the number of surface states, using different photoanode materials, or passivation strategies is necessary to successfully employ alternative redox couples.[67]

1.1.4 Counter Electrode

The most important task for the CE is the efficient regeneration of the redox pair. The regeneration mechanism can affect the current–voltage characteristic of a DSC, and poor regeneration leads to a lowered fill factor.[85] Using conducting glasses such as FTO ensures good electron transport to the surface, but the very high charge transfer resistance to the redox pair is limiting.[86] By deposition of a catalytic thin layer of platinum, the charge transfer resistance is lowered significantly, and efficient regeneration of the redox mediator is ensured. Very low Pt-loadings of $\approx 5\ \mu\mathrm{gcm}^{-2}$ are needed, because the CE needs to be transparent. A durable coating can be achieved, for example, by thermal decomposition of platinum chloride compounds.[87] Moreover, carbon materials,[88–90] conducting polymers,[91–93] and cobalt sulfides[94] have been applied successfully as alternative CE materials.

1.1.5 Electrolyte

The remaining key fragment for a complete DSC is, of course, the electrolyte.[95] The electrolyte influences the dye/TiO_2 interface, the redox pair/dye interface, the redox pair/CE interface, and is the solvent for the redox pair and all additives. As such, it plays a very crucial role in the overall performance of the cell,[54] and the electrolyte has to meet certain requirements for optimum performance:[96–98]

(i) The electrolyte must enable fast transport of charge carriers between CE and photoanode for efficient dye regeneration.

(ii) The electrolyte is required to be durable, including chemical, thermal, interfacial, optical, and electrochemical stability.

(iii) The electrolyte should not compete with the dye on light absorption. Ideally, the electrolyte does not absorb light in the UV, visible, or near infrared region.

Generally, all electrolytes can be classified into three major categories: (i) liquid electrolytes,[99,100] (ii) quasi-solid electrolytes,[96,101] and (iii) solid-state conductors.[102,103]

In the case of quasi-solid electrolytes, the most noteworthy and successful approaches are thermosetting polymer electrolytes,[104] thermoplastic polymer electrolytes,[105] composite polymer electrolytes,[102] and quasi-solid ionic liquid electrolytes.[100] As far as solid-state electrolytes are concerned, those worth mentioning are ionic conductors,[106–109] inorganic hole transport materials,[102,110–112] and organic hole transport materials.[103,113–115]

Whereas all of the abovementioned technologies can be assigned to categories (ii) and (iii), the following will focus on liquid electrolytes. In addition to the aforementioned prerequisites, a suitable liquid electrolyte should additionally be a good solvent for the redox pair and potential additives, by which it should not dissolve the adsorbed dye, the TiO_2 nanoparticles, or other components such as the platinum coating of the CE. The electrolyte should have a low viscosity to guarantee fast diffusion of the redox shuttle and good interfacial contact at the dye/TiO_2 and CE interfaces. It should have a wide liquid range, ideally from $-20°C$ to $100°C$, which is mandatory for outdoor working conditions. With respect to competitiveness, a low cost and a low toxicity of the electrolyte are very advantageous.

Traditionally employed, and still one of the most frequently used electrolyte solvents, is acetonitrile (MeCN). Possible alternatives with a history of application include water, ethanol, diethyl carbonate, propionitrile, valeronitrile (BuCN), or glutaronitrile, and all mixtures thereof.[95] Unfortunately, until now, there is no optimum solvent that fulfills all requirements perfectly. The best performing modern DSCs usually use a mixture of MeCN and BuCN (v/v 50/50[116] or 85/15[117]) when tested under laboratory conditions. The excellent stability, low viscosity, and compatibility with almost all components are ideal for testing new dyes, redox shuttles, cell geometries, or other parameters, and simultaneously grant a certain comparability and reproducibility between different setups, or even laboratories. For industrial use however, the relatively low boiling point of MeCN (82°C) is critical and causes long term-stability issues due to loss through evaporation and leakage, and the relatively high toxicity of MeCN is also troubling. This durability limit is a common denominator for most volatile organic solvents, and solutions are being found in the form of the aforementioned quasi-solid and solid-state electrolytes, or by utilization of ionic liquids (ILs).

1.2 Ionic Liquids

Ionic liquids are liquids entirely composed of ions, which have by definition a melting point below 100°C. In a more narrow sense, ILs are often required to have a melting point much lower than 100°C to be useful in various applications, which is why room-temperature ionic liquids—ILs with melting point well below standard conditions—are distinguished. A typical ionic liquid is composed of ions with low symmetry and delocalized charges, which reduces attractive Coulombic forces between the ions and hinders

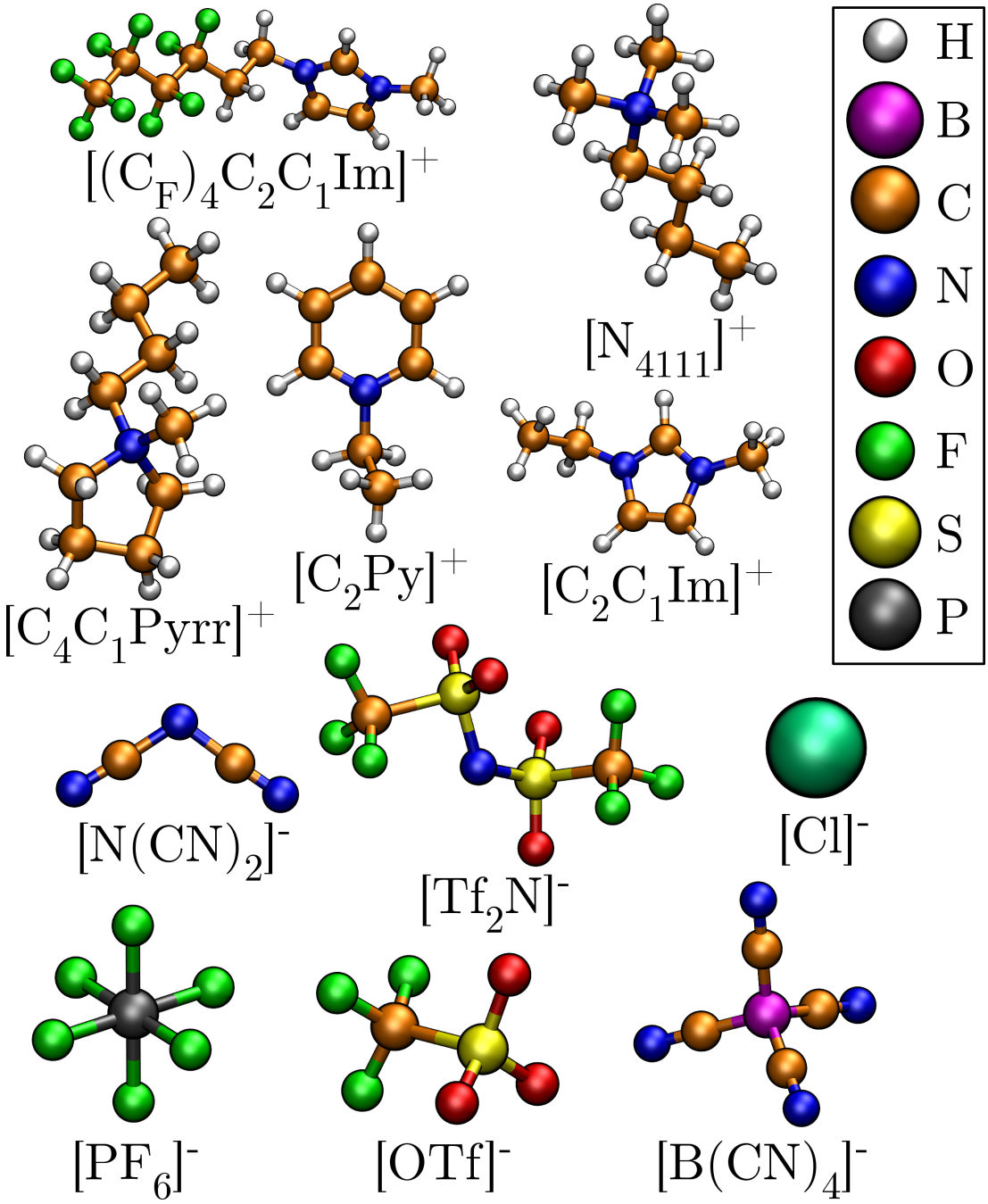

Figure 1.5: Typical IL building blocks. Cations: $[(C_F)_4C_2C_1Im]^+$ = 1-(3,3,4,4,5,5,6,6,6-nonafluorohexyl)-3-methylimidazolium, $[N_{4111}]^+$ = butyl-trimethylammonium, $[C_4C_1Pyrr]^+$ = 1-butyl-1-methylpyrrolidinium, $[C_2Py]^+$ = 1-ethylpyridinium, $[C_2C_1Im]^+$ = 1-ethyl-3-methylimidazolium. Anions: $[N(CN)_2]^-$ = dicyanamide, $[Tf_2N]^-$ = bis(trifluoromethylsulfonyl)imide, $[Cl]^-$ = chloride, $[PF_6]^-$ = hexafluorophosphate, $[OTf]^-$ = triflate, $[B(CN)_4]^-$ = tetracyanoborate.

the building of a highly ordered crystal structure. Common cations and anions—the building blocks of modern ILs—are shown in Figure 1.5.

In addition, conscious choice of the cation–anion combination can lead to exceptional properties of the resulting IL, most notably negligible vapor pressure, high thermal, chemical, optical, and electrochemical stability, low toxicity up to biodegradability, high ionic conductivity, and non-flammability. Ionic liquids have been proven useful in various applications, especially in the energy sector,[133] for example in the context of advanced battery technologies (*e.g.*, lithium-ion cells,[134–138] sodium-ion cells,[139,140] magnesium batteries,[141–143] or primary and secondary metal-air batteries[141,144,145]), fuel cells,[146–148] thermo-electrochemical cells,[149] supercapacitors,[150–152] actuators,[153] water splitting,[154,155] and CO_2 capture and separation.[156–159] These highly promising properties of ILs and their wide-ranged applications were not unnoticed in the DSC community, and many attempts to replace the volatile organic electrolyte with the IL electrolyte have been reported.

1.2.1 Ionic Liquids in Dye-Sensitized Solar Cells

A non-exhaustive overview of recent and promising IL-electrolyte-based DSCs is given in Table 1.1. The decisive incentive to use ILs in DSCs is to overcome stability issues caused by degradation, evaporation, or leakage of the traditional electrolytes. A high durability is required before DSCs can be commercialized. Without this consistency, DSCs could not compete with rivaling technologies.

As can be seen from Table 1.1, none of the cell-defining parameters are outstanding with regard to the maximum possible. The efficiencies reported are usually lower in regards to the best performing electrolyte, mostly composed by the aforementioned organic solvents such as MeCN. The cause of this is often lower values of I_{SC}, which arise due to mass transport limitations of the redox pair. Multiple approaches reduce this problem. The viscosity of the IL is crucially related to the diffusion of the redox shuttle. Therefore, reduction of the ILs viscosity by either choosing low-viscosity ILs such as $[C_2C_1Im][N(CN)_2]$ or $[C_2C_1Im][B(CN)_4]$,[120,121,160–165] or by using eutectic mixtures of different ILs to reach lower viscosities than the individual components[131,166–168] was shown to yield significantly enhanced results. Additionally, when using the I^-/I_3^- redox pair in viscous ILs, mass transport limitations can be reduced by exploiting the Grotthus-type diffusion of iodide.[64,65,100,169] This type of transport can be stimulated by higher concentrations of iodide, which are easily achievable by adding a respective iodide-IL (*e.g.*, $[C_3C_1Im][I]$), and is enhanced by the strong ionic field in ILs due to the kinetic salt effect.[65] It should be noted that the maximum content of the I^-/I_3^- redox pair is limited as certain drawbacks of the redox pair become dominant at high concentrations, such as corrosion, photoabsorption, or increased recombination with conduction band electrons.

An interesting way to tune the device properties are electrical additives in the elec-

Table 1.1: Overview of Different Ionic Liquid Based DSCs Taken from References 100 and 95 with Characteristic Parameters[a]

electrolyte composition	$D(I_3^-)$ / cm^2s^{-1}	I_{SC} / $mAcm^{-2}$	V_{OC} / mV	FF	η / %	dye	Ref.
0.2 M I_2, 0.5 M NMBI in $[C_3C_1Im][I]$/ $[C_2C_1Im][C(CN)_3]$ (v/v 1/1)	6.3×10^{-7}	12.8	752	0.764	7.4	**Z907Na**	118
5 mM I_2, $[C_6C_1Im][I]$/ $[C_2C_1Im][Tf_2N]$ (v/v 1/9)	3.4×10^{-7}	11.8	570	0.72		**N3**	64
0.2 M I_2, 0.14 M [Guan][SCN], 0.5 M TBP in $[C_3C_1Im][I]$/ $[C_2C_1Im][SCN]$ (v/v 13/7)	2.95×10^{-7}	13.3	746	0.72	7.0	**Z907**	119
0.1 M I_2, 0.1 M LiI, 0.45 M NMBI in $[C_3C_1Im][I]$/ $[C_2C_1Im][N(CN)_2]$ (v/v 13/7)	4.4×10^{-7}	12.8	707	0.727	6.6	**Z907**	120
0.2 M I_2, 0.5 M NMBI, 0.1 M [Guan][SCN] in $[C_3C_1Im][I]$/ $[C_2C_1Im][B(CN)_4]$ (v/v 13/7)	3.42×10^{-7}	13.55	736	0.698	7.0	**Z907Na**	121
0.8 M $[C_3C_1Im][I]$, 0.15 M I_2, 0.1 M [Guan][SCN], 0.5 M NMBI in MPN		15.1	747	0.699	8.0	**K19**	122
0.5 M I_2, 0.1 M CuI in $[C_6C_1Im][I]$		13.6	538	0.62	4.5	**N3**	123
0.2 M I_2, 0.5 M NMBI, 0.1 M [Guan][SCN] in $[AllylC_2Im][I]$/ $[AllylC_2Im][Tf_2N]$ (v/v 13/7)		13.54	700	0.717	6.8	**K60**	124
0.2 M I_2 in $[C_3C_1Im][I]$/ $[C_2C_1Im][Tf_2N]$/ $[C_2C_1Im][OTf]$ ($v/v/v$ 2/2/1)	2.48×10^{-7}	16.13	612	0.676	6.7	**D149**	125
0.2 M I_2, 0.5 M NMBI in $[C_3C_1Im][I]$	1.9×10^{-7}	13.07	678	0.71	6.3	**K19**	126
0.2 M I_2, 0.5 M NMBI, 0.12 M [Guan][SCN] in $[C_3C_1Im][I]$/ $[C_2C_1Im][SCN]$ (v/v 13/7)	3×10^{-7}	13.99	707	0.71	7.1	**K19**	127
0.12 M I_2, 0.5 M KI, 0.9 M $[C_4C_1Im][I]$ in GBL		17.65	602	0.58	6.2	**N3**	128
0.05 M $[Co((C_1Im\text{-}Bpy)PF_6)_3][(PF_6)_2]$, 0.02 M $[NO][BF_4]$, 0.14 M [Guan][SCN], 0.5 M TBP in $[C_3C_1Im][I]$/ $[C_2C_1Im][SCN]$ (v/v 13/7)		15.1	706	0.691	7.4	**N719**	128
1 M $[C_3C_1Im][I]$, 0.1 M I_2, 0.2 M $[Li][Tf_2N]$, 0.5 M NBB in MPN		15.3	661	0.669	6.8	**D205**	129
1 M $[C_3C_1Im][I]$, 0.1 M 4-OH-TEMPO, 0.01 M $[NO][BF_4]$, 0.2 M $[Li][Tf_2N]$, 0.5 M NBB in MPN		17.4	710	0.58	7.2	**D205**	129
1 M $[C_3C_1Im][I]$, 0.1 M $[C_1Im\text{-}TEMPO][Tf_2N]$, 0.01 M $[NO][BF_4]$, 0.2 M $[Li][Tf_2N]$, 0.5 M NBB in MPN		18.4	729	0.608	8.2	**D205**	129
0.1 M I_2, 0.1 M LiI in $[C_3C_1Im][I]$/ $[C_2C_1Im][BOB]$ (v/v 3/1)		13.91	539	0.65	5.4	**N719**	130
1 M $[C_1C_1Im][I]$, 0.15 M I_2, 0.5 M NBB, 0.1 M [Guan][SCN] in MPN		17.51	771	0.709	9.6	**C103**	131
1 M $[C_1C_1Im][I]$, 0.15 M I_2, 0.5 M NBB, 0.1 M [Guan][SCN], 50 mM NaI in BN	4.6×10^{-5}	17.9	733	0.76	10.0	**C106**	132

[a]The parameters are: Diffusion constant D of I_3^-, open-circuit voltage V_{OC}, short-circuit current I_{SC}, fill factor FF, and device efficiency η. Parameters were measured under 1000 Wm^{-2} illumination intensity at AM 1.5 G. NMBI is *N*-methylbenzimidazole, MPN is 3-methoxy-propionitrile, TBP is 4-*tert*-butylpyridine, TEMPO is 2,2,6,6-tetramethyl-piperidine-1-oxyl, Guan is guanidinium, GBL is γ-butyrolactone, NBB is *N*-butyl-benzimidazole, BN is butyronitrile, and BOB is bis(oxalate)borate.

trolyte, which can positively influence the redox couple potential, the electrolyte–semiconductor interface, the semiconductor's conduction band edge and Fermi energy, and various kinetics, ultimately improving the overall DSC performance.[170,171] A very good example is 4-*tert*-butylpyridine (TBP): The molecule adsorbs on the TiO_2 surface,[172] elevating the conduction band edge of the semiconductor.[173,174] This causes an increase of V_{OC}, and consequently the efficiency η, if the other key parameters of Equation (1.1.1) can be kept constant. Not surprisingly, TBP and analogs soon became one of the most frequently used additives in modern electrolytes.[19,172,174–178] TBP's counterpart with respect to the energy level alignment are cationic additives, most notably lithium ions (Li^+) and guanidinium ions ($[Guan]^+$, $[C(NH_2)_3]^+$). The cations adsorb on the semiconductor's surface as well, causing an energetic downward shift of the band levels.[28,177,179–183] While decreasing V_{OC} on first sight, the electron injection k_2 is enhanced due to a more favorable offset between the excited dye energy and the conduction band energy, which increases the short-circuit current I_{SC}. Additionally, adsorption of the cations at the semiconductor interface builds a blocking layer, which decreases electron recombination (k_7) and effectively increases V_{OC}.[183–185] Paradoxically, while the addition of basic molecules and cations to the electrolyte has contrary effects on the energetics of the semiconductor, simultaneous use is reported to be superior to separate use and both benefits can operate together: The conduction band edge is elevated by the Lewis base, increasing V_{OC}, and the cations form a blocking layer at the surface suppressing electron recombination.[131,167,177,180,186]

Interestingly, ILs can partly function as those additives. In fact, the guanidinium ion is usually introduced to the electrolyte by adding [Guan][SCN] (guanidinium thiocyanate), which has a melting point of 120°C and is therefore almost an ionic liquid. In typical ILs, the cations will take the role of surface adsorption, building the blocking layer, and lowering the conduction band edge. Consequently, the anions carry out the role of the Lewis base such as TBP, which means elevating the conduction band level. For example, differences in performance of DSCs utilizing a $[C_2C_1Im][N(CN)_2]$ IL electrolyte or $[C_2C_1Im][B(CN)_4]$ IL electrolyte could be traced to differences in V_{OC} from different conduction band positions caused by the different coordination strengths of the anions.[161] A detailed investigation on the capabilities of ILs in this regard is part of the present thesis and presented in Section 3.4. Moreover, IL electrolyte based DSCs can be enhanced by additives in the same way as traditional organic solvent DSCs. With this approach, the band level of TiO_2 in a $[C_2C_1Im][N(CN)_2]$ IL electrolyte DSC could be gradually changed by the addition of Li^+, tailoring the band levels to reach a maximum efficiency of 8.4 %.[162]

Apart from the favorable physical properties of ILs that enhance their durability and function at the various interfaces, ILs are also chemically very interesting because of their potential to be functionalized and tuned in numerous ways. In this regard, the term "task-specific ionic liquid" (TSIL) was formed in 2000 by Davis and cowork-

ers,[187] which generally describes an IL that was functionalized in a way to perform a certain task better than the unfunctionalized analog or to enable a certain functionality. In order to use a $Co^{II/III}$-based redox shuttle in IL-DSCs, Xu *et al.* designed the ligands of the central cobalt atom to be hybrid IL/bipyridine, which significantly increases the solubility of the redox shuttle in the electrolyte (see Table 1.1, Reference 128). An efficiency of 7.37 % under 1000 Wm^{-2} AM 1.5 G illumination was reported, which was superior to the comparable I^-/I_3^- cell. In an analog way, a TEMPO(2,2,6,6-tetramethyl-piperidine-1-oxyl)-functionalized imidazolium IL, $[C_1Im\text{-}TEMPO][Tf_2N]$, was synthesized to be used as an alternative redox pair in conjunction with iodide.[129] It is stated that the TEMPO-IL suppresses the formation of I_3^- in the usual redox cycle (see reaction (1.1.7)). Instead, $I_2^{-\bullet}$ reacts with $[C_1Im\text{-}TEMPO]^+$, forming $2\,I^-$ and the oxidized $[C_1Im\text{-}TEMPO]^{2+}$, which is regenerated at the CE. In this way, the dye regeneration overpotential is reduced, which is one of the common drawbacks when using the I^-/I_3^- redox pair, and superior cell performance is achieved (see Table 1.1, Reference 129).

1.3 Computational Chemistry as Powerful Tool in DSC Research

An essential point to consider is that many of the recent developments and advances have been achieved because a detailed understanding of the underlying physical and chemical phenomena was pursued, giving guidance to forthcoming design and exploration. Of course, many experimental techniques are available when it comes to the characterization of certain systems, but additionally, computational chemistry can be the powerful toolbox needed.

A premium example of the incorporation of computational chemistry in PV research is the engineering of dyes for the use in DSCs. As discussed earlier, an efficient dye has to meet certain requirements, but synthesis and characterization of a multitude of dyes can be a very time-consuming and inefficient way to tackle the problem. The characterization of spectroscopic properties can routinely be done with efficient quantum chemical models, such as time-dependent density functional theory (TD-DFT).[188–191] The potential of different dyes, functionalizations, and modifications can be evaluated quickly, and insights on trends and opportunities can be gained. Additional information, such as the alignment of HOMO and LUMO energy, or localization of the respective orbitals can be extracted to further aid evaluating the potential of a dye before it is actually synthesized. Nowadays, the TD-DFT characterization of new dyes is routinely done and accompanies the experimental documentation in numerous works. In this regard, Mathew *et al.* explored and optimized the light-harvesting capabilities and compatibility with a $Co^{II/III}$ redox pair of a **Do**–π–**Acc**-kind panchromatic porphyrin dye aided by TD-DFT, achieving the record efficiency of 13.0 %.[34] In a purely computational

work, Bayliss *et al.* used DFT and TD-DFT methods to find and modify a number of organic dyes and their respective spectral response to assess the applicability of the dyes in DSCs, with a special emphasis on their suitability for co-sensitization.[192]

Apart from electronic characterization, computational chemistry can be used to gain detailed insight into molecular arrangements, configurations, or adsorption behavior when it comes to the different interfaces in a DSC. An established method to extract structural as well as dynamical information of a system is molecular dynamics (MD). Here, the system is propagated in real time, and the course of the system—the trajectory—contains an overwhelming amount of information ready to be evaluated. While it is very hard to simulate a whole DSC system, reasonable subsystems can be modeled with MD simulations. Especially the liquid phase, including the electrolyte with possible additives, and the related interfaces with the semiconductor, dye, or the counter electrode are appealing targets for MD.

MD—classical or *ab initio*—is very capable of describing complicated systems, such as an IL/crystalline surface interface. As an example, the layering behavior and surface-charge effects of a $[C_4C_1Im][Tf_2N]$ IL thin film deposited on a mica surface was characterized using classical MD,[193] complementing atomic force microscopy measurements. In another case, high-resolution X-ray reflectivity studies on a $[C_2C_1Im][Tf_2N]$/sapphire surface were not only reproduced by classical MD, the simulation could then be used to gain insight on an atomistic level, revealing the importance of surface layering and surface hydroxyl groups for this specific system.[194]

In the context of DSCs, Byrne *et al.* used *ab initio* MD (AIMD) simulations to investigate the adsorption of the ruthenium dye **N719** on an anatase (101) surface in the liquid phase, namely the $[C_4C_1Im][Tf_2N]$ IL.[195] It was concluded that the IL solvation influences the adsorption geometry, and stabilizes binding of the dye at the surface. The authors also stress the importance of explicit solvation in their study, as a comparable AIMD *in vacuo* showed strongly deviating results.[195] Moreover, the adsorption modes of **N719** were also investigated with explicit MeCN solvation utilizing AIMD methods.[196] The adsorption mode was found to be influenced by the protonation of the titania surface, and conversion of bidentate and monodentate binding modes was observed.[196] Related work also includes other ruthenium dyes,[197] the influence of additives such as TBP or Na^+,[198] or the TD-DFT absorption spectrum of adsorbed ruthenium dyes including the surface.[199]

First-principle investigations were also extended to TiO_2 surfaces with organic sensitizers and water or acetonitrile solvent.[200] Again, crucial effects of explicit solvation on the dye's binding motifs were reported, but also on titania's density of states (DOS), which is significantly upshifted with respect to the vacuum levels.[200]

Information and knowledge about the surface-adsorbate electronic structure is of importance, because this determines the rate of the electron injection and recombination processes, which are key mechanisms in the working cycle of DSCs. In this regard, the

electronic structure of the surface/dye interface of benzoic acid as a model dye adsorbed on rutile (110) and anatase (101) was inspected as a first step toward the modeling of injection and recombination rates.[201] Furthermore, the average spatial separation between a Ru-dye's HOMO and the TiO_2 surfaces (001) and (101) was examined by De Angelis *et al.*[197] The larger distance for the (001) surface translates to a retardation of charge recombination kinetics, which is in agreement with experimental findings.[197]

Using TD-DFT, the squarine-sensitized TiO_2 surface was described on an atomistic level, and domination of an indirect electron injection mechanism for this system was verified.[202] This study was followed by the complete characterization of the TiO_2/dye/solvent heterointerface by combined MD and static calculations involving the squarine dye with water as solvent.[203] The desorption process of the dye in the presence of water was modeled by AIMD, and the spectroscopic properties of the whole, now solvated, system could be determined via TD-DFT.[203]

Moreover, the interesting alizarin/TiO_2 system could be understood with the help of nonadiabatic real-time AIMD simulations.[204] The distinguishing mark of this system is that the photoexcited state of the azirin dye is energetically slightly below the titania's CB, which essentially means that there is no driving force for the electron injection, and yet ultrafast electron injection in the order of 6 fs is observed.[205] Due to the finite temperature effects in the AIMD, in contrast to static calculations at 0 K, fluctuations in the energy levels and atomic positions occur, enabling the fast injection.[204] On one hand, this study shows the power of AIMD simulations to accurately model and understand such systems. On the other hand, the system itself is very intriguing because there is no energetic loss due to the missing electron injection overpotential, providing new design opportunities within the general concept of a DSC.

Some work also focused purely on the electrolyte/semiconductor interface, as understanding this subsystem is crucial for the perception of the whole DSC. Consequently, AIMD simulations were performed for different pure solid/liquid interfaces, including H_2O/anatase(101),[206–208] H_2O/brookite(210),[207] H_2O/rutile(110),[209] HCOOH/anatase(101),[207] HCOOH/brookite(210),[207] MeCN/anatase(101)[210,211] and MeCN/H_2O/anatase(101).[211]

In summary, the electrolyte plays a crucial role in the DSC, and most of the drawbacks arising from volatile and sometimes toxic organic solvents can be overcome to a good extent upon replacement with ILs, unfortunately at the price of lower device efficiencies. One must keep in mind that, while high efficiencies are definitely desired, they are not the sole defining parameter of a good DSC. The position that DSCs would seize in a future energy market needs to be considered, which is to give a cheap, readily available, and universally applicable method to harvest sunlight even under difficult conditions. DSCs will probably never compete in sectors where cost is a minor issue and performance is the decisive parameter, for example in astronautics. Therefore, offering a small portion of the possible maximum efficiency for a dramatically increased

durability by using ionic liquid electrolytes seems like a fair trade.

2 Methods

2.1 Hartree–Fock Theory

The foundation of modern electronic structure theory is the time-independent Schrödinger equation,

$$\mathscr{H}|\Phi\rangle = \mathscr{E}|\Phi\rangle, \tag{2.1.1}$$

with the Hamiltonian operator $\mathscr{H}$, the time-independent wavefunction (WFN) $\Phi(\mathbf{r}_i, \mathbf{R}_A)$, depending on positions of all electrons $\mathbf{r}_i$ and nuclei $\mathbf{R}_A$, and the energy eigenvalue of the system $\mathscr{E}$. For a system containing N electrons and M nuclei, the Hamiltonian in atomic units reads

$$\begin{aligned}\mathscr{H} &= \mathbf{T}_\mathrm{e} + \mathbf{T}_\mathrm{n} + \mathbf{V}_\mathrm{en} + \mathbf{V}_\mathrm{ee} + \mathbf{V}_\mathrm{nn} \\ &= -\sum_{i=1}^{N} \frac{1}{2}\nabla_i^2 - \sum_{A=1}^{M} \frac{1}{2M_A}\nabla_A^2 - \sum_{i=1}^{N}\sum_{A=1}^{M} \frac{Z_A}{r_{iA}} + \sum_{i=1}^{N}\sum_{j>i}^{N} \frac{1}{r_{ij}} + \sum_{A=1}^{M}\sum_{B>A}^{M} \frac{Z_A Z_B}{R_{AB}}.\end{aligned} \tag{2.1.2}$$

The Hamiltonian is a sum of different operators, describing the kinetic energy of the electrons $\mathbf{T}_\mathrm{e}$ and the nuclei $\mathbf{T}_\mathrm{n}$, as well as electron–nuclei ($\mathbf{V}_\mathrm{en}$), electron–electron ($\mathbf{V}_\mathrm{ee}$), and nucleus–nucleus ($\mathbf{V}_\mathrm{nn}$) Coulombic interactions. The expression contains the Nabla-operator ∇, which implies spatial differentiation, the mass M_A and nuclear charge Z_A of nucleus A, and the electron–nucleus distance $r_{iA} = |\mathbf{r}_i - \mathbf{R}_A|$, the electron–electron distance $r_{ij} = |\mathbf{r}_i - \mathbf{r}_j|$, and the nucleus–nucleus distance $R_{AB} = |\mathbf{R}_A - \mathbf{R}_B|$.

Born–Oppenheimer Approximation. The mass of any nucleus is much larger than the mass of an electron. Therefore, the nuclei's movements are much slower with respect to the electrons, and we can consider the movement of electrons in a field of heavy, fixed nuclei. This ansatz is the popular Born–Oppenheimer approximation. Regarding Equation (2.1.2), the kinetic energy of the nuclei $\mathbf{T}_\mathrm{n}$ vanishes, because they are fixed, and the Coulombic interaction $\mathbf{V}_\mathrm{nn}$ reduces to a constant. The remaining term is the

electronic Hamiltonian

$$\begin{aligned}\mathscr{H}_{\text{elec}} &= \mathbf{T}_{\text{e}} + \mathbf{V}_{\text{en}} + \mathbf{V}_{\text{ee}} \\ &= -\sum_{i=1}^{N} \frac{1}{2}\nabla_i^2 - \sum_{i=1}^{N}\sum_{A=1}^{M} \frac{Z_A}{r_{iA}} + \sum_{i=1}^{N}\sum_{j>i}^{N} \frac{1}{r_{ij}}.\end{aligned} \tag{2.1.3}$$

Using $\mathscr{H}_{\text{elec}}$, a solution to the electronic Schrödinger function

$$\mathscr{H}_{\text{elec}}|\Phi_{\text{elec}}\rangle = \mathscr{E}_{\text{elec}}|\Phi_{\text{elec}}\rangle \tag{2.1.4}$$

can be found with the electronic WFN Φ_{elec}, which explicitly depends on the electron positions $\mathbf{r}_i$, and only parametrically on the nuclear coordinates $\mathbf{R}_A$. Consequently, the electronic energy depends parametrically on the nuclear coordinates (*i.e.*, $\mathscr{E}_{\text{elec}} = \mathscr{E}_{\text{elec}}(\{\mathbf{R}_A\})$), and the total energy of a system within the Born–Oppenheimer approximation would have to contain $\mathbf{V}_{\text{nn}}$ as well, which means

$$\mathscr{E}_{\text{tot}} = \mathscr{E}_{\text{elec}} + \sum_{A=1}^{M}\sum_{B>A}^{M} \frac{Z_A Z_B}{R_{AB}}. \tag{2.1.5}$$

If Φ_{elec} is known, the Born–Oppenheimer approximation can be extended to describe the motion of the nuclei. With the same justification of electrons moving much faster than the nuclei due to their small mass, it is reasonable to assume that moving nuclei experience only the average field of the electrons, which can be deduced from the electronic WFN. The nuclear Hamiltonian describing the motion of nuclei in the mean field of electrons is then given by

$$\begin{aligned}\mathscr{H}_{\text{nucl}} &= \mathbf{T}_{\text{n}} + \mathscr{E}_{\text{elec}} + \mathbf{V}_{\text{nn}} \\ &= -\sum_{A=1}^{M} \frac{1}{2M_A}\nabla_A^2 + \mathscr{E}_{\text{tot}}(\{\mathbf{R}_A\}).\end{aligned} \tag{2.1.6}$$

Figuratively speaking, Equation (2.1.6) states that the nuclei move on a potential surface $\mathscr{E}_{tot}$ obtained by solving the electronic Schrödinger equation. Given that the solution to the nuclear Schrödinger equation is $\Phi_{\text{nucl}}(\mathbf{R}_A)$, the Born–Oppenheimer approximation to the total WFN is

$$\Phi(\{\mathbf{r}_i\};\{\mathbf{R}_A\}) = \Phi_{\text{elec}}(\{\mathbf{r}_i\};\{\mathbf{R}_A\})\Phi_{\text{nucl}}(\{\mathbf{R}_A\}). \tag{2.1.7}$$

The corresponding energy contains the electronic, vibrational, rotational, and translational energy of the molecular system. In the following, we will concentrate on solutions to the electronic WFN and therefore, the subscript "elec" is dropped subsequently for the electronic Hamiltonian and related quantities.

Slater Determinant. A possible explicit expression for the electronic WFN is given by Slater determinants. The antisymmetric spin-orbital WFN Ψ of an N-electron system can be expressed as a Slater determinant:

$$\Psi(\mathbf{x}_1, \mathbf{x}_2, \ldots, \mathbf{x}_N) = \frac{1}{\sqrt{(N!)}} \begin{vmatrix} \chi_i(\mathbf{x}_1) & \chi_j(\mathbf{x}_1) & \ldots & \chi_k(\mathbf{x}_1) \\ \chi_i(\mathbf{x}_2) & \chi_j(\mathbf{x}_2) & \ldots & \chi_k(\mathbf{x}_2) \\ \vdots & \vdots & \ddots & \vdots \\ \chi_i(\mathbf{x}_N) & \chi_j(\mathbf{x}_N) & \ldots & \chi_k(\mathbf{x}_N) \end{vmatrix} \tag{2.1.8}$$

with the spin-orbitals $\chi_k(\mathbf{x}_N)$ and a normalization factor. The coordinate $\mathbf{x}$ unites the spatial coordinates $\mathbf{r}$ and the spin variable ω to a collective variable $\mathbf{x} = \{\mathbf{r}, \omega\}$. The Slater determinant is antisymmetric, which means that the many-electron WFN changes the sign with the interchange of any two electrons of the system, and it obeys the Pauli exclusion principle, which means that any spin-orbital can be occupied by at most one electron, otherwise the determinant vanishes. A short hand notation of the Slater determinant only involves the diagonal elements, and the electron labels are always chosen to be in the order $\mathbf{x}_1, \mathbf{x}_2, \ldots, \mathbf{x}_N$, which leads to

$$\Psi(\mathbf{x}_1, \mathbf{x}_2, \ldots, \mathbf{x}_N) = |\chi_i(\mathbf{x}_1), \chi_j(\mathbf{x}_2), \ldots, \chi_k(\mathbf{x}_N)\rangle = |\chi_i \chi_j \ldots \chi_k\rangle. \tag{2.1.9}$$

It is important to note that the Slater determinant includes exchange correlation for electrons of the same spin, but electrons with different spin are uncorrelated. Therefore, single Slater determinant wavefunctions are usually referred to as uncorrelated wavefunctions.

Hartree–Fock Approximation. Considering an N-electron system, the simplest antisymmetric WFN to describe the ground state of an electronic system with the corresponding electronic Hamiltonian $\mathscr{H}$ is given in the form of a Slater determinant

$$|\Psi_0\rangle = |\chi_1 \chi_2 \cdots \chi_a \chi_b \cdots \chi_N\rangle. \tag{2.1.10}$$

Following the variation principle, the best WFN yields the lowest energy E_0 of the system,

$$E_0 = \langle \Psi_0 | \mathscr{H} | \Psi_0 \rangle. \tag{2.1.11}$$

By variation of the spin-orbitals χ with respect to minimizing E_0 and constraining them to be orthonormal (*i.e.*, $\langle \chi_a | \chi_b \rangle = \delta_{ab}$), the Hartree–Fock (HF) equations are derived (in abbreviated notation, *i.e.*, $\chi_a(\mathbf{x}_j) = \chi_a(j)$), which determine the optimal

spin orbitals:

$$f(i)\chi_a(i) = \varepsilon_a \chi_a(i) \tag{2.1.12}$$

$$\left[h(i) + \sum_b \left(\mathscr{J}_b(i) - \mathscr{K}_b(i)\right)\right] \chi_a(i) = \varepsilon_a \chi_a(i) \tag{2.1.13}$$

with
$$h(i)\chi_a(i) = \left[-\frac{1}{2}\nabla_i^2 - \sum_A \frac{Z_A}{r_{iA}}\right] \chi_a(i) \tag{2.1.14}$$

and
$$\mathscr{J}_b(i)\chi_a(i) = \left[\int d\mathbf{x}_j |\chi_b(j)|^2 r_{ij}^{-1}\right] \chi_a(i) \tag{2.1.15}$$

and
$$\mathscr{K}_b(i)\chi_a(i) = \left[\int d\mathbf{x}_j \chi_b^*(j)\chi_a(j) r_{ij}^{-1}\right] \chi_b(i). \tag{2.1.16}$$

In these HF equations, $f(i)$ is the Fock-operator, which is an effective one-electron operator that yields the orbital energy ε_a of spin-orbital χ_a. $f(i)$ consists of three parts: (i) the core-Hamiltonian operator $h(i)$, describing the kinetic energy of a single electron and its Coulomb interaction with a field of fixed nuclei, (ii) the Coulomb operator $\mathscr{J}_b(i)$, which describes the average electrostatic potential at $\mathbf{x}_i$ originating from the electron in spin-orbital χ_b, and (iii) the exchange-operator $\mathscr{K}_b(i)$. The exchange-operator does not have a simple classical translation as for example $\mathscr{J}_b(i)$. It involves exchange of electrons i and j, and it is a nonlocal operator as it depends on the values of $\chi_a(j)$ throughout all space. Coulomb and Exchange are often summarized to be the Hartree–Fock potential ν^{HF}, reading

$$\nu^{\mathrm{HF}}(i) = \sum_b \left(\mathscr{J}_b(i) - \mathscr{K}_b(i)\right). \tag{2.1.17}$$

The Hartree–Fock equation

$$f|\chi_a\rangle = \varepsilon_a|\chi_a\rangle \tag{2.1.18}$$

is recognized as an eigenvalue equation, where the spin-orbitals χ_a are eigenfunctions and the spin-orbital energies ε_a are their corresponding eigenvalues.

In summary, the many-electron problem is approximated to be a one-electron problem, and the electron–electron interaction is considered on an averaged basis described by ν^{HF}. Unfortunately, the Fock-operator depends on the solutions of $\{\chi_a\}$, which means this set of equations is commonly solved iteratively. This is done by self-consistent field (SCF) methods.

In practice, the spin-orbitals are expanded in a finite set of known spatial basis functions $\phi_\mu(\mathbf{r}), \mu = 1, 2, \ldots, K$, which replace the spatial part of the spin-orbitals with spin α, and β, respectively. Both expansions can then be inserted in the eigenvalue Equations (2.1.18) to build the matrix eigenvalue equations of the expansion coefficients, which are the Roothaan equations. Using a set of K spatial basis functions,

solution of the Roothaan equations yields a set of $2K$ spin-orbitals, with the N lowest energy spin-orbitals being the occupied orbitals, and the remaining $2K - N$ orbitals being the unoccupied, or virtual, orbitals. The single Slater determinant of the N lowest energy spin-orbitals is then the variational single-determinant approximation to the ground-state WFN Ψ_0 of the system.

The quality of the solution, that means the ground-state energy E_0, can be improved by considering more basis functions. The exact solution to this equation is the Hartree–Fock limit, which is approached only for a complete basis set. Practically, of course, a finite basis set is used, and the quality of the solution will depend on the size of the basis set.

Another important aspect to keep in mind is that even for a complete basis set, the HF solution to an electronic system would not contain Coulomb correlation, which is the correlated motion of two electrons arising due to Coulomb repulsion. The reason is that this interaction is approximated by the average interaction between electrons, which is the basic idea of HF. The lack of correlation energy E_c is therefore the difference between the HF energy E_HF and the exact energy of the system, E_exact:

$$E_\mathrm{c} = E_\mathrm{exact} - E_\mathrm{HF}. \tag{2.1.19}$$

Methods beyond the HF approximation, called post-HF methods, are trying to exactly calculate or at least approximate E_c in order to improve the result, which often comes at the price of very high computational effort. Examples of post-HF methods that include electron correlation are configuration interaction methods, coupled cluster methods, or perturbation theory. As mentioned, these methods are usually much more expensive in terms of computational cost, and are therefore generally not suitable to study large systems, which is predominantly done in the present work. Consequently, these methods were not used to obtain the results presented herein, and will therefore not be discussed.

2.2 Density Functional Theory

The previously described methods require the calculation of the WFN, which can be a troublesome task for extended systems. In 1964, Hohenberg and Kohn stated that not only the WFN contains all information and properties of the system, but also the electron density $\rho(\mathbf{r})$ of a system is uniquely related to the ground state energy and further properties of the system,[212] which is one of two basic theorems in density functional theory (DFT). As the electron density $\rho(\mathbf{r})$ is a function itself, the energy E is a functional of $\rho(\mathbf{r})$:

$$E[\rho(\mathbf{r})] = \int V_\mathrm{ext}(\mathbf{r})\rho(\mathbf{r})d\mathbf{r} + F[\rho(\mathbf{r})]. \tag{2.2.1}$$

The first term includes all interactions of the electrons with an external potential V_{ext}, such as the potential of fixed nuclei within the Born–Oppenheimer approximation, and the second term $F[\rho(\mathbf{r})]$ is the functional containing the kinetic energy of the electrons and contributions from all electron–electron interactions. This means that we are interested in obtaining the electron density rather than the electronic WFN in order to calculate the desired properties. It is an interesting approach, because the electron density does only depend on three spatial coordinates $\mathbf{r}$, compared to the $4N$ coordinates of an N-electron WFN.

Unfortunately, the exact form of $F[\rho(\mathbf{r})]$ is not known, and Kohn and Sham suggested to approximate it by the sum [213]

$$F[\rho(\mathbf{r})] = E_{\text{KE}}[\rho(\mathbf{r})] + E_{\text{H}}[\rho(\mathbf{r})] + E_{\text{XC}}[\rho(\mathbf{r})] \tag{2.2.2}$$

with the kinetic energy $E_{\text{KE}}[\rho(\mathbf{r})]$, the Hartree electrostatic energy $E_{\text{H}}[\rho(\mathbf{r})]$, and the exchange and correlation energy $E_{\text{XC}}[\rho(\mathbf{r})]$.

Furthermore, Kohn and Sham reintroduced one-electron orthonormal orbitals $\psi_i(\mathbf{r})$, which are the Kohn–Sham orbitals in this formulation. The system of non-interacting electrons occupying the Kohn–Sham orbitals has the same electron density as the real system. Thus, the electron density can then be expressed as

$$\rho(\mathbf{r}) = \sum_{i=1}^{N} |\psi_i(\mathbf{r})|^2. \tag{2.2.3}$$

With the aid of these Kohn–Sham orbitals, the kinetic energy $E_{\text{KE}}[\rho(\mathbf{r})]$ in Equation (2.2.2) is then defined in the same manner as in the HF approximation, which is the kinetic energy of non-interacting electrons with the same electron density $\rho(\mathbf{r})$ as the real system:

$$E_{\text{KE}}[\rho(\mathbf{r})] = E_{\text{KE}}[\{\psi_i(\mathbf{r})\}] = \sum_{i=1}^{N} \int \psi_i(\mathbf{r}) \left(-\frac{\nabla^2}{2}\right) \psi_i(\mathbf{r}) d\mathbf{r}. \tag{2.2.4}$$

The Coulomb interaction energy, or Hartree electrostatic energy $E_{\text{H}}[\rho(\mathbf{r})]$, is calculated by the classical interaction of charge densities and summing over all possible pairs:

$$E_{\text{H}}[\rho(\mathbf{r})] = \frac{1}{2} \iint \frac{\rho(\mathbf{r}_1)\rho(\mathbf{r}_2)}{|\mathbf{r}_1 - \mathbf{r}_2|} d\mathbf{r}_1 d\mathbf{r}_2. \tag{2.2.5}$$

If we assume the external potential to arise only from the fixed nuclei, the variational Kohn–Sham equations read

$$\left[-\frac{\nabla^2}{2} - \sum_{A=1}^{M} \frac{Z_A}{|\mathbf{r} - \mathbf{R}_A|} + \int \frac{\rho(\mathbf{r}_1)}{|\mathbf{r} - \mathbf{r}_1|} d\mathbf{r}_1 + V_{\text{XC}}[\rho(\mathbf{r})]\right] \psi_i(\mathbf{r}) = \varepsilon_i \psi_i(\mathbf{r}), \tag{2.2.6}$$

with the exchange-correlation (XC) functional $V_{\mathrm{XC}}[\rho(\mathbf{r})]$, yielding the Kohn–Sham orbital energies ε_i. The XC functional V_{XC} is related to the exchange-correlation energy E_{XC} from Equation (2.2.2) by the relation:

$$V_{\mathrm{XC}}[\rho(\mathbf{r})] = \frac{\delta E_{\mathrm{XC}}[\rho(\mathbf{r})]}{\delta \rho(\mathbf{r})}. \tag{2.2.7}$$

The Kohn–Sham equations can be solved iteratively in a self-consistent fashion, but the last piece missing is the exchange-correlation (XC) functional V_{XC}. Unfortunately, the explicit form of this functional is unknown, and best approximation to V_{XC} has to be found. Different solutions will be discussed and summarized in the following.

Local Density Approximation. In a first attempt, the uniform electron gas, where the electron density is constant throughout all space is considered as a model system. The exchange-correlation energy per electron $\varepsilon_{\mathrm{XC}}[\rho(\mathbf{r})]$ in the uniform electron gas, which is again a functional of the electron density, is known analytically for all densities. If we assume that the XC energy of an electron in the real system equals the XC energy of an electron in the uniform electron gas with the same electron density, the total XC energy would be obtained by integration over the whole space:

$$E_{\mathrm{XC}}[\rho(\mathbf{r})] = \int \rho(\mathbf{r}) \varepsilon_{\mathrm{XC}}[\rho(\mathbf{r})] d\mathbf{r}. \tag{2.2.8}$$

Differentiation according to Equation (2.2.7) then yields the exchange-correlation functional:

$$V_{\mathrm{XC}}^{\mathrm{LDA}}[\mathbf{r}] = \rho(\mathbf{r}) \frac{\delta \varepsilon_{\mathrm{XC}}[\rho(\mathbf{r})]}{\delta \rho(\mathbf{r})} + \varepsilon_{\mathrm{XC}}[\rho(\mathbf{r})]. \tag{2.2.9}$$

This means, the XC energy is calculated based on the assumption that any point $\mathbf{r}$ in the inhomogeneous real electron density is surrounded by a constant electron density with the same value as at this point. Consequently, only the local density is considered, and therefore it is called the local density approximation (LDA). This simple approximation yields surprisingly good results and shows the power of density functional theory. Extending the LDA to open-shell systems is straightforward and called the local spin density approximation (LSDA).

Generalized Gradient Approximation. The basic idea of gradient-corrected (GC) functionals is to not only incorporate the value of the electron density at a given point in space as in the LDA, but also the changes to $\rho(\mathbf{r})$, *i.e.*, the gradient. Therefore, XC functionals that incorporate the derivative of $\rho(\mathbf{r})$ are summarized as generalized gradient approximation (GGA) functionals. Usually, the exchange and the correlation part are described independently, and the total exchange-correlation functional consequently consists of an exchange functional and a correlation functional.

A popular exchange functional was presented by Becke in 1988 (B88), which corrects the LDA exchange expression by an additional term including the gradient of $\rho(\mathbf{r})$.[214] It includes an empirical parameter, which was derived by fitting the exact exchange energies from HF calculations of noble gases. An equally popular expression for the correlation energy introduced by Lee, Yang, and Parr (LYP) incorporates local and non-local contributions as well as gradient contributions.[215] The corresponding parameters were derived by fitting to the correlation energy of helium. A complete GC exchange-correlation functional would then be built by both parts—exchange and correlation—such as the B-LYP (Becke – Lee, Yang, Parr) functional. A common and frequently used alternative functional is the Perdew–Burke–Ernzerhof (PBE) XC functional.[216–218] The exchange and correlation expressions contain enhancement factors for the respective LDA expressions, and are, in contrast to the B-LYP functional, free of empirical parameters.

As a logic extension, functionals that include higher order gradients to the electron density, or other higher order properties such as the orbital kinetic energy density, are summarized as meta-GGA functionals. The Becke95 (B95)[219] or the Tao–Perdew–Staroverov–Scuseria (TPSS)[220] functionals are examples in this category.

Hybrid Hartree–Fock and Density Functional Theory. If we compare HF and DFT theory in their orbital-based formulations, a significant difference is the explicit incorporation of exchange and correlation by definition within the DFT framework, since the HF theory is lacking the correlation energy. But, whereas DFT misses an explicit expression for the exchange energy, this contribution is calculated in an exact way in the HF approximation. Therefore, it is not surprising that attempts were made to include the exact HF exchange energy $E_{\mathrm{X}}^{\mathrm{HF}}$ obtained by the Slater determinant of the Kohn–Sham orbitals in the DFT energy. These mixed HF and DFT functionals are called hybrid functionals.

Unfortunately, replacing the DFT exchange energy completely by the HF exchange energy does not yield very good results, but a mixing of the different contributions was observed to be very favorable. In this regard, different hybrid functionals varying the mixing of all energies were presented in the last two decades. The more popular ones are, for example, the B3-LYP functional, which contains the contributions:

$$E_{\mathrm{XC}}^{\text{B3-LYP}} = (1-a_0)E_{\mathrm{X}}^{\mathrm{LDA}} + a_0 E_{\mathrm{X}}^{\mathrm{HF}} + a_{\mathrm{X}}\Delta E_{\mathrm{X}}^{\mathrm{B88}} + a_{\mathrm{C}}E_{\mathrm{C}}^{\mathrm{LYP}} + (1-a_{\mathrm{C}})E_{\mathrm{C}}^{\mathrm{LDA}} \quad (2.2.10)$$

with the parameters $a_0 = 0.20$, $a_{\mathrm{X}} = 0.72$, and $a_{\mathrm{C}} = 0.81$, which were derived by fitting to ionization potentials, proton affinities, and atomic energies.[221] Again, an empirical-parameter free alternative exists with the PBE0 hybrid functional,[216,217,222] which uses 25% of the HF exchange energy. Therefore, the PBE0 energy expression

reads

$$E_{\mathrm{XC}}^{\mathrm{PBE0}} = E_{\mathrm{C}}^{\mathrm{PBE}} + 0.75E_{\mathrm{X}}^{\mathrm{PBE}} + 0.25E_{\mathrm{X}}^{\mathrm{HF}}. \tag{2.2.11}$$

Many more hybrid functionals using different mixing recipes exist and all have different advantages and drawbacks. In general, inclusion of the exact exchange is found to significantly improve the overall results, but which fraction to use often depends on the property of interest. Most notably, the self-interaction error (SIE) is reduced, because the HF theory is completely free of the SIE.

A possible extension to hybrid functionals is to use the briefly mentioned correlated post-HF methods to also correct the correlation energy, for example by including non-local perturbation corrections to the correlation energy. These methods are commonly titled double-hybrid functionals, with the B2PLYP functional as a popular representative.[223]

Range-Separated Functionals. While the discussed functionals perform reasonably well for numerous applications, some problems are not described satisfactorily, for example the polarizability of long chains, excitations to Rydberg states or charge transfer (CT) excitations. This is mostly traced to the erroneous long-range behavior of the exchange potential. As the exact HF exchange provides the correct long-range behavior, this drawback can be overcome by long-range corrected (LC) functionals, which use different expressions for the short-range and long-range part of the exchange functional.

Exemplarily mentioned are the CAM-B3LYP[224] functional (CAM = Coulomb-attenuating method), which uses the B3LYP functional to describe the short-range section (19 % HF exchange), and a mixture of 65 % HF exchange and 35 % B88 exchange at long ranges. A smooth transition between both potentials is achieved by using a standard error function in the intermediate region. Another popular LC functional is ωB97X-D3,[225] which uses 100 % HF exchange for the long-range part. ωB97X-D3 also includes a dispersion correction, which will be discussed in the following.

Dispersion in DFT. One of the strongest areas of application of current DFT methods at the GGA level are extended, condensed phase systems, which are too large to be handled by higher-order methods. In the condensed phase, the importance of the ubiquitous van der Waals interactions, or London dispersion, is undoubted. Unfortunately, while standard GGA functionals describe the electron–electron interactions at short distances very well, they fail to describe the long-ranged London dispersion.[226–228] A multitude of different approaches to tackle this shortcoming have emerged in recent times,[229] but whereas most of these techniques cause a considerable additional computational effort, a semi-classical correction scheme seems to be sufficient for most problems. This correction, called DFT-D3 in it's latest iteration, adds a dispersion

energy E_{disp} to the DFT (or DFT/HF for hybrid functionals) energy:

$$E_{\text{tot}} = E_{\text{DFT/HF}} + E_{\text{disp}}. \tag{2.2.12}$$

The dispersion energy consists of a two-body term

$$E_{\text{disp}}^{(2)} = -\frac{1}{2} \sum_{A \neq B} \sum_{n=6,8} s_n \frac{C_n^{AB}}{r_{AB}^n (1 + 6(r_{AB}(s_{r,n} R_0^{AB})^{-1})^{-\alpha_n})}, \tag{2.2.13}$$

and optionally a three-body term

$$E_{\text{disp}}^{(3)} = \frac{1}{6} \sum_{A \neq B \neq C} \frac{C_9^{ABC} (3 \cos\theta_a \cos\theta_b \cos\theta_c + 1)}{r_{ABC}^9 (1 + 6(r_{ABC} R_0^{-1})^{-\alpha})}, \tag{2.2.14}$$

with the averaged isotropic n^{th}-order dispersion coefficients C_n for atom pairs AB and atom triples ABC, and density-functional dependent scaling parameters s_n.[230] As this analytic expression only depends on the positions of the nuclei, the whole D3 dispersion correction can be calculated at negligible cost compared to the computational cost of the simultaneous electronic structure calculation. Application of the dispersion correction is usually denoted by adding "-D3" to the used density functional, as in "PBE-D3". The D3 method accounts for an accurate yet efficient way to include dispersion correction for functionals of all qualities, and should be included at all times in modern DFT calculations, if no other dispersion correction scheme is used.

2.3 Time-dependent DFT

Up to now, only the electronic ground state of molecular systems is described—except for the case of the briefly mentioned correlated post-HF methods. However, the excited state is important to accurately describe a large group of properties, such as photoabsorption (UV/VIS spectroscopy), non-linear optics, or photochemistry. In DFT, the excited state can be accessed via time-dependent DFT (TD-DFT). The Runge-Gross theorem builds the foundation for this method; it is shown that if a TD perturbation is introduced to the ground state system, then the TD external potential is determined by the TD electronic charge density $\rho(\mathbf{r}, t)$ by an additive TD function.[231] This TD external potential can then be included in the calculation with the aid of linear-response (LR) theory.[188]

In the adiabatic approximation, which means the XC potential changes instantaneously and without memory to temporal changes, the TD density $\rho(\mathbf{r}, t)$ can be substituted by the time-independent density $\rho_t(\mathbf{r})$, which only depends parametrically on the time. In LR theory, the TD-DFT eigenvalue problem can then be formulated in

the matrix form

$$\begin{bmatrix} \mathbf{A} & \mathbf{B} \\ \mathbf{A}^* & \mathbf{B}^* \end{bmatrix} \begin{pmatrix} \mathbf{X} \\ \mathbf{Y} \end{pmatrix} = \omega \begin{bmatrix} 1 & 0 \\ 0 & -1 \end{bmatrix} \begin{pmatrix} \mathbf{X} \\ \mathbf{Y} \end{pmatrix}, \tag{2.3.1}$$

with single-electron excitation ($\mathbf{X}$) and de-excitation ($\mathbf{Y}$) eigenvectors, and the excitation energy ω. The matrix elements of $\mathbf{A}$ and $\mathbf{B}$ are defined as

$$A_{ia,jb} = \delta_{ij}\delta_{ab}(\varepsilon_a - \varepsilon_i) + 2\langle ia|jb\rangle - a_0\langle ij|ab\rangle + (1-a_0)\langle ia|f_{\mathrm{XC}}|jb\rangle, \tag{2.3.2}$$

$$B_{ia,jb} = 2\langle ia|bj\rangle - a_0\langle ib|aj\rangle + (1-a_0)\langle ia|f_{\mathrm{XC}}|bj\rangle \tag{2.3.3}$$

where the indices i, j refer to occupied orbitals, and a, b to unoccupied orbitals. The Fock-exchange mixing parameter a_0 occurs if hybrid functionals are used. The two electron integrals are defined as

$$\langle ia|jb\rangle = \iint \psi_i(\mathbf{r}_1)\psi_a(\mathbf{r}_1)\frac{1}{r_{12}}\psi_j(\mathbf{r}_2)\psi_b(\mathbf{r}_2)d\mathbf{r}_1 d\mathbf{r}_2. \tag{2.3.4}$$

The exchange-correlation kernel in the adiabatic approximation is finally given as

$$f_{\mathrm{XC}}(\mathbf{r}_1, \mathbf{r}_2) = \frac{\delta^2 E_{\mathrm{XC}}[\rho(\mathbf{r})]}{\delta\rho(\mathbf{r}_1)\delta\rho(\mathbf{r}_2)}. \tag{2.3.5}$$

With respect to the calculation of vertical excitations, the excitation energy of excitation I is ω_I, given already by Equation (2.3.1), and the corresponding intensity, or oscillator strength f_I can be calculated from the respective ground state (Ψ_0) and exited state (Ψ_I) stationary wavefunctions by

$$f_I = \frac{2}{3}\omega_I|\langle\Psi_0|\mathbf{r}|\Psi_I\rangle|^2. \tag{2.3.6}$$

In order to simplify the LR-TD-DFT eigenvalue problem, within the Tamm–Dancoff Approximation (TDA), matrix $\mathbf{B}$ of Equation (2.3.1) is neglected, which yields a new variational eigenvalue equation:[232]

$$\mathbf{A}\mathbf{X}_{\mathrm{TDA}} = \omega_{\mathrm{TDA}}\mathbf{X}_{\mathrm{TDA}}. \tag{2.3.7}$$

This approximation is accompanied by certain advantages apart from being computationally simpler. In the case of time-dependent HF (TD-HF), the TDA exactly yields the configuration interaction case for singles (CIS), and therefore, the excited state WFN is readily available as the linear combination of singly excited HF configurations. In the CIS case, the excited-state expectation values are then straightforwardly calculated by the reduced difference density matrix.[233] Moreover, by neglect of $\mathbf{B}$, the excitations are decoupled from de-excitations, and the ground-state stability problem is decoupled from the excited state problem.[234–236] Hence, considering that TDA is

an approximation, it often yields improved potential energy surfaces with respect to TD-DFT and is thus often superior to the original formulation.

Recently, a further simplification of the TDA was presented, called simplified TDA (sTDA).[237] In this framework, the response of the XC functional is neglected, and two-electron integrals are evaluated as damped Coulomb interactions between transition and charge density monopoles. Therefore, the simplified matrix $\mathbf{A'}$ results as:

$$A'_{ia,jb} = \delta_{ij}\delta_{ab}(\varepsilon_a - \varepsilon_i) + \sum_{A,B}^{M} \left(s_k q_{ia}^A \gamma_{AB}^K q_{jb}^B - q_{ij}^A \gamma_{AB}^J q_{ab}^B \right), \tag{2.3.8}$$

with the transition and charge density monopoles q_{pq} on atoms A and B, respectively, and Mataga–Nishimoto–Ohno–Klopman damped Coulomb operators for exchange-type integrals (γ_{AB}^K) and coulomb-type integrals (γ_{AB}^J).[238–240] The transition and charge density monopoles are derived via Löwdin population analysis,[241] and s_k takes values of $s_k = 2$ for singlet-singlet excitations, and $s_k = 0$ for singlet-triplet excitations, effectively enforcing the spin-restriction of electronic excitation.

Beyond that, the full TD-DFT eigenvalue problem (Equation (2.3.1)) may be solved in a similar manner, by also simplifying matrix $\mathbf{B}$ to:

$$B'_{ia,jb} = \sum_{A,B}^{M} \left(s_k q_{ia}^A \gamma_{AB}^K q_{bj}^B - a_0 q_{ib}^A \gamma_{AB}^K q_{aj}^B \right), \tag{2.3.9}$$

with the amount of exact HF exchange a_0, as earlier. This approximation is called simplified TD-DFT (sTD-DFT), and has been shown to yield improved transition moments in terms of excitation energy ω and oscillator strength f_0.[242]

2.4 Molecular Dynamics

Up to now, only fixed nuclei were assumed, but much can be learned by allowing the nuclei to move. Apart from geometry optimizations, which try to minimize the electronic energy with respect to the nuclear coordinates by following numeric or analytic gradients, a realistic real-time movement of molecules can be simulated with molecular dynamics (MD). In the MD framework, the nuclei are considered to be classical particles, and therefore obey Newton's second law of motion,

$$\frac{d^2 x_i}{dt^2} = \frac{F_{x_i}}{m_i}, \tag{2.4.1}$$

with a coordinate x_i, mass of the particle m_i, and the force component along x_i, F_{x_i}, acting on that particle. In a dense system with many particles, it is nearly impossible to describe the motion of a particle analytically due to the coupled nature of the particles' motions. Whenever a particle moves, other particles are likely to move as well, and the

force acting on the particle changes whenever it changes position.

Therefore, it is reasonable to approximate the continuous motion by finite differences. Within this approach, the continuous integration over time is replaced by a sum over small, discrete time steps δt, typically in the region of femtoseconds. Being able to calculate the force on a particle in a given configuration, that is at time t, acceleration and velocity at time t can easily be derived. Assuming that the force on a particle does not change within the small time step δt, the new position ($\mathbf{r}$), velocity ($\mathbf{v}$), and acceleration ($\mathbf{a}$) at time $t + \delta t$ after moving for a time δt can be calculated using a Taylor series expansion:

$$\mathbf{r}(t+\delta t) = \mathbf{r}(t) + \delta t\mathbf{v}(t) + \frac{1}{2}\delta t^2\mathbf{a}(t) + \frac{1}{6}\delta t^3\mathbf{b}(t) + \frac{1}{24}\delta t^4\mathbf{c}(t) + \dots \tag{2.4.2}$$

$$\mathbf{v}(t+\delta t) = \mathbf{v}(t) + \delta t\mathbf{a}(t) + \frac{1}{2}\delta t^2\mathbf{b}(t) + \frac{1}{6}\delta t^3\mathbf{c}(t) + \dots \tag{2.4.3}$$

$$\mathbf{a}(t+\delta t) = \mathbf{a}(t) + \delta t\mathbf{b}(t) + \frac{1}{2}\delta t^2\mathbf{c}(t) + \dots \tag{2.4.4}$$

$$\mathbf{b}(t+\delta t) = \mathbf{b}(t) + \delta t\mathbf{c}(t) + \dots \tag{2.4.5}$$

Usually, the Taylor series is truncated after term $\mathbf{a}$. A practical implementation is the velocity Verlet algorithm,[243] where the new positions and velocities are calculated as:

$$\mathbf{r}(t+\delta t) = \mathbf{r}(t) + \delta t\mathbf{v}(t) + \frac{1}{2}\delta t^2\mathbf{a}(t) \qquad \text{and} \tag{2.4.6}$$

$$\mathbf{v}(t+\delta t) = \mathbf{v}(t) + \frac{1}{2}\delta t\left[\mathbf{a}(t) + \mathbf{a}(t+\delta t)\right] \tag{2.4.7}$$

Therefore, the new positions $\mathbf{r}(t+\delta t)$ are evaluated at first. Then, the forces at the new positions $\mathbf{a}(t+\delta t)$ are calculated, and finally the velocities are updated. Apart from the velocity Verlet algorithm, many different time-integration schemes exist. For example the Verlet algorithm[244] or the leap-frog algorithm,[245] which are qualitatively similar, or higher order predictor–corrector methods,[246] which involve multiple prediction and correction steps.

The interesting aspect to be discussed now is: Where do the forces come from? It is possible to derive forces from any of the previously discussed electronic structure methods, but mostly DFT at the GGA level is chosen because of large system sizes. Although the nuclei move, the Born–Oppenheimer approximation is still viable, because the electronic structure will adjust instantaneously to the nuclear movements. Practically, for a given conformation at time t, the nuclei are stationary and the electronic problem is solved, thus giving the ground state WFN. With this, forces are available, and the nuclei positions can be updated for the new time $t + \delta t$. The forces are derived *ab initio*, therefore this method is called *ab initio* molecular dynamics (AIMD). For very large systems however, electronic structure methods cannot be afforded anymore, and empirical models have to be considered.

2.5 Force Field Methods

Studying extended systems with MD simulations, especially in the condensed phase, can give enormous insight into structure and dynamics of a system, but usually cannot be afforded by electronic structure methods. An empirical approach includes the use of force fields (FFs). Within this approach, molecules are explicitly defined in contrast to electronic structure methods, where only particles with electrons exist, and thus, intra- and intermolecular interactions arise. Intramolecularly, the molecule's internal degrees of freedom can be exploited, and functions to describe bonds, angles, and dihedrals are introduced. In most cases, quadratic functions are used to describe bonds and angles, and periodic functions are used for torsions, but anharmonic corrections or anharmonic functions like the Morse potential for bonds can be used. The intermolecular interactions can normally be broken down to Coulombic interactions and van der Waals type interactions. A typical classical FF is the OPLS/AA FF,[247] whose functional form is:

$$
\begin{aligned}
V = & \sum_{ij}^{\text{bonds}} k_{r,ij}(r_{ij} - r_{0,ij})^2 \\
& + \sum_{ijk}^{\text{angles}} k_{\theta,ijk}(\theta_{ijk} - \theta_{0,ijk})^2 \\
& + \sum_{ijkl}^{\text{dihedrals}} \sum_{m=1}^{4} V_{m,ijkl}\left[1 - (-1)^m \cos(m\phi_{ijkl})\right] \\
& + \sum_{ijkl}^{\text{impropers}} k_{\chi,ijkl}(\chi_{ijkl} - \chi_{0,ijkl})^2 \\
& + \sum_{i<j}^{\text{nonbonds}} \left\{ 4\varepsilon_{ij}\left[\left(\frac{\sigma_{ij}}{r_{ij}}\right)^{12} - \left(\frac{\sigma_{ij}}{r_{ij}}\right)^{6}\right] + \frac{1}{4\pi\varepsilon_0}\frac{q_i q_j}{r_{ij}} \right\},
\end{aligned}
\tag{2.5.1}
$$

with r, θ, ϕ, and χ being bond length, bond angle, torsion angle, and improper dihedral angle, respectively, $k_{r,\,\theta,\,\chi}$ being the force constants of the harmonic bond, angle and improper dihedral potential, r_0, θ_0 and χ_0 being the equilibrium bond length, bond angle and improper dihedral angle, and V_m is the potential of the torsional barrier for the m-th multiplicity. The intermolecular interactions are described by a classical Coulomb interaction potential between to constant point charges q_i and q_j, and a Lennard-Jones potential is used to approximate van der Waals interactions. All force constants $k_{r,\,\theta,\,\chi}/V_m$, equilibrium parameters $r_0/\theta_0/\chi_0$, Lennard-Jones parameters σ/ε, and partial charges q are empirical parameters that are derived by fitting to experimental or calculated data. Despite their simplicity and pairwise additivity, FF methods are widely used and have been very successful. Of course, in terms of accuracy, they cannot compete with the aforementioned electronic structure methods, they are predetermined by the input of the empirical parameters, and aspects like electronic excitation cannot

be described standardly. However, they offer the opportunity to study systems on a time scale reaching microseconds, and system sizes as large as millions of particles, which is well beyond any method that treats the electronic structure explicitly.

The presented OPLS/AA FF is non-polarizable, which means the Coulomb interaction between two particles does only depend on the positions of both particles, and is not affected by the environment. The accuracy and applicability of classical FFs can be increased by accounting for polarizability. In the classical sense, a molecule's dipole moment $\boldsymbol{\mu}$ is affected by an electric field $\mathbf{E}$, causing an induced dipole moment $\boldsymbol{\mu}_{\text{ind}}$. For weak electric fields, this is a linear relationship:

$$\boldsymbol{\mu}_{\text{ind}} = \boldsymbol{\alpha}\mathbf{E} \tag{2.5.2}$$

with the anisotropic polarizability tensor $\boldsymbol{\alpha}$ being the constant of proportionality.

In a classical MD simulation without external electric field, $\mathbf{E}$ is built by all charged components, *i.e.*, nuclei, and therefore depends on the positions of the nuclei: $\mathbf{E} = \mathbf{E}(\mathbf{r})$. Many different approaches to include polarizability in classical FFs exist. For example, without changing the functional form or adding terms in Equation (2.5.1), polarizability can be introduced by changing the fixed partial charges q to flexible charges $q(\mathbf{r})$, summarized as fluctuation charge (FQ) models. A method utilizing this approach is the charge equilibration from Rappé and Goddard.[248] Based on electron affinity and ionization potential and within certain restraints, an electric energy can be calculated. Minimizing this electric energy then gives new partial charges. The charges can also be treated as dynamic variables which evolve during the simulation, and it is not required to evaluate them in every time step.[249]

Another approach is based on adding induced dipole moments on every center of interest,[250] which is not necessarily every atom. The magnitude of the induced dipole at center i is then given by

$$\boldsymbol{\mu}_{\text{ind},i} = \alpha_i \mathbf{E}_i, \tag{2.5.3}$$

with the atomic polarizability of center i, α_i, usually assumed to be isotropic, and the respective electric field $\mathbf{E}_i$ at this point. Following the variational principle, the induced dipoles are derived by minimization of the polarization energy:

$$E_{\text{pol}} = -\frac{1}{2}\sum_i \boldsymbol{\mu}_{\text{ind},i} \cdot \mathbf{E}_i. \tag{2.5.4}$$

The electric field will of course depend on all fixed charges, dipoles, and induced dipoles at other centers. Therefore, this problem can only be solved iteratively in an SCF approach. Noteworthily, the polarizable ion model (PIM) described and used in Section 3.3 is based on using induced dipole moments.

3 Results and Discussion

As could be seen earlier, most of the published work deals with the adsorbed dye/surface interface, and some articles even incorporated the necessary solvent, but ILs as a solvent can be a fairly complicated system on their own.

Therefore, focusing on pure IL systems, the first section of this chapter is dedicated to study three of the most promising ILs used in DSCs, which are the cyano-based ILs $[C_2C_1Im][B(CN)_4]$, $[C_2C_1Im][N(CN)_2]$, and $[C_2C_1Im][SCN]$. The ILs are investigated by means of AIMD simulations in Section 3.1 to elucidate similarities and differences of the pure bulk liquid structure and dynamics. The ILs show significant differences in, for example, hydrogen bonding ability of the anions, and the molecular alignment of cations, *i.e.*, π–π stacking. These deviations could be correlated to, for example, the diverse experimental viscosities of the ILs, and mark points of attention if these ILs are to be used in DSCs or other electrolyte applications.

Furthermore, to gain systematic insights into the working principles and basic processes of a DSC, the main part of this work is attributed to the electrolyte/surface interface. To approach the IL/TiO_2 surface, a systematic study of the adsorption characteristics of isolated ions and ion pairs of selected ionic liquids is presented in Section 3.2. This gives insight into common interaction modes, and how to accurately model the interface on a quantum chemical level.

In order to get a more realistic picture of the bulk IL/TiO_2 interface, polarizable FF MD was executed to model this subsystem of the DSC in Section 3.3. As no classical FF was available, a protocol to merge the two existing FFs for the singular systems—IL and TiO_2, respectively—is presented, which approximates the missing interactions by a classic pairwise potential fitted to match *ab initio* reference calculations. With this approach, the $[C_2C_1Im][B(CN)_4]$/anatase (101) and the $[C_2C_1Im][SCN]$/anatase (101) interfaces could be investigated for dimensions beyond the capabilities of QM calculations. A layered surface structure of the IL extending a few nanometers into the bulk, and an excess of cations adsorbed onto the surface was found, which would not have been possible by static calculations.

Moreover, the capability of ionic species to shift the titania's DOS was classified for a large number of ILs in a standardized order in Section 3.4. A high correlation between the amount of charge transferred from and to the surface with the DOS shift was found, and trends for different IL classes match experimental observations. This catalog of ILs with their expected influence on titania's DOS should give guidance for the use of ILs in future applications to deliberately fine-tune the energy level alignments in the DSC.

In the last section of this chapter, the dye/IL subsystem is examined in Section 3.5. The main objectives are to recognize the influences of certain ILs on the spectroscopic properties of common dyes, and to identify characteristic interactions and interaction sites. As fundamental research, the influence of explicit solvation shell size, XC functional, and the method to calculate the excitation properties is investigated. The coordination of the IL's anion at metal atoms or hydrogen bond donor sites was found to be of importance, and a universal bathochromic shift of the dye's electronic excitation spectrum upon IL solvation with respect to gas phase simulations was observed.

3.1 Complex Structural and Dynamical Interplay of Cyano-Based Ionic Liquids

Henry Weber[†] and Barbara Kirchner[†]*

The Journal of Physical Chemistry B, **2016**, Volume *120*, Pages 2471–2483.

DOI:	10.1021/acs.jpcb.6b00098
Received:	January 5, 2016
Revised:	February 16, 2016
Published:	February 16, 2016

Contributions to the manuscript:

- Setup and maintenance of all calculations.
- Analysis and evaluation of all results.
- Writing of major parts of the manuscript.

[†]Mulliken Center for Theoretical Chemistry, Universität Bonn, Beringstr. 4+6, D-53115 Bonn, Germany.
*Corresponding Author E-mail: kirchner@thch.uni-bonn.de.

Abstract

We carried out *ab initio* molecular dynamics simulations for the three cyano-based ionic liquids, 1-ethyl-3-methylimidazolium tetracyanoborate ($[C_2C_1Im][B(CN)_4]$), 1-ethyl-3-methylimidazolium dicyanamide ($[C_2C_1Im][N(CN)_2]$), and 1-ethyl-3-methylimidazolium thiocyanate ($[C_2C_1Im][SCN]$). We found that the [SCN]-based ionic liquid is much more prone to π–π stacking interactions as opposed to the other two ionic liquids, contrary to the fact that all liquids bear the same cation. Hydrogen bonding is strong in the dicyanamide- and the thiocyanate-based ionic liquids and it is almost absent in the tetracyanoborate liquid. The anion prefers to stay on-top of the imidazolium ring with the highest priority for the $[N(CN)_2]^-$ anion followed by the $[B(CN)_4]^-$ anion. We find that experimental viscosity trends cannot be correlated to the hydrogen bond dynamics which is fastest for $[B(CN)_4]^-$ followed by $[SCN]^-$ and $[N(CN)_2]^-$. For the dynamics of the cation on-top of itself, we find the order of $[B(CN)_4]^-$ followed by $[N(CN)_2]^-$ and finally by $[SCN]^-$. Interestingly, this trend correlates well with the viscosity, suggesting a relation between the cation–cation dynamics and the viscosity at least for these cyano-based ionic liquids. These findings, especially the apparent correlation between cation–cation dynamics and the viscosity, might be useful for the suggestion of better ionic liquids in electrolyte applications.

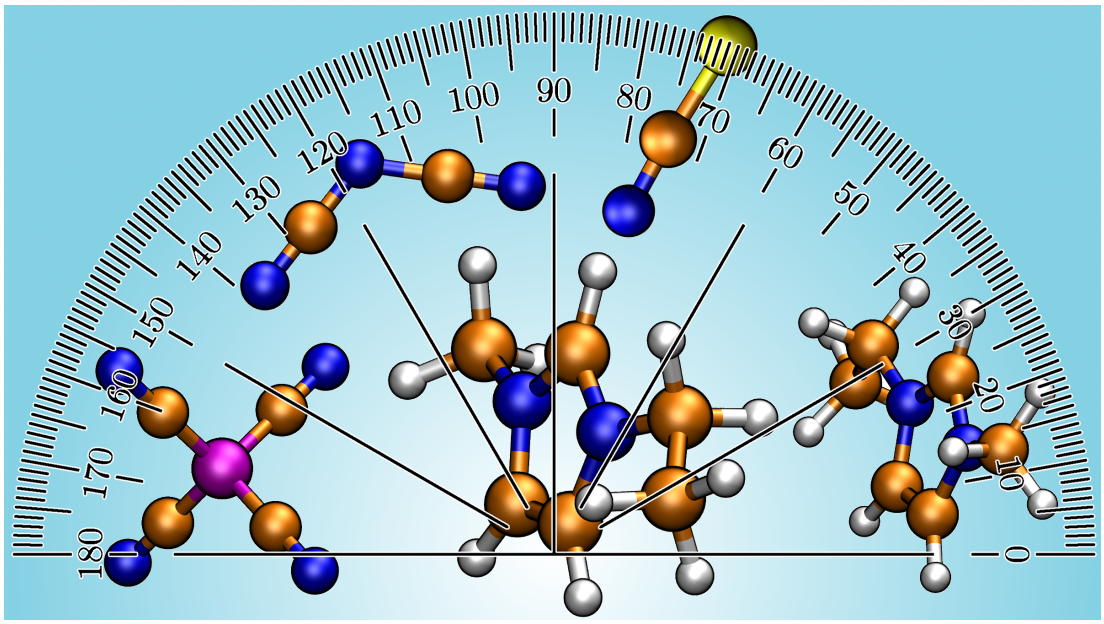

3.1.1 Introduction

Not only for academic curiosity[251] but also driven by the urge to create more environmentally benign procedures,[252] the quest for alternative reaction media becomes more and more important, since the solvent is usually the major compound of the solution.[253] The solution for making a process more environmentally benign and efficient might not always lie in using a less toxic solvent but in changing the way it works. In that regard ionic liquids[254]—liquids entirely composed of ions—provide an interesting playing ground for which we witnessed a large increase in popularity and which often came with some perhaps even fruitful, but harsh, debates.[253]

The task specific application of ionic liquids—such as them being employed in energy application—can only be improved by fully understanding the underlying microscopic principles. A very useful aid in gaining such knowledge is provided by means of theoretical methods.[255,256] These are molecular dynamics (MD) simulations based on parametrized force fields with large numbers of particles and thus explicit solvation as well as temperature and dynamical effects.[257,258] Furthermore, *ab initio* molecular dynamics (AIMD) simulations which treat the forces on the fly and hence are restricted in particle size, but similarly include explicit solvation as well as temperature and dynamical effects, were often employed for elucidating the structure and fast dynamical properties, especially when exact force fields are unknown or spontaneous events need to be monitored. Nowadays many insights into the direct solvation of particles within ILs were gained by AIMD; for example CO_2 absorption[259] and transient carbene formation[260] could be understood in terms of solvent modes with the aid of AIMD. Static quantum chemical (QC) calculations which work in an isolated molecule ansatz solving the electronic Schrödinger equation have the advantage of allowing very high accuracy.[261] In order to gain a full picture of ILs, combinations of all approaches in a multiscalar approach are required.[256]

In this article, we focus on comparing three ionic liquids:

1 1-ethyl-3-methylimidazolium tetracyanoborate ($[C_2C_1Im][B(CN)_4]$);

2 1-ethyl-3-methylimidazolium dicyanamide ($[C_2C_1Im][N(CN)_2]$);

3 1-ethyl-3-methylimidazolium thiocyanate ($[C_2C_1Im][SCN]$),

which we have studied from AIMD. We choose these liquids, since there is a current interest of them being employed in many interesting applications and we wish to understand what are their common features and differences on the microscopic level. These cyano-based ILs find various applications.

In the context of dye sensitized solar cells, imidazolium-based ionic liquids with the $[B(CN)_4]^-$ anion,[121,160–162] the $[N(CN)_2]^-$ anion,[120,160–165] and the $[SCN]^-$ anion[119,126,163,166] are frequently studied. The $[C_2C_1Im][B(CN)_4]$ and $[C_2C_1Im][N(CN)_2]$ ILs showed as electrolytes in solar cells favorable influences on their energetics, *e.g.*,

in terms of TiO_2 band levels, of good availability, and, of low viscosities.[160–162] The absorption behavior of ionic liquid ions and ion pairs[262] as well as the development of a polarizable force field[263] for describing the liquid–solid interface between TiO_2 and the $[C_2C_1Im][B(CN)_4]$ and the $[C_2C_1Im][SCN]$ ILs was carried out recently.[262,263]

In addition, $[C_nC_1Im][N(CN)_2]$ is employed as solvent and electrolyte for electrodeposition of different transition metals.[264] $[N(CN)_2]$-based ILs are clearly outperforming other ILs with, *e.g.* $[BF_4]$, $[PF_6]$, or $[Tf_2N]$ anions because of the good solubility of metal chlorides in $[N(CN)_2]$-based ILs which can be attributed to the strong complexing ability of $[N(CN)_2]^-$ as the ligand.[264,265] In another interesting article,[265] one example of the rare room-temperature metal-containing ionic liquids $[C_nC_1Im][Au(SCN)_2]$ (1-alkyl-3-methylimidazolium bis(thiocyanato)aurate(I), $n = 1, 2, 4, 6$) was synthesized, and their structural as well a luminescent properties were investigated. The UV/VIS absorption spectra revealed interactions between thiocyanate anions and the formation of colloidal gold particles could be ruled out as being responsible for the relevant peaks.[265]

Moreover, thiocyanate anions in imidazolium-based ILs are recently tested as local probe of structure and dynamics in 2D-IR experiments.[266] The $[SCN]^-$ anions are sensitive to different local conditions within the liquid and do not interact with each other or change the local dynamics, thus they can serve as a probe in IR experiments.[266] Ludwig and co-workers[267] showed for $[C_2C_1Im][SCN]$ and $[C_2C_1Im][N(CN)_2]$ ILs among others that far-infrared spectroscopy is a sensitive probe for detecting the cation–anion interaction strength in imidazolium-based ionic liquids and that the frequency shifts stem mainly from varying interaction strength rather than from different reduced masses of the anions.[267] A Raman band shape analysis of the C≡N stretching mode together with MD simulations was carried out for ionic liquids based on $[SCN]^-$, $[N(CN)_2]^-$, $[C(CN)_3]^-$, $[B(CN)_4]^-$ with the common cation $[C_2C_1Im]^+$.[268] The fastest reorientational time correlation function was found for the $[SCN]^-$ anion.[268] In AIMD simulations,[269,270] the $[C_2C_1Im][SCN]$ was studied in order to gain insight into the hydrogen bond dynamics[269] and the dispersion effects.[270] The role of the hydrogen bonding was reviewed at the example of $[C_4C_1Im][N(CN)_2]$ ionic liquid ion pairs and clear indications for hydrogen bonding was found considering orbitals as well as the geometry of several conformers.[271]

For CO_2 dissolution and CO_2/N_2 separation, nitrile based ILs[272–274] are constantly being employed.[272] $[C_2C_1Im][B(CN)_4]$ showed best performance with high CO_2 permeance and high selectivity—even outperforming the popular $[C_2C_1Im][Tf_2N]$ IL. $[B(CN)_4]$-based ILs find also use in the extraction of aromatic hydrocarbons from mixtures of aliphatic and aromatic compounds.[275] For the unusual high SO_2 absorption in $[C_2C_1Im][SCN]$,[276] the $O(SO_2)$–H(cation) hydrogen bonds were found to be responsible together with a S(anion)–$S(SO_2)$ sulfur bridge such that the SO_2 is situated between cation and anion and that it leads to a linker effect which might also result

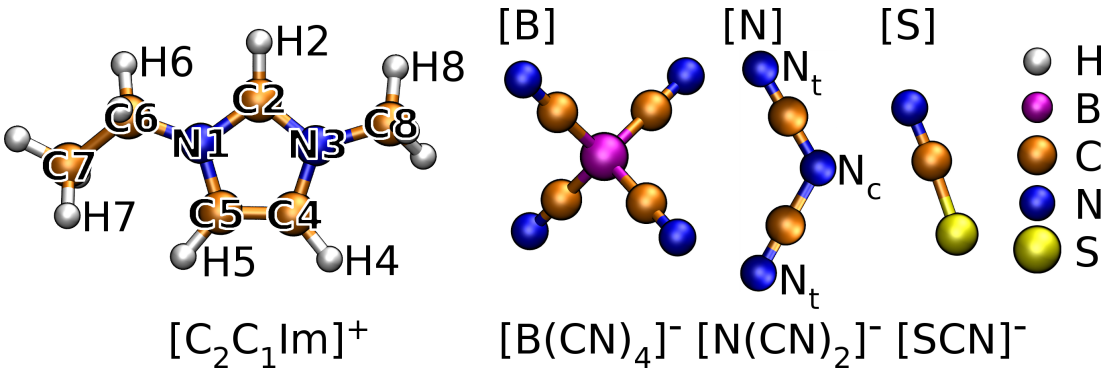

Figure 3.1: Labeling of the ILs components 1-ethyl-3-methylimidazolium $[C_2C_1Im]^+$, tetracyanoborate $[B(CN)_4]^-$, dicyanamide $[N(CN)_2]^-$, and thiocyanate $[SCN]^-$. [B], [N], and [S] denote the whole IL, respectively. All terminal anion nitrogen atoms are called N_t.

in the weakening[277] of the cation–anion interaction. Both CO_2 and SO_2 absorption behaviors were studied for many ionic liquids from static calculations including the $[N(CN)_2]^-$ and the $[SCN]^-$ anion.[278,279] $[C_2C_1Im][SCN]$ serves for the extraction of thiophene or pyridine from heptane.[280] The desulfurization of gasoline is important for the petroleum industry. Furthermore, $[C_2C_1Im][SCN]$ shows high selectivity for thiophene and pyridine. The sulfur content in model gasoline and model diesel is reduced by ≈ 90 %. $[C_4C_1Im][N(CN)_2]$ aids in the extraction of biomolecules in aqueous biphasic systems. E.g., a high partition coefficient of caffeine is achieved in the extraction process from aqueous phase.[281]

As precursor in synthesis of a boron-rich carbon,[282] the $[B(CN)_4]^-$ anion achieves a controllable porosity of the derived carbon if the right mixture and pyrolysis temperature are chosen. Using $[C_2C_1Im][N(CN)_2]$ in the process of carbonization to yield porous nitrogen-rich carbon, shows high catalytic activity for metal free oxygen reduction, which is interesting in the context of fuel cells,[283] because it is sustainable and cheap. $[C_4C_1Im][SCN]$ is deployed as a task specific solvent and reactant in the conversion of alkyl halides to alkyl thiocyanates.[284] The reaction is efficient, and the IL can be recycled. This is also observed for the efficient hydrothiocyanation of chalcogenes using this IL in a one pot reaction.[285] The $[C_4C_1Im][SCN]$ IL can be recycled after the reaction.[285]

In the next section we briefly discuss the details of the AIMD methodology. This is followed by analyzing the structural and dynamical results in order to elucidate the complicated microscopic-level picture. We end the article by providing a summary and conclusion of our detailed AIMD study.

3.1.2 Computational Methodologies and Systems Investigated

All *ab initio* molecular dynamics (AIMD) simulations were carried out with the CP2K program package,[286] using the QUICKSTEP module.[287] This approach utilizes hybrid Gaussian and plane waves basis sets to calculate the energies and forces on atoms.

To compare structural and dynamical properties of the ionic liquids, we utilized the BLYP functional[214,215] with the empirical dispersion correction (BLYP-D3),[230] because the necessity to correct for dispersion has been shown several times in static calculations[288–290] as well as in AIMD.[270] The molecularly optimized double-ζ basis set (MOLOPT-DZVP-SR-GTH)[291] with corresponding Goedecker–Teter–Hutter pseudopotentials for core electrons[292–294] was applied for all atoms. A 280 Ry density CUTOFF criterion with the finest grid level for the DFT calculations was employed together with multigrids number 5 (NGRID 5 and REL_CUTOFF 30) and with the smoothing for the electron density (NN10_SMOOTH) and its derivative (NN10).[287]

The starting structure for our AIMD simulation stems from classical simulations. A pre-equilibration was performed employing classical molecular dynamics simulations within periodic boundary conditions using the LAMMPS program package.[295] The classical simulation box was set up by replication of a single ion pair, followed by a classical NPT simulation run of at least 1 ns simulation time. For the classical description of the ionic liquids, the force field developed by Pádua and Canongia Lopes was used,[296] employing the popular OPLS/AA force field,[247] with the exception of newly derived partial charges.

Subsequently, CP2K simulations were started on the last snapshot of the classical MD trajectory at the BLYP-D3 level of theory. The sequence of a preequilibration with massive Nosé–Hoover thermostats[297–299] for individual atoms, followed by an equilibration phase with global thermostats succeeded by the actual production run was conducted for all systems. The thermostat time constant was set to 16.68 fs, the simulation time step was chosen to be $\tau = 0.5$ fs. All MD simulations were conducted at T =398 K to enhance the sampling of different configurations.

In order to obtain self-diffusion coefficients D, only data points in the last half of each respective mean squared displacement function was considered for the linear regression.

Time-dependent autocorrelation functions (ACFs) $c(t)$ were evaluated in the present work. They have the general form

$$c(t) = \frac{\langle h(t_0)h(t)\rangle}{\langle h(t_0)^2\rangle} \tag{3.1.1}$$

with the population variable h and time t. For different criteria, as, *e.g.*, the on-top or hydrogen bond criteria mentioned below, $h = 1$ if the criteria are fulfilled, and $h = 0$ otherwise; t_0 is the starting time of the correlation. The ACFs were recorded in a continuous fashion, *i.e.*, $h(t) = 1$ if the criteria are fulfilled at time t and all the time beginning from time t_0. Lifetimes τ are evaluated by the integral of the ACFs, *i.e.*:

$$\tau = 2\int_0^\infty c(t)dt \tag{3.1.2}$$

To avoid numerical integration, the ACFs were fitted by a sum of exponential func-

Table 3.1: Simulation Details of AIMD Simulations with the Number of Ion Pairs n, the Experimental Density ρ_e and Simulated Density ρ_{MD} at Different Temperatures, the Simulation Time for Massive Preequilibration t_{peq}, Global Equilibration t_{eq}, and Production Run Time t_{prod}

	$[C_2C_1Im][B(CN)_4]$	$[C_2C_1Im][N(CN)_2]$	$[C_2C_1Im][SCN]$
n	22	32	32
ρ_e(298.15 K) / kgm^{-3}	1036.1	1104.0	1117.0
ρ_{MD}(300 K) / kgm^{-3}	1009.8	1051.3	1101.4
ρ_{MD}(398 K) / kgm^{-3}	990.2	975.5	1078.9
t_{peq} / ps	4	5	6
t_{eq} / ps	8.5	6	10
t_{prod} / ps	42	60	45

tions $f(t)$

$$f(t) = \sum_{i=1}^{k} a_i e^{b_i\, t} \tag{3.1.3}$$

with the fit parameters a_i and b_i. Usually, the best fit was obtained with $k = 2$ or 3 with very good regression coefficients of $R > 0.99$, and therefore, the error of τ is expected to be less than 5 % in general.

Criteria used to define the on-top position were $d_{\mathrm{CoR(+)–X}} \leq 500$ pm and $0° \leq \angle$(RN, CoR(+)–X) $\leq 45°$ and $135° \leq \angle$(RN, CoR(+)–X) $\leq 180°$, with X as the cation's center of ring (CoR(+)) or the anion's center of mass (CoM(−)), RN is the ring normal. The hydrogen bond was also defined via geometrical criteria, namely $d_{\mathrm{H\cdots Y}} \leq 300$ pm and $135° \leq \angle(\mathrm{X–H\cdots Y}) \leq 180°$ with X–H being the hydrogen bond donor and Y the hydrogen bond acceptor. An ion pair was defined by a cation and counterion determined by the shortest distance between CoR(+) and CoM(−).

In the case of the velocity autocorrelation function, $h(t)$ in Equation (3.1.1) is replaced by the velocity $v(t)$.

3.1.3 Results: Structure

For the ionic liquids 1-ethyl-3-methylimidazolium ($[C_2C_1Im]$) tetracyanoborate ($[B(CN)_4]$), dicyanamide ($[N(CN)_2]$), and thiocyanate ([SCN]) the labeling of the single IL ions is depicted in Figure 3.1. In the following, the ILs are abbreviated as [B], [N], and [S], respectively. Simulation details for the different AIMD runs are listed in Table 3.1. As no experimental densities are available at 398 K, classical force field simulations were performed to obtain estimated densities and good starting conformations. At room temperature, the simulated densities reasonably agree with experimental densities, see Table 3.1, and the trend of increasing densities in the order [B]<[N]<[S] is captured as well. In the case of the high temperature simulations, this ordering changes to [N]<[B]<[S], which might be a shortcoming of the used force fields. However, the densities agree very well at room temperature, thus the simulated densities at 398 K may be used as a good estimate.

3.1.3.1 Ion–Ion Structure

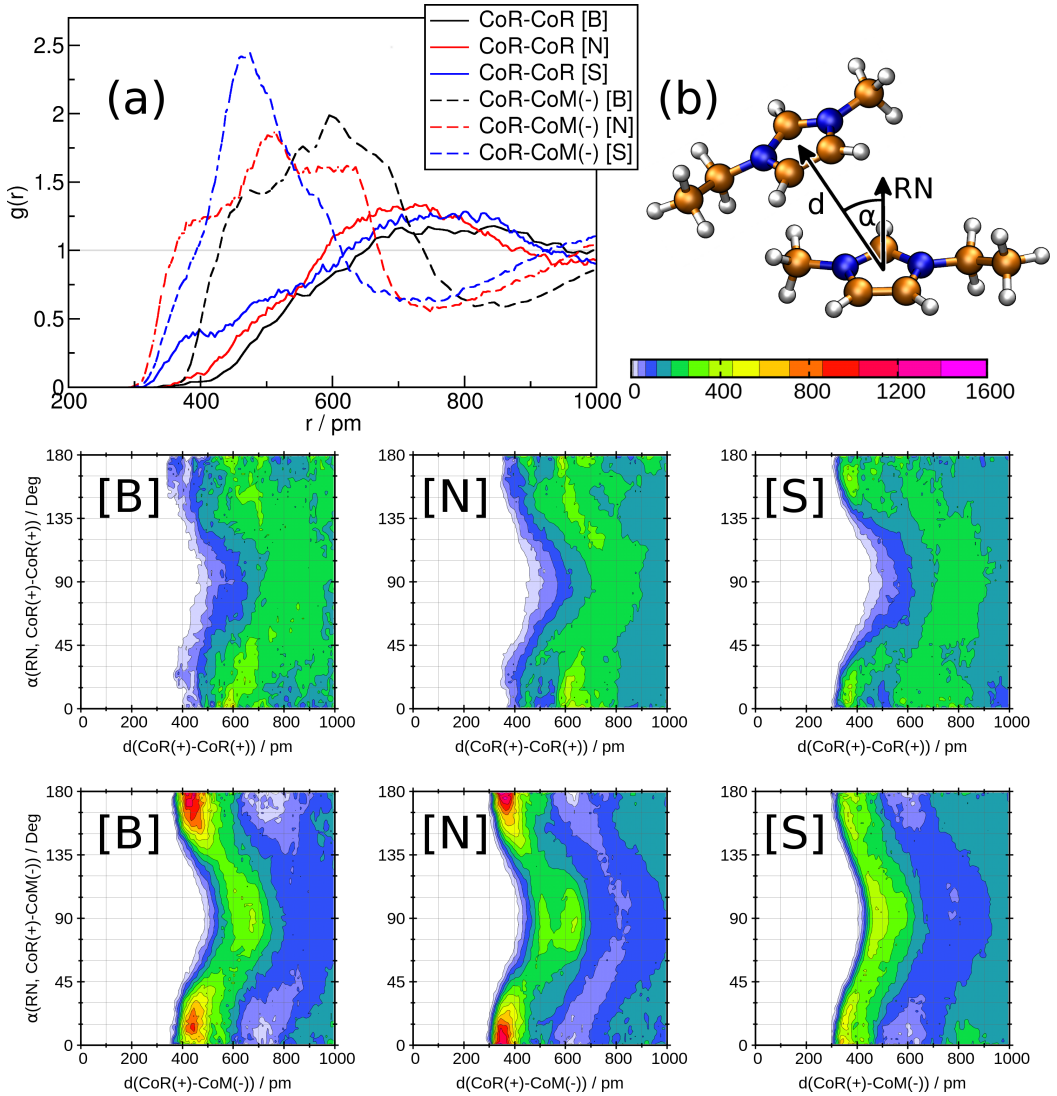

Figure 3.2: (a) Radial distribution functions showing the ion–ion structure of the liquid. CoR indicates the center of ring of the cation and CoM(−) indicates the center of mass of the anion. Combined distribution functions reflecting on the in-plane and on-top distribution, illustrated in the top right panel (b) with relative intensity color coding. Plotted is the angle α versus the cation–cation distribution in the middle panel and the bottom panels show angle α versus the cation–anion distribution.

In order to examine the ion–ion structuring of the ILs, in Figure 3.2 several functions are depicted. The RDFs (Figure 3.2(a)) indicate a pronounced cation–anion interaction as expected[269,270,300] with a strong first solvent shell peak between 400 and 600 pm for $[C_2C_1Im][N(CN)_2]$ (red) and $[C_2C_1Im][SCN]$ (blue) and between 500 and 700 pm for $[C_2C_1Im][B(CN)_4]$ (black).

Typical cation–cation interaction for imidazolium–type ILs occur as stacking of imidazolium rings due to favorable π–π interactions.[301–303] This interaction is most pronounced in the $[C_2C_1Im][SCN]$ IL, compare Figure 3.2 middle panels in which more

Table 3.2: Neighbor Count Analysis of Ions in On-Top Position of the Cation[a]

Ion	anion label	$P(n=0)$ / %	$P(n=1)$ / %	$P(n=2)$ / %	n_{avg}
$[C_2C_1Im]^+$	[B]	91.1	8.8	0.1	0.09
$[C_2C_1Im]^+$	[N]	80.8	18.1	1.1	0.20
$[C_2C_1Im]^+$	[S]	59.1	36.2	4.7	0.46
$[B(CN)_4]^-$	[B]	39.4	48.2	12.4	0.73
$[N(CN)_2]^-$	[N]	28.7	52.5	18.6	0.90
$[SCN]^-$	[S]	34.3	50.0	15.5	0.81

[a]The exact criteria are listed in Section 3.1.2. $P(n)$ is the probability of finding n ions on-top of the cation, n_{avg} is the expected average number of ions on top of the cation.

entries at 180 and 0° and at approximately 400 pm are visible for the $[SCN]^-$ anion, see right panel [S]. In liquid benzene[304] an intermolecular distance of 410 pm corresponds to the case of plane-parallel molecular arrangement. Similarly, in a previous article[302] we identified the distance between two butylimidazolium center-of-ring points to be approximately 400 pm.

For $[C_2C_1Im][B(CN)_4]$ and $[C_2C_1Im][N(CN)_2]$, the anion occupies the on-top space, blocking this position for the cation. The red high intensity regions for [B] and [N] in Figure 3.2 panels below indicate the preferred on-top conformation of the anion. In the case of $[C_2C_1Im][SCN]$, Figure 3.2 lower panel [S], the anion is likely to be found on-top of the imidazolium ring too, but also in-plane, enabling favorable hydrogen bond like interactions. These hydrogen bond like arrangements in turn generate the space for cation–cation on-top configurations as discussed before.

To put this qualitative picture onto solid grounds, we list in Table 3.2 the probability of finding no ($n = 0$), 1 ($n = 1$) and 2 ($n = 2$) ion(s) on-top of a cation. There are at least 9%, 20%, and 40% cations on-top of the cation for the $[B(CN)_4]$-, the $[N(CN)_2]$-, and the [SCN]-based ionic liquids. Thus, π–π stacking occurs rather often in the $[C_2C_1Im][SCN]$ ionic liquid; in 36% the cation possesses one other cation as neighbor, and in 5% the cation is even arranged like in a sandwich, *i.e.*, surrounded by two other cations which must lead to different performances in certain applications of this liquid compared to the other two liquids. See for example the higher viscosity[305] of the [SCN]-based IL as compared to the $[B(CN)_4]$- and the $[N(CN)_2]$-based IL. For the sequence [B], [N], [S] this π–π stacking behavior increases systematically. The on-top behavior of the anion is not completely inversely related to the cation–cation behavior. While in 70% cases the $[N(CN)_2]^-$ anion is on-top, in 65% cases the $[SCN]^-$ anion and in 60% cases the $[B(CN)_4]^-$ anion occupy the on-top space. In 40% cases the $[B(CN)_4]^-$ anion, in 35% the $[SCN]^-$ and in 30% the $[N(CN)_2]^-$ anion is not on-top, which means they can occupy also in-plane arrangements.

As has been pointed out by Matthews et al.,[303] the interplay between π–π stacking and hydrogen bonding seems to be important, as this leads to a stabilization. Thus, anions can stabilize the π–π stacking if they are in-plane forming hydrogen bonds.

It was discussed further that one motif in ion pair dimers is identified by parallel-stacked cations, with the two anions lying in a middle plane, between the cation rings. These structures are consistent with π–π structural arrangements observed for benzene dimers, *i.e.*, stacked, T-shape, and parallel displaced.[303] As the $[SCN]^-$ anion prefers the in-plane position,[301] it is able to support the cation–cation π–π interaction. The other two anions are sterically more demanding (*i.e.*, the case of $[B(CN)_4]^-$) or compete with the cation–cation π–π stacking, because they prefer to occupy more the on-top position (*i.e.*, see the case of $[N(CN)_2]^-$), Table 3.2.

3.1.3.2 Hydrogen Bonds

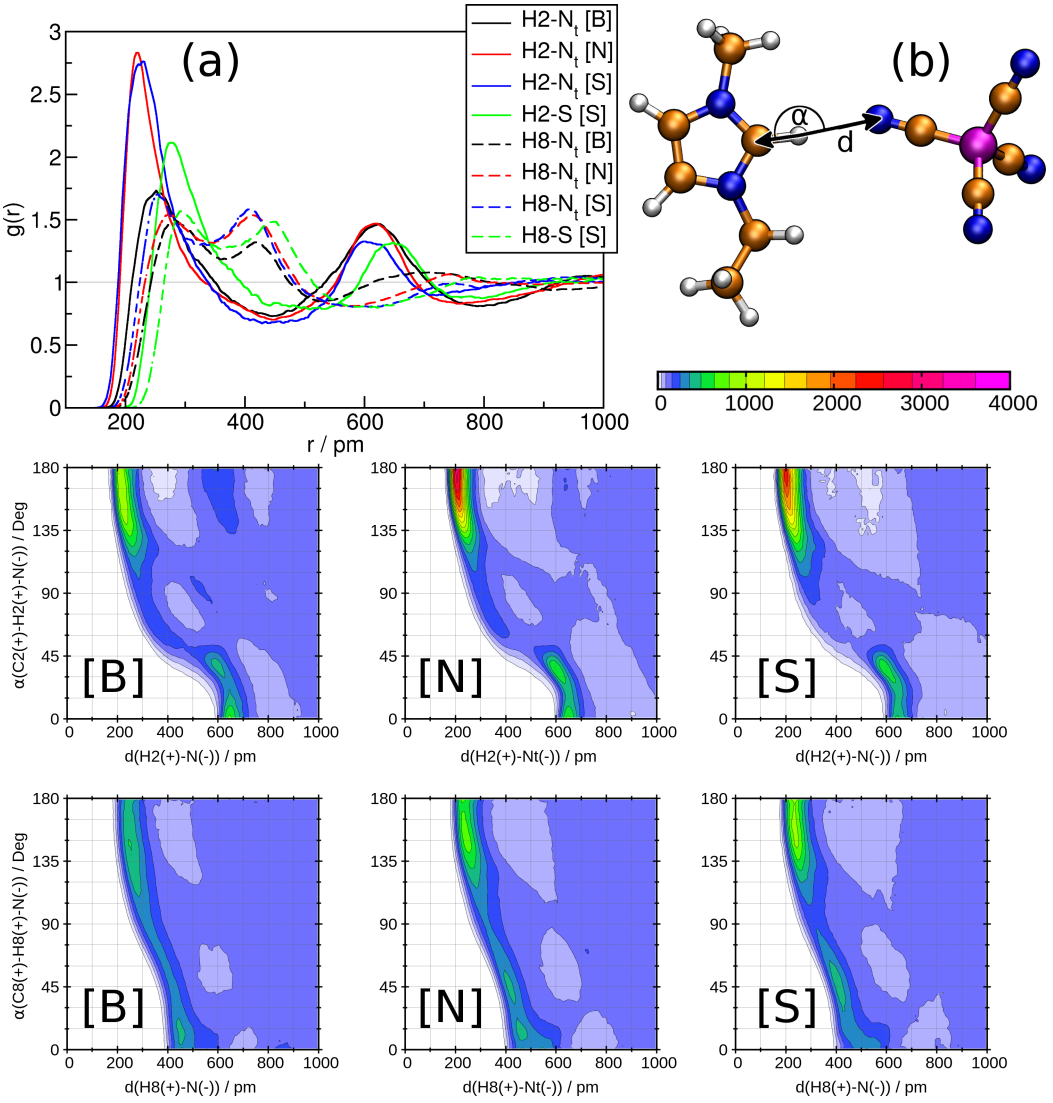

Figure 3.3: (a) Radial distribution functions showing the hydrogen bond structure. Combined distribution functions illustrated and relative intensity color coding in part (b) showing hydrogen bond geometry, the C2–H2$\cdots$N$_t$ hydrogen bond geometry in the middle panels, and C8–H8$\cdots$N$_t$ in the bottom panels.

As observed in the previous section, directed hydrogen bond-like interactions between cation and anion play an important role in balancing other interactions like π–π stacking between different cations. The existence of hydrogen bonds in imidazolium-based ILs and also in others has been discussed previously.[271,303,306] The most pronounced interaction is observed between the acidic hydrogen atom H2[307,308] and the nitrogen atoms of the particular anions; see Figure 3.3. Hydrogen bonds established at H4 and H5 position are qualitatively the same, and are therefore omitted for the sake of clarity in Figure 3.3. Second, longer and thus weaker hydrogen bonds can be established with H6 and H8 hydrogen atoms as hydrogen bond donors, see Figure 3.1 for labeling. Please note that the peak height might be as well related to the number of neighbors rather than to the particular strength of the hydrogen bond; therefore, we discuss the hydrogen bond in terms of accentuation, which means here both in terms of strength and number of neighbors.

The most emphasized hydrogen bonds are observed for $[C_2C_1Im][N(CN)_2]$ and $[C_2C_1$-Im][SCN] between the imidazolium ring hydrogen atoms and the terminal nitrogen atoms of $[N(CN)_2]^-$ (red) and the nitrogen atom of $[SCN]^-$ (blue) for the studied ILs. Interestingly, the sulfur atom of the $[SCN]^-$ (green) possesses a higher peak than the nitrogen atom of the $[B(CN)_4]^-$ anion (black) in this hydrogen bond. This might allow the $[SCN]^-$ anion still to establish a hydrogen bond network or interlinking interactions similar to the multiple CN-ligands of the other two anions. Because of the nature of the $[B(CN)_4]^-$ anion, *i.e.*, the sterical demands and the strong delocalization, an overall weakening of the hydrogen bonding is apparent. These findings are in line with a recent study of Batista et al., investigating water mixtures of the studied ILs.[309] $[N(CN)_2]^-$ and $[SCN]^-$ were found to act as the strongest hydrogen bond acceptors, and the acceptor strength of $[B(CN)_4]^-$ was observed to be significantly lower.[309] Most likely due to conjugation (see HOMO-1 of Fig.8 in Reference 271), the central nitrogen atom of $[N(CN)_2]^-$ is unlikely to act as a hydrogen bond acceptor, distinguishing it from the nitrogen atoms in the nitrile groups (see Supporting Information for respective RDFs). The hydrogen bonds with H6 and H8 as donor atoms acquire different characteristics. In this case only the $[SCN]^-$ anion not the $[N(CN)_2]^-$ shows the most pronounced and shortest peaks for both atoms the nitrogen as well as the sulfur. The height of the H8–N([SCN]) peak even matches the one of the H2–N([$B(CN)_4$]) peak.

Further conclusions on the hydrogen bond behavior can be drawn from the respective CDFs in Figure 3.3, middle and lower panels. These CDFs reveal a directed hydrogen bond geometry with distances $d \approx 150-300$ pm and angles $\alpha \approx 135-180°$. The strong H2–N hydrogen bonds in $[C_2C_1Im][N(CN)_2]$ and $[C_2C_1Im][SCN]$ are readily visible from Figure 3.3([N] and [S] in the middle panel). Although the weak hydrogen bonds only show a very minor RDF peak, they clearly possess the distinct hydrogen bond geometry. Interestingly, again it is apparent that the H8–N hydrogen bonds in $[C_2C_1Im][N(CN)_2]$ and $[C_2C_1Im][SCN]$ are as strong as the H2–N hydrogen bond in $[C_2C_1Im][B(CN)_4]$.

The secondary peaks at low angles and larger distances in all CDFs originate from the rear hydrogen atoms H4 and H5 and the two other H8 hydrogen atoms of the methyl group.

To summarize, we can say, in order to characterize the hydrogen bonding not only the distance should be considered, but it should be also kept in mind that the peak height of the RDF indicates stronger hydrogen bonds although it might be related rather to the number of neighbors than to the strength of the hydrogen bond. Directionality, as well as sterical demands and delocalization, *i.e.*, basicity of the anion, together with the ability to build up a network due to more than one acceptor possibilities (be it due to a very negative hydrogen bond acceptor or due to many acceptor atoms in the anion), will determine the complicated interplay of the anions with the cations in terms of hydrogen bonding.

3.1.3.3 Anion Coordination

Before we considered the hydrogen bond arrangement C–H$\cdots$N of all ILs, now we consider the nitrile group arrangement X$\cdots$N–C–Y (X=H2, C8; Y=B, N_C, S of the anion) toward different cationic groups. The RDFs in Figure 3.4a illustrate the structure of cationic sites with the anion's nitrile groups. The orientation of the nitrile group coordination is apparent in the subsequent CDFs Figure 3.4, middle and lower panels. A ball-and-stick model in Figure 3.4b is given for illustration; angles of 180° indicate linear X$\cdots$N–C–Y alignment. The CDFs describing the coordination at ring hydrogen atoms (Figure 3.4 middle panels) reveal, that the anion's nitrile groups point directly toward the cation's ring hydrogen atoms ($\alpha = 135-180°$) when the nitrogen approaches the cation toward the nearest interacting atom ($d = 200-300$ pm). This directionality is given for all three systems, but most intense in $[C_2C_1Im][N(CN)_2]$, weaker and less intense in terms of peak height in $[C_2C_1Im][B(CN)_4]$ and very weak ($\alpha = 90-180°$) in $[C_2C_1Im][SCN]$. For $[B(CN)_4]^-$, this trend probably arises because of the reduced acceptor ability caused by large charge delocalization within all four nitrile groups and the steric demand of the ion. For the $[SCN]^-$ anion, the simultaneous coordination of the nitrogen atom and the sulfur atom might play a role.

In order to study the anion coordination behavior toward the weak hydrogen bond donor groups, the central carbon atom of the respective alkyl group was chosen as a reference atom. The CDFs (Figure 3.4 lower panels) indicate favorable perpendicular alignments of the anion's nitrile groups toward the cation's alkyl groups, see the high intensity regions at $d = 300-400$ pm and $\alpha = 60-90°$. A possible linear arrangement was observed in the C–H$\cdots$N hydrogen bond for these groups (Figure 3.3 lower panels). Thus, a simultaneous linear alignment of hydrogen bond and nitrile group is found only at the positions of the ring hydrogen atoms.

In addition, in Figure 3.4B (lower left panel), a distinct and isolated maximum is apparent at large distances ($d = 600-700$ pm) for very small angles of $\alpha = 0-15°$.

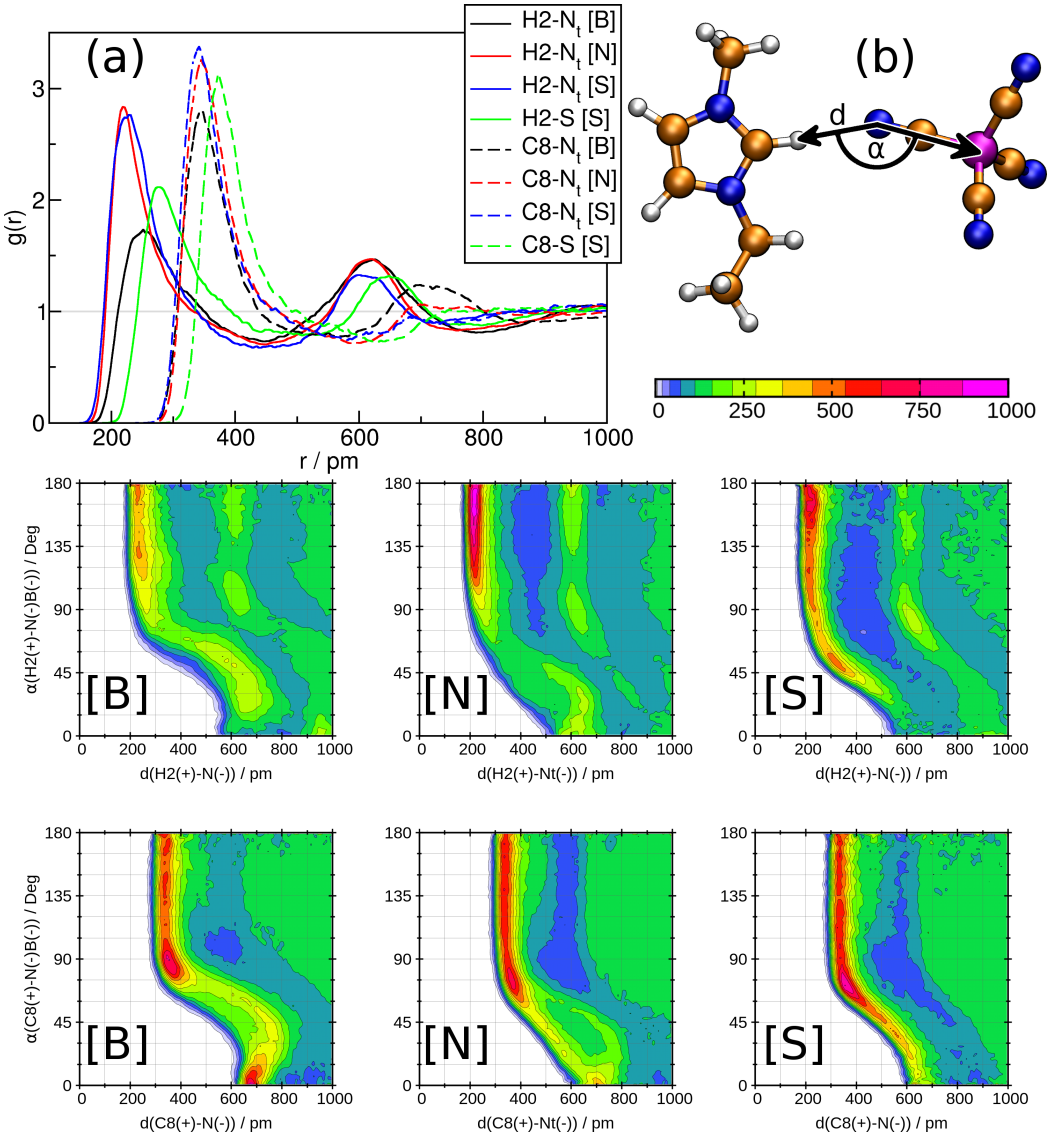

Figure 3.4: (a) Radial distribution functions between the anion's nitrogen atoms and different parts of the cation. (b) Sketch depicting the combined distribution functions and relative intensity color coding. The distance d is always the distance between the cation and the anion's nitrile nitrogen atoms, α is the cation–N–X angle. $\alpha = 180^\circ$ corresponds to a linear cation–N–X alignment. Nitrile coordination at H2 shown in the middle panels; nitrile coordination at C8 shown in the bottom panels.

Table 3.3: Average Neighbor Count of Surrounding Ions in the AIMD Systems from Radical Voronoi Analysis

	$[C_2C_1Im]^+$	$[B(CN)_4]^-$
$[C_2C_1Im]^+$	8.4	8.5
$[B(CN)_4]^-$	8.5	5.8
	$[C_2C_1Im]^+$	$[N(CN)_2]^-$
$[C_2C_1Im]^+$	11.0	7.9
$[N(CN)_2]^-$	7.9	3.2
	$[C_2C_1Im]^+$	$[SCN]^-$
$[C_2C_1Im]^+$	11.3	7.7
$[SCN]^-$	7.7	2.4

This peak shows, that the rear nitrogen atom of $[B(CN)_4]^-$ is in a straight X$\cdots$B–N line, indicating a coordination with the whole face of the tetrahedron, rather than a directed coordination with the CN ligand as it is the case for the ring hydrogen bonds.

It should be kept in mind that the directed hydrogen bonds and the directionality of the nitrile coordination at the ring hydrogen atoms are established only in the in-plane conformation of the anion, but the preferred space occupied by the anion is still the on-top position for $[C_2C_1Im][B(CN)_4]$ and $[C_2C_1Im][N(CN)_2]$, see lower panels [B] and [N] in Figure 3.2, as discussed above.

3.1.3.4 Voronoi Analysis

Recently, we introduced functions derived from the radical Voronoi analysis, with which one investigates the general cell composition based on connectivity.[310] The average neighbor count presented in Table 3.3 shows the number of neighboring ions to a certain reference ion based on connectivity in terms of a shared Voronoi face. For the three investigated systems, the average cation–cation contact number is unexpectedly large, with numbers of 8.4 in [B], 11.0 in [N], and 11.3 in [S]. This correlates well with the above discussed π–π stacking behavior of the cations. As opposed to this trend, the anion–anion contact number count is decreasing in the same manner as the cation–cation count is increasing, see Table 3.3. This behavior is most likely explained by the decreasing size of the anion. Interestingly, the average number count of cation–anion contact number is decreasing in the row [B], [N], and [S]. This, most likely, is also explained by the decreasing anion size, as a large anion such as $[B(CN)_4]^-$ can share interactions with multiple cations simultaneously in the condensed phase. In this regard, the surface coverage of the cation with the anion was evaluated with the Voronoi analysis as well; 67 % of the Voronoi surface of the cation in $[C_2C_1Im][B(CN)_4]$ is covered by the anion, 50 % in $[C_2C_1Im][N(CN)_2]$ and 43 % in $[C_2C_1Im][SCN]$. This finding is in line with the previous statements, as the average number of anions around the cation decreases, and the anions also decrease in size.

Table 3.4: Numerical Values of Self Diffusion Coefficients (Cation D_+, Anion D_-, IL Average $D = (D_+ + D_-)/2$), Experimental Viscosities (at 363.15 K), and Lifetimes τ of Different Autocorrelation Functions $c(t)$ Obtained by Integration[a]

	[B]	[N]	[S]	
D_+ / pm^2ps^{-1}	808.1 ± 5.1	194.9 ± 0.8	726.1 ± 1.9	
D_- / pm^2ps^{-1}	739.9 ± 1.1	244.4 ± 1.1	988.9 ± 3.4	
D / pm^2ps^{-1}	774.0	219.7	857.5	
η(363 K) / mPas	3.8 ± 0.15[b]	4.229 ± 0.05[b]	5.485 ± 0.063[b]	
		Lifetimes		
			[S]	
	[B]	[N]	Y=N	Y=S
τ(HB H2) / ps	0.23	0.49	0.34	0.31
τ(HB H4) / ps	0.22	0.39	0.31	0.36
τ(HB H5) / ps	0.23	0.46	0.43	0.41
τ(HB H6) / ps	0.14	0.20	0.19	0.22
τ(HB H8) / ps	0.12	0.17	0.17	0.17
τ(IP) / ps	2.34	3.27	1.42	
τ(on-top, +−) / ps	1.80	3.81	1.72	
τ(on-top, ++) / ps	0.78	1.51	1.87	

[a] τ(HB) are hydrogen bond lifetimes, τ(IP) ion pair lifetimes, τ(on-top) are on-top dynamic lifetimes, ++ between cations, +− between cation and anion. Y denotes the hydrogen bond acceptor atom in system [S]. [b] Neves et al.[305]

3.1.4 Results: Dynamics

Since dynamical effects are captured in AIMD as well, we focus now on several dynamical functions; *e.g.* those which can be obtained from time correlation functions. It should be noted here, that owing to the great computational effort of AIMD simulations, only short physical simulation times can be achieved. As a consequence, long-time correlations and slow dynamics such as diffusion, viscosity prediction, or meso- and macroscopic rearrangement are not well described via AIMD and results thereof should be treated with caution. Short-timed dynamics, however, such as near order changes or hydrogen bond dynamics do not require diffusion over large distances and are therefore excellently captured by AIMD simulations and thus these results should be more robust with respect to experimental data if available.

The mean squared displacement functions of the ions in all systems are given in Figure 3.5, and the calculated diffusion coefficients from the mean squared displacement functions are presented in Table 3.4. The diffusion coefficients and mean squared displacement functions reveal, that the $[C_2C_1Im][SCN]$ IL is moving slightly faster than $[C_2C_1Im][B(CN)_4]$, and that $[C_2C_1Im][N(CN)_2]$ is considerably slower. Unfortunately, experimental data on self-diffusion coefficients are very rare. For $[C_2C_1Im][B(CN)_4]$, D_+ was measured to be 128 pm^2ps^{-1} and $D_- = 125.5$ pm^2ps^{-1} at 318.15 K[311] which deviates largely from our absolute values and is obviously due to the fact that we work at much higher temperatures (398 K) in our simulations. However, in agreement to our simulations, the cation is slightly more mobile in the IL. For higher temperatures, the self-diffusion coefficient of $[C_2C_1Im][BF_4]$ at 373 K was measured to be

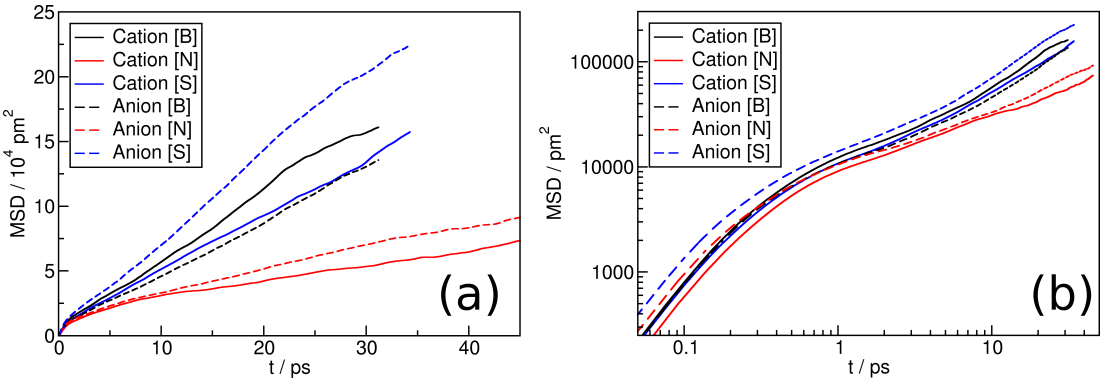

Figure 3.5: Mean squared displacement functions of cation and anion center of mass in (a) linear–linear and (b) logarithmic–logarithmic representation. [B] denotes the $[C_2C_1Im][B(CN)_4]$ IL, [N] the $[C_2C_1Im][N(CN)_2]$ IL, and [S] the $[C_2C_1Im][SCN]$ IL.

561 pm^2ps^{-1},[312] which is in the order of magnitude of our results.

For the given ILs, Neves et al. reported decreasing viscosities in the order [S] > [B] > [N] at 298 K.[305] Increasing the temperature to 363 K changes the order to [S] > [N] > [B], as reported in Table 3.4, but [S] is still the most viscous liquid. In this article, the very high dependence of temperature and viscosity was demonstrated, and dissimilar temperature dependencies of the IL's viscosities were reported. The comparison of calculated diffusion coefficients to experimental viscosities, which are often assumed to behave inversely to diffusion coefficients, shows that the diffusion coefficients for $[C_2C_1Im][SCN]$ are too high if this relation holds, as it has the highest viscosity with respect to the other ILs, although the measurements were done at lower temperatures. The disagreement may have several reasons,[305] *e.g.* the density is maybe underestimated, leaving more space for the ions to diffuse. As mentioned earlier, long term dynamic properties such as viscosity are very hard to determine for relatively small-sized and short-timed AIMD simulations. It is possible that the transition between the two different behaviors in the order at the two experimental temperatures are apparent at different simulation temperatures or changes occur again within the experiment. Of course additional simulations at several temperatures are out of the scope of this article due to intensive computer time. In addition, the IL's viscosities show varying temperature dependencies, further complicating the comparison between calculated and experimental data at different temperatures. Also it should be kept in mind that depending on the purity of the IL variations up to a factor of 2 were observed, see for example $[C_4C_1Im][N(CN)_2]$ in the supporting info of Reference.[313]

Turning now to the detailed hydrogen bond dynamics,[314] a geometrical criterion of $d_{H\cdots Y} \leq 300\,pm$, $135° \leq \angle(X–H\cdots Y) \leq 180°$ was chosen to decide whether a conformation is considered a hydrogen bond or not. From the RDFs and CDFs in Figure 3.3, it is apparent that the hydrogen bonds in $[C_2C_1Im][SCN]$ are more pronounced than in $[C_2C_1Im][B(CN)_4]$, and that they are almost equal to the hydrogen bonds in $[C_2C_1Im][N(CN)_2]$ concerning the structure. However, at equal structural character-

istics, the lifetimes of the respective hydrogen bonds τ(HB) are higher in the case of $[C_2C_1Im][N(CN)_2]$, especially at the H2 position. In almost all cases the hydrogen bond lifetime τ(HB) develops as [B]<[S]<[N], except for the H8. Interestingly, the hydrogen bond at the rear H5 hydrogen atom τ(HB H5) is always higher than the lifetime at H4, τ(HB H4), respectively. This is maybe caused by additional favorable interactions between the anion and the cation's ethyl chain in the vicinity of H5, see Figure 3.1. As in the case of the diffusion coefficient these dynamical properties of the hydrogen bond dynamics can also not be related to the viscosity behavior and rather contradict their trends; *i.e.*, a stronger hydrogen bond does not necessarily lead to a more viscous liquid. The ability to form a decent hydrogen bond was shown [314] to flatten the potential energy surface of imidazolium-based ionic liquids, making them more liquid in contrast to the higher interaction energies between cation and anion. [267]

No correlation of the fast dynamics to the viscosity [268] is reflected as well in the ion pair dynamics τ(IP), which are presented in Table 3.4 as well, and which are calculated according to Kohagen et al. [315,316] and Zhang et al. [317] Because of the shorter time scale of AIMD simulations compared to classical MD simulations, we did not allow reformation of ion pairs in our analysis, *i.e.*, the autocorrelation function was recorded in a continuous fashion. This function describes the lifetime of a distinct ion pair based on a nearest neighbor criterion. In the work of Zhang, the self-diffusion coefficients showed a direct correlation to the inverse of the ion pair lifetime. In our study, the lifetimes increase in the order [S]<[B]<[N] in line with the ordering of the calculated diffusion coefficients and more importantly in line with the short-time reorientation of the anion measured by Penna et al. [268]

As discussed earlier, anion and cation can occupy the space on-top of the cation's imidazolium ring. The average lifetime of such a conformation is quantified by the respective on-top dynamics autocorrelation function with the criteria $d_{\mathrm{CoR(+)–X}} \leq 500$ pm and $0° \leq \angle$(RN, CoR(+)–X) $\leq 45°$ and $135° \leq \angle$(RN, CoR(+)–X) $\leq 180°$, where X is the cation's center of ring or the anion's center of mass. It was deduced from Figure 3.2 that the anion is preferably on-top in $[C_2C_1Im][B(CN)_4]$ and $[C_2C_1Im][N(CN)_2]$, which is nicely reflected in the lifetimes showing values of the anion staying on-top twice as large as for the cation in the same IL, respectively (see Table 3.4). As opposed to this, the cation–cation on-top lifetime τ(on-top, ++) in $[C_2C_1Im][SCN]$ is larger than the cation–anion lifetime τ(on-top, +−). For the different ILs the cation–anion on-top lifetime (τ(on-top, +−)) increases in the order [S]<[B]<[N], while for the cation–cation (τ(on-top, ++)) the order complies with [B]<[N]<[S] in line with the ion pair dynamics. These results imply several connections. First of all, they imply that the cation–anion association is rather determined by the on-top than by the in-plane dynamics, *i.e.*, the hydrogen bond dynamics. More interestingly, the cation–cation on-top dynamics is the only dynamics reflecting the viscosity trends and thus it might explain the higher viscosity of the [SCN]-based IL than the other two cyano-based ILs. Therefore,

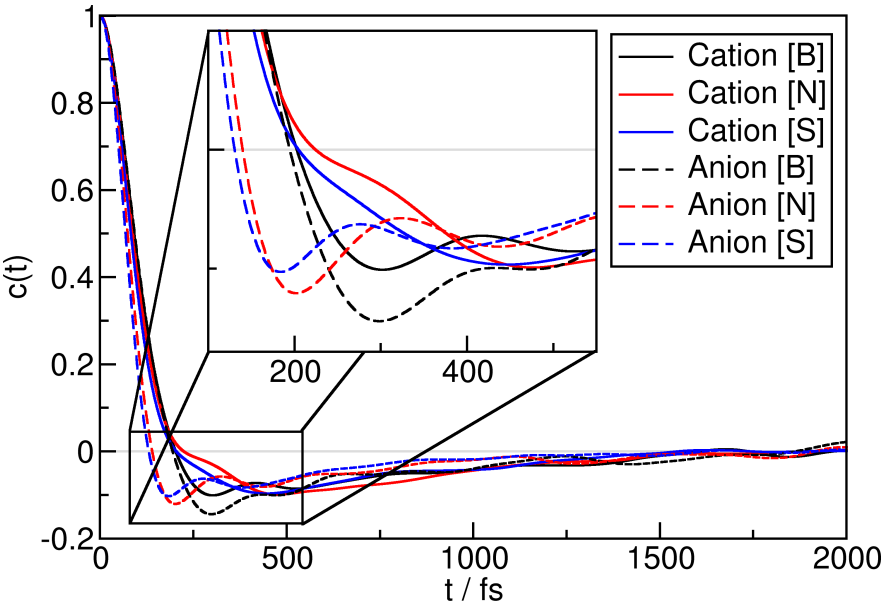

Figure 3.6: Velocity autocorrelation functions of the ion's center of mass normalized to fit $c(0) = 1$. [B] denotes the $[C_2C_1Im][B(CN)_4]$ IL, [N] the $[C_2C_1Im][N(CN)_2]$ IL, and [S] the $[C_2C_1Im][SCN]$ IL.

Table 3.5: Characteristic Values of Velocity Autocorrelation Functions Presented in Figure 3.6 with the Collision Time t_{coll} ($c(t) = e^{-1}$), Reversion Time t_{rev} ($c(t) = 0$), and Time at the First Minimum t_{min} with Corresponding Value of $c(t_{min})$

Ion	IL	M / gmol^{-1}	t_{coll} / fs	t_{rev} / fs	t_{min} / fs	$c(t_{min})$
$[C_2C_1Im]^+$	[B]	111.19	112	203	302	−0.101
$[C_2C_1Im]^+$	[N]	111.19	107	224	476	−0.099
$[C_2C_1Im]^+$	[S]	111.19	100	204	446	−0.097
$[B(CN)_4]^-$	[B]	114.89	113	195	299	−0.144
$[N(CN)_2]^-$	[N]	66.05	88	140	202	−0.121
$[SCN]^-$	[S]	58.08	81	131	184	−0.103

it might be instructive to study a possible correlation in several ionic liquids between the cation–cation dynamics rather than the cation–anion dynamics and the viscosities. And although again seeing connections for all ionic liquids might be too simple, for the series of the cyano-based ionic liquids the ability to form increased π–π-stacked conformations of $[C_2C_1Im][SCN]$ might explain the viscosity trends. This hypothesis is supported by a relatively slower diffusion of the cation in [S] compared to [B].

Another interesting dynamic quantity closely related to the image of an ion cage is the velocity autocorrelation function of an ion's center of mass.[318] Figuratively speaking, an ion cage consists of a central ion and is formed by all surrounding counterions in the first solvent shell, as described by Kohagen et al.[315,316] The velocity autocorrelation function starts at the value of 1 and decreases by definition. Assuming monoexponential decay, the first collision takes place when the function is decayed to the value of e^{-1}. After further decay, the velocity autocorrelation function reaches negative values, *i.e.*, the initial direction of the ion's movement is reversed. After passing through a

minimum, it eventually shows an oscillatory shape, demonstrating frequent collisions of the ion and other components, and then converges to zero. The velocity autocorrelation functions of the investigated systems are depicted in Figure 3.6 and characteristic values are listed in Table 3.5. It can be seen, that the function of all ions in all systems decay rather fast with collision times of 81 to 113 fs, which matches other AIMD simulations, *e.g.*, of $[C_4C_1Im][OTf]$ or $[C_2NH_3][NO_3]$.[318] This fast dynamics indicates dissociated ions, as opposed to long-lived ion pairs.[318,319] The cation's function shows a distinct minimum only in the case of the $[C_2C_1Im][B(CN)_4]$ IL, for the other two systems, there is only a shoulder in this region; they oscillate more slowly and smoothly. Thus, a potential anion cage can be broken rather rapidly in those cases of the [N] and [S] ILs. This is probably not only due to the fact of equivalent molecular masses of cation and anion for the [B] IL, whereas $[N(CN)_2]^-$ and $[SCN]^-$ are considerably lighter than $[C_2C_1Im]^+$, but also due to the weak hydrogen bond and the larger charge delocalization of $[B(CN)_4]^-$ leading to a more persistent anion cage which is also reflected in the Voronoi neighbor count, see in Table 3.3 the high $[B(CN)_4]^-$ neighbor count with itself. All anions show a weak oscillatory behavior, indicating the interaction with the ion cage. The dynamics of $[N(CN)_2]^-$ and $[SCN]^-$ are significantly faster compared to $[B(CN)_4]^-$, which is in line with their smaller molecular weight.

Interestingly, the velocity autocorrelation function of both ions in $[C_2C_1Im][B(CN)_4]$ are somewhat synchronized. Both components share a very equal molecular weight, are probably comparable in size, and were observed to have closely matching diffusion coefficients. However, it should be noted that as was nicely shown by Fumino et al.[267] and by Neves et al.[305] considering only the weight does not fully explain the microscopic behavior.

3.1.5 Summary and Conclusion

The three ionic liquids $[C_2C_1Im][B(CN)_4]$, $[C_2C_1Im][N(CN)_2]$ and $[C_2C_1Im][SCN]$ were investigated with the aid of *ab initio* molecular dynamics. All liquids pose interesting applications as electrolytes, and the microscopic level behavior has to be understood to learn about their possible applications. The ionic liquids share a common cation, the imidazolium, which is capable of donating hydrogen bonds at the ring positions and weak hydrogen bonds for all other hydrogen atoms of the methyl and methylene groups. All anions consist of one or more nitrile groups connected to a central atom, influencing the hydrogen bond acceptor ability of the anion.

The findings of our *ab initio* molecular dynamics simulations are summarized in Table 3.6 together with some experimental values from literature.[268,305]

The hydrogen bonding within the ionic liquids is very pronounced for $[N(CN)_2]^-$ and $[SCN]^-$ and much weaker for the $[B(CN)_4]^-$ anion, see first two entries in Table 3.6. All anions are mostly located on-top of the cation instead of in-plane. However, $[SCN]^-$ and $[N(CN)_2]^-$ form strong hydrogen bonds[267] and thus they can be situated also

Table 3.6: Structural and Dynamical Behavior of the Investigated Ionic Liquids[a]

property	order	values
	Structure	
H2 hydrogen bond	B $\ll$ S $\approx$ N	–
H8 hydrogen bond	B < N < S	–
+− on-top structure	B < S < N	60% < 65% < 70%
++ on-top structure	B < N < S	9% $\ll$ 20% $\ll$ 40%
	Dynamics	
D / pm^{2}ps^{-1}	N < B < S	220 < 774 < 858
τ(HB H2) / ps	B < S < N	0.23 < 0.34 < 0.49
τ(IP) / ps	S < B < N	1.42 < 2.34 < 3.37
τ(on-top, +−) / ps	S < B < N	1.72 < 1.80 < 3.81
τ(on-top, ++) / ps	B < N < S	0.78 < 1.51 < 1.87
t_{coll}(+) / ps	S < N < B	0.10 < 0.11 < 0.11
t_{coll}(−) / ps	S < N < B	0.08 < 0.09 < 0.11
	Experiment	
η^b 298 K / mPas	N < B < S	16.1 < 18.6 < 24.5
η^b 363 K / mPas	B < N < S	3.8 < 4.2 < 5.5
M / gmol^{-1}	S < N < B	58.08 < 66.05 < 114.89
Raman - reorientation[c]	S < B < N	–

[a] B indicates $[C_2C_1Im][B(CN)_4]$. N: $[C_2C_1Im][N(CN)_2]$. S: $[C_2C_1Im][SCN]$. "+" indicates the cation and "−" indicates the anion. "t" coins the collision time of velocity autocorrelation function. τ indicates lifetimes of the according correlation functions. The complete data are given in Table 3.2, Table 3.4 and Table 3.5. [b] Neves et al.[305] [c] Penna et al.[268]

in-plane of the cation ring. For all ionic liquids, the cation–cation interaction revealed distinct π–π stacking conformations for the [SCN]-based ionic liquid which decrease dramatically for $[C_2C_1Im][N(CN)_2]$ and the $[C_2C_1Im][B(CN)_4]$ liquid. The small size of the $[SCN]^-$ anion together with the strong hydrogen bonding ability might stabilize those cation–cation arrangements which was already pointed out by Matthews et al.[303] for imidazolium chloride ionic liquid dimer clusters. While these observations show that the structural characteristics of the cyano-based ionic liquids are rather various and multifaceted, the dynamics is even more extreme in terms of diversity. One might be tempted to attribute the higher viscosity[305] of $[C_2C_1Im][SCN]$ to the strong hydrogen bondings, however, their fast decay in terms of lifetimes compared to the $[N(CN)_2]$– and the $[B(CN)_4]$–liquid together with the different sequence exclude this explanation. Also the ion pair dynamics does not meet the viscosity order, but it relates rather to the cation–anion on-top dynamics than to the hydrogen bond dynamics indicating that the on-top structures govern the ion pair formations. Both ion pair dynamics and cation–anion on-top dynamics relate well to the experimental anion reorientation dynamics.[268] Contrary to the hydrogen bonding, the order of occurrence of the cation–cation on-top conformations correlates well with the order of this cation–cation on-top dynamics. Both structural as well as dynamical behavior show the same sequence as the viscosity of these ionic liquids, inferring that the higher viscosity of the $[C_2C_1Im][SCN]$ ionic liquid might be related to enhanced π–π interaction. Thus, in order to make these liquid even more fluid reducing the π–π stacking ability seems to be a promising

route. The velocity autocorrelation function showed that there seem to be cation and anion cages for the counterions each, however, the anion cage is more persistent in the case of the $[B(CN)_4]^-$ anion and maybe only weakly present for the $[SCN]^-$ and the $[N(CN)_2]^-$ anion. The collision times from these functions vary mildly and can be related to the mass of the anions, see Table 3.6. Altogether, the complicated interplay between interactions, dynamics and structures lead for this family of cyano-based ionic liquids as well to the conclusion that ionic liquids are very complicated liquids and their macroscopic behavior is difficult to be related to the microscopic characteristics.

However, this detailed knowledge about the preferred interaction sites within the ionic liquids should help to determine whether an ionic liquid is suited for a given application, *e.g.*, as electrolyte in solar cells, or which property of the ionic liquid has to be addressed to tailor it for a specific application.

Supporting Information

Figures showing all derived partial charges for the classical preequilibration and additional radial distribution functions. The Supporting Information is available free of charge on the ACS Publications website at DOI: 10.1021/acs.jpcb.6b00098 and is attached in Section A.1.

Acknowledgments

B.K. would like to express thanks for the support from the Deutsche Forschungsgemeinschaft under the SPP 1708 Project KI768/12-1. B.K. as well as H.W. gratefully acknowledges the Fonds der chemischen Industrie.

3.2 Adsorption Behavior of the 1,3-Dimethylimidazolium Thiocyanate and Tetracyanoborate Ionic Liquids at Anatase (101) Surface

Henry Weber,[†] Thomas Bredow,[†] and Barbara Kirchner[†]*

The Journal of Physical Chemistry C, **2015**, Volume *119*, Pages 15137–15149.

DOI:	10.1021/acs.jpcc.5b02347
Received:	March 10, 2015
Revised:	June 5, 2015
Published:	June 10, 2015

Contributions to the manuscript:

- Setup and maintenance of all calculations.
- Analysis and evaluation of all results.
- Writing of the manuscript.

[†]Mulliken Center for Theoretical Chemistry, Universität Bonn, Beringstr. 4+6, D-53115 Bonn, Germany.
*Corresponding Author E-mail: kirchner@thch.uni-bonn.de.

Abstract

The adsorption behavior of the ionic liquids 1,3-dimethylimidazolium thiocyanate and 1,3-dimethylimidazolium tetracyanoborate on the anatase (101) surface is studied through theoretical methods. This includes a comparison of the PBE and PBE0 functionals as well as the D3 and D3M+ dispersion correction schemes for the calculation of energetic and structural properties. The PBE functional was found to underestimate interaction energies, and the D3 dispersion correction was observed to overbind. While the surface titanium atoms predominantly form contact with anion's nitrogen atoms, the oxygen atoms of anatase interact in hydrogen-bond-like structures with the acidic hydrogen atoms of the imidazolium cation in addition to ubiquitous electrostatic and dispersive interactions. Ionic liquid ion pairs remain stable after adsorption and closely match the geometry of the isolated ions. A band shift of the density of states of TiO_2, possibly resulting in higher values of the open-circuit voltage in complete solar cells, is attributed to the adsorption, which might be interesting for application of these ionic liquids in real dye-sensitized solar cell devices.

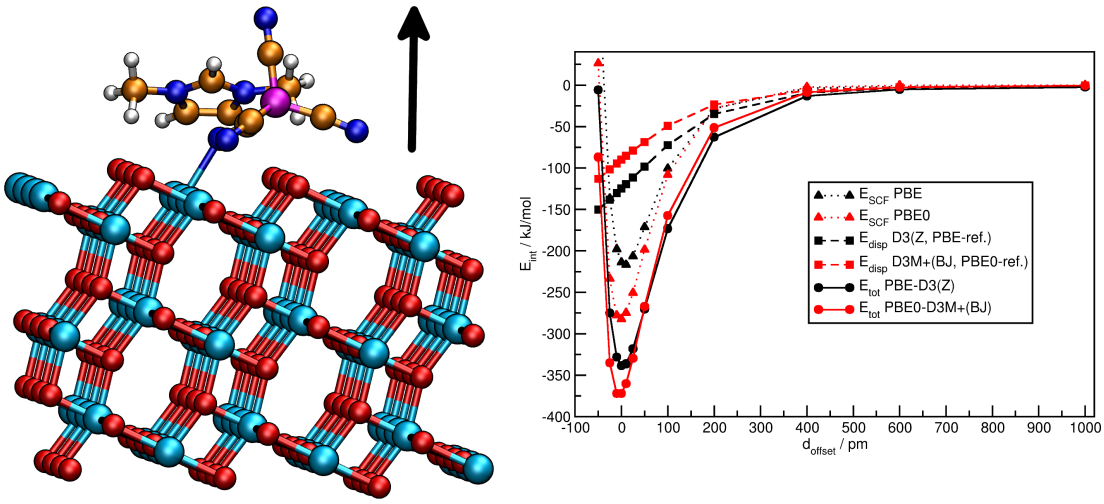

3.2.1 Introduction

Titanium dioxide is by far the most studied metal oxide nowadays.[320] It has been addressed extensively in experimental as well as in theoretical works. Titanium dioxide naturally occurs in three different modifications, namely, rutile, anatase, and brookite. While rutile is the most widely studied and the most stable modification under ambient conditions,[321] the anatase modification has experienced increasing interest with progress of scientific work into the *nanoage*.[320,322] Titanium dioxide is applied in numerous technical processes due to the huge variety in properties. For example, it is used in heterogeneous catalysis because of the photocatalytic properties,[323] as electrode material to produce hydrogen or electric energy,[324,325] in diverse photovoltaic applications,[326] as gas and bio sensors,[327] and in biomedical applications.[328]

Many of these applications involve the surfaces of titanium dioxide, which therefore became a fruitful field for experimentalists and theoreticians.[329] The most stable rutile modification with the prominent (110) surface was intensively investigated, along with other low-index planes such as (001) and (100).[321,322,329] It was shown that the phase stability of titanium dioxide is dependent on the particle size. For particles below a certain threshold, anatase becomes the most stable modification.[330,331] For anatase nanoparticles, (101) and (100)/(010) surface planes are found,[332] whereas the thermodynamically most stable one is the (101) surface for single crystals. A very recent comprehensive theoretical study on low-index planes of rutile, anatase, and brookite by Esch *et al.* also indicates the anatase (101) surface as one of the most stable TiO_2 surfaces along with rutile (110).[333]

There was a significant and sudden increase in publications as well as citations concerning TiO_2 nanoparticles starting from 1991, the year of Michael Grätzel's breakthrough article concerning dye-sensitized solar cells (DSCs).[13] In that article, the use of TiO_2 nanoparticles covered with a dye to harvest sunlight in DSCs was described and the increase in device efficiency was attributed to the drastically increased specific surface by using nanoparticles. Since then, breathtaking progress has been made in the topic of photovoltaics, especially DSCs.[326] Research focused on using different dyes, redox-mediators, cell geometries, as well as different electrolytes. For example, computationally guided design has led to a molecularly engineered porphyrin dye with maximized electrolyte compatibility and improved light-harvesting properties, resulting in an overall power conversion efficiency of 13 %.[34] One shortcoming of conventional molecular electrolytes such as acetonitrile when used in a DSC is the electrolyte loss due to leakage and evaporation; even photodegradation or thermal degradation play a role. For this purpose, besides the use of p-type semiconductors,[334,335] hole conducting materials,[114,336] and polymeric solid-state electrolytes,[106,337,338] ionic liquids (ILs)[256] were investigated to replace volatile organic solvents.[100] The IL's negligible volatility, high thermal and chemical stability, the wide electrochemical stability window, as well

as their superior solvent properties make them excellent candidates for use as electrolytes in DSCs. One shortcoming of commonly used ILs is their viscosity, but it was shown that binary mixtures of different ILs can significantly decrease the viscosity.[166] Additionally, ILs have the ability to be more than a diffusive medium for the redox mediator; they can affect electron–hole recombination rates in the solar cell, band edge positions of the semiconductor (*e.g.*, TiO_2) and the chemical reaction of dye regeneration.[166] The pioneering work by Fredin *et al.*[166] employing ILs in DSCs showed that the overall efficiency and distinct DSC device functionalities are crucially affected by the molecular structure of the IL. In detail, the IL 1-ethyl-3-methylimidazolium thiocyanate ($[C_2C_1Im][SCN]$) was observed to yield device efficiencies higher than that of the IL 1-ethyl-3-methylimidazolium tetracyanoborate ($[C_2C_1Im][B(CN)_4]$) for a ruthenium dye-based DSC. This behavior was partly attributed to the formation of pseudohalides, such as $[I_2SCN]^-$, lowering the I_3^- concentration, which was not observed in the case of $[C_2C_1Im][B(CN)_4]$. In contrast, studies by Armel *et al.*[339,340] focusing on porphyrin-sensitized DSCs revealed an opposing trend in device efficiency employing the same ILs.

The pure IL $[C_2C_1Im][SCN]$[269,270] and binary mixtures with $[C_2C_1Im][Cl]$[301,308] were already investigated by means of *ab initio* molecular dynamics (AIMD). It was found that for the AIMD simulation of pure $[C_2C_1Im][SCN]$ with the PBE functional, it is crucial to account for dispersive interactions. From theoretical studies,[256] the importance of dispersion correction[341] for the simulation of ILs has been shown,[289,342] especially for the accurate description of hydrogen bonding in ILs.[306,343,344] The capability and advantages of using theoretical methods to tackle these demanding systems were highlighted recently by Zahn *et al.*[345] and Kirchner *et al.*[256] In a very recent study of Firaha *et al.*, the excellent solvent properties of $[C_2C_1Im][SCN]$ regarding SO_2 were investigated by means of AIMD.[276] $[C_2C_1Im][SCN]$ proves to be a very promising and interesting ionic liquid for diverse applications.[276] For binary mixtures of $[C_2C_1Im][SCN]$ with $[C_2C_1Im][Cl]$,[301,308] it was shown that the IL's properties are affected ideally and nonideally upon mixing, depending on the investigated property. Furthermore, the behavior of $[C_2C_1Im][SCN]$ at a liquid–solid interface was showcased recently by Pensado *et al.*, observing $[C_2C_1Im][SCN]$ at a carbon interface in the context of supercapacitors.[346] A strong adsorption of the IL at the graphene surface along with multiple solvation layers at the interface was recorded. Similarly, the IL's properties should be affected at the interface to different solids, such as the anatase nanoparticles used as electrode material in DSCs. To the best knowledge of the authors, the interface of anatase (101) and different ILs has not been studied in detail to date, but knowledge of the specific interactions between electrolyte and electrode might be crucial to fully understand IL-based DSC devices.

In the present study, the adsorption of the ILs 1,3-dimethylimidazolium tetracyanoborate

([C_1C_1Im][$B(CN)_4$]) and 1,3-dimethylimidazolium thiocyanate ([C_1C_1Im][SCN]) and their isolated components [C_1C_1Im]$^+$, [$B(CN)_4$]$^-$ and [SCN]$^-$ on anatase (101) is investigated with periodic density functional theory (DFT) methods.

In the following, the computational details are briefly described in Section 3.2.2. In Section 3.2.3, the investigated systems are introduced and the computational challenges, namely the self-interaction error, supercell size and background charge and their effects on the calculated properties are examined. Next, detailed insight of the adsorption physics of the ILs components and the IL ion pairs is given. Finally, the effects of adsorption on TiO_2's density of states and band shifts are investigated and the article closes with the conclusion.

3.2.2 Computational Methods

Some of the calculations were performed with the CP2K program package[286] employing the QUICKSTEP[287] module. The Perdew–Burke–Ernzerhof (PBE)[216–218] functional for exchange and correlation was used in combination with Godecker–Teter–Hutter (GTH)[292,293] pseudopotentials and the MOLOPT-DZVP-SR-GTH basis sets.[291] To account for van der Waals type interactions, the D3 dispersion correction[230] was employed in different variations, including the D3 dispersion correction with zero (Z) and Becke–Johnson (BJ) damping[347] as well as specific D3 coefficients for titanium designated for use in a TiO_2 solid.[348,349] Application of these special D3 parameters is denoted D3M+ in the following.[348,349] Three-dimensional periodic boundary conditions (PBCs) were applied for bulk calculations. PBCs must be applied to minimize boundary effects that inevitably occur in finite models.[350] Slab calculations were performed with two-dimensional PBCs. The correct decay behavior of the wave function in nonperiodic directions was ensured by a Martyna–Tuckerman Poisson solver.[351] To allow a comparison of the functional, further calculations were carried out utilizing the program package CRYSTAL14,[352] employing the hybrid PBE0 functional.[216,217,222] This program was selected because it offers an efficient implementation of exact Hartree–Fock exchange calculations. The atomic basis sets used in the CRYSTAL calculations were the D'Arco basis set (Ti: 86-411G(d31))[353,354] for titanium and the Muscat basis set (O: 8-411G)[355] for oxygen. With both approaches, a reasonable agreement was obtained for calculated and experimental bulk lattice parameters (see Supporting Information, Table 1).

To obtain the geometry of the pure anatase slab, a full geometry optimization of the bulk phase was performed first, where the cell parameters and atomic positions were relaxed. The anatase surface models were generated by rotation of the crystal cell so that the surface normal matches the z axis, and the atoms of the layers were then selected by their z coordinate. The number of layers was chosen to yield two identical surfaces and a vanishing dipole moment in the z direction for the pure anatase slab. The optimal model slab in terms of the number of layers was tested in preliminary

surface energy calculations (see Supporting Information, Table 2 and Figure 1).

Minimum energy conformations of the different species adsorbed on the surface were determined by a full geometry optimization at the PBE-D3-MOLOPT-DZVP-SR-GTH level with the CP2K program package, employing the six stoichiometric layer model, where the two stoichiometric bottom layers of TiO_2 were held fixed. Note that a vanishing dipole moment cannot be ensured upon one-side adsorption of a molecule. However, this approach was previously shown to yield reasonable results.[356–358] While modeling these systems, especially the separate ions at the TiO_2 surface employing periodic boundary conditions, the problem of non-neutral simulation boxes is encountered.[359] The geometry optimizations were started from a large number of different, random starting geometries and were observed to converge to similar optimized structures in the case of the isolated ions. Regarding the huge conformational freedom of the ion pairs on the surface, starting geometries were extracted from classical molecular dynamics simulations at high temperatures between 350 and 700 K with preliminary force field parameters (see Supporting Information). Specific geometries of the species investigated in Section 3.2.3.4 were derived from constrained geometry optimizations, where the whole TiO_2 substrate was held fixed, combined with constraining adequate internal degrees of freedom of the molecules to yield the desired conformation. The energy profiles were then calculated by iterative changing of the surface–molecule distance while no relaxation was allowed at each point.

To determine the charge transfer (CT) between adsorbate and substrate, Mulliken[360] as well as Blöchl[361] population analyses were used.

To evaluate the interaction between adsorbate and anatase, basis set superposition error (BSSE) corrections were calculated using the counterpoise correction (CP) method.[362] The BSSE-corrected interaction energy $E_{\mathrm{int}}(\mathrm{AB})$ between A and B is given by

$$E_{\mathrm{int}}(\mathrm{AB}) = E_{\mathrm{AB}}^{\mathrm{AB}} - E_{\mathrm{A}}^{\mathrm{AB}} - E_{\mathrm{B}}^{\mathrm{AB}} \tag{3.2.1}$$

with $E_{\mathrm{AB}}^{\mathrm{AB}}$ the total energy of the complete system, $E_{\mathrm{A}}^{\mathrm{AB}}$ the total energy subsystem A with the complete basis of A and B, and $E_{\mathrm{B}}^{\mathrm{AB}}$ the total energy of the subsystem B with the complete basis of A and B in the geometry of the adsorption structure.

The density of states (DOS) and the projected density of states (PDOS) were evaluated for various systems with the properties tool included in the CRYSTAL14 program package.[352] Employing a Fourier–Legendre technique,[363,364] the DOS was calculated between -0.5 and 0.5 hartree at 1001 discrete points by expanding the DOS with 10 Legendre polynomials. The DOS was projected onto a set of atomic orbitals (AO) derived from Mulliken population analysis[360] to compute the PDOS.

The visual molecular dynamics (VMD) program package was used to visualize molecular structures.[365] Graphical representations were created using the GRACE program

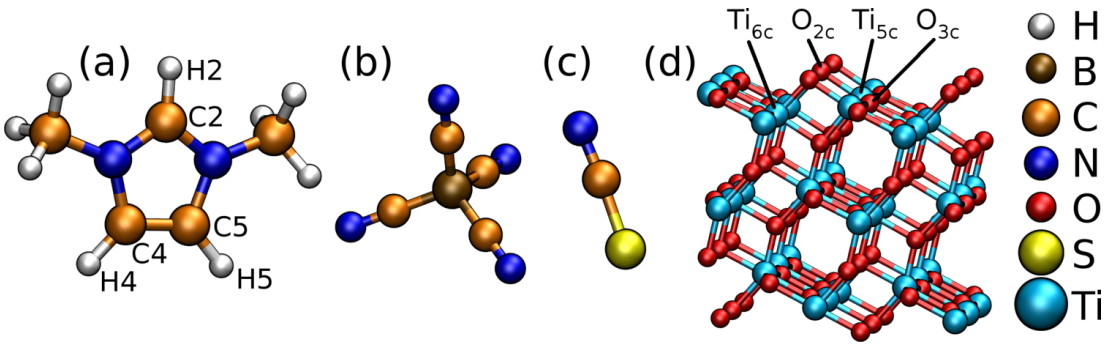

Figure 3.7: Labeling of the ILs components $[C_1C_1Im]^+$ (a), $[B(CN)_4]^-$ (b), and $[SCN]^-$ (c) as well as the anatase (101) surface (d). In the case of the symmetric imidazolium cation, H4 and H5 (C4 and C5, respectively) are indistinguishable.

package.[366]

In the following, all results corresponding to the PBE functional were obtained with the CP2K program package, and all results corresponding to the PBE0 hybrid functional were obtained with the CRYSTAL14 program package unless stated otherwise. Two different programs were employed only because of computational efficiency reasons; the aim of this work is not to compare these program packages.

3.2.3 Results and Discussion

3.2.3.1 Systems Investigated

The ionic liquids 1,3-dimethylimidazolium tetracyanoborate ($[C_1C_1Im][B(CN)_4]$) and 1,3-dimethylimidazolium thiocyanate ($[C_1C_1Im][SCN]$) were chosen for the investigation of their interaction with the (101) anatase surface. Both ILs showed promising applications in real DSC devices, but differences in device performance could be attributed only partly to the molecular structure of the ILs.[166,339,340] The labeling of the ILs is shown in Figure 3.7.

3.2.3.2 Self-Interaction Error

The self-interaction error (SIE) is inherent in approximate functionals used in Kohn–Sham DFT.[367] This well known problem leads to an artificial spreading out of the electron density, which ultimately leads to an erroneous decrease in energy, *i.e.*, overstabilization. For the particular systems investigated, *i.e.*, adsorption of an ion at the TiO_2 surface, the SIE manifests itself in an artificial charge transfer (CT) between the surface and the adsorbate at long distances which are considered to be noninteracting. This unphysical charge transfer was observed previously for molecules on metal surfaces, where it caused an overestimation of the electronic conductance.[368,369] The interaction energy of $[C_1C_1Im]^+$ and anatase with the corresponding CT is shown in Figure 3.8a. It can be seen that the interaction energy between surface and adsor-

bate decreases with increasing distance for separations above the equilibrium distance, which is physically sound. At $d_{\text{surf-CoR}}$ greater than approximately 800 pm, however, the charge transfer is starting to increase, which is causing an artificial lowering of the energy, reflected in the simultaneously decreasing interaction energy. That means configurations with a large distance between adsorbate and surface, which can hardly be considered adsorbed at such distances, are artificially stabilized.

The SIE can be reduced when hybrid functionals with a fraction of exact exchange, *i.e.*, Hartree–Fock exchange, are used,[370] and can be even further minimized upon the usage of functionals specifically designed to minimize the delocalization error such as the rCAM-B3LYP or the MCY3 functionals.[371] As can be seen from Figure 3.8a, the SIE artifact is not present upon the utilization of the PBE0 hybrid functional. However, for a system of this size it is too expensive to calculate the full potential energy curve with exact Hartree–Fock exchange. Therefore, the potential energy curve is probed only at selected points, *i.e.*, at the PBE-D3 local minimum energy geometry, at $d \approx 830$ pm, where the PBE CT is minimal, and at $d \approx 1430$ pm, where the PBE-D3 calculation revealed a significant unphysical CT.

Apart from the above-mentioned specialized functionals, methods exist to correct the standard functionals for the SIE, briefly denoted as self-interaction correction (SIC). The first of these methods was proposed by Perdew and Zunger in 1981,[372] which was then further improved by Mauri and co-workers.[373] Application of the SIC is considered to improve the total energy, accurate binding energies for negatively charged ions, orbital eigenvalues, long-range behavior of the one-electron potential and density, and overall description of the electron density.[372] Furthermore, these SIC schemes were also shown to be applicable to *ab initio* molecular dynamics simulations, where they were used to accurately model a hydroxyl radical in an aqueous solution.[374] The different corrections were tested for the present systems; however, the application of these techniques did not result in any beneficial effects for the PBE calculations, because most of the corrections focus on systems with unpaired electrons.

3.2.3.3 Supercell Size and Background Charge

Calculating charged species in a non-neutral unit cell with periodic boundary conditions is a nontrivial task.[359,375] By definition, a charged cell repeated infinitely would yield an infinite, self-interacting charge and therefore an infinitely large electrostatic energy. To prevent this, a common workaround is to distribute a homogeneous background charge density of opposite sign in the simulation box to ensure overall neutrality. This leads to finite energies, but it prevents neither the Coulombic interaction of charged species with their own periodic images nor the interaction of the charged species with the background charge, leading ultimately to problems when calculating absolute energies.[376,377]

The interaction energy of a $[C_1C_1Im]^+$ ion in flat conformation on the (101) anatase

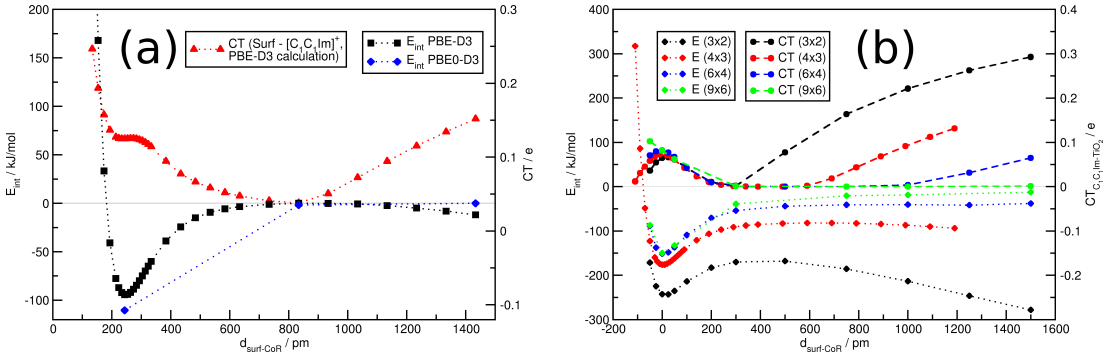

Figure 3.8: Left y-axis: interaction energy, E_{int}, of anatase (101) and $[C_1C_1Im]^+$ in flat conformation (see Figure 3.15 for details) on a 4×3 supercell. Right y-axis: corresponding charge transfer between anatase and $[C_1C_1Im]^+$. $d_{\text{surf-CoR}}$ indicates distance between surface oxygen atoms and center of the imidazolium ring (CoR) of $[C_1C_1Im]^+$. (a) Comparison between PBE and PBE0 functional; Blöchl charges were used to determine the CT for the CP2K results. (b) Dependence on supercell dimensions; Mulliken charges were used to determine charge transfer. See Supporting Information for numerical values.

surface for systematically increased supercell size of almost quadratic shape along with the corresponding charge transfer between surface and ion is depicted in Figure 3.8b. Numerical values of Figure 3.8b and explicit box dimensions are given in the Supporting Information; the supercell dimensions are given by multiples of the a cell vector times multiples of the b cell vector, $a \times b$. It can be seen that the potential energy curve of the cation on the anatase surface at various distances shows a clear minimum. This curve should converge to zero because relative BSSE-corrected energies are plotted for the interaction of the cation with anatase, and this interaction vanishes for large separations. In Figure 3.8b, two separate effects can be noticed for small unit cells. On the one hand, the PBE-D3 interaction energy does not converge to zero for increasing separation of cation and surface, it converges to a certain negative, *i.e.*, attractive, energy. On the other hand, the energy decreases again for large separations, which is strongly pronounced for the small systems. As can be seen, this effect vanishes for very large super cells. One possible explanation is that this charge transfer is induced by the energetically unfavorable interaction of the cation with its periodic images because the significantly decreased charge on the cation reduces this long-range electrostatic repulsion. As the simulation cell becomes larger, the electrostatic interaction of the cation and the periodic images diminishes, and consequently the total energy cannot be lowered by reducing the cations total charge. Because the artificial energy lowering at 1400 pm in not observed with PBE0-D3, it can be concluded that it is partly due to the SIE.

The first mentioned effect, *i.e.*, the energy not converging to zero, is attributed to the interaction of the positively charged cation with the homogeneously distributed negative background charge. As the supercell size increases, the background charge is "diluted"; therefore, the magnitude of this effect decreases with increasing box size.

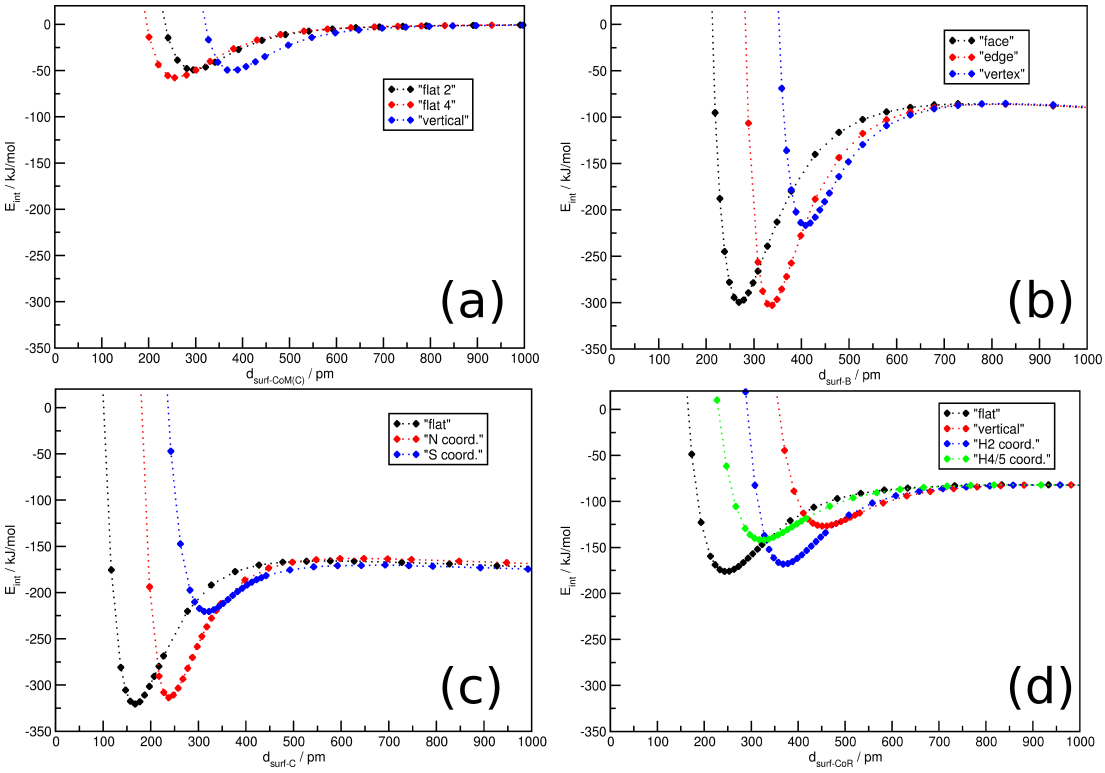

Figure 3.9: PBE-D3 interaction energies, E_{int}, of different species at different conformations with (101) anatase surface. $d_{\text{surf-}*}$ indicates z-distance of surface oxygen atoms to (a) carbon center of mass (CoM) of C_4H_{10}, (b) B of $[B(CN)_4]^-$, (c) C of $[SCN]^-$, or (d) center of the imidazolium ring (CoR) of $[C_1C_1Im]^+$.

Interestingly, for box sizes equal to or larger tha 6×4 units, the minimum energy is not affected anymore (compare blue and green curves of Figure 3.8b at $d_{\text{surf-CoR}} = 0$ pm), whereas the interaction energy for large distances is still not converged to less than 1 kJmol^{-1} for the very large 9×6 supercell (see Figure 3.8b, green curve).

3.2.3.4 Adsorption Behavior

Based on the results of the previous section, the adsorption behavior of three different species, namely the tetracyanoborate anion ($[B(CN)_4]^-$), the thiocyanate anion ($[SCN]^-$) and the 1,3-dimethylimidazolium cation ($[C_1C_1Im]^+$) on the (101) anatase surface was investigated using a 4×3 supercell, six stoichiometric layers of the substrate and the CP2K-PBE-D3 level of theory. BSSE-corrected interaction energies of the species in different orientations are shown in Figure 3.9. The energy profiles depicted in Figure 3.9 were computed under different restraints, see computational details in Section 3.2.2. All calculations were carried out with the 4×3 supercell, which was observed to give minimum positions and interaction energies close to the larger unit cells at a small fraction of the computational cost. Because of the aforementioned interaction with the spurious background charge and the periodic images, energy values can only be used qualitatively to compare between different conformations or species.

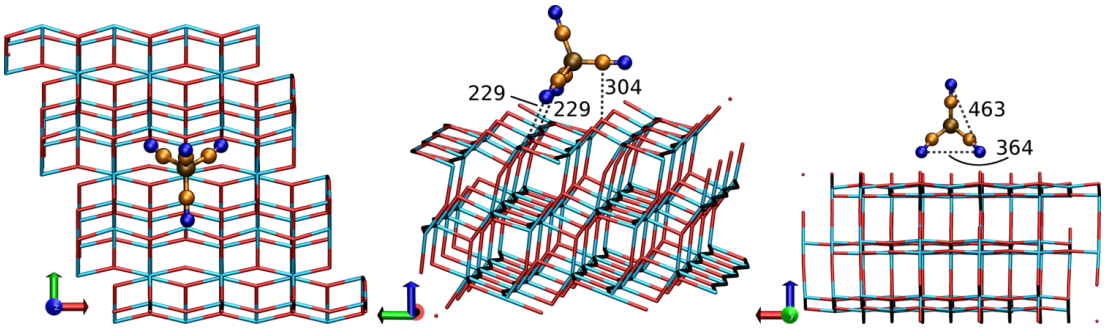

Figure 3.10: $[B(CN)_4]^-$ minimum energy adsorption geometry. Labeled distances are in picometers; color code is depicted in Figure 3.7.

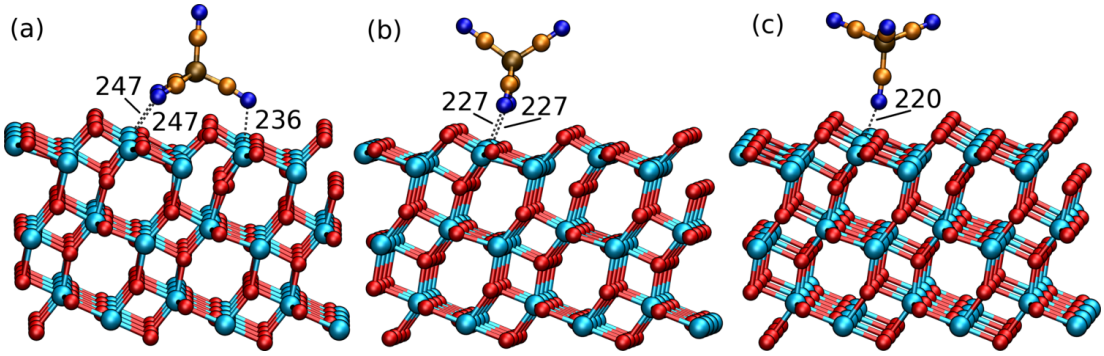

Figure 3.11: $[B(CN)_4]^-$ adsorption geometries: (a) "face" conformation, (b) "edge" conformation and (c) "vertex" conformation. Labeled distances are in picometers, color code is depicted in Figure 3.7.

The potential energy of C_4H_{10} is included for comparison with a neutral system. It can be seen that none of the aforementioned effects, namely delocalization error and interaction with a background charge, are present for this system. Quantitative results are extracted from calculations of the ion pair in an overall neutral box, *vide infra*.

$[B(CN)_4]^-$. The common IL anion $[B(CN)_4]^-$ was adsorbed on the (101) anatase surface; the geometry is shown in Figure 3.10. The tetrahedral molecule aligns in a fashion that three negatively charged nitrogen atoms point toward positively charged titanium atoms; more precisely, they point toward the unsaturated and therefore more reactive Ti_{5c} atoms. Short nitrogen–titanium distances of $d_{N–Ti} \approx 229$ pm indicate a strong interaction. The $[B(CN)_4]^-$ tetrahedron is distorted in order to maximize the N–Ti interactions; the resulting N–N distance of two ligands is $d_{N–N} = 364$ pm. For comparison, the equilibrium N–N distance in a gas phase anion of $[B(CN)_4]^-$ is $d_{N–N} \approx 450$ pm at the same level of theory. Experimentally, favorable N–Ti interactions were identified for ammonia adsorbed on TiO_2, supporting our observed binding mode.[378–381]

Furthermore, the following three conformations were manually chosen and constrained: the "face" conformation with three ligands pointing toward the surface (Figure 3.11a), the "edge" conformation with two ligands pointing toward anatase (Fig-

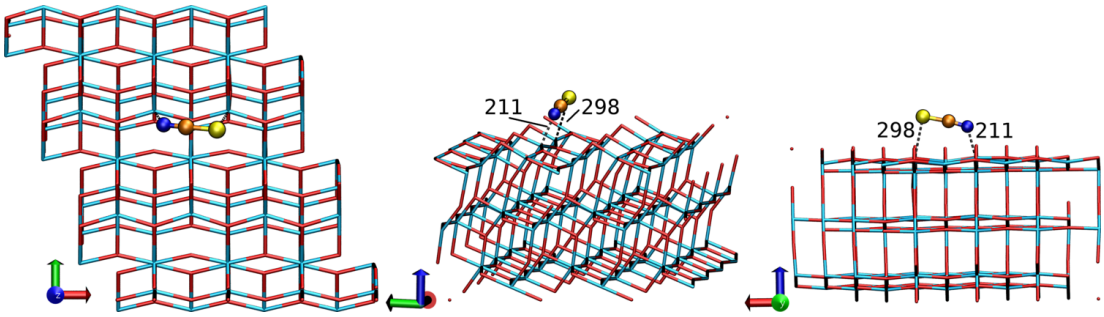

Figure 3.12: $[SCN]^-$ minimum energy adsorption geometry. Labeled distances are in picometers, color code is depicted in Figure 3.7.

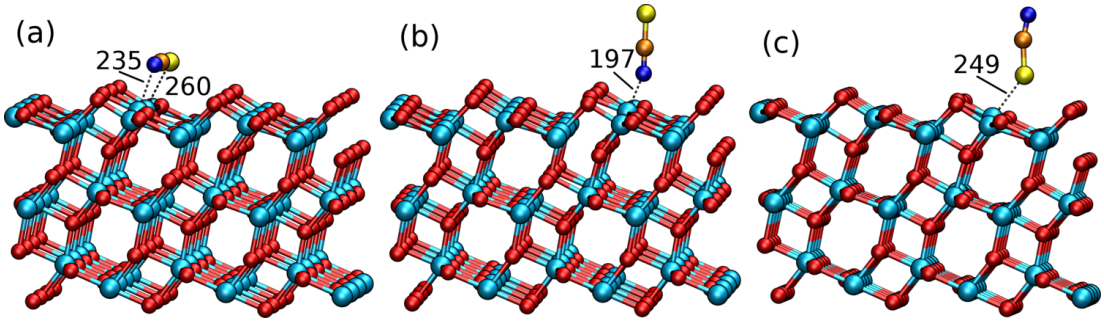

Figure 3.13: $[SCN]^-$ adsorption geometries: (a) "flat" conformation, (b) "N coordination" conformation, and (c) "S coordination" conformation. Labeled distances are in picometers, color code is depicted in Figure 3.7.

ure 3.11b), and the "vertex" conformation with one ligand pointing toward anatase (Figure 3.11c). Conformations (a) face and (b) edge match closely the minimum energy conformation without constraints; they differ only by a slight rotation, where two N–Ti interactions stay intact. Both conformations are close in energy, but the edge conformation is slightly favored in spite of the missing third N–Ti interaction (see Figure 3.9b). For the face conformation, three simultaneous N–Ti interactions can be established only by bridging the O_{2c} oxygen atom ridge. In the case of the edge conformation, two CN units can approach the surface and coordinate to the unsaturated Ti_{5c} atoms, yielding much stronger individual interactions, as can be deduced from Figure 3.9b as well as from the very short N–Ti distance of $d_{\text{N-Ti}} = 227$ pm. For the vertex conformation, only one N–Ti interaction prevails, which accounts for a significantly smaller interaction energy. Changing from (a) to (b) to (c), the surface–B distance increases, which might play a crucial role in the condensed phase, because there is limited space in that case.

$[SCN]^-$. The unconstrained geometry optimization of the thiocyanate anion $[SCN]^-$ reveals a rather flatly aligned anion in a hollow of the (101) anatase surface, see Figure 3.12. The short N–Ti distance of $d_{\text{N–Ti}} = 211$ pm indicates a strong interaction, as seen before in the case of $[B(CN)_4]^-$, but as the thiocyanate is not pointing toward the

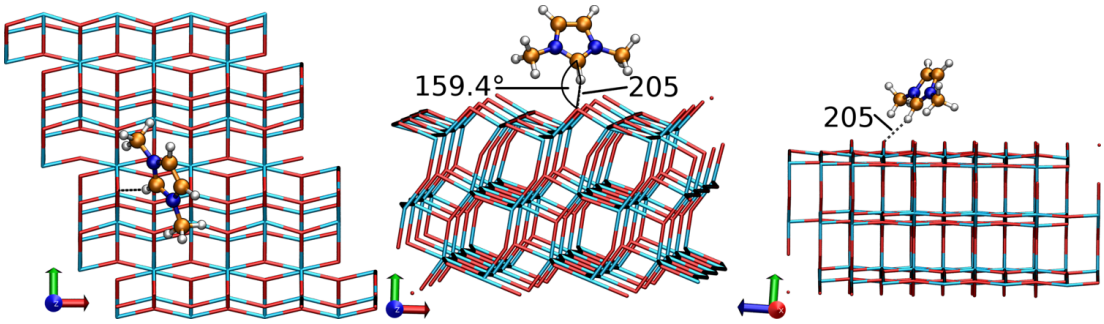

Figure 3.14: $[C_1C_1Im]^+$ minimum energy adsorption geometry. Labeled distances are in picometers, color code is depicted in Figure 3.7.

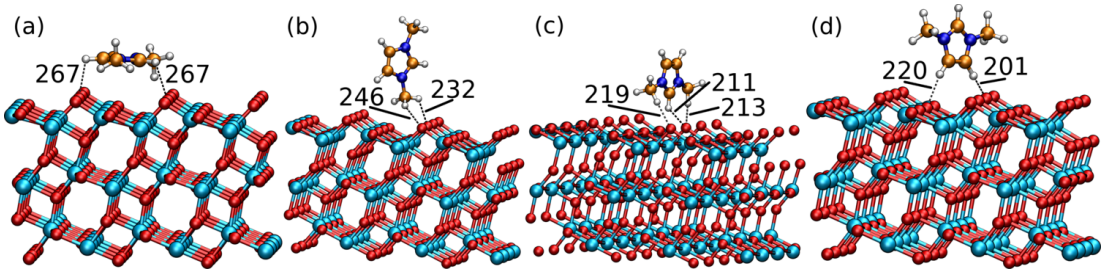

Figure 3.15: $[C_1C_1Im]^+$ adsorption geometries: (a) "flat" conformation, (b) "vertical" conformation, (c) "H2 coordination" conformation, and (d) "H4/5 coordination" conformation. Labeled distances are in picometers, color code is depicted in Figure 3.7.

titanium, the interaction has probably a high Coulombic character. There is a similar interaction of sulfur and titanium; the distance $d_{\text{S-Ti}} = 298$ pm is larger due to the higher van der Waals radius of sulfur compared to nitrogen.

In the following, $[SCN]^-$ was constrained to three conformations, see Figure 3.13: (a) is considered the "flat" conformation, (b) the "N coordination" conformation, and (c) the "S coordination" conformation. To maintain a flat conformation, the z coordinates of N and S where constrained to be the same throughout the geometry optimization. This leads, in contrast to the minimum energy conformation, to a higher N–Ti and a shorter S–Ti distance. In conformation Figure 3.13b, $[SCN]^-$ was constrained to be perpendicular to the surface with the nitrogen atom pointing toward the surface. A pronounced N–Ti interaction with the unsaturated Ti_{5c} atom is observed, indicated by the very short distance of $d_{\text{N-Ti}} = 197$ pm. During this interaction, the titanium atom counterpart is significantly displaced from the original lattice position in contrast to the other titanium atoms of the surface. The same effect is observed for the S–Ti interaction, Figure 3.13c, although it is less pronounced. Interaction energies in Figure 3.9c also indicate a much weaker S–Ti interaction compared to N–Ti. Energetically, the flat and the N coordination conformations are considerably close.

$[C_1C_1Im]^+$. For the sake of simplicity, the symmetric cation 1,3-dimethylimidazolium ($[C_1C_1Im]^+$) was chosen for the investigation rather than asymmetric versions with

different alkyl groups. The fully relaxed structure of the cation on the (101) anatase surface is shown in Figure 3.14. The predominant feature of the conformation is the strong interaction of the acidic H2 hydrogen atom and an unsaturated O_{2c} surface oxygen atom. With the geometrical descriptors $d_{H–O} = 204.7$ pm and $\angle CHO = 159.4°$, this interaction can be considered a hydrogen bond. For comparison, the hydrogen bond between anion and cation in the IL $[C_1C_1Im][OAc]$ is characterized by a $d_{H–O} \approx 200$ pm distance and a $\angle CHO = 135 - 180°$ angle.[343] The imidazolium ring itself is not perpendicular to the surface; it shows a tilted conformation, probably because of favorable Coulombic and dispersive interactions of the cation's body with the surface. From theoretical studies, this competition between *in-plane* (coordination at H2 or H4/5) and *on-top* (coordination above/below the imidazolium ring) conformations was found previously, involving different static calculations[271,306,307] as well as AIMD[270,342,343] and classical[302] simulations. From experiments, it is known that aromatic systems tend to align flatly on the TiO_2 surface, *e.g.*, phenol on rutile (110),[382] or pyridine and 2,6-dimethylpyridine on rutile (110).[383] Additionally, the formation of hydrogen bonds to the unsaturated O_{2c} surface oxygen atoms was observed experimentally for water and methanol at the anatase (101) surface,[384] which also have weakly acidic hydrogen atoms.

Consequently, conformational degrees of freedom of $[C_1C_1Im]^+$ were constrained. As depicted in Figure 3.15, the conformations are (a) flat, with the imidazolium ring plane parallel to the surface, with the imidazolium ring plane perpendicular to the surface and (b) the methyl group pointing toward the surface, (c) the front hydrogen atom and (d) the rear hydrogen atoms pointing toward the surface. According to Figure 3.9d, the lowest-energy conformations are (a) and (c). The earlier described lowest-energy conformation can roughly be described as a mixture between these two conformations. In the flat conformation, there are strong Coulombic and dispersive interactions as well as a $p_O \rightarrow \pi_{[C_1C_1Im]^+}$ charge transfer, supported by the mixing of the specific orbitals (see Supporting Information for graphical description). The coordination via H2, conformation (c), is observed to result in a very stable conformation, whereas the coordination via H4/5 is weaker, as previously observed in ion pair calculations.[271,307,342] This might be caused by the weaker polarization of the C–H4/5 bonds, as H2 is known to be the most acidic hydrogen atom in imidazolium ILs[307,385] and thus is expected to form the stronger hydrogen bonds.[302,306,308] Additionally, there is a hydrogen-bond-like interaction of two methyl hydrogen atoms with the unsaturated O_{2c} atoms, further stabilizing this conformation. The capability of these methyl hydrogen atoms to form weak hydrogen bonds was confirmed in previous studies.[307,386,387] Observing the surface–center of ring (CoR) distance, it increases in the order (a), (d), (c), and (b). With the overall increasing distance between surface and the positively charged part of the molecule, energetically favorable Coulombic and dispersive interactions decrease. Consequently, the "vertical" conformation is observed to be the highest in energy for

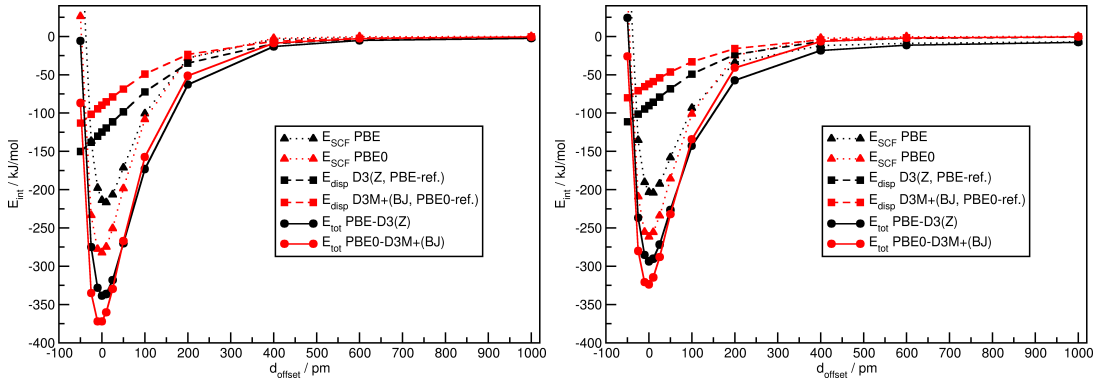

Figure 3.16: Interaction energy of a single $[C_1C_1Im][B(CN)_4]$ ion pair (left panel) and a single $[C_1C_1Im][SCN]$ ion pair (right panel) with the anatase (101) surface for different methods. d_{offset} depicts the offset of the ion pair from optimized minimum position in the z-direction. The energy is split into the energy from the SCF part of the calculation (E_{SCF}), dispersion correction energy (E_{disp}), and total interaction energy ($E_{\mathrm{tot}} = E_{\mathrm{SCF}} + E_{\mathrm{disp}}$).

the investigated conformations. This might also arise from the lack of hydrogen bonds and $p \rightarrow \pi$ charge transfer in combination with the increased distance of the positively charged imidazolium ring.

Ion Pairs. The conformational freedom of one IL ion pair on the anatase surface is very high; thus, multiple local energy minima were identified. Therefore, a large number of different starting conformations (over 20) were sampled via classical molecular dynamics simulation. In contrast to the calculations of the isolated ions, the whole ion pair calculations are not flawed by the aforementioned errors, as they do not suffer so much from the unwanted Coulomb interaction with the images (greatly diminished CT between ion pair and surface for high separation, see Supporting Information) and there is no spurious background charge (neutral simulation cell). Therefore, absolute energies can be used to determine quantitative interaction energies of the ion pair and the anatase surface. The BSSE-corrected interaction energy of a single ion pair with the anatase surface with different methods is shown in Figure 3.16. The PBE functional as well as the more expensive PBE0 hybrid functional were applied. The PBE0 functional is known to describe structural and electronic properties of TiO_2 well,[388] and it was employed to give reasonable adsorption energies of, for example, formic acid and glycine on the anatase (101) face.[358] It was observed that the PBE functional yields interaction energies smaller than those of the PBE0 hybrid functional in general. For increasing distances to the surface, the interaction energies smoothly converge to zero except for the PBE calculation of the $[C_1C_1Im][SCN]$ ion pair. In this case, only the SIE-reduced calculation with the PBE0 functional yields the correct asymptotical behavior.

On top of the electronic structure method, different D3 dispersion correction schemes were employed.[347] It was found that there was no difference between the zero damp-

ing and Becke–Johnson damping approach. The application of the TiO_2-specific D3 parameters in D3M+ [349] was observed to yield interaction energies smaller than those with the common D3 correction ($E_{\mathrm{D3}}^{\mathrm{PBE0–BJ}} = -138.3\,\mathrm{kJmol^{-1}}$ versus $E_{\mathrm{D3M+}}^{\mathrm{PBE0–BJ}} = -89.9\,\mathrm{kJmol^{-1}}$ for $[C_1C_1Im][B(CN)_4]$ at minimum energy geometry and $E_{\mathrm{D3}}^{\mathrm{PBE0–BJ}} = -95.8\,\mathrm{kJmol^{-1}}$ versus $E_{\mathrm{D3M+}}^{\mathrm{PBE0–BJ}} = -62.0\,\mathrm{kJmol^{-1}}$ for $[C_1C_1Im][SCN]$ at minimum energy geometry).

Taking the above-mentioned considerations into account, the PBE0 functional is expected to give interaction energies that are more accurate than those of the PBE functional, and the D3M+ dispersion correction is considered more accurate than the common D3 correction for the given system. Consequently, the PBE0-D3M+ method is expected to yield the most accurate results presented in this work. Interestingly, the PBE-D3 energy is considerably close to the PBE0-D3M+ results by compensation of errors, as the PBE functional underestimates the interaction energy and the D3 dispersion interaction overestimates the attractive energy.

Because the calculation of PBE-D3 interaction energies is computationally less demanding, a set of $[C_1C_1Im][B(CN)_4]$ in different starting conformations on the anatase surface was investigated at this level of theory. A full geometry optimization of the IL and the top four layers of the slab was performed; the average BSSE-corrected interaction energy for the seven minimum conformations is $E_{\mathrm{int,\,[C_1C_1Im][B(CN)_4]}}^{\mathrm{avg}} = -282 \pm 32\,\mathrm{kJmol^{-1}}$. The lowest-energy conformation identified in this work was computed to yield $E_{\mathrm{int,\,[C_1C_1Im][B(CN)_4]}}^{\mathrm{min}} = -332\,\mathrm{kJmol^{-1}}$. In the same fashion, the average interaction energies of three traced low-energy conformations of $[C_1C_1Im][SCN]$ on the anatase (101) surface were computed to yield an average of $E_{\mathrm{int,\,[C_1C_1Im][SCN]}}^{\mathrm{avg}} = -347 \pm 18\,\mathrm{kJmol^{-1}}$. The lowest-energy conformation found was computed to yield $E_{\mathrm{int,\,[C_1C_1Im][SCN]}}^{\mathrm{min}} = -367\,\mathrm{kJmol^{-1}}$. $[C_1C_1Im][SCN]$ binds stronger to the anatase surface, which can be mainly attributed to the directed interactions of thiocyanate. The lowest-energy conformations of the ion pairs on the surface found in this study are illustrated in Figure 3.17. The low-energy conformations of the whole ion pairs show a remarkable resemblance to the low-energy conformations of the isolated ions, *i.e.*, each individual part of the IL aligns separately with respect to the surface, but the ion pair remains in contact because of energetically favorable interactions between the parts of the IL. The simulation by Pensado *et al.* of $[C_2C_1Im][SCN]$ at the graphene interface revealed a flat conformation of both anion and cation. [346] The flat cation conformation is in agreement with our studies at the anatase (101) surface. The difference in anion conformation might be caused by stronger directed interactions in the case of the anatase substrate. Additionally, the bulk phase was studied in the case of the graphene substrate, which may enforce flat conformations because of limited space.

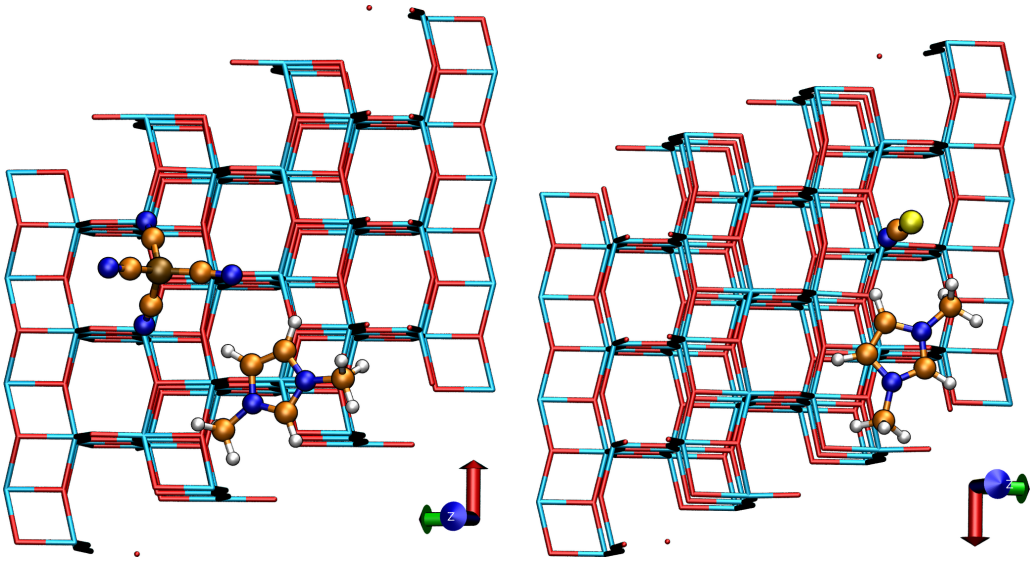

Figure 3.17: Lowest-energy conformations of $[C_1C_1Im][B(CN)_4]$ ion pair (left panel) and a single $[C_1C_1Im][SCN]$ ion pair (right panel) on the anatase (101) surface identified in this work. Color code is depicted in Figure 3.7.

3.2.3.5 Band Shifts due to Adsorption

The performance of a DSC device is partly determined by the corresponding open-circuit voltage, V_{OC}, which in turn depends on the particular density of states and Fermi energy, E_F, of the employed semiconductor TiO_2, which can be tailored by adsorption of different molecules on the surface. This effect is known and exploited in DSCs upon the addition of 4-*tert*-butylpyridine (4TBP),[19,172,174,176–178] causing a shift of $\Delta E_F \approx 0.3$ eV in real devices, depending on electrolyte composition and concentration.[177,178] A theoretical investigation of the band shift of TiO_2 was conducted by Kusama *et al.* in 2008,[356,357] where the adsorption of 4TBP resulted in a shift of 0.51 eV in E_F on a PBE-6-31G** level of theory. Additionally, band shifts of a number of N-containing heterocycles were computed, *e.g.*, imidazole (0.60 eV), pyridine (0.47 eV), and pyrimidine (0.30 eV). Experimental evaluation revealed a direct correlation of the theoretically observed band shift and the experimentally measured V_{OC} with the corresponding additive in the electrolyte. In this work, the DOS as well as Fermi energies, E_F, for anatase with and without adsorbed ILs were calculated for all minimized IP structures at the PBE-D3 level and for the one selected conformation at the PBE0-D3M+ level (Figure 3.18), which was also used in Figure 3.16. Numeric values are summarized in Table 3.7.

The absolute value of E_F depends strongly on the method used. PBE0 results ($E_F^{PBE0} = -7.8$ eV) match closely the experimental value of $E_F^{exp} \approx -7.5$ eV,[389] whereas the PBE calculation yields a much smaller value of $E_F^{PBE} = -5.8$ eV, which is a known shortcoming of pure GGA functionals.[390,391] However, the shift in E_F, ΔE_F, is less dependent on the employed theory. It can be seen that the adsorption of both ILs re-

Table 3.7: Calculated Interaction Energies (E_{int}), Fermi Energies (E_{F}) and Band Shifts (ΔE_{F}) for Different Species in Minimized Geometry on the 4×3 Anatase (101) Surface at PBE and PBE0 Level of Theory

system	$E_{\mathrm{int}}^{\mathrm{PBE-D3}}$ / kJmol^{-1}	$E_{\mathrm{F}}^{\mathrm{PBE}}$ / eV	$\Delta E_{\mathrm{F}}^{\mathrm{PBE}}$ / eV	$E_{\mathrm{F}}^{\mathrm{PBE0}}$ / eV	$\Delta E_{\mathrm{F}}^{\mathrm{PBE0}}$ / eV
anatase (101)	–	−5.93	–	−7.83	–
anatase (101) + $[C_1C_1Im][B(CN)_4]$	-282 ± 32	-5.67 ± 0.12	0.26	−7.36	0.47
anatase (101) + $[C_1C_1Im][SCN]$	-347 ± 18	-5.15 ± 0.05	0.78	−7.05	0.78
anatase (101) + C_4H_{10}	−46.96	−5.88	0.04	–	–

sults in a shift of E_{F} toward higher potentials, thus possibly increasing the open-circuit voltage V_{OC} of a DSC device. Values for the different methods employed match exactly in the case of $[C_1C_1Im][SCN]$ ($\Delta E_{\mathrm{F}}^{\mathrm{PBE0}} = \Delta E_{\mathrm{F}}^{\mathrm{PBE}} = 0.78$ eV) and differ slightly in the case of $[C_1C_1Im][B(CN)_4]$ ($\Delta E_{\mathrm{F}}^{\mathrm{PBE0}} = 0.47$ eV, $\Delta E_{\mathrm{F}}^{\mathrm{PBE}} = 0.26$ eV). The latter discrepancy can be attributed to sampling, as E_{F} of only one minimum energy conformation of $[C_1C_1Im][B(CN)_4]$ was evaluated with PBE0, and the average of all PBE calculations is shown. ΔE_{F} for the specific conformation of $[C_1C_1Im][B(CN)_4]$ are approximately equal and are given as $\Delta E_{\mathrm{F}}^{\mathrm{PBE0}} = 0.47$ eV and $\Delta E_{\mathrm{F}}^{\mathrm{PBE}} = 0.48$ eV. Compared to the aforementioned value of 0.51 eV for 4TBP, adsorption of $[C_1C_1Im][B(CN)_4]$ results in a smaller shift and adsorption of $[C_1C_1Im][SCN]$ results in a significantly larger shift. From this we might extrapolate that using $[C_1C_1Im][SCN]$ as electrolyte in a real DSC device is expected to yield larger values of the open-circuit voltage as V_{OC} is determined by the corresponding Fermi level of TiO_2. It should be noted here that this not necessarily leads to an enhanced device performance, as similarly the short-circuit current, J_{SC}, is expected to decrease, and other vital parts of the cell may be affected, which cannot be deduced from the calculations made herein.

From the PDOS of the pure anatase (101) slab (Figure 3.18b) it can be seen that the highest occupied molecular orbitals (HOMOs) are mainly composed of orbitals of O_{2c} surface oxygen atoms and the lowest unoccupied molecular orbitals (LUMOs) are mainly composed of orbitals of the Ti_{5c} surface titanium atoms, which is perfectly in line with the common assumption that the surface of a crystal is the most active region. When the adsorbate is introduced, the valence bands are shifted toward more positive energies. An additional peak arises, constituting the new HOMO, which is composed of the states of the oxygen surface atoms from the IL adsorption site. It can also be seen that the unoccupied states higher in energy than E_{F} are similarly shifted toward higher energies. A special feature has to be noticed for the $[C_1C_1Im][SCN]$ system. Here, the $[SCN]^-$ anion introduces occupied electronic states higher in energy than the TiO_2 valence band top, yielding a value of $E_{\mathrm{F}}^{\mathrm{PBE0}} = -5.84$ eV. Thus, E_{F} has to be taken from the highest-energy band composed of TiO_2 states in order to calculate ΔE_{F} accurately, which then is the value of $E_{\mathrm{F}}^{\mathrm{PBE0}} = -7.05$ eV, also given in Table 3.7.

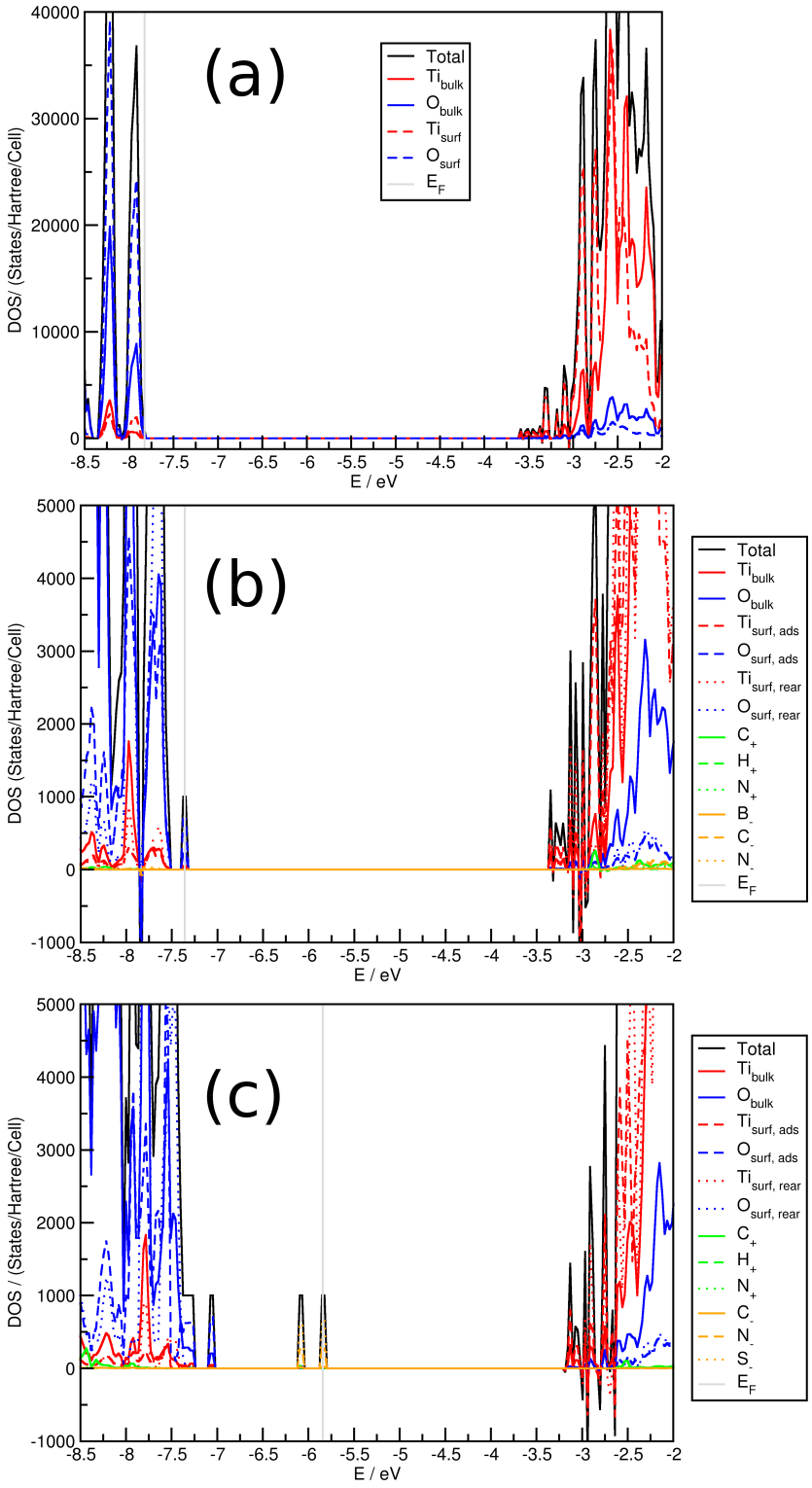

Figure 3.18: Projected density of states (PDOS) of anatase (101) slab (a) with adsorbed $[C_1C_1Im][B(CN)_4]$ IP (b) and adsorbed $[C_1C_1Im][SCN]$ IP (c). Ti_{bulk} and O_{bulk} denote Ti_{6c} and O_{3c}; Ti_{surf} and O_{surf} denote Ti_{5c} and O_{2c}; $C/H/N_+$ denote the cation's atoms; and $C/N/B/S_-$ denote the anion's atoms.

3.2.4 Conclusion

The adsorption behavior of the two ionic liquids $[C_1C_1Im][B(CN)_4]$ and $[C_1C_1Im][SCN]$ on the (101) anatase surface was studied. The description of anatase bulk and surface properties with the PBE-D3 as well as with with PBE0-D3 method was observed to yield reasonable agreement with experimental data. The qualitative description of the interaction of the IL's components with the (101) surface of anatase was assessed on the PBE-D3 level and showed that strong directed and nondirected forces are dominant in the adsorption behavior. For anionic species, strong directed N–Ti_{5c} interactions were identified. The cation $[C_1C_1Im]^+$ showed strong hydrogen-bond-like interactions between the most acidic H2 hydrogen atom and the O_{2c} surface oxygen atoms as well as strong nondirected electrostatic and van der Waals interactions.

Subsequently, the computationally more demanding PBE0-D3M+ method was employed to give accurate interaction energies of the IL ion pair with the anatase surface. While the components behaved similar to the isolated systems with respect to the surface geometry, all low-energy conformations comprised a contact ion pair. The dispersive energy is estimated to be $\approx 20 - 30$ % of the total interaction energy in these systems. By compensation of errors, the lower-level method PBE-D3 was observed to yield results comparable to those of the PBE0-D3M+ method and can thus be used with care as a cheaper alternative.

Finally, the density of states and projected density of states was evaluated for the different systems. The frontier orbitals are composed of orbitals of the surface atoms. A positive band shift was observed for both ILs, and the band shift for the adsorption of $[C_1C_1Im][SCN]$ was more pronounced. Consequently, the application of this IL in a real DSC device is expected to yield higher values of V_{OC}.

Supporting Information

Details on the calculation of the anatase bulk and pure (101) surface slab, numerical data of Figure 3.8b, and details concerning the classical molecular dynamics to produce starting geometries. The Supporting Information is available free of charge on the ACS Publications website at DOI: 10.1021/acs.jpcc.5b02347 and is attached in Section A.2.

Acknowledgments

This work was financially supported by the DFG project KI-768/12-1 "Materialsynthese nahe Raumtemperatur" and the SFB 813 "Chemie an Spinzentren: Konzepte, Mechanismen, Funktionen". The support for H.W. by the Fonds der Chemischen Industrie (FCI) is gratefully acknowledged. The authors are thankful for helpful scientific discussions with Jan Gerit Brandenburg and Stefan Grimme.

3.3 Toward an Accurate Modeling of Ionic Liquid–TiO_2 Interfaces

Henry Weber,[†] Mathieu Salanne,[‡§] and Barbara Kirchner[†]*

The Journal of Physical Chemistry C, **2015**, Volume *119*, Pages 25260–25267.

DOI:	10.1021/acs.jpcc.5b08538
Received:	September 1, 2015
Revised:	October 15, 2015
Published:	October 16, 2015

Contributions to the manuscript:

- Setup and maintenance of all calculations.
- Programming of the interface to fit the force field.
- Analysis and evaluation of all results.
- Writing of the manuscript.

[†]Mulliken Center for Theoretical Chemistry, Universität Bonn, Beringstr. 4+6, D-53115 Bonn, Germany.
[‡]Sorbonne Universités, UPMC Univ Paris 06, CNRS, Laboratoire PHENIX, F-75005, Paris, France.
[§]Maison de la Simulation, USR 3441, CEA-CNRS-INRIA–Université Paris-Sud–Université de Versailles, F-91191 Gif-sur-Yvette, France.
*Corresponding Author E-mail: kirchner@thch.uni-bonn.de.

Abstract

Structural properties of the ionic liquids 1-ethyl-3-methylimidazolium thiocyanate and tetracyanoborate at the anatase (101) surface are of crucial interest for energy harvesting and storage devices, but their investigation via molecular dynamics requires large simulation cells. Thus, two classical interaction potentials with and without polarization effects were parametrized in order to accurately model the interface between the liquid and solid. The parameters were fitted to match *ab initio* reference interaction energies. Application of the generated force field to model the interface is demonstrated. The adsorption profiles of the ionic liquid's components reveal a very dense surface layer with an excess of cations, which has some possible implications for the use of the ionic liquids as electrolytes, for example in solar cells.

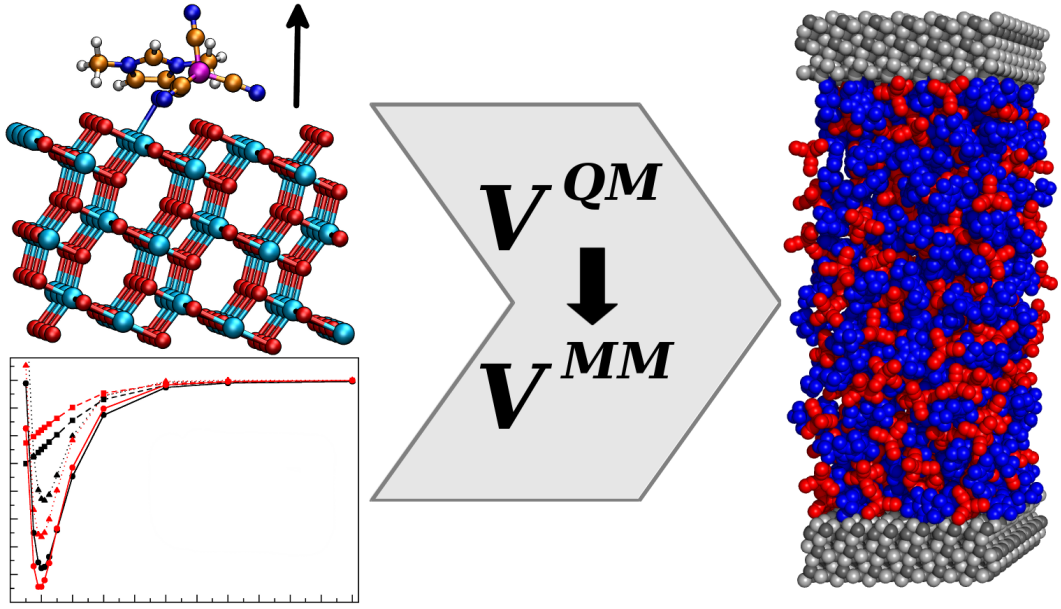

3.3.1 Introduction

Ionic liquids (ILs) are a hot topic, even a century after their revival.[256,392,393] Unique characteristics define this class of liquids, and by this time, different applications have emerged. Ionic liquids were successfully applied as electrolytes,[133,394] *e.g.*, in fuel cells,[146,395,396] batteries,[133,135] supercapacitors,[133,151,152] and dye sensitized solar cells (DSCs).[100]

For the latter one, ionic liquids (ILs) were investigated to replace volatile organic solvents,[100] as they offer great potential benefits. Beyond being a simple diffusive medium, ILs can affect band edge positions of the employed semiconductor, and electron–hole recombination rates in the DSC, and the chemical dye regeneration reaction.[166] Pioneering work by Fredin *et al.*[166] employing ILs in DSCs pointed out that DSC key parameters as well as overall efficiency are crucially affected by the IL's nature. In particular, the ILs 1-ethyl-3-methylimidazolium thiocyanate ($[C_2C_1Im][SCN]$) and 1-ethyl-3-methylimidazolium tetracyanoborate ($[C_2C_1Im][B(CN)_4]$) were used as electrolytes in ruthenium-based DSCs, resulting in varying device efficiencies partly attributed to the formation of pseudohalides such as $[I_2SCN]^-$ and thus lowering the I_3^- concentration.[166] In contrast to this study, employing the same ILs in porphyrin-based DSCs has led to an opposing trend concerning device efficiency.[339,340] These findings show that a deeper insight in the specific interactions between all components of a DSC is required to fully understand and predict the device properties. Recent *ab initio* molecular dynamics (AIMD) studies of the pure IL $[C_2C_1Im][SCN]$[269,270] and mixtures with SO_2[276] demonstrated the excellent solvent properties and the potential for diverse applications of this IL. However, many properties are not accessible via AIMD, because large system sizes or long simulation times are sometimes required. Classical molecular dynamics (MD) is able to fill this gap and give new insights.[257,317] For example, the phenomenon of microheterogeneity in ILs was discovered with the aid of classical MD simulations.[397] Furthermore, interfacial studies often require classical methods because of their size.[398]

At interfaces, ILs exhibit a three-dimensional structure which varies markedly from the bulk liquid.[399] The behavior of $[C_2C_1Im][SCN]$ at a graphene interface in the context of supercapacitors was showcased recently by Pensado *et al.*[346] Strong adsorptions of the IL with multiple solvation layers were observed, and the cation majorly displayed flat conformations at the surface. Concerning metal oxides, the $[C_4C_1Im][NTf_2]$–sapphire interface was studied in a combined classical MD and X-ray reflectivity study. Hydrogen bonding was attributed to induce an ordered adsorption layer with an excess of cations, which in turn caused a multidimensional bilayering profile.[194] Such bilayered morphology was also proven experimentally for a series of pyrrolidinium ILs.[400]

The main difficulty for predicting the properties of these interfaces is the lack of accurate force fields. A detailed static quantum chemical study of the ILs $[C_1C_1Im][SCN]$

and $[C_1C_1Im][B(CN)_4]$ at the anatase (101) surface was previously conducted by us.[262] This interface is of particular interest in DSC research, as detailed knowledge of the electrolyte–semiconductor interactions may shed light onto device differences concerning performance or durability. In an attempt to study this interface, computational efficiency limits are reached for a quantum chemical description. Therefore, we developed an efficient classical description which allows us to investigate structural and dynamic properties of the IL–solid interface in detail.

3.3.2 Computational Details

For the classical description of the ionic liquid, the force field (FF) developed by Pádua *et al.* was used[296] with the exception of newly derived partial charges, employing the popular OPLS/AA force field:[247]

$$\begin{aligned} V = & \sum_{ij}^{\text{bonds}} k_{r,ij}(r_{ij} - r_{0,ij})^2 \\ & + \sum_{ijk}^{\text{angles}} k_{\theta,ijk}(\theta_{ijk} - \theta_{0,ijk})^2 \\ & + \sum_{ijkl}^{\text{dihedrals}} \sum_{m=1}^{4} V_{m,ijkl}\left[1 - (-1)^m cos(m\phi_{ijkl})\right] \\ & + \sum_{ijkl}^{\text{impropers}} k_{\chi,ijkl}(\chi_{ijkl} - \chi_{0,ijkl})^2 \\ & + \sum_{i<j}^{\text{nonbonds}} \left\{ 4\varepsilon_{ij}\left[\left(\frac{\sigma_{ij}}{r_{ij}}\right)^{12} - \left(\frac{\sigma_{ij}}{r_{ij}}\right)^{6}\right] + \frac{1}{4\pi\varepsilon_0}\frac{q_i q_j}{r_{ij}} \right\}. \end{aligned} \tag{3.3.1}$$

Here, $k_{r,\,\theta,\,\chi}$ refers to the force constants of the harmonic bond, angle, and improper dihedral potential, respectively, with r_0, θ_0, and χ_0 being the equilibrium bond length, bond angle, and improper dihedral angle. V_m is the potential of the torsional barrier for the mth multiplicity.

The substrate titanium dioxide was described with the polarizable ion model[401] (PIM) using the latest parametrization of Corradini *et al.*[402] The PIM is briefly summarized in the following. At first, all point-charge interactions are considered as usual in a Coulomb sum

$$V_{\text{Coulomb}} = \frac{1}{4\pi\varepsilon_0}\sum_i \sum_{j>i} \frac{q_i q_j}{r_{ij}}. \tag{3.3.2}$$

Formal charges were used as partial charges on the oxygen atoms ($q_{\text{O}} = -2$ e) and the titanium atoms ($q_{\text{Ti}} = +4$ e) to ensure transferability.

Repulsive and dispersive forces were incorporated with the Born–Mayer–Huggins

(BMH) potential,[403,404] which reads as

$$V_{\mathrm{BMH}} = \sum_i \sum_{j>i} \left(A_{ij} e^{-a_{ij} r_{ij}} - f_6^{ij}(r_{ij}) \frac{C_6^{ij}}{r_{ij}^6} - f_8^{ij}(r_{ij}) \frac{C_8^{ij}}{r_{ij}^8} \right) \tag{3.3.3}$$

with the repulsion parameter A_{ij}, the ion pair dependent length parameter a_{ij}, the van der Waals parameters C_6^{ij}, and C_8^{ij} and the Tang–Toennies[405] type damping functions f_n^{ij} given as

$$f_n^{ij} = 1 - e^{b_D^{ij}\, r_{ij}} \sum_{k=0}^{n} \frac{(b_D^{ij}\, r_{ij})^k}{k!} \tag{3.3.4}$$

with the repulsive range parameter b_D^{ij}.

In order to accurately describe the many-body electrostatic interactions, the induced dipole moments μ_i are obtained by minimizing the polarization energy

$$V_{\mathrm{Pol}} = \sum_i \frac{1}{2\alpha_i} |\mu_i|^2 + \frac{1}{4\pi\varepsilon_0} \sum_i \sum_{j>i} \left(g^{ij}(r_{ij}) q_i \mathbb{T}_1^{ij} \mu_j - g^{ji}(r_{ij}) q_j \mathbb{T}_1^{ij} \mu_i - \mu_i \mathbb{T}_2^{ij} \mu_j \right). \tag{3.3.5}$$

The equation contains the atomic polarizabilities α_i, the charge–dipole and dipole–dipole interaction tensors $\mathbb{T}_1$ and $\mathbb{T}_2$, respectively, and the Tang–Toennies[405] type polarization damping functions

$$g^{ij}(r_{ij}) = 1 - c_{ij} e^{-b_{ji} r_{ij}} \sum_{k=0}^{4} \frac{(b_{ij} r_{ij})^k}{k!} \tag{3.3.6}$$

with the additional parameter c_{ij}, which specifies the importance of short-range corrections.

3.3.2.1 Classical Molecular Dynamics Simulation Details

Nonbonded interactions within the IL are described via the Lennard-Jones potential, including potential well depth ϵ_{ij} and the zero energy cross point σ_{ij}. A cutoff distance r_c of 1.5 nm was used to truncate the Lennard-Jones potential. Lorentz–Berthelot mixing rules ($\varepsilon_{ij} = \sqrt{\varepsilon_i \varepsilon_j}$ and $\sigma_{ij} = (\sigma_i + \sigma_j)/2$) were applied to obtain unlike atom pair parameters for IL–IL interactions. Electrostatic interactions were calculated using a standard Ewald sum technique with an accuracy of 10^{-6} Hartree beyond a real-space cutoff of $r_c = 1.5$ nm. The new partial charges q_i were obtained using a restrained electrostatic potential (RESP)[406] fit of the isolated ions at the HF 6-31++G** level[407,408] with subsequent scaling to ±0.8 e on each individual ion, because it was shown that ±0.8 e is about the amount of the charge transfer and leads to better description of dynamic properties.[256]

256 ion pairs of the IL $[C_2C_1Im][SCN]$ and 200 ion pairs of the IL $[C_2C_1Im][B(CN)_4]$ were simulated between slabs of titanium dioxide in anatase modification with revealed (101) surface. Anatase was described by the force field of Corradini *et al.*[402] Cell parameters were chosen to match experimental data ($a = b = 378.2$ pm, $c = 950.2$ pm).[409] A slab with 10 stoichiometric layers of TiO_2 was taken and rotated such that the cell vector a matches the x-axis and the surface normal of the (101) surface matches the z-axis of the system, in order to allow an easier analysis of surface related properties. A 9×6 supercell was then created, leading to an anatase slab of the dimensions $a = 3403.8$ pm, $b = 3271.17$ pm, $\alpha = \beta = 90°$, $\gamma = 110.2947°$, and a thickness of ≈ 1640 pm, containing a total of 540 stoichiometric units of TiO_2. During the simulation, the inner 6 layers were constrained to stay immobile. The outer layers of the anatase slab and the ionic liquid were time-integrated in the N, V, T-ensemble. The CSVR (canonical sampling through velocity rescaling) thermostat[410] with a time constant of $\tau = 100$ fs was utilized to ensure a constant temperature of $T = 343.15$ K. It was shown by Bussi *et al.* that the CSVR thermostat yields a canonical distribution, and leaves static and dynamic properties largely unaffected by the thermostat parameters, and that it is more ergodic than the widely used Nosé–Hoover thermostats.[410] Starting geometries were obtained with the aid of the Packmol program package.[411] Densities of the ionic liquids between the slabs was chosen to match the experimental densities, see Supporting Information. Both systems were equilibrated for at least 50 ps and a subsequent production run to yield 500 ps of simulation time with a time step of $\Delta t = 0.5$ fs was carried out. The relatively short simulation time can be justified by the very low viscosity of the ILs, summarized alongside further details in the Supporting Information.

Radial distribution functions (RDFs), z-density profiles, spatial distribution functions (SDFs) and combined distribution functions (CDFs) are computed with the aid of the Travis program package.[412] Computational details on these analyses are given in the respective reference.[412] The visual molecular dynamics (VMD) program package was used to show molecular structures and SDFs.[365] Graphical representations were produced with the Grace program package.[366] CDFs were generated using the Gnuplot software.

3.3.3 Results and Discussion

3.3.3.1 Generation of the Force Field

We propose the interaction potential V_{int} between the ionic liquid and TiO_2 to be a sum of the nonbonded interaction terms:

$$\begin{aligned} V_{\text{int}} =& V_{\text{LJ}}^{\text{int}} + V_{\text{electrostatic}}^{\text{int}} && \text{with} \\ V_{\text{LJ}}^{\text{int}} =& V_{\text{repulsive}}^{\text{int}} + V_{\text{dispersive}}^{\text{int}} \\ =& \sum_{i\in\text{IL}} \sum_{j\in\text{TiO}_2} 4\varepsilon_{ij} \left[\left(\frac{\sigma_{ij}}{r_{ij}} \right)^{12} - \left(\frac{\sigma_{ij}}{r_{ij}} \right)^{6} \right] && \text{and} \\ V_{\text{electrostatic}}^{\text{int}} =& V_{\text{Coulomb}}^{\text{int}} + V_{\text{polarizable}}^{\text{int}} \\ =& \frac{1}{4\pi\varepsilon_0} \sum_{i\in\text{IL}} \sum_{j\in\text{TiO}_2} \left(\frac{q_i q_j}{r_{ij}} - g^{ij}(r_{ij}) q_i \frac{r_{ij}\mu_j}{r_{ij}^3} \right) && (3.3.7) \end{aligned}$$

with the Lennard-Jones parameters σ and ε, partial charges q, induced dipole moments μ, and the Tang–Toennies[405] type polarization damping functions $g^{ij}(r_{ij})$ as seen before (Equation (3.3.6)). As the ionic liquid is not polarizable, it follows that their induced dipole moments $\mu_{i\in\text{IL}}$ are zero.

To match the *ab initio* reference, two alternative ways are presented. The first one excluding the polarizability of TiO_2 only uses LJ and Coulomb interactions, subsequently called the LJ FF, and the second approach, including the polarizable TiO_2 is called the PIM FF in the following. While the simple LJ FF is computationally less expensive, the clear drawbacks are that the TiO_2 substrate must be constrained to stay in fixed positions all the time, resulting in a less detailed description of the system. We included this approach because some applications do not require this level of detail, *e.g.*, large scale simulations or rough sampling, and this force field might be sufficient. Utilizing the PIM FF on the other hand, the anatase substrate is able to adapt and respond to its surroundings, resulting in a more sophisticated and detailed description of the interface, though at the price of higher computational demand.

In previous work, the quantum chemical description of this system was investigated.[262] It was found that the PBE-D3 level serves as an efficient trade-off between computational demand and accurate results.[216,230] Therefore, a total of 631 reference structures were calculated, and the BSSE-corrected interaction energies $E_{\text{int}}^{\text{QM}}$ were evaluated according to our previous work[262] with Goedecker–Teter–Hutter pseudopotentials[292,293] and the MOLOPT-DZVP-SR-GTH[291] basis sets. A detailed overview of the composition of the reference structures is given in Table 3.10. The training set consisted of either small ion pair clusters of $[C_1C_1Im][SCN]$ or $[C_1C_1Im][B(CN)_4]$ or a condensed bulk phase of $[C_2C_1Im][SCN]$ or $[C_2C_1Im][B(CN)_4]$. Clusters of 1, 2, or 3 ion pair size were calculated on a 6 stoichiometric layer anatase slab in a 4×3 super-

cell, revealing the (101) surface. These reference structures were derived with classical MD utilizing a preliminary force field,[262] and to some extent from *ab initio* molecular dynamics (AIMD) for the 1 IP systems. The bulk reference structures were obtained from AIMD simulations of the respective IL in a simulation cell including a 6×4, 6 layer anatase slab with exposed (101) surface at the same level of theory.

To ensure transferability, *i.e.*, keeping the force fields of Pádua *et al.* for simulating the IL and of Corradini *et al.* for the description of TiO_2, only the interaction parameters σ_{ij} and ε_{ij} from Equation (3.3.7) with $i \in$ IL and $j \in TiO_2$ were adjusted in the fitting procedure. Parameters of the Tang–Toennies[405] type polarization damping function g_{ij} (Equation (3.3.6)) were set to fixed standard values of $b_{ij} = 200\ \mathrm{pm}^{-1}$ and $c_{ij} = 1.0$ and were not fitted in order to limit the number of fitting parameters.

The best set of parameters is determined by minimizing the objective function

$$O = \frac{\sum_k^N \left(E_{\mathrm{int}}^{\mathrm{QM}} - E_{\mathrm{int}}^{\mathrm{MM}}\right)^2}{\sum_k^N \left(E_{\mathrm{int}}^{\mathrm{QM}}\right)^2} \tag{3.3.8}$$

targeting the minimal difference in energy over all N reference conformations. $E_{\mathrm{int}}^{\mathrm{QM}}$ is the BSSE-corrected quantum chemical interaction energy, $E_{\mathrm{int}}^{\mathrm{MM}}$ is the force field interaction energy derived in a similar fashion

$$E_{\mathrm{int}}^{\mathrm{MM}} = E_{\mathrm{AB}} - E_{\mathrm{A}} - E_{\mathrm{B}} \tag{3.3.9}$$

with the energy of the whole system E_{AB} and the energy of the interacting subsystems E_{A} and E_{B} in the adsorption geometry. Quantum chemical interaction energies were chosen as target for the fitting rather than forces in usual force-matching approaches, because the forces on the IL and Ti/O atoms are dominated by the intramolecular IL forces and the interatomic Ti/O forces, respectively. The objective function was minimized with the aid of the Minuit program package,[413,414] using first the downhill–simplex method and subsequently the `MIGRAD` minimization.

The final fitted parameters for the LJ and PIM FF are listed in Tables 3.8 and 3.9. As can be seen from Table 3.10, the overall agreement of interaction energies E_{int} between quantum chemical calculations and force field results is within a standard deviation σ of 6.8 % with minimum deviation of 1.7 % and a maximum deviation of 22.2 % for the LJ FF, and $\sigma = 5.6$ % with minimum deviation of 1.4 % and maximum deviation of 17.9 % for the PIM FF, respectively. Dividing the training sets, the deviation is larger for the single ion pair references, and decreases for an increasing number of ion pairs in the reference system. This is probably due to cooperative effects,[415,416] which are different in the quantum chemically described system. These effects can be identified by considering differences in the mean interaction energies, *e.g.*, the differences in $\langle E_{\mathrm{int}}^{\mathrm{QM}} \rangle$ in comparison of the 1 IP to the 2 IP, and the 3 IP energies of the $[C_1C_1Im][SCN]$

systems are ≈ 144 and ≈ 209 kJmol^{-1}. $\langle E_{\text{int}}^{\text{QM}} \rangle$ is not doubled or tripled by doubling or tripling the number of IPs, because the ILs components interact with each other, which in turn influences the IL–anatase interaction. The proposed PIM FF is able to incorporate this effect to a much larger extent than the LJ FF, yielding a better overall agreement of the PIM FF to the QM reference. The LJ FF is only partly able to describe the cooperativity, as nonpolarizable force fields often fail to describe such effects.[417]

Table 3.8: Derived Classical Force Field Parameters ϵ_{ij} and σ_{ij} for the PIM FF[a]

i	j	ϵ_{ij} / kJmol^{-1}	σ_{ij} / Å
C2	O	0.45903	3.082
C4/5	O	0.04690	3.234
C6/8	O	1.25415	3.108
C7	O	0.04185	1.645
H2	O	0.07930	2.263
H4/5	O	0.23332	2.281
H6/8	O	0.06714	2.480
H7	O	0.04251	2.821
N1/3	O	1.25520	2.988
C ([SCN]$^-$)	O	0.70668	3.119
N ([SCN]$^-$)	O	0.04207	2.663
S ([SCN]$^-$)	O	0.15137	3.442
B ([B(CN)$_4$]$^-$)	O	0.31804	3.053
C ([B(CN)$_4$]$^-$)	O	0.04768	2.129
N ([B(CN)$_4$]$^-$)	O	0.90257	3.033
C2	Ti	1.25499	2.673
C4/5	Ti	0.09018	3.724
C6/8	Ti	1.25411	2.960
C7	Ti	0.29064	1.568
H2	Ti	1.25495	1.983
H4/5	Ti	1.25478	1.135
H6/8	Ti	0.98123	1.848
G H7	Ti	0.04472	2.639
N1/3	Ti	0.36281	3.939
C ([SCN]$^-$)	Ti	0.22721	3.574
N ([SCN]$^-$)	Ti	0.36838	2.853
S ([SCN]$^-$)	Ti	0.09612	3.274
B ([B(CN)$_4$]$^-$)	Ti	1.10119	4.637
C ([B(CN)$_4$]$^-$)	Ti	0.17774	3.047
N ([B(CN)$_4$]$^-$)	Ti	0.48288	2.516

[a]For the labeling see Figure 3.19.

Table 3.9: Derived Classical Force Field Parameters ϵ_{ij} and σ_{ij} for the LJ FF[a]

i	j	ϵ_{ij} / kJmol^{-1}	σ_{ij} / Å
C2	O	1.25520	2.816
C4/5	O	1.25520	2.883
C6/8	O	1.25520	3.033
C7	O	1.25520	3.130
H2	O	1.05189	1.740
H4/5	O	1.25520	1.792
H6/8	O	0.05313	1.399
H7	O	0.04363	1.667
N1/3	O	1.25518	3.237
C ([SCN]$^-$)	O	1.25518	2.958
N ([SCN]$^-$)	O	0.40148	1.861
S ([SCN]$^-$)	O	1.25477	3.069
B ([B(CN)$_4$]$^-$)	O	1.25520	2.908
C ([B(CN)$_4$]$^-$)	O	0.12037	1.259
N ([B(CN)$_4$]$^-$)	O	1.25520	2.785
C2	Ti	1.25520	3.193
C4/5	Ti	1.25409	2.939
C6/8	Ti	1.25493	3.180
C7	Ti	1.25509	2.798
H2	Ti	1.25520	3.000
H4/5	Ti	1.25520	2.686
H6/8	Ti	0.43577	2.784
H7	Ti	1.25491	2.500
N1/3	Ti	1.25519	3.482
C ([SCN]$^-$)	Ti	1.25520	3.146
N ([SCN]$^-$)	Ti	0.82132	2.507
S ([SCN]$^-$)	Ti	0.08240	3.312
B ([B(CN)$_4$]$^-$)	Ti	1.25520	4.272
C ([B(CN)$_4$]$^-$)	Ti	1.25520	3.026
N ([B(CN)$_4$]$^-$)	Ti	1.20871	2.116

[a]For the labeling see Figure 3.19.

Ultimately, the purpose of the derived force field is to describe the adsorption of the IL at the anatase interface. Both presented FFs show reasonable agreement of $\langle E_{\text{int}}^{\text{QM}} \rangle$ and $\langle E_{\text{int}}^{\text{MM}} \rangle$ for the reference cells involving bulk IL systems.

Table 3.10: Overview of Training Set Used To Fit the Classical Force Field Parameters[a]

System	#	$\langle E_{\text{int}}^{\text{QM}} \rangle$ / kJmol^{-1}	$\langle E_{\text{int}}^{\text{LJ}} \rangle$ / kJmol^{-1}	$\langle E_{\text{int}}^{\text{PIM}} \rangle$ / kJmol^{-1}	σ^{LJ} / kJmol^{-1}	σ^{LJ} / %	σ^{PIM} / kJmol^{-1}	σ^{PIM} / %
full	631	−700.3	−687.0	−691.6	47.5	−6.8	39.5	−5.6
1 IP $[C_1C_1Im][SCN]$	125	−265.3	−212.8	−225.1	58.9	−22.2	47.6	−17.9
2 IP $[C_1C_1Im][SCN]$	100	−409.2	−397.0	−408.2	44.6	−10.9	32.3	−7.9
3 IP $[C_1C_1Im][SCN]$	100	−618.8	−644.3	−634.8	43.9	−7.1	38.9	−6.3
bulk $[C_2C_1Im][SCN]$	32	−3602.5	−3575.1	−3600.5	70.8	−2.0	50.1	−1.4
1 IP $[C_1C_1Im][B(CN)_4]$	150	−243.4	−246.6	−242.2	24.5	−10.1	26.4	−10.9
2 IP $[C_1C_1Im][B(CN)_4]$	50	−624.2	−564.1	−579.5	66.9	−10.7	51.8	−8.3
3 IP $[C_1C_1Im][B(CN)_4]$	50	−812.6	−814.2	−818.5	28.6	−3.5	28.8	−3.5
bulk $[C_2C_1Im][B(CN)_4]$	24	−3429.1	−3437.3	−3438.9	58.8	−1.7	59.1	−1.7

[a] Mean BSSE-corrected reference energies $\langle E_{\text{int}}^{\text{QM}} \rangle$ and mean force field interaction energies for the LJ force field $\langle E_{\text{int}}^{\text{LJ}} \rangle$ and the polarizable force field $\langle E_{\text{int}}^{\text{PIM}} \rangle$ are given as well as the standard deviations σ in SI units and in percent of the QM reference energy.

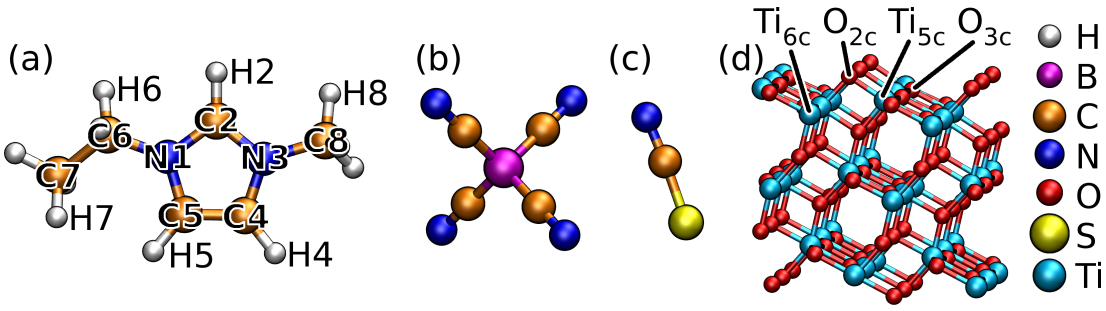

Figure 3.19: Labeling of the ILs components (a) $[C_2C_1Im]^+$, (b) $[B(CN)_4]^-$, and (c) $[SCN]^-$ (c) as well as the (d) anatase (101) surface. In the case of the symmetric imidazolium cation $[C_1C_1Im]^+$, H4 and H5 (C4 and C5, respectively) are indistinguishable.

3.3.3.2 Application of the Generated Force Field

At first, the pure bulk ILs were simulated with the IL FF, since the original charges were altered. The force field performs reasonably well, reproducing experimental densities very well, and even viscosities, which are arguably hard to determine from MD simulations, are reproduced well concerning trends and absolute values (numbers are given in Table 3, Supporting Information). As we only introduced a very minor change to the original FF, the quality of the IL FF is conserved.

As a case study using the derived FFs, the ionic liquids $[C_2C_1Im][B(CN)_4]$ and $[C_2C_1Im]$ [SCN] were simulated in the confined region between two parallel slabs of anatase with exposed (101) surface; the components are shown in Figure 3.19. In the following, only results using the more accurate PIM FF are shown, because we aim at high accuracy to gain new insights on the structure of the interface. The feasibility of the LJ FF was tested as well, information on the results are given in the Supporting Information.

The z-dependent density ρ_z (Figure 3.20a,b, note that the surface normal (SN) of the anatase slab coincides with the z-axis of the simulation box) reveals a strong aggregation of both ILs at the surface, because relative density at the surface is observed to be

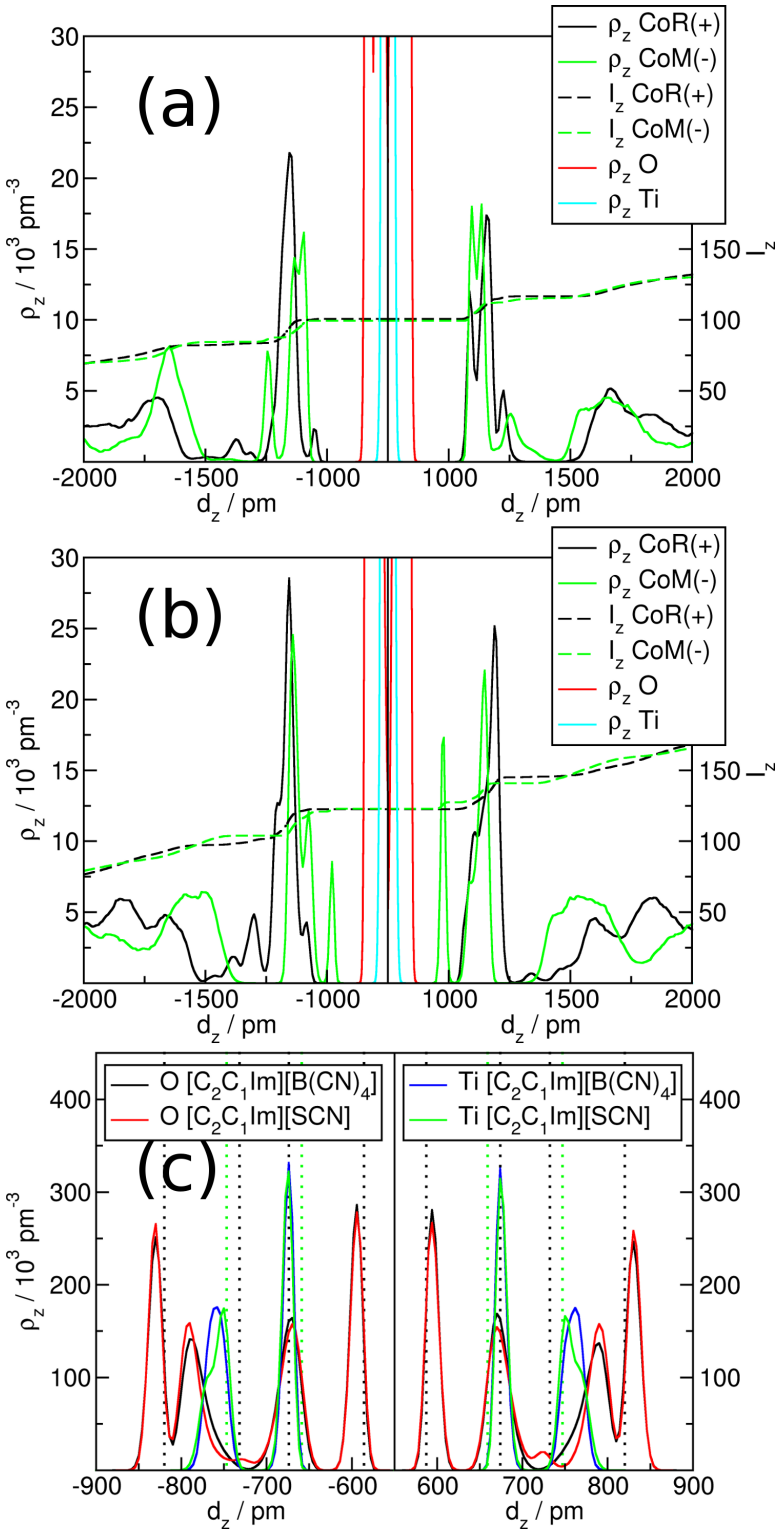

Figure 3.20: Density profiles ρ_z and the volume-integrated density I_z yielding the number count: (a) for $[C_2C_1Im][B(CN)_4]$ and (b) for $[C_2C_1Im][SCN]$. CoR(+) is the center of the imidazolium ring, and CoM(−) is the anion's center of mass. z is defined to be zero in the middle of the slab, because the outer layers are flexible. (c) A detailed view on the surface layers of TiO_2 in both ILs. The dotted lines indicate unperturbed crystal positions.

Table 3.11: Surface Number Count of Molecules N and Surface Number Density σ_S of the Components at the Surface[a]

	$[C_2C_1Im][B(CN)_4]$		$[C_2C_1Im][SCN]$	
component	N	σ_S / nm^{-2}	N	σ_S / nm^{-2}
$[C_2C_1Im]^+$	34.0	1.6	47.6	2.3
anion, sum	30.7	1.5	36.9	1.8
anion, conf 1	24.6	1.2	6.6	0.3
anion, conf 2	6.1	0.3	30.4	1.5

[a] $[B(CN)_4]^-$ conf 1 = face conformation, conf 2 = vertex conformation. $[SCN]^-$ conf 1 = flat conformation, conf 2 = perpendicular. Detailed descriptions of these conformations are found in our previous work.[262]

approximately 6 times the bulk density. This tightly adsorbed layer extends ≈ 400 pm in z direction, followed by ≈ 200 pm of a very low density region for $[C_2C_1Im][B(CN)_4]$ and ≈ 100 pm for $[C_2C_1Im][SCN]$, where almost no molecules are found throughout the simulation. ρ_z shows two distinct peaks for the $[SCN]^-$ anion and $[B(CN)_4]^-$ anion, which will be discussed later in detail with the aid of combined distance–angle distribution functions. The observed layer thickness correlates well with a computationally and experimentally verified thickness of approximately 450 pm for the IL $[C_2C_1Im][NTf_2]$.[194] As we employ a polarizable FF for the substrate TiO_2, the outer layers are flexible and are deflected by the IL, see Figure 3.20c. It can be seen that Ti_{5c} (see Figure 3.19) atoms are more homogeneously pulled into the direction of the bulk in the $[C_2C_1Im][B(CN)_4]$ system (blue curve), whereas a distinct shoulder emerges for the $[C_2C_1Im][SCN]$ system (green curve). This is probably due to more distinct and more stable N(SCN)–Ti_{5c} interactions, in contrast to more fluctuating, more homogeneous N$(B(CN)_4)$–Ti_{5c} interactions. A combined distance–distance distribution function (SI Figure 3) shows clearly that Ti_{5c} is pulled toward the bulk upon coordination of $[SCN]^-$. The O_{3c} oxygen atoms of the first surface layer are consistently moved toward the bulk of the IL. An additional peak arises in the $[C_2C_1Im][SCN]$ system for the surface oxygen atoms at $d_z \approx \pm 720$ pm (red curve). This peak is most probably caused by O–C($[SCN]^-$) interactions, when the thiocyanate aligns flatly in a hollow of the surface, while nitrogen and sulfur can interact simultaneously with two Ti_{5c} titanium atoms. This assumption is supported by a respective distance–distance distribution function, provided in the Supporting Information (SI Figure 4). It can also be seen that the second stoichiometric layer of TiO_2 is significantly less affected by surface phenomena; thus, it is probably reasonable to fix the positions of the substrate atoms for inner layers.

Evaluating the integrated z-density, I_z, the surface coverage can be quantified, which is summarized in Table 3.11. On average, the anatase (101) surface is covered by 1.6 cations and 1.5 anions per nm^2 for the $[C_2C_1Im][B(CN)_4]$ IL, and by 2.3 cations and 1.8 anions for the $[C_2C_1Im][SCN]$ IL, which translates to an excess of cations at the surface. The ratio of cations to anions at the surface is ≈ 1.1 for the $[C_2C_1Im][B(CN)_4]$ system and ≈ 1.3 for the $[C_2C_1Im][SCN]$ system. Although the $[SCN]^-$ anion shows a

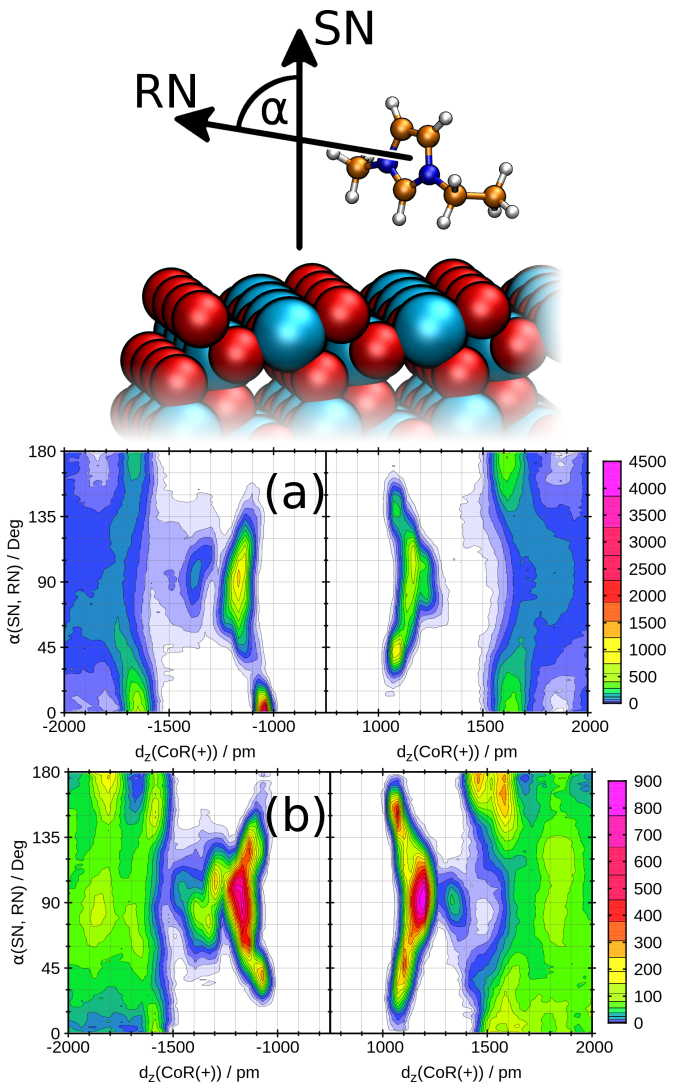

Figure 3.21: Combined distance–angle distribution functions showing the surface orientation of cations toward the surface (a) in $[C_2C_1Im][B(CN)_4]$ and (b) in $[C_2C_1Im][SCN]$. The distance between the center of ring (CoR(+)) and the surface is shown in combination with the angle between the surface normal (SN) and the ring normal (RN).

higher surface number density than the $[B(CN)_4]^-$ anion, the smaller sterical demand of the former probably allows for a much higher surface concentration of the cation, leading to a higher cation excess at the surface for the $[C_2C_1Im][SCN]$ IL. A comparable excess of cations was also recently found for the IL $[C_2C_1Im][NTf_2]$ at a neutral Al_2O_3 surface.[194] This finding might be interesting for the use of these ILs as electrolytes, *e.g.*, a positively charged surface might accumulate negatively charged species from the bulk of the liquid or changes the respective Fermi energy E_F of the adsorbent material.[174] For the latter, individual contributions of the ILs have to be considered.[262] The excess of cations leads to a multilayered structure, where anion-rich and cation-rich layers alternating. This effect is more pronounced for the $[C_2C_1Im][SCN]$ IL, which is in agreement with the higher cation excess at the surface. The multilayering can be

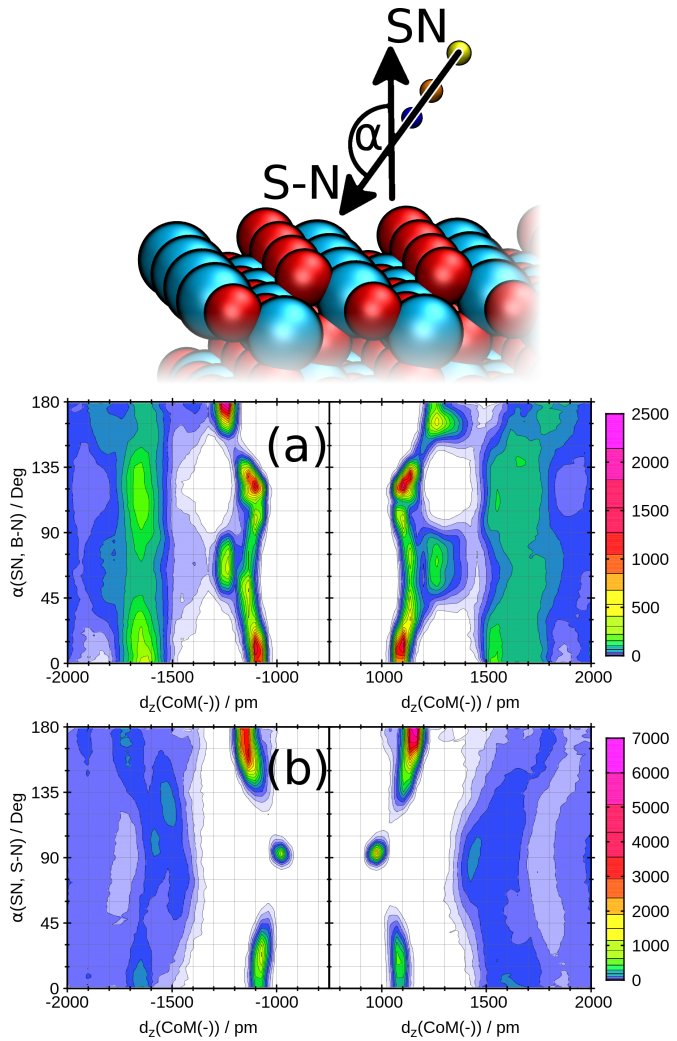

Figure 3.22: Combined distance–angle distribution functions showing the surface orientation of anions toward the surface (a) in $[C_2C_1Im][B(CN)_4]$ and (b) in $[C_2C_1Im][SCN]$. The anion's center of mass (CoM(−)) distance from the surface is shown in combination with the angle between all B–N vectors and the SN for $[C_2C_1Im][B(CN)_4]$, or the S–N vector and the SN for $[C_2C_1Im][SCN]$, respectively.

identifed by looking at the long-range part of the z-density profile, provided in the Supporting Information (SI Figure 1). This behavior was also found earlier for the $[C_2C_1Im][NTf_2]$ IL at the Al_2O_3 surface.[194]

With consideration of the molecular structure of the IL's components, it is apparent that they will have different coordination modes at the surface,[262] which can be distinguished by combined distance–angle distribution functions (CDFs). For the IL $[C_2C_1Im][B(CN)_4]$, the cation (Figure 3.21a) features flat ($\alpha \approx 0/180°$) and perpendicular ($\alpha \approx 90°$) conformations on one side of the surface, and aligns exclusively perpendicular on the other side (Figure 3.21a). Perpendicular conformations enable favorable interactions between acidic ring hydrogen atoms, especially the most acidic H2 hydrogen atoms, and O_{2c} surface oxygen atoms (see SI Figure 5 for the strong

H2–O_{2c} interactions). Favorable hydrogen-bond-like H2–$O_{surface}$ interactions were previously identified for the IL $[C_2C_1Im][NTf_2]$ at the Al_2O_3 surface.[194] The CDF in Figure 3.22a reveals two different $[B(CN)_4]^-$ surface conformations. The close conformation with angles at $\approx 0°$ and $\approx 125°$ indicates a flat conformation with three CN ligands pointing to the surface, and the fourth CN pointing into the bulk. As indicated by the ρ_z intensities from Figure 3.20, Table 3.11 and Figure 3.22a, this is the preferred $[B(CN)_4]^-$ surface conformation, which closely resembles this component's minimum energy conformation on that surface.[262] This is probably the preferred conformation, because multiple energetically favorable N–Ti interactions are established at the same time, and van der Waals interactions between anion and surface are maximized.

A second, less pronounced conformation is identified, with one CN group pointing directly to the surface, and the remaining three pointing to the bulk, which is the vertex conformation. This conformation is more strongly populated on the surface with the flat cations, drawing the whole picture: If the cations align flatly on the surface, there is only enough space for the anion to coordinate with one nitrogen atom. If the cations align perpendicular, the anion can coordinate with three ligands. The components compete for the surface coordination.

In the case of $[C_2C_1Im][SCN]$, the cation exclusively aligns in perpendicular, or at least somewhat tilted, conformations ($\alpha \approx 45 - 135°$, Figure 3.21b). The $[SCN]^-$ anion aligns in a close flat conformation, $\alpha \approx 90°$, or in the majorly populated N atom coordination conformation, $\alpha \approx 180°$, Figure 3.22b. The S atom coordination conformation is less preferred.

3.3.4 Conclusion

We presented a parametrization of Lennard-Jones type interaction potentials between the ionic liquids $[C_2C_1Im][B(CN)_4]$ and $[C_2C_1Im][SCN]$, and the anatase (101) surface, in order to merge the existing force fields for the pure compounds. As the TiO_2 force field is able to describe all TiO_2 modifications, the presented force field should in principle be applicable to study these ILs at other TiO_2 surfaces with minor changes, too.

The application of the derived polarizable force field was illustrated. For both ILs, a cation excess at the surface was observed, leading to a positively charged surface. The very dense surface layer extends roughly 400 pm into the bulk, followed by an almost unpopulated slab of $100 - 200$ pm prior to the bulk phase. The $[C_2C_1Im]^+$ cation aligns preferably perpendicular to the surface, with the acidic H2 hydrogen atom pointing toward the surface. In the IL $[C_2C_1Im][B(CN)_4]$, flat conformations of the cation are observed as well. The $[B(CN)_4]^-$ anion majorly exhibits the face conformation, where three CN groups interact with the surface. Less populated vertex conformations with one CN–TiO_2 interaction are also observed. Favorable N–Ti interactions are also discovered for the $[SCN]^-$ anion at the surface, resulting primarily in perpendic-

ular conformations with the nitrogen atom closest to the surface. Less abundant, flat conformations and S atom coordination conformations were found as well.

Furthermore, these findings have implications on the use of the ILs as electrolytes, *e.g.*, in DSCs. The strong adsorption of the IL might hinder other components from reaching the surface, which can be useful to prevent charge recombination mechanisms, or the positively charged surface might shift the Fermi level of the surface more than can be anticipated from single ion pair calculations.

Supporting Information

Information about the MD runs, z-density profiles for simulations with the PIM and the LJ FF, detailed distance–distance distribution functions and all reference structures used for the fitting procedure. The Supporting Information is available free of charge on the ACS Publications website at DOI: 10.1021/acs.jpcc.5b08538 and is attached in Section A.3.

Acknowledgments

This work was financially supported by the DFG project KI-768/12-1 “Materialsynthese nahe Raumtemperatur” and the SFB 813 “Chemie an Spinzentren: Konzepte, Mechanismen, Funktionen”. The support for H.W. by the Fonds der Chemischen Industrie (FCI) is gratefully acknowledged. M.S. is grateful for computing resources on Occigen (CINES), Curie (TGCC), and Turing (IDRIS) obtained through the Projects x2014096728 and x2015096728.

3.4 Ionic Liquid Induced Band Shift of Titanium Dioxide

Henry Weber[†] and Barbara Kirchner[†]*

ChemSusChem, **2016**, Volume *9*, Pages 2505–2514.

Received:	June 24, 2016
Revised:	August 11, 2016
Published:	August 11, 2016

Contributions to the manuscript:

- Setup and maintenance of all calculations.
- Analysis and evaluation of all results.
- Writing of the manuscript.

[†]Mulliken Center for Theoretical Chemistry, Universität Bonn, Beringstr. 4+6, D-53115 Bonn, Germany.
*Corresponding Author E-mail: kirchner@thch.uni-bonn.de.

Abstract

Ionic liquids have become an established option for the use as electrolytes in dye sensitized solar cells. In the present study, the adsorption of a multitude of different ionic liquids on a TiO_2 surface is studied systematically, focusing on energetic modifications of the semiconductor. The cation was found to generally cause an energetic downward shift of the TiO_2 band levels by accepting electron density from the surface, and the anions were observed to function contrarily, raising the energy levels by donating electron density. Both effects counterbalance each other, leaving the desired outcome dependent on the choice of the specific ionic liquid, *i.e.*, the choice of the cation–anion combination. The correlation of band levels with the IL's properties was successfully attempted. The dipole moment of the adsorbed ionic liquid species showed little to no correlation with the semiconductor energetics, but the charge transfer calculated by radical Voronoi tessellation revealed a high correlation. The current findings contribute to a deeper understanding of the role of the electrolyte in dye sensitized solar cells, and ionic liquids in general, and help choosing and tuning of electrolyte solutions in current applications.

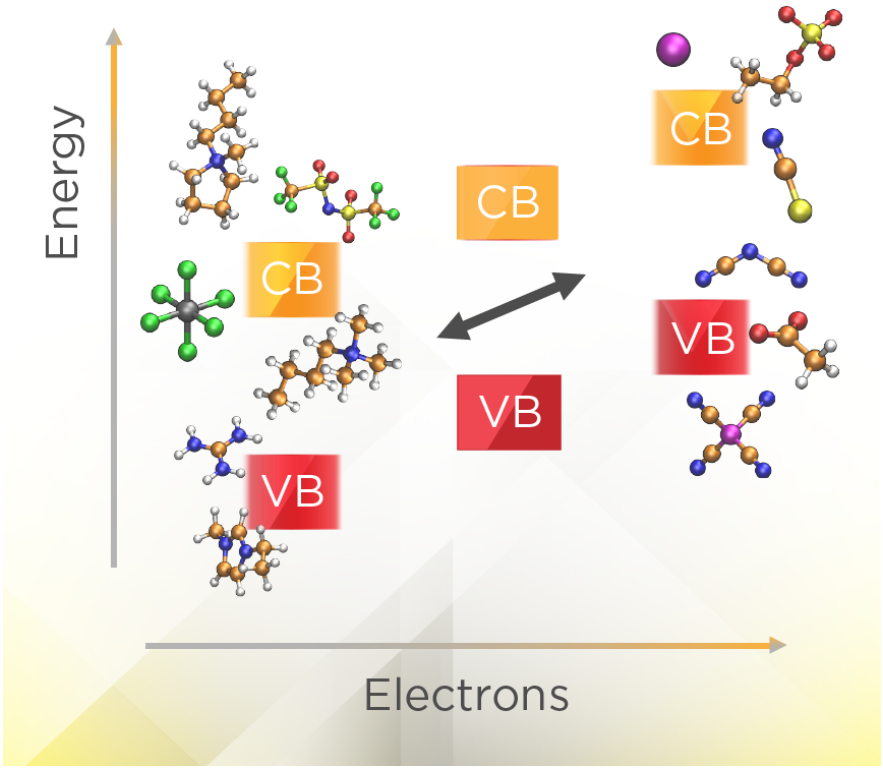

3.4.1 Introduction

In recent times, more and more applications arise for ionic liquids (ILs), especially in the energy sector.[133] The functional range is huge, including the use as electrolytes[133,394] *e.g.*, in fuel cells,[146,395,396] batteries,[133,135,418] supercapacitors,[133,151,152] and dye sensitized solar cells (DSCs).[100,418] They are excellently suited to capture CO_2 for further reactions or waste gas treatment,[419–421] and in the context of water splitting.[154,155]

Recently, scientists focused on the application of ILs as an electrolyte in DSCs.[169] The opportunities that arise from different IL properties such as the wide electrochemical window, thermal and chemical stability, and negligible volatility are vast. In the beginning, ILs were used as electrolytes mainly because of their low volatility, since common DSCs based on molecular electrolytes had a low long-term stability due to leakage.[64,119,120,422] Major obstacles in these attempts could mostly be traced back to the high viscosity of the employed ILs, limiting diffusion, and ultimately performance. Consequently, mixtures of ILs were utilized, which decreases the viscosity and results in overall good performing solar cells.[118,166]

Obviously, the electrolyte viscosity is not the sole parameter that influences the cell performance of a complete DSC device; all parts, interfaces, and interactions together determine the performance.[85,423,424] One vital parameter is the energy level alignment of the excited dye's LUMO state and the semiconductor's conduction band edge.[425] The conduction band edge determines the open-circuit voltage V_{OC} of the cell, which should be as high as possible. The energy difference between these two states determines the rate constant of the electron transfer from the excited dye LUMO state into the conduction band, which in turn determines the short-circuit current I_{SC}.[174,175] A large gap would imply a high driving force of the electron transfer, which means high values of I_{SC}, but at the expense of V_{OC}. Additionally, the electron transfer can be hindered electronically if the dye's LUMO energetically matches conduction band areas with a low density of states (DOS).[426] Consequently, an optimum has to be found that matches all requirements in the best possible way.

Soon after the pioneering works of Grätzel *et al.*[13] it was clear that the energy levels can be shifted upon addition of auxiliary components to the electrolyte, such as lithium ions,[162,177,181,427] or pyridines, with the most prominent known as 4-*tert*-butylpyridine (4-TBP).[19,172,174–178] The electrolyte itself can play an important role in this regard, especially as ionic liquids were shown to have a very active surface science.[428] In particular, Zhang *et al.* showed the capability of the IL anions tetracyanoborate and dicyanamide to affect the conduction band edge, resulting in a pure IL-electrolyte DSC.[161] This approach was taken further by Bai *et al.* where the imidazolium dicyanamide IL was used because of some advantageous properties like low viscosity and good availability.[162] In the final DSC device, the energetic upward shift of the conduction band edge caused by the IL's anion was gradually countered by the addition

of lithium ions, fine-tuning the conduction band level to yield the best performance of 8.4 % at 100 mW cm^{-2}, employing the C106 ruthenium-dye.[162] Subsequently, Zhou *et al.* used these two ILs in a DSC employing the organic C218 dye, and came to the conclusion that the tetracyanoborate IL performs better than the dicyanamide IL. As in the previous studies, tetracyanoborate causes a downward shift of the conduction band edge, which results in an unfavorable lowering of V_{OC}. Fortunately, this is compensated by the generation of a beneficial energy offset at the TiO_2/Dye interface for electron injection, leaving the tetracyanoborate IL as the better choice for the given system.[160]

This important aspect shows that all criteria and components have to be tuned and harmonized to achieve an optimum performance, which means a certain dye or electrolyte might not be the best option in every situation. Changing the dye for example can mean that the electrolyte has to be changed as well to obtain the best performance.

The electrolyte is an essential part of the common dye sensitized solar cell, and ionic liquids showed true potential in this matter. Moreover, auxiliary ions have been used to affect the TiO_2 surface, band edge positions, and blocking layer behavior. Therefore, a systematic study aiming to reveal the applicability of certain ILs to influence the semiconductor energetics is presented.

In the following, the computational details are given in Section 3.4.2. Afterwards, the results are discussed in general, and universal corrections are deduced. Subsequently, trends and correlations are evaluated for each group of ILs independently, and the article closes with the conclusion.

3.4.2 Computational Details

42 different ILs were calculated on the anatase (101) surface. An overview over all ILs studied can be found in Table 3.12, a list of the full names can be reviewed from the supporting information. The ILs were calculated as single ion pairs on a 4x3 supercell of titanium dioxide in anatase modification in 2D periodic boundary conditions. The crystal slab was cut to reveal the stable (101) surface and rotated so that the surface normal matches the nonperiodic z-direction. The slab has a thickness of six stoichiometric TiO_2 layers. The cut plane was chosen to yield a vanishing dipole moment of the pure crystal slab in z-direction. Experimental lattice parameters were chosen for the anatase slab ($a = b = 378.2$ pm, $c = 950.2$ pm),[409] resulting in the final cell parameters $a = 1512.8$ pm, $b = 1635.59$ pm, $c = 6000$ pm, $\alpha = \beta = 90°$, and $\gamma = 110.2947°$. During the geometry optimizations, only the IL atoms were allowed to relax, and the surface atoms were constrained to stay in fixed positions. 10 different randomly generated starting structures were optimized for each IL. All geometries were inspected visually, if they match an adsorbed conformation, *i.e.*, they are not far apart from the surface. The closest surface–ion distances for each individual conformation were

usually well below 300 pm. The optimized structures were then used to derive dipole moments, density of states (DOS), charges, and interaction energies.

Geometries, interaction energies, and dipole moments were evaluated with the aid of the CP2K program package,[286] using the QUICKSTEP routine.[287] The MOLOPT-DZVP-SR-GTH basis sets[291] were employed along with Godecker-Teter-Hutter[292,293] (GTH) pseudopotentials. The Perdew–Burke–Ernzerhof (PBE) functional with zero damping D3 dispersion correction[230] was used to calculate the electronic structure. The Martyna–Tuckerman Poisson solver[351] was employed to achieve a good description of the wavefunction in the non-periodic direction. Basis set superposition error corrected interaction energies were obtained with the counterpoise correction method.[362] Dipole moments were obtained either by radical Voronoi tessellation[429] or from maximally localized Wannier centers.[430] The analyses were carried out with the aid of the TRAVIS program package.[412] Population analyses were conducted with radical Voronoi tessellation and via density fitting according to Blöchl.[361] For the radical Voronoi tessellation, the consistent van der Waals radii of Mantina *et al.* were used: $r(\mathrm{H}) = 110$ pm, $r(\mathrm{B}) = 192$ pm, $r(\mathrm{C}) = 170$ pm, $r(\mathrm{N}) = 155$ pm, $r(\mathrm{O}) = 152$ pm, $r(\mathrm{F}) = 147$ pm, $r(\mathrm{P}) = 180$ pm, $r(\mathrm{S}) = 180$ pm, $r(\mathrm{Cl}) = 175$ pm, $r(\mathrm{Br}) = 185$ pm, and $r(\mathrm{I}) = 198$ pm.[431] Unfortunately, there is no documented van der Waals radius for titanium. Therefore, two different atomic radii were applied, the empiric atomic radius $r_{\mathrm{emp}}(\mathrm{Ti}) = 140$ pm[432] and the calculated atomic radius $r_{\mathrm{calc}}(\mathrm{Ti}) = 176$ pm,[433] resulting in two different tessellations v_{emp} and v_{calc}, respectively.

The density of states (DOS) and projected density of states (PDOS) were evaluated with the CRYSTAL14[352] program package, employing the PBE0 hybrid functional.[216,217,222] The PBE0 functional for the calculation of the energetic properties of TiO_2 was chosen, because hybrid functionals are known to describe absolute Fermi energies and band gaps much better than pure GGA functionals in general,[390,391] and in particular for TiO_2.[388] Basis sets used in the PBE0 calculations were Ti: 86-411G(d31);[353,354] O: 8-411G;[355] H: 3-11G;[434] B:6-311G;[435] C: 6-311G;[434] N: 6-311G;[434] F:6-31G*;[436] P: 6-31G*;[408] S: 86-311G;[437] Cl: 86-311G;[438] Br: 6-31G*;[439] and a $[4s5p3d2f]$ seven valence electron pseudopotential for I.[440] Results obtained with the I pseudopotential basis set were compared to all electron calculations with the 6-311G*[441] basis set and were found to be in a reasonable agreement (see SI for further information). The DOS and projected DOS (PDOS) were evaluated employing a Fourier–Legendre technique,[363,364] which is implemented in the properties tool of CRYSTAL14.

All abbreviated IL notations are introduced in the SI. To increase readability, the corresponding positive and negative charges are omitted when the short notation is used.

Table 3.12: Overview of All Investigated ILs With Calculated and Averaged TiO_2 Valance Band Edge Shift ΔE_H, Conduction Band Edge Shift ΔE_L, Band Gap Shift $\Delta\Delta$ and Mean Interaction Energy E_{int} Between Ion pair and Surface

n	cation	anion	Reference[a]	ΔE_H / eV	ΔE_L / eV	$\Delta\Delta$ / eV	E_{int} / kJ mol^{-1}
1	$[C_2C_1Im]$	$[B(CN)_4]$	121,160–162	0.33 ± 0.10	0.14 ± 0.10	−0.19 ± 0.10	−333 ± 46
2	$[C_2C_1Im]$	$[C(CN)_3]$	118,163	0.54 ± 0.17	0.27 ± 0.17	−0.27 ± 0.08	−320 ± 75
3	$[C_2C_1Im]$	$[N(CN)_2]$	120,160–165	0.67 ± 0.15	0.32 ± 0.15	−0.34 ± 0.08	−318 ± 62
4	$[C_2C_1Im]$	[SCN]	119,163,166, 126	0.71 ± 0.26	0.38 ± 0.15	−0.33 ± 0.16	−290 ± 60
5	$[C_2C_1Im]$	[Cl]		0.75 ± 0.16	0.39 ± 0.09	−0.36 ± 0.17	−306 ± 34
6	$[C_2C_1Im]$	[Br]		0.69 ± 0.15	0.35 ± 0.10	−0.33 ± 0.16	−286 ± 33
7	$[C_2C_1Im]$	[I]	166,422	0.63 ± 0.22	0.30 ± 0.14	−0.33 ± 0.13	−268 ± 46
8	$[C_2C_1Im]$	$[BF_4]$	164–166	−0.37 ± 0.47	−0.46 ± 0.36	−0.09 ± 0.14	−141 ± 69
9	$[C_2C_1Im]$	$[PF_6]$	165,442	−0.72 ± 0.18	−0.77 ± 0.16	−0.05 ± 0.03	−118 ± 17
10	$[C_2C_1Im]$	[FAP]		−0.45 ± 0.26	−0.56 ± 0.23	−0.11 ± 0.04	−145 ± 21
11	$[C_2C_1Im]$	[OTf]	64,125,166	0.32 ± 0.38	0.10 ± 0.30	−0.22 ± 0.13	−261 ± 61
12	$[C_2C_1Im]$	$[Tf_2N]$	64,125,165	0.40 ± 0.12	0.12 ± 0.18	−0.27 ± 0.10	−278 ± 29
13	$[C_2C_1Im]$	$[Pf_2N]$		−0.01 ± 0.44	−0.17 ± 0.35	−0.16 ± 0.10	−192 ± 72
14	$[C_2C_1Im]$	[OAc]		0.73 ± 0.20	0.34 ± 0.12	−0.38 ± 0.15	−372 ± 39
15	$[C_2C_1Im]$	[TFA]	166	0.67 ± 0.19	0.28 ± 0.10	−0.39 ± 0.18	−322 ± 36
16	$[C_2C_1Im]$	$[NO_3]$		0.52 ± 0.13	0.28 ± 0.11	−0.24 ± 0.15	−307 ± 34
17	$[C_2C_1Im]$	[DP]	100	0.42 ± 0.21	0.15 ± 0.20	−0.27 ± 0.17	−436 ± 52
18	$[C_2C_1Im]$	$[EtSO_4]$		0.42 ± 0.33	0.21 ± 0.25	−0.21 ± 0.10	−319 ± 68
19	$[C_1C_1Im]$	$[B(CN)_4]$		0.34 ± 0.17	0.17 ± 0.17	−0.16 ± 0.09	−317 ± 31
20	$[C_3C_1Im]$	$[B(CN)_4]$		0.33 ± 0.11	0.16 ± 0.11	−0.18 ± 0.08	−334 ± 31
21	$[C_4C_1Im]$	$[B(CN)_4]$		0.23 ± 0.18	0.08 ± 0.17	−0.15 ± 0.09	−308 ± 59
22	$[C_6C_1Im]$	$[B(CN)_4]$		0.29 ± 0.10	0.17 ± 0.09	−0.13 ± 0.04	−364 ± 49
23	$[C_1C_1Im]$	[I]	422	0.64 ± 0.17	0.24 ± 0.07	−0.40 ± 0.14	−256 ± 30
24	$[C_3C_1Im]$	[I]	164,422,443	0.72 ± 0.10	0.28 ± 0.05	−0.44 ± 0.09	−263 ± 37
25	$[C_4C_1Im]$	[I]	422,443,444	0.63 ± 0.15	0.29 ± 0.06	−0.35 ± 0.16	−297 ± 27
26	$[C_6C_1Im]$	[I]	64,422,445, 443	0.67 ± 0.11	0.26 ± 0.04	−0.41 ± 0.13	−321 ± 23
27	$[(C_F)_2C_2C_1Im]$	[I]		0.58 ± 0.18	0.23 ± 0.12	−0.35 ± 0.16	−260 ± 34
28	$[(C_F)_4C_2C_1Im]$	[I]	444	0.67 ± 0.19	0.32 ± 0.11	−0.35 ± 0.16	−238 ± 32
29	$[(C_F)_6C_2C_1Im]$	[I]		0.59 ± 0.18	0.26 ± 0.11	−0.34 ± 0.14	−257 ± 44
30	$[(C_F)_2C_2C_1Im]$	$[BF_4]$		0.50 ± 0.20	0.20 ± 0.15	−0.30 ± 0.15	−230 ± 63
31	$[(C_F)_4C_2C_1Im]$	$[BF_4]$		0.54 ± 0.23	0.28 ± 0.18	−0.26 ± 0.11	−208 ± 55
32	$[(C_F)_6C_2C_1Im]$	$[BF_4]$		0.37 ± 0.30	0.14 ± 0.24	−0.23 ± 0.15	−207 ± 59
33	[Guan]	[I]	121,185,446, 119,126	0.39 ± 0.18	0.05 ± 0.14	−0.34 ± 0.17	−356 ± 124
34	$[AllylC_1Im]$	[I]	124	0.62 ± 0.11	0.22 ± 0.04	−0.40 ± 0.13	−293 ± 33
35	$[C_2C_1C_1Im]$	[I]		0.72 ± 0.17	0.33 ± 0.16	−0.39 ± 0.14	−262 ± 34
36	$[C_4C_1Pyrr]$	[I]	447	0.66 ± 0.44	0.34 ± 0.31	−0.32 ± 0.20	−252 ± 48
37	$[C_2Py]$	[I]		0.62 ± 0.16	0.25 ± 0.07	−0.37 ± 0.16	−234 ± 20
38	$[C_4Py]$	[I]		0.63 ± 0.17	0.26 ± 0.10	−0.37 ± 0.15	−264 ± 21
39	$[N_{1111}]$	[I]	448	0.70 ± 0.15	0.41 ± 0.05	−0.30 ± 0.12	−194 ± 22
40	$[N_{2222}]$	[I]	448	0.83 ± 0.14	0.43 ± 0.03	−0.40 ± 0.16	−260 ± 31
41	$[N_{4444}]$	[I]	448	0.88 ± 0.11	0.47 ± 0.05	−0.41 ± 0.13	−349 ± 35
42	$[N_{4111}]$	[I]	448	0.74 ± 0.19	0.40 ± 0.04	−0.34 ± 0.16	−253 ± 26

[a] References are listed, if the IL, or very similar ones, were employed in real DSC devices.

3.4.3 Results and Discussion

The investigated ionic liquids range from the popular class of imidazolium ionic liquids to pyridinium, pyrrolidinium, and ammonium ionic liquids. To compare different anion effects, a range of different anions was computed while keeping the 1-ethyl-3-methylimidazolium cation ($[C_2C_1Im]$) constant. This cation was chosen because it is widely used among different ionic liquids. Moreover, we previously studied this cation in the context of TiO_2 adsorption.[262,263] Consequently, different cations were investi-

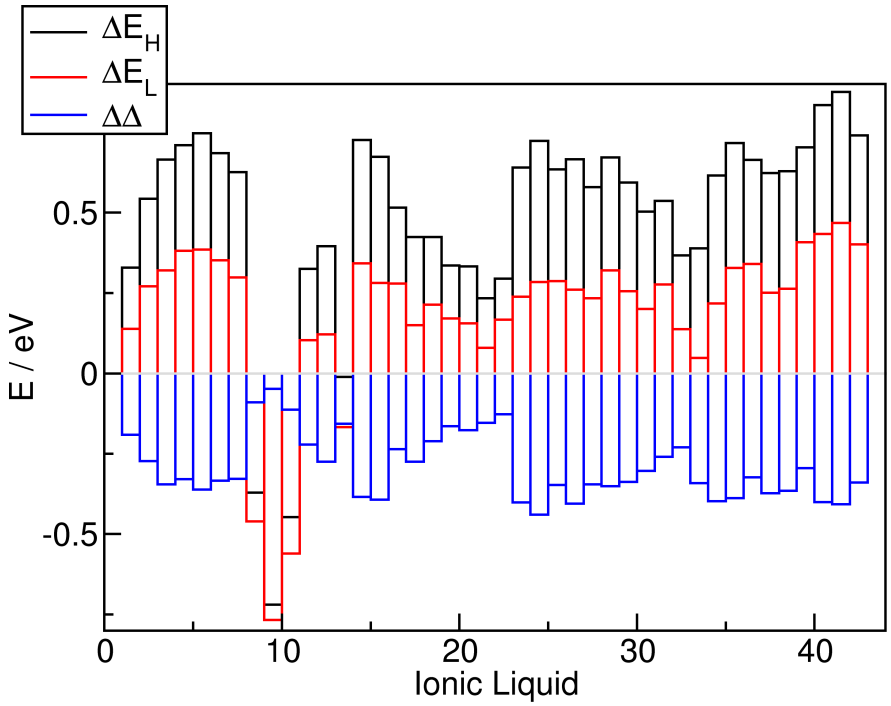

Figure 3.23: Graphical representation of average energetic quantities from the PDOS calculations. ΔE_{H} is the valence band edge shift, ΔE_{L} the conduction band edge shift and $\Delta\Delta$ the band gap shift. The number of the IL is according to Table 3.12.

gated by keeping the anion constant as iodide. The iodide anion was chosen because of the small conformational freedom, as it should reliably find similar adsorption places on the surface, minimizing the variance of the anion influence. Additionally, the iodide is often used as a component in DSCs as redox mediator in the I^-/I_3^- redox pair. Different averaged global quantities of the investigated systems can be inspected in Table 3.12.

A universal trend is the energetic upward shift of the valence band edge ΔE_{H} of TiO_2 by $\approx 0.2 - 1$ eV and the conduction band edge ΔE_{L} by $\approx 0.1 - 0.5$ eV, see also Figure 3.23. The effect on the valence band is larger in most cases, which leads to a general decrease of the semiconductors band gap $\Delta\Delta$ by $\approx 0.1 - 0.4$ eV.

ILs with fluorinated anions are clearly deviating from this trend, namely $[C_2C_1Im][BF_4]$, $[C_2C_1Im][PF_6]$, $[C_2C_1Im][FAP]$, and $[C_2C_1Im][Pf_2N]$. These ILs show an energetic downward shift of the TiO_2's valence band edge. The downward shift is even more pronounced for the conduction band edge, which results in a decreased band gap as seen for the other ILs.

The energetic level of an occupied state is raised when the amount of electrons is increased. Regarding the present TiO_2 system, this is most likely accomplished by coordination of the electron-rich anion, donating electron density to the semiconductor. Consequently, the energetic level of the occupied state is lowered upon decrease of electron density, *i.e.*, coordination of the electron-poor cation, accepting charge density from the surface. As the ionic liquids are adsorbed as ion pairs, both effects act

Table 3.13: Results From Linear Regression of Different Correlations of the General Form $y = a + bx$ and Correlation Coefficients R [a]

x	y	R	R^2	a	b
ΔE_H	ΔE_L	0.98	0.96	-0.166	0.740
ΔE_H	CT(v_{emp})	-0.60	0.36	0.119	-0.285
ΔE_H	CT(v_{calc})	-0.83	0.68	-0.114	-0.350
ΔE_H	CT(Blöchl)	-0.71	0.51	-0.113	-0.427
ΔE_L	CT(v_{emp})	-0.49	0.24	0.040	-0.306
ΔE_L	CT(v_{calc})	-0.77	0.59	-0.200	-0.432
ΔE_L	CT(Blöchl)	-0.63	0.40	-0.223	-0.499
$\Delta\Delta$	CT(v_{emp})	0.78	0.62	0.344	1.239
$\Delta\Delta$	CT(v_{calc})	0.82	0.68	0.057	1.164
$\Delta\Delta$	CT(Blöchl)	0.80	0.63	0.146	1.592
ΔE_H	μ_z(v_{emp})	0.37	0.14	-2.793	3.108
ΔE_H	μ_z(v_{calc})	0.42	0.18	-0.361	3.359
ΔE_H	μ_z(Wannier)	0.07	0.01	-4.378	0.757
ΔE_L	μ_z(v_{emp})	0.34	0.11	-2.012	3.778
ΔE_L	μ_z(v_{calc})	0.44	0.19	0.376	4.637
ΔE_L	μ_z(Wannier)	0.08	0.01	-4.236	1.167
$\Delta\Delta$	μ_z(v_{emp})	-0.38	0.14	-4.419	-10.706
$\Delta\Delta$	μ_z(v_{calc})	-0.30	0.09	-1.092	-8.058
$\Delta\Delta$	μ_z(Wannier)	-0.03	0.00	-4.317	-1.041

[a] ΔE_H is the TiO_2 valance band edge shift, ΔE_L the conduction band edge shift, $\Delta\Delta$ the band gap shift, CT the charge transfer and μ_z the z-component of the IL's dipole vector.

simultaneously, competing and canceling each other to some extent. As can be seen, the anion effect is dominant in most cases, resulting in the discussed energetic upward shift of valence and conduction band edge.

Investigation of the distinct adsorption geometries shows that the adsorption of the fluorinated anions $[BF_4]^-$, $[PF_6]^-$, $[FAP]^-$, and $[Pf_2N]^-$ is rather weak, leading to only very small amounts of electron density donated to the surface. In these cases, the electron withdrawing effect of the cation is dominant, resulting in the energetic downward shift of valence and conduction band of TiO_2. Thus, it is only consequent to correlate the amount of charge transferred with the band edge shifts. Unfortunately, this kind of information can only be gathered by population analyses of the electronic structure, which are inherently empiric, as an electronic population is not an observable quantity. Different approaches to obtain the charge transfer and the correlation will be discussed in the next section.

3.4.3.1 Correlation of Band Shift

Finding a systematic dependence of the energetic shift of the titanium's DOS and another quantity specifically characterized by the IL is a primary goal of the present study. As seen in Figure 3.23, the shift of TiO_2's valence (black lines) and conduction band edge (red lines) are not identical, leading to altering band gaps (blue lines). The correlation of valence band edge shift ΔE_H and conduction band edge shift ΔE_L shown in Figure 3.24(a) demonstrates a dominant linear dependence of both quantities. The

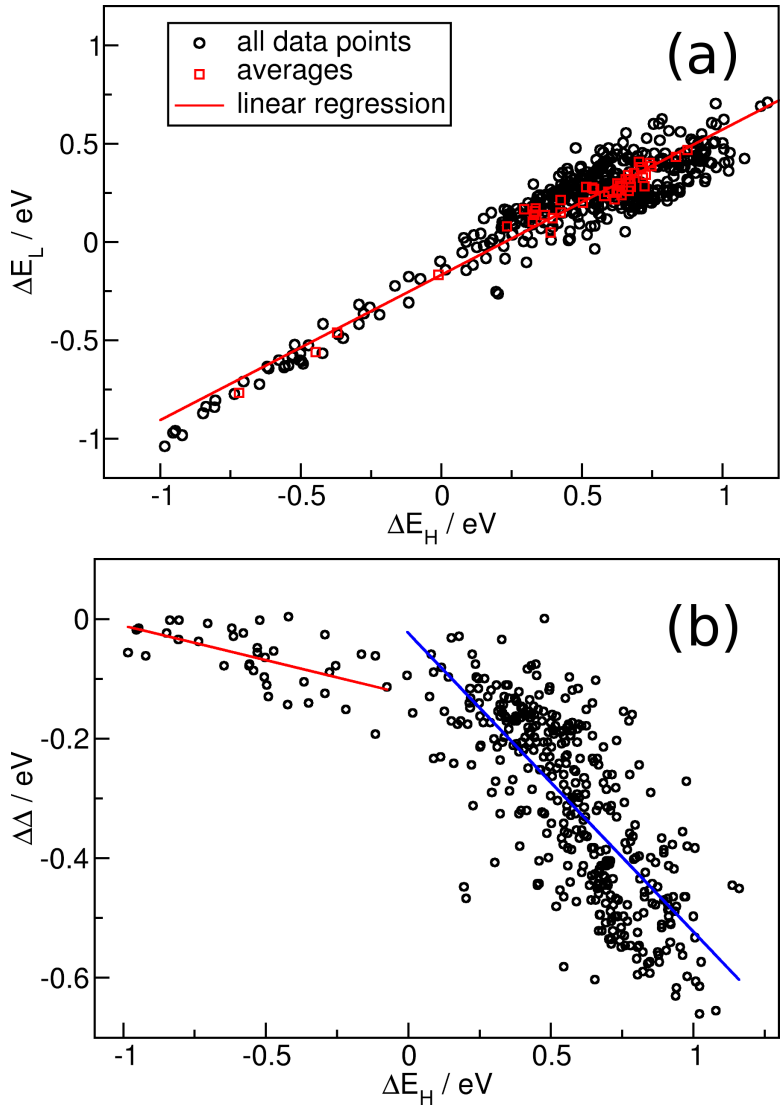

Figure 3.24: (a) Correlation of TiO_2 HOMO energy shift ΔE_{H} and TiO_2 LUMO energy shift ΔE_{L} with linear regression and (b) correlation of ΔE_{H} and TiO_2 band gap shift $\Delta\Delta$ with region specific regressions for $\Delta E_{\mathrm{H}} < 0$ and $\Delta E_{\mathrm{H}} > 0$.

corresponding linear regression equation is calculated to be $\Delta E_{\mathrm{L}} = -0.166 + 0.74\Delta E_{\mathrm{H}}$ with a squared correlation coefficient of $R^2 = 0.96$. Both, interception and slope explain the decreasing band gap, which is observed for all systems. The positive slope with a value smaller than one accounts for a conduction band shift that is smaller than the valence band shift, leading to smaller band gaps for energetic upward shifts. The negative interception generally translates into smaller band gaps, because even for systems with no valence band shift or weak downward shifts, the conduction band edge is lowered.

As we observed, the adsorbents band gap Δ decreases always upon IL adsorption, but is there a dependence from the valance band edge shift? The respective correlation is shown in Figure 3.24(b). The plot suggests that there are maybe two different cases.

In situations of an energetic upward shift of the valance band edge ($\Delta E_{\mathrm{H}} > 0$), the band gap is strongly decreased by values of $\Delta\Delta \approx -0.1$ to -0.6 eV. For an energetic downward shift of the valence band edge ($\Delta E_{\mathrm{H}} < 0$), the band gap is only slightly decreased by values ranging from $\Delta\Delta \approx 0$ to -0.2 eV. The underlying physical processes are not obvious and will require further investigation, but the different coordination bahavior of anion and cation on the surface are most probably involved. The positively charged cations tend to coordinate the surface oxygen atoms, and consequently the negatively charged anions tend to coordinate the formally positively charged surface titanium atoms. Given that the valence band edge is mostly comprised by the oxygen atoms, it will be more affected by the IL's cations. Similarly, the TiO_2's conduction band edge comprised by the states of titanium will be more affected by the anions in general. The two groups observed in Figure 3.24(b) could then possibly be strongly and weakly coordinating anions.

Different linear regressions done in this work are listed in Table 3.13. Originating from the work of Rühle *et al.*, a linear dependence of the solar cell's open-circuit voltage V_{OC} and the dipole moment of a coadsorbed acid was found.[449] Zhou *et al.*[160] used this correlation to explain the energetic shifts of the TiO_2's DOS when two different IL based electrolytes were used — $[C_2C_1Im][B(CN)_4]$ and $[C_2C_1Im][N(CN)_2]$. Unfortunately, V_{OC} is not directly accessible via our calculations, but it is linked to the semiconductor's conduction band edge, E_{L}, and recent calculations showed a linear dependence between calculated shifts of the conduction band edge and the measured shifts of V_{OC}.[356,357]

In the present study, the conduction band edge shift was correlated with the total dipole moment of the IL and only the z-component of the dipole vector. Regardless of the employed method to obtain the dipole moments, the total dipole moments of the IL showed no correlation with the energetic shifts at all. Taking only the z-component of the dipole vector, μ_{z}, some correlation could be found, which is most pronounced for the $\mathrm{v}_{\mathrm{calc}}$ dipole moments, but all in all the correlation is low. This finding is maybe due to the obstructions which make dipole moments especially hard to obtain for adsorbed ionic liquids, and better dipole moments may result in better correlations. However, different trends within certain groups of ILs will be discussed subsequently, the correlation is depicted in Figure 3.25. As argued earlier, the energy of a certain electronic state should in principle depend on the amount of the electronic charge present. This suggests a possible correlation of the band edge shifts and the total charge of the titanium dioxide slab, *i.e.*, the charge transfer between IL and adsorbent, presented in Figure 3.26. A linear correlation of the TiO_2's cluster charge and the conduction band shift was already proven by Ronca et al.[450] Furthermore, the amount of charge transferred from an absorbed dye into the surface could be successfully correlated with the conduction band shift.[450] In the present study, the correlation of the IL charge transfer with the band shifts yields the best correlation of all investigated IL properties. Especially, the charge transfer obtained from the radical Voronoi tessellation with the

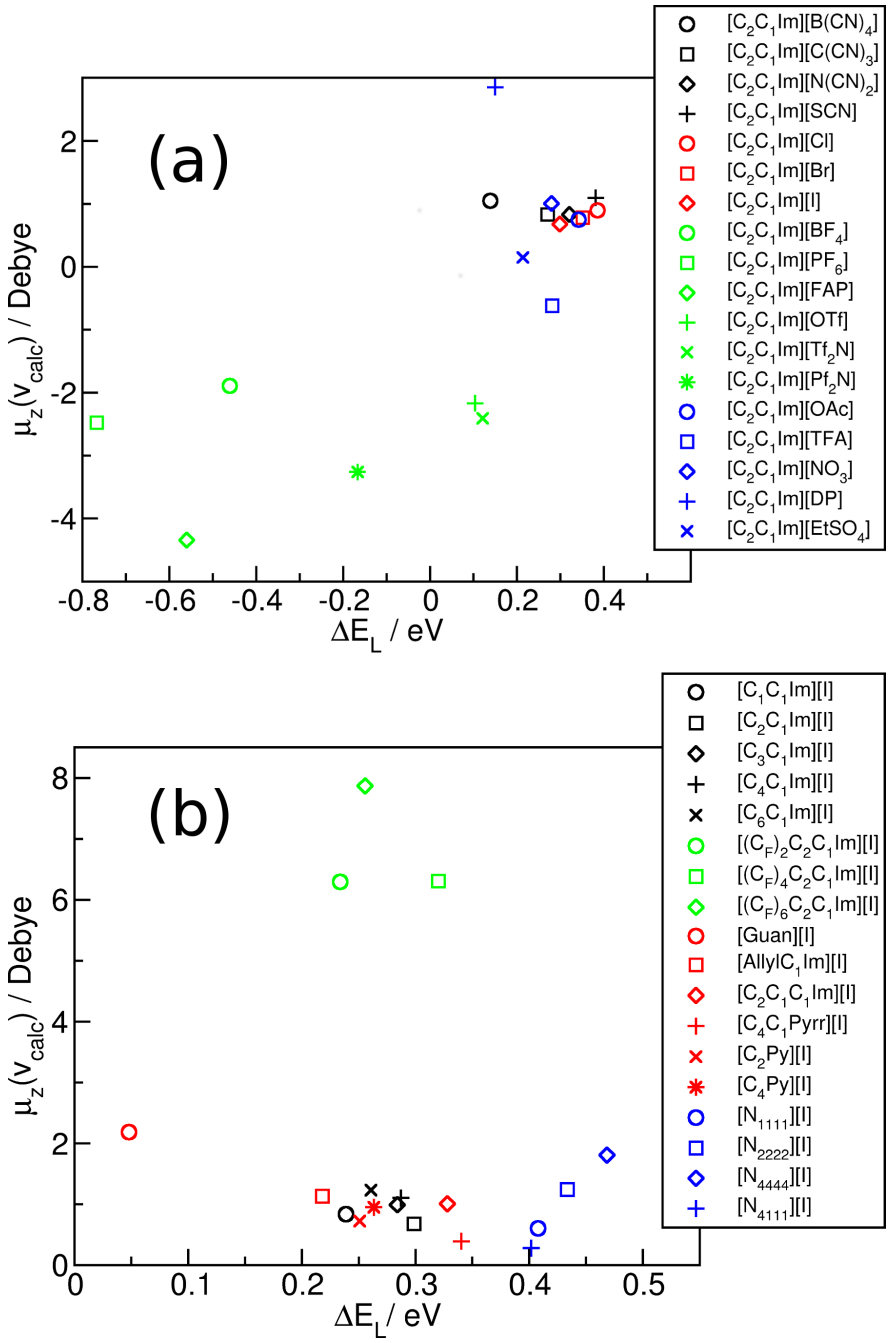

Figure 3.25: Detailed correlation of TiO_2 LUMO energy shift ΔE_L and z-component of the IL's dipole vector μ_z calculated with the v_{calc} method for all ionic liquids with (a) the [C_2C_1Im] cation and (b) the $[I]^-$ anion.

calculated titanium radius ($CT(v_{calc})$) excels in terms of the best correlation coefficient, see also Table 3.13.

In the following, the individual groups of ILs regarding their adsorption and energetic properties are discussed in detail.

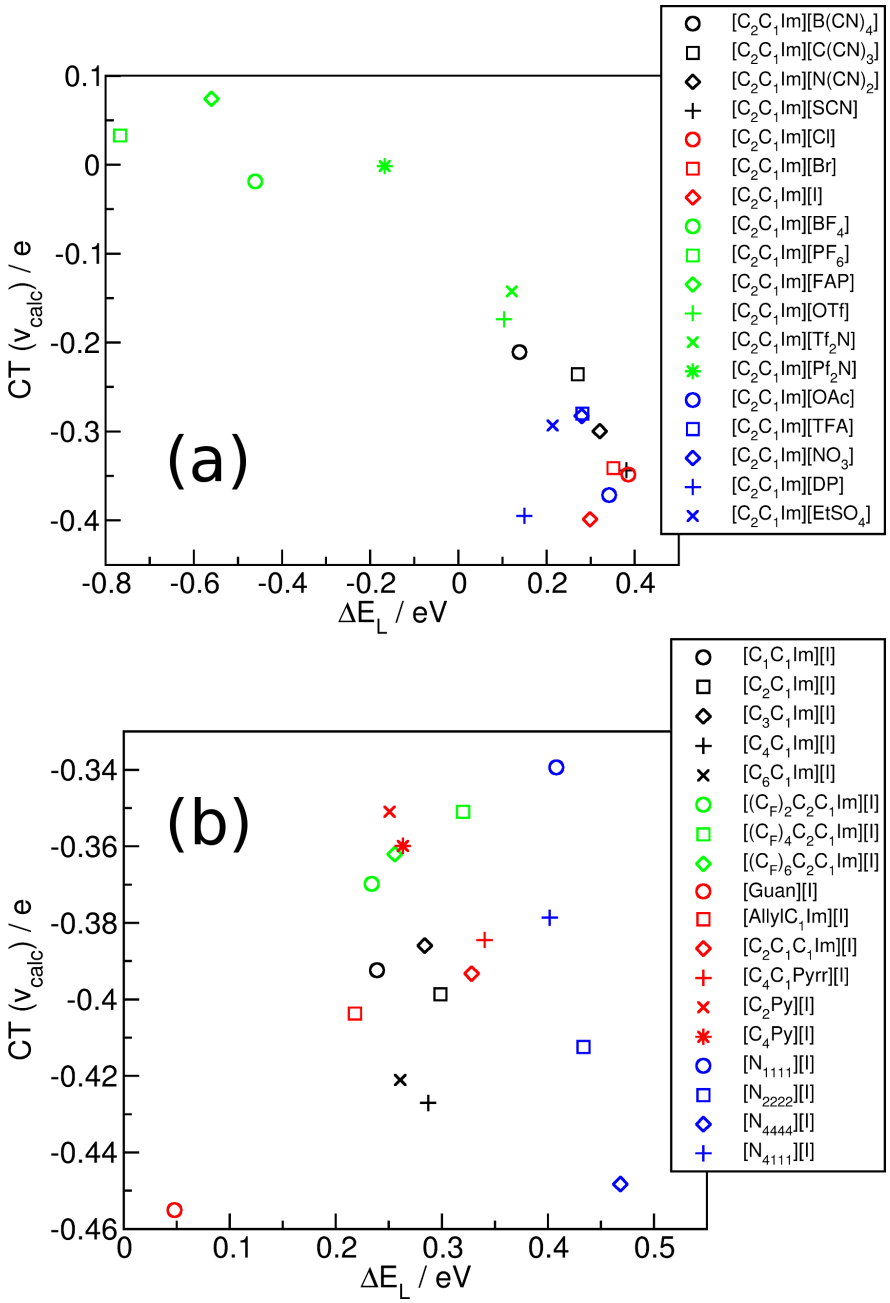

Figure 3.26: Detailed correlation of TiO_2 LUMO energy shift ΔE_L and charge transfer CT calculated with the v_{calc} method for all ionic liquids with (a) the $[C_2C_1Im]^+$ cation and (b) the $[I]^-$ anion.

Nitrile Ionic Liquids. The group of nitrile ILs consists of the $[C_2C_1Im]$ cation with the $[B(CN)_4]$, $[C(CN)_3]$, $[N(CN)_2]$, or [SCN] anion. From literature it is known that $[N(CN)_2]$ should cause a larger upward shift of the conduction band edge of TiO_2 than $[B(CN)_4]$.[160] This behavior is captured by our calculations, showing an increasing upward shift from $[B(CN)_4]$ with $\Delta E_L = 0.14$ eV along the homologous row to a maximum upward shift of $\Delta E_L = 0.38$ eV for [SCN]. As stated in the literature, the varying dipole moment was mentioned to be the cause of this observation. In contrast, our

studies reveal no such trend. Neither the total dipole moment nor the z-component show a correlation with the energetic shift of the DOS, see Figure 3.25(a). In theory, it is true that $[N(CN)_2]$ has a larger dipole moment than the symmetric $[B(CN)_4]$ anion, but this only holds true for the optimum gas phase geometry. Adsorbed on the surface, due to strong polarization and conformational changes, the dipole moment is strongly altered in comparison to the ideal gas phase structure. If, however, the charge transfer is considered (see Figure 3.26(a)), a consistently increasing negative charge on TiO_2 is found along the homologous row, showing a clear correlation with the conduction band edge. This is also consistent with the earlier made statement that the band energy level should increase upon addition of electron density.

Halide Ionic Liquids. Different halides were investigated, namely chloride, bromide, and iodide with the same cation $[C_2C_1Im]$. Additionally, the cation influence was evaluated by keeping the iodide anion, which will be discussed later. The three halide ILs, consisting of $[C_2C_1Im]$ with either [Cl], [Br], or [I] show only minor differences in the caused energetic shifts of TiO_2's DOS, ranging from the largest shift of $\Delta E_L = 0.39$ eV for [Cl] to $\Delta E_L = 0.30$ eV for [I]. These differences are neither captured by the dipole moments nor by the charge transfer. Whereas [Cl] and [Br] show an almost equivalent charge transfer, the adsorption of the iodide IL leads to a higher negative charge on TiO_2, which in principle should translate to a higher energetic upward shift. This discrepancy maybe arises from the employed van der Waals radii for the radical Voronoi tessellation, which does not describe the partition of the electron density well enough. However, differences in the energetic levels of the DOS are rather small within different halide ILs. In the context of all investigated imidazolium ILs, the halide imidazolium ILs account for the largest energetic upward shifts of the conduction band edge.

Fluorous Ionic Liquids. Fluorination of ionic liquids can have a huge impact on the IL's properties,[302,310,451–453] and many commonly used ILs contain fluorous moieties, mostly in the anion. In this study, the fluorous anions $[BF_4]$, $[PF_6]$, [FAP], [OTf], $[Tf_2N]$, and $[Pf_2N]$ were investigated alongside the $[C_2C_1Im]$ cation. This group of ILs was observed to have a huge impact on the conduction band edge shift. The majorly fluorinated anions $[BF_4]$, $[PF_6]$, and [FAP] cause a large energetic downward shift of the valance and conduction band edge in the order of -0.37 to -0.77 eV in combination with the imidazolium cation, see also Table 3.12. This is probably not explained by a strong interaction of the anion with the surface, but by the lack of it. On the one hand, the fluorous anions do interact with TiO_2 only weakly, also indicated by the comparably low interaction energies of the IL and the surface (Table 3.12). Thus, these anions are donating few to no electrons to the surface. On the other hand, the cation's adsorption is majorly unaffected by the anions, causing a positive net charge of the surface. This effect is also observed for the other three fluorous anions, although

less pronounced. Whereas [Pf_2N] still causes a minor energetic downward shift of $\Delta E_L = -0.17$ eV, the anions [OTf] and [Tf_2N] already show a slight energetic upward shift of E_L. The reason is probably that [OTf] and [Tf_2N] have fluorous moieties, but they are comparably small, and these anions have exposed nucleophilic coordination sites, causing a net charge transfer of ≈ -0.15 e.

Additionally, the fluorous moiety was introduced in the imidazolium's side chain, leading to the investigated fluoroalkylimidazolium ILs [$(C_F)_nC_2C_1Im$][I] ($n = 2, 4, 6$). As can be seen from Table 3.12, these ILs do behave very similar to their alkyl analogs in terms of affecting the DOS. This functionalization yields very high μ_z values, but the conduction band edge is largely unaffected, showing once more that there is probably no direct correlation between these two quantities. The fluorous cations and their alkyl analogs share the same imidazolium group, on which most of the positive charge is localized.[302] This charged group is most likely responsible for the major part of the charge transfer, and is unaffected by the side chain due to the commonly used ethylene spacer between the fluoroalkyl group and the imidazolium ring.

In addition, the aforementioned fluoroalkylimidazolium ILs were also calculated with the [BF_4] anion. A similar energetic downward shift of the conduction band edge as for [C_2C_1Im][BF_4] is expected, but not observed. E_L is only lowered by approximately 0.1 eV, which is much smaller than expected. Visual inspection of the adsorption geometries also reveals that in the case of the fluorinated cations, the [BF_4] anions adsorb much better. For the [C_2C_1Im][BF_4] IL, the geometry optimization yielded mostly weakly bound conformations of the anion. This is also in line with interaction energies E_{int} and CT, which are higher for the [$(C_F)_nC_2C_1Im$][BF_4] ILs than for [C_2C_1Im][BF_4], see also Table 3.12.

Increasing Alkyl Chain Length. The homologous series of [C_nC_1Im][I] and [C_nC_1Im] [$B(CN)_4$] with $n = 1, 2, 3, 4, 6$ was included in the study. For both series, the semiconductor's DOS is largely unaffected by the alkyl chain length. This is probably because of two reasons: Firstly, the main interaction site of the cation with the surface is the imidazolium ring, and in contrast to structural or dynamic properties of a bulk IL, the electronic structure of the imidazolium head group is largely unaffected by the alkyl chain length.[454] This effect was also observed for the fluorinated side chains in [$(C_F)_nC_2C_1Im$][I] ($n = 2, 4, 6$), *vide supra*. Secondly, the alkyl side chain interacts only weakly with the anion, which itself has a significant impact on the DOS. It is important to note that the increasing alkyl chain length increases also size and volume of the cation, which may affect the cation's surface concentration for the bulk IL/TiO_2 interface. In this case, the alkyl side chain length may translate into conduction band edge shifts, in contrast to the single ion pair calculations.

Basic Anions. Another selection of ILs studied are grouped according to their basic anions, including the $[C_2C_1Im]$ ILs with the anions [OAc], [TFA], $[NO_3]$, [DP], and $[EtSO_4]$. These anions, which are also well known as inorganic acids in their protonated form, share the motif of partially negatively charged oxygen atoms. These oxygen atoms are nucleophilic in general, are good hydrogen bond acceptors and have a tendency to strongly coordinate. Although the nucleophilicity is affected by the remaining functionalities in the anion, all were observed to coordinate the surface titanium atoms, causing a net charge transfer of $CT(\mathrm{v_{calc}})$=−0.3 to −0.4 e. The resulting conduction band edge shifts amounts to $\Delta E_\mathrm{L} = 0.15$ eV for $[C_2C_1Im]$[DP] as the lowest and $\Delta E_\mathrm{L} = 0.34$ eV for $[C_2C_1Im]$[OAc] as the highest. Internally, *e.g.*, ΔE_L is lower for [TFA] than for [OAc], which is in line with a smaller CT for [TFA]. This is physically sound because of the electron withdrawing effect of the -$(CF)_3$ group, reducing the nucleophilicity and negative charge on the coordinating oxygen atoms. Overall, this class of ILs, or anions, is on the top end in terms of CT and upward conduction band edge shift, compared to all investigated ILs.

Alkylammonium, Pyrrolidinium, and Pyridinium Ionic Liquids. The alkylammonium ILs $[N_{nnnn}]$[I] ($n = 1, 2, 4$) and $[N_{4111}]$[I] were investigated as adsorbates in this study. Compared to other cations, this group of ILs accounts for the largest energetic upward shift of the conduction band edge with a maximal value of $\Delta E_\mathrm{L} = 0.47$ eV for $[N_{4444}]$[I]. This is most probably caused by the very good screening of the ammonium's positive charge by the alkyl chains, effectively prohibiting charge transfer from the surface to the cation. With decreasing chain length, the screening is diminished, the charge transfer less hindered, and ΔE_L consequently decreases (see Figure 3.26(b)). Additionally, there seems to be a good correlation between μ_z and ΔE_L within the group of alkylammonium ILs, see Figure 3.25(b), as both quantities increase collectively. Maybe the dipole moment is a good descriptor in this case because of the lack of specific directed coordinative interactions.

Moreover, the pyrrolidinium IL $[C_4C_1Pyrr]$[I] might be approximated as a rigid $[N_{4221}]$[I] ammonium IL. As such, the calculated CT is similar to $[N_{4111}]$, but ΔE_L is smaller. This is probably due to the more exposed central nitrogen atom in the case of the strained pyrrolidinium ring, allowing for a higher Coulombic interaction with the surface.

Taking the transformation further, the pyridinium ILs $[C_2Py]$[I] and $[C_4Py]$[I] were investigated. Due to the plain ring and only one alkyl substituent, the nitrogen atom is more accessible. Furthermore, the aromatic ring, delocalizing the charge, is very similar to the imidazolium ring. Thus, it is not surprising that the pyridinium ILs show a smaller net charge transfer than the ammonium ILs (except for $[N_{1111}]$[I]) and the pyrrolidinium IL, and a conduction band edge shift similar to the alkylimidazolium ILs is observed.

Miscellaneous Ionic Liquids. Further derivatives of the archetypical imidazolium cation were investigated, namely the ILs [AllylC_1Im][I] and [$C_2C_1C_1$Im][I]. The allyl functionalization causes a smaller conduction band edge shift compared to the other alkylimidazolium cations, and the C2 methylation causes a slightly larger conduction band edge shift. In the latter case, this is probably due to the disabled H2-O_{2c} interaction, which is a significant interaction pattern of imidazolium ionic liquids with the anatase (101) surface.[262,263] However, the magnitude of deviation of ΔE_L from the alkylimidazolium cation is still comparably small.

The IL [Guan][I] contains the guanidinium cation, which, on the one hand, is protic with relatively strong electrophilic -(NH_2) groups. On the other hand, compared to the other cations, the protic character caused a hydrogen atom abstraction during the geometry optimization in two of ten cases, leading to a new O_{2c}-H bond and a neutral guanidine. Furthermore, the strong electrophilic character caused strong coordination at the surface oxygen atoms, leading by far to the smallest values of ΔE_L compared to the other iodide ILs. This is not reflected by the charge transfer, but is most likely a drawback of the charge transfer evaluation. The radical Voronoi tessellation uses static radii, in this case the van der Waals radii, as they are very well suited to describe physical adsorption. However, in the case of guanidinium where the interaction has a high covalent character, van der Waals radii fail to distribute the electron density correctly, leading to a bad description of the charge transfer. Utilization of covalent radii for these specific chemisorbed cases should account for a better description of the situation.

Comparison to Experimental Data. Experimental data on pure ILs in DSCs are rare, because mixtures of different ILs with a lowered viscosity are used usually. Furthermore, different dyes, electrode coatings, device geometries, or redox mediators are used in different studies, which have a significant impact on the properties. Nonetheless, properties derived for different ILs within a constant setup of a study can be compared.

Fredin *et al.* investigated a series of binary IL mixtures with cation [C_4C_1Im] and the anions [I], [BF_4], [SCN], [TFA], and [OTf].[166] Under 1000 W m^{-2} and 250 W m^{-2} illumination, the [SCN] IL was observed to yield the highest open circuit voltage V_{OC}, [TFA] and [I] yielded lower values, and the lowest values were observed for the [BF_4] and [OTf] ILs. This finding is exactly in line with the calculated valence and conduction band edge shifts. It should be stressed again that the correlation of open circuit voltage and theoretically derived band shifts was demonstrated before.[356,357]

In 2002, Kubo *et al.* conducted a systematic study on the alkylimidazolium ILs [C_nC_1Im][I] ($n = 3 - 9$).[443] Increasing values of J_{SC} and V_{OC} were observed with increasing chain length up to $n = 7$. This was attributed to the increased diffusion coefficient of the injected electron in the TiO_2 electrode caused by a multi layer ab-

sorption of the IL cations. The increasing values of V_{OC} do not match our calculations on first sight, which predict steady values of E_L. This discrepancy follows probably from the calculation of single ion pairs on the surface, whereas there is the bulk IL in the DSC. Regarding the increasing size of the cations with increasing chain length, the surface concentration of imidazolium probably decreases with increasing chain length, which would explain the increasing values of V_{OC}.

In a work of Abate *et al.* the ILs $[C_4C_1Im][I]$ and $[(C_F)_4C_2C_1Im][I]$ were used in electrolyte mixtures and compared when used in a DSC.[444] Both ILs gave close values of V_{OC}, with a slightly higher for $[C_4C_1Im][I]$. J_{SC} and the device efficency η was significantly increased upon the use of $[(C_F)_4C_2C_1Im][I]$, which was mainly attributed to the higher diffusion coefficient of the triiodide redox mediator in the bulk IL and the formation of an imidazolium cation layer at the surface. This cation layer is hindering the approach of I^-/I_3^-, and thus, back electron transfer from TiO_2 to the redox pair.

The use of quaternary ammonium iodide ILs of the form $R_2R'_2$ (R=CH_3, C_2H_5, R'=C_5H_{11}, C_6H_{13}) was described by Santa-Nokki *et al.*[448] Main differences in cell performance were attributed to electrolyte viscosity and could be correlated to the cation's alkyl chain length. Reported values of V_{OC} for the cations are: $[N_{5511}]$ 0.55 V, $[N_{5522}]$ 0.61 V, $[N_{6611}]$ 0.60 V, $[N_{6622}]$ 0.62 V. The correlation of V_{OC} and the cation's alkyl chain length is clearly visible: the open circuit voltage increases upon increasing chain length, which is perfectly in line with the calculated values of ΔE_L.

3.4.4 Conclusion

The influence of ionic liquid adsorption on the density of states of the adsorbent TiO_2 was examined. Most of the investigated ionic liquids caused an energetic upward shift of the valence and conduction band edge, simultaneously decreasing the band gap. The energetic shift of the states could be attributed to the amount of charge transferred from the IL to the surface or vice versa. If electron density is transferred to the surface, which is mostly induced by the anion, then the states of TiO_2 experience an energetic upward shift. If, however, electron density is transferred from the surface to the IL, preferably to the cation, then the decreased remaining electron density on the surface accounts for an energetic downward shift. Obviously, both effects take place simultaneously and counteract each other. The identity of the IL then ultimately decides about the net charge transfer and the resulting total shift of the DOS.

Coordinating anions such as the nitrile composed anions, the halides, and the weak basic anions caused an overall energetic upward shift in combination with the $[C_2C_1Im]$ cation. In this context, the highest energetic upward shift was calculated for $[C_2C_1Im]$ [Cl]. The imidazolium ILs with fluorinated anions were observed to account for energetic downward shifts of the DOS, which could be attributed to the lack of interaction and, thus, charge transfer between anion and surface, leaving the cation effect dominant. The largest energetic downward shift could be attributed to $[C_2C_1Im][PF_6]$.

The cation's alkyl chain length was observed to have little to no influence on the DOS. As the alkyl chain length is known to influence bulk IL structural and dynamic properties, this could be utilized to tune specific IL properties by simultaneously keeping the electronic interaction with the surface constant.

Overall, only a small cation influence was observed, compared to the huge span in different shifts for different anions. Worth mentioning here are the alkylammonium ILs, which are linked to the largest energetic upward shifts due to the very good screening of the cations positive charge. Consequently, if the design of an IL is aimed to achieve the maximum energetic upward shift of the DOS, it should consist of a cation with a maximally delocalized or screened positive charge, and the interaction with the surface should be minimal. However, the anion should interact strongly with the surface, donating as much electron density as possible.

On the contrary, the guanidinium cation was found to interact very strongly with the surface, causing a large transfer from the surface to the cation, lowering the DOS energies.

The presented results may help experimentalists and engineers to decide for a certain IL as solvent for a given DSC setup. The IL can be changed systematically to increase or decrease the band edge positions in order to match the band levels appropriately. Thus, the highest performance can be achieved by keeping other cell parameters such as the employed dye constant. Additionally, if the band levels are aligned satisfactory, different ionic liquids which presumably yield similar band shifts can be employed in order to improve other aspects of the solar cell, such as compatibility of the electrolyte with dye and redox mediator or the cell sealing material, minimizing the light absorption of the electrolyte or improve diffusion of the redox mediator and other additives.

Supporting Information

The supporting information contains all full names of the abbreviated ILs and comparison of full core and pseudopotential calculations with iodide and is attached in Section A.4.

Acknowledgments

This work was financially supported by the DFG project KI-768/12-1 'Materialsynthese nahe Raumtemperatur' and the SFB 813 'Chemie an Spinzentren: Konzepte, Mechanismen, Funktionen'. The support for H.W. by the Fonds der Chemischen Industrie (FCI) is gratefully acknowledged. Valuable scientific input of Thomas Bredow is greatly appreciated.

3.5 Ionic Liquid Influence on Excitation of Promising Dyes for Dye-Sensitized Solar Cells

Henry Weber,[†] Christoph Bannwarth,[†] Stefan Grimme,[†] and Barbara Kirchner[†]*

Manuscript in preparation.

Contributions to the manuscript:

- Setup and maintenance of all calculations concerning cluster geometries and excitation spectra.
- Analysis and evaluation of all results.
- Writing of the manuscript.

[†]Mulliken Center for Theoretical Chemistry, Universität Bonn, Beringstr. 4+6, D-53115 Bonn, Germany.
*Corresponding Author E-mail: kirchner@thch.uni-bonn.de.

Abstract

Dye-sensitized solar cells have the potential to become a competitive renewable source of energy, but constant investigation and development is necessary to improve this technology. A crucial part in a complete device is the dye–electrolyte interface, where the essential dye regeneration takes place. In this work, we investigate the electrolyte–dye interface of 4 dyes and 3 ionic liquids, focusing mainly on the excitation spectra of the dye. The main findings are that the excitation spectra are generally expected to redshift when ionic liquids are used as electrolytes with respect to organic solvents, due to the dielectric effect. Additionally, specific interactions of basic anions such as dicyanamide and thiocyanate coordinating suitable dye acceptor sites or forming hydrogen bonds account for further modifications of the spectra. These findings will help to understand the role and implications of using a certain electrolyte, specifically ionic liquids as electrolytes in dye-sensitized solar cells or other electrochemical devices.

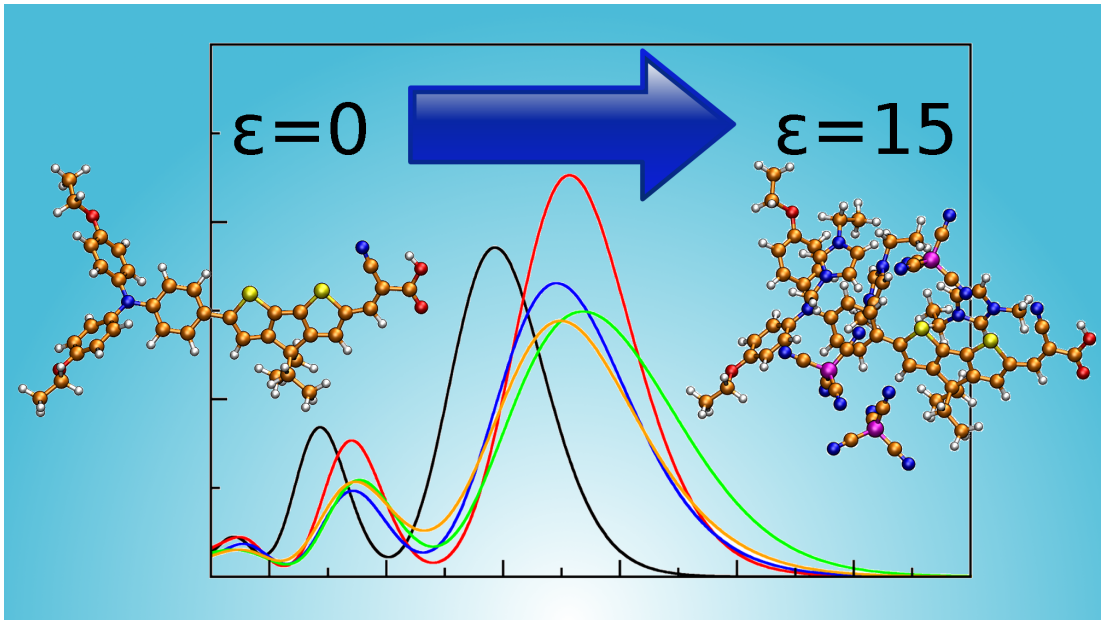

3.5.1 Introduction

The society's urge for new and improved energy harvesting devices is ongoing. Especially renewable energy sources are in the focus of attention, as the demand for a green and sustainable energy market remains very high. Among possible solutions, dye-sensitized solar cells (DSCs) have emerged as a promising technology to harvest sunlight in a very favorable way.[424]

During the past decades, many drawbacks of this technology could be resolved.[418] The initially very small light harvesting efficiency could be drastically increased upon utilization of nano-sized TiO_2 particles with an immensely increased active, dye-covered surface.[13] Potentially toxic, expensive, and rare transition metal dyes like the famous ruthenium dyes **N3** or **N749** are slowly challenged by environmentally friendly, non-toxic, and widely available organic dyes such as porphyrin,[37,116,455] indoline,[43] coumarin,[44] triarylamine,[39,51–53] and many others with a huge variety of customization options.[85]

However, up to now, no unified ansatz to tackle the problem of low long-term stabilities of complete devices is found. It arises due to leakage, evaporation, photodegradation, and thermal degradation of the volatile electrolytes used.[85,185,423] Approaches employing solid state electrolytes involve inorganic p-type semiconductors, organic hole conduction materials, most noteworthy spiro-MeOTAD,[114] and polymeric electrolytes.[54] While an increase of long-term stability was often achieved, problems such as a reduced cell performance were encountered regularly. Attention was given to ionic liquids (ILs) to overcome the aforementioned problems, as ILs exist that still provide a liquid, diffusive medium, but have superior properties compared to volatile organic solvents like very low volatility, high thermal and electrochemical stability, and thus can potentially provide a high long-term stability.[100] Consequently, a significant amount of scientific work appeared reporting good long term stabilities of IL-based DSCs, however, always at the cost of reduced cell efficiency with respect to the best performing volatile organic electrolytes.[100,133,165,169,339]

In a very detailed impedance and steady-state study, the main limitations in the application of IL electrolytes compared to organic solvent electrolytes could be summarized to be a higher recombination rate of charges in the semiconductor and a lower injection rate of charges from the excited dye to the semiconductor's conduction band, causing lower open circuit photopotentials.[126] Reasons might be slower dye regeneration caused by diffusion limitations, an energetic shift of the conduction band position, and a larger diffusion resistance of the IL electrolyte.[126]

The three cyano based ionic liquids $[C_2C_1Im][B(CN)_4]$ (1-ethyl-3-methylimidazolium tetracyanoborate, [B]), $[C_2C_1Im][N(CN)_2]$ (1-ethyl-3-methylimidazolium dicyanamide, [N]), and $[C_2C_1Im][SCN]$ (1-ethyl-3-methylimidazolium thiocyanate, [S]) have been shown to be promising candidates for the use as electrolytes in DSCs.[119–121,126,160–166]

They fulfill the basic requirements such as relatively low viscosity, high stability and good solubility of the redox pair. Additionally, they can have further beneficial effects, such as an induced shift of the TiO_2's band edge positions. In this context, [B] and [N] were tested in an IL-electrolyte solar cell with the **C218** dye, and application of [B] was observed to yield a better performance than [N] because of a more favorable offset between dye and TiO_2 conduction band edge energy.[160] A very good efficiency of $\eta = 8.44$ % at AM 1.5 G was reported.[160]

In an attempt to create durable DSCs, the **GD2** dye was used in cells with different IL electrolyte mixtures, including the three cyano-based ILs [B], [N], and [S], and other imidazolium, ammonium, and phosphonium ionic liquids.[339] Employing [B] in the electrolyte mixture was measured to yield the highest device efficiency, [N] and [S] were observed to be inferior if **GD2** is chosen as the sensitizer. The varying performance is attributed to changes of the open circuit voltage V_{OC} and the short circuit current I_{SC}. Differences in V_{OC} are most likely linked to IL-TiO_2 interactions, shifting the band edge energies.[160,456] Changes of I_{SC} can be attributed to band edge energies of TiO_2. A decrease in I_{SC} also follows from slow diffusion of the I^-/I_3^- redox pair, mainly connected to the viscosity of the IL electrolyte.[339] Armel et al. pointed out, that [S] and [N] are highly hygroscopic and distinctly basic with respect to [B], which might cause different interactions with the dye.[339]

The ionic liquids [B] and [N] were also employed in DSCs using the ruthenium based dye **C106**.[161] For the tetracyanoborate cell, a beneficial faster electron injection from the dye into the conduction band of TiO_2 was observed, which could be traced to the notably lower titania band edge for the [B] cell. Concerning the dye–IL interaction, a shorter photoluminescence lifetime of the dye was observed for the tetracyanoborate electrolyte, but no notable differences could be observed in the absorption or emission spectra of the dye. The excellent long term durability and thermal stability of a $[C_2C_1Im][B(CN)_4]$ electrolyte based DSC was showcased by Grätzel et al., where a stable device performance of 7.0 % at AM 1.5 G was observed under accelerated thermal stress and light soaking for 1000 h at 60°C.[121]

From the literature and our own past studies, a deeper understanding of the electrolyte–semiconductor interactions could be gained, such as the molecular structure of ionic liquid adsorption or band level alignments of TiO_2.[160,161,262,263,456] Furthermore, implications of ionic liquid electrolyte properties such as viscosity on the mobility of the redox pair and other additives were elaborated in the literature as well.[124,163,169,457]

However, in this work, we aim to study the influence of the IL on the optical properties of the dye, as a deeper understanding of this crucial interface seems to be missing. The absorption spectrum of the employed dyes is of special interest, because absorption of the incident photon is a key step in the working cycle of the DSC. The calculation of accurate excited state properties is still a demanding task in computational chemistry, but there are many versatile tools to choose from. Notably, time-dependent DFT (TD-

DFT)[188–191] has proven to consistently outperform computationally cheaper methods such as ZINDO/S[458,459] while being considerably less computationally expensive than electron-correlated wavefunction approaches such as CAS-PT2,[460] MR-CI,[461] or SCS-CC2.[462,463] While the choice of the density functional is crucial, several studies suggest that the expected results are consistent with the Jacob's ladder,[464] which means the accuracy improves when going to more refined, and usually more expensive, functionals for exchange and correlation.[465–467] Therefore, the use of double-hybrid functionals is desirable if affordable, as demonstrated by Goerigk et al.[465] at the organic molecule benchmark set of Schreiber et al.[468] and at a test set of 12 organic dyes.[466] Among the rung of hybrid functionals, the PBE0 functional has been proven to provide reliable results, often outperforming similar-rung functionals like B3-LYP.[465,469] Long-range corrected functionals such as the ωB97X-D3[225] or the CAM-B3LYP[224] functional or global hybrid functionals with large amounts of Hartree–Fock exchange can be used to improve the quality of TD-DFT spectra, offering a better description, for example of charge transfer excitations.

Apart from the functional, another way to improve the quality of calculated excitation spectra is to account for the experimental matrix, *i.e.*, the solvent in most cases. A feasible approach to cover solvent effects are continuum models, which mimic the average interaction of a solvent based on their dielectric constant.[470] Usually, a bathochromic shift of the excitation spectrum is observed when the system is embedded in a dielectric. That is, because the excited state typically has a more polar character than the respective ground state and is therefore better stabilized in the dielectric, or polar solvent. Application of continuum models for the calculation of excited states properties have been shown to reproduce inhomogeneous broadening, to account for transition energy shifts, and to improve peak positions and optical line-shapes of calculated excitation spectra with respect to experiment.[471–476] Unfortunately, all continuum solvation models suffer from the lack of specific solute–solvent interactions, as they can obviously only be described with explicit solvation.[467,470]

Therefore, the energetics and excitation spectra obtained from sophisticated quantum chemical calculations of different classic and modern dyes are investigated under the influence of implicit and explicit IL solvation. This study aims to shed light on the fundamental interactions and influences of explicit IL solvation on characteristic dye properties. In the following sections, the computational details on the methods used and systems investigated are elaborated shortly. The influences of the IL solvent shell size, the sample size, and exchange-correlation functional dependence on an exemplary dye are investigated first. Secondly, a variety of IL–dye combinations is studied. The use of a pure continuum model and combination with explicit solvation is shown. Distinct interactions and their impact on the final excitation spectra are discussed. All important findings are summarized in the end of the article.

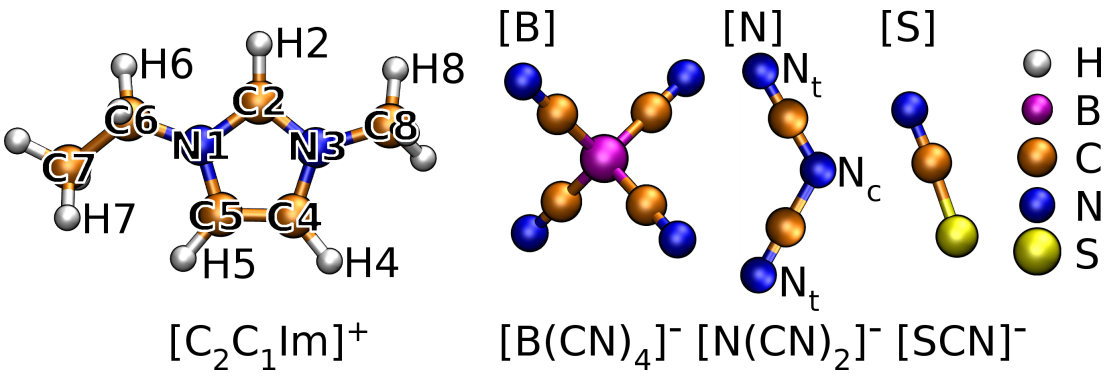

Figure 3.27: Labeling of the IL's components 1-ethyl-3-methylimidazolium $[C_2C_1Im]^+$, tetracyanoborate $[B(CN)_4]^-$, dicyanamide $[N(CN)_2]^-$, and thiocyanate $[SCN]^-$. [B], [N], and [S] denote the whole IL, respectively. All terminal anion nitrogen atoms are called N_t.

3.5.2 Computational Details

Two porphyrin based dyes **ZnTPP**[477] (Figure 3.30) and **GD2**[37] (Figure 3.32), the organic dye **C218s**[53] (**C218s** is the original dye **C218** with shortened alkyl chains, Figure 3.33), and the ruthenium based dye **N749**[32] (Figure 3.35), also known as black dye, were investigated together with three different ILs, the 1-ethyl-3-methylimidazolium tetracyanoborate IL ($[C_2C_1Im][B(CN)_4]$, [B]), the 1-ethyl-3-methylimidazolium dicyanamide IL ($[C_2C_1Im][N(CN)_2]$, [N]), and the 1-ethyl-3-methylimidazolium thiocyanate IL ($[C_2C_1Im][SCN]$, [S]), all shown in Figure 3.27.

Structure optimizations were performed with the TURBOMOLE V7.0 program package[478] at the DFT level with the B-LYP[214,215] functional and the def-TZVP basis sets.[479] An effective core potential was used in the case of ruthenium.[480] It was shown, that the use of pseudopotentials for the metal atoms in transition metal complexes has little influence on the UV/VIS excitation properties.[469] The D3 dispersion correction[230] with Becke–Johnson damping was employed.[347]

All TD-DFT calculations were run with the PBE0[216,217,222] hybrid functional employing the TURBOMOLE V7.0 program package. The required ground state electronic structure was also derived with the PBE0 functional and tight convergence of the SCF energy of 10^{-8} Hartree on a $m4$ grid. The PBE0 functional was shown to yield transition properties obtained with TD-DFT in good agreement with experiments, comparable to post-Hartree–Fock methods.[469] Furthermore, the PBE0 functional provided excellent results in a study of solvated dyes with respect to other hybrid functionals like M06, M06-2X, B3LYP and CAM-B3LYP.[467] In each case, the first 50 singlet excitations have been calculated. Vertical excitation energies are used throughout the present work, as corrections that involve the optimized excited state geometries are computationally too expensive at this level of theory, given the huge dimensions of the dyes plus the explicit solvent shell. Derived oscillator spectra were broadened with Gaussian functions of 0.2 eV half width at e^{-1} maximum in the energy regime.

Additionally, sTD-DFT calculations were performed as described in the References 237,242,481 on the basis of PBE0, CAM-B3LYP,[224] and ωB97X-D3[225] ground state wavefunctions with very tight convergence of the SCF energy of 10^{-8} Hartree. The CAM-B3LYP and ωB97X-D3 calculations were performed with the ORCA program package and the def2-TZVP basis set.[482]

The density of states (DOS) was evaluated from the PBE0 molecular orbital energies, which were broadened by Gaussian functions of 1 eV full width at half maximum. A continuous embedding of the molecules and clusters via the conductor-like screening model (COSMO) was achieved with the COSMO package,[483] which is available in the TURBOMOLE and ORCA program packages. Parameters of $\varepsilon = 15$[159] and $rsolv = 1.3$ were used together with tabulated default radii. The COSMO embedding was used for all conformations with explicit solvation.

Configurations for the large solvent shell studies in Section 3.5.3.1 were taken from *ab initio* molecular dynamics via a cluster ansatz.[484,485] The molecular dynamics simulations were performed with the CP2K program package[286] employing the QUICKSTEP[287] module. The B-LYP functional[214,215] with D3 dispersion correction (zero-damping)[230] was used with Godecker-Teter-Hutter (GTH)[292,293] pseudopotentials and the MOLOPT-DZVP-SR-GTH basis sets.[291] 30 ps of a constant N, V, T simulation at $T = 398$ K employing Nosé–Hoover chain thermostats[297,299,486] were produced including 2.5 ps of massive preequilibration and 7.5 ps of global equilibration. The total simulation cell consists of one **GD2** dye molecule and 32 ion pairs (IPs) of $[C_2C_1Im][B(CN)_4]$. From the 20 ps production run, snapshots were taken equally distributed over the course of the simulation, and the solvent shell cluster was extracted by the nearest distance between the dye and the ions based on their respective center of masses. Additionally, explicit solvation of the polar groups independent of the center of mass is indicated by an asterisk symbol. Energies and spectra presented in Section 3.5.3.1 are averaged over all calculated values.

Conformations of the solvated dyes in Section 3.5.3.3 to Section 3.5.3.6 were obtained by geometry optimization of different randomized starting geometries. The starting geometries were generated by densely packing the ionic liquid ions around the dye with the aid of the PACKMOL program package[411] with a tolerance radius of 300 pm. For each combination of IL–dye cluster, 5 different configurations were optimized and averaged results are presented. In the case of **GD2**, solvation of the malonic acid group apart from the molecule's center of mass was enforced.

The calculated spectra of each configuration were weighted according to their respective Boltzmann-factor p_i at temperature $T = 298$ K:

$$p_i = \frac{e^{(-\Delta G_i/kT)}}{\sum_i e^{(-\Delta G_i/kT)}}. \tag{3.5.1}$$

The free energies G_i of each structure i were computed following the multilevel protocol presented in Ref. 487.

$$G_i = E_i^{el.} + G_i^{rovib.} + \delta G_i^{solv.} \tag{3.5.2}$$

To obtain $E_i^{el.}$, the optimized geometries (BLYP-D3(BJ)/def-TZVP+COSMO) were used for single point calculation energies at the PW6B96-D3(BJ)/def2-QZVP [480,488,489] level. On a large test set,[490] this global hybrid functional performed particularly well for thermochemistry and non-covalent interactions. The free energy contribution to the free energy due to solvation $\delta G_i^{solv.}$ is treated with the COSMO-RS approach [483,491,492] (2012 parameterization, based on BP86/TZVP [214,479,493] single point calculations). The respective ionic liquid solution is described as a 1:1 mixture of cation and anion.

Rovibrational contributions to the free energy $G_i^{rovib.}$ are calculated based on harmonic frequencies obtained at the HF-3c [494]+COSMO($\epsilon = 15$) level. The latter were computed with the SNF program [495] on re-optimized geometries. If present, imaginary frequencies (at most, $i\omega > -50\,\mathrm{cm}^{-1}$) were neglected.

Frequencies $< 100\,\mathrm{cm}^{-1}$ are treated as mixed rigid-rotor/harmonic-oscillator as described in Ref. 487. The TURBOMOLE suite of programs (version 7.0.2) [478] was used in the calculations mentioned above employing the resolution-of-the-identity [496,497] approximation along with matching auxiliary basis sets.[498,499]

3.5.3 Results and Discussion

3.5.3.1 Solvent Shell Size

In order to study the impact of the solvent shell size, we simulated the largest of the four dyes, **GD2**, with *ab initio* molecular dynamics in the $[C_2C_1Im][B(CN)_4]$ IL (see Figure 3.32 for the dye and Figure 3.27 for the IL). From the trajectory, 10 clusters of **GD2**, each with $n = 0, 1, 3, 6, 10$ and 20 ion pairs composing the solvent shell were extracted. Unfortunately, traditional TD-DFT with the PBE0 hybrid functional is computationally very expensive with regard to the largest clusters and therefore, we decided to calculate the excitation spectra with the computationally less demanding sTD-DFT technique.[237,242] A comparison of sTD-DFT and TD-DFT spectra with different exchange-correlation functionals will follow later, but for now we focus on the influence of the solvent shell size. Besides, apart from a total shift of excitation energies, similar spectra for TD-DFT and sTD-DFT calculations were already reported in the original works.[242,481,500]

In a previous work,[501] the solvent shell size of water solvating alanine was investigated. The conclusions have been that a cluster ansatz including two solvent shells around the polar groups and one solvent shell around the aliphatic group was enough to account for 98 % of permanent dipole moment in the bulk environment. Additionally,

Table 3.14: Influence of Solvation with n $[C_2C_1Im][B(CN)_4]$ Ion Pairs on the Ground State HOMO Energy E_H, LUMO Energy E_L and Band Gap Δ of **GD2**[a]

n	E_H / eV	E_L / eV	Δ / eV
0	-5.61 ± 0.07	-3.16 ± 0.25	2.45 ± 0.26
1	-5.57 ± 0.11	-3.17 ± 0.23	2.40 ± 0.26
3	-5.75 ± 0.11	-3.27 ± 0.21	2.48 ± 0.28
6	-5.77 ± 0.12	-3.30 ± 0.22	2.47 ± 0.29
10	-5.77 ± 0.14	-3.28 ± 0.22	2.49 ± 0.29
20	-5.81 ± 0.12	-3.44 ± 0.24	2.37 ± 0.30
6*	-5.71 ± 0.13	-3.30 ± 0.26	2.40 ± 0.28

[a]Values are averaged over 10 configurations for each solvent shell size.

a conductor-like screening model shows similar effects as one additional solvent shell, which means that explicit solvation of the crucial functional groups with simultaneous application of a continuous embedding should lead to better results than neglecting it. Therefore, the COSMO embedding was applied on top of the explicit IL solvation at all times in this work.

The influence of the solvent shell size on the energetics of **GD2** is shown in Table 3.14. It can be seen that the HOMO and LUMO energies are decreasing with increasing solvent shell size, and the band gap Δ is slightly increasing with respect to plain COSMO solvation, except for $n = 20$ and $n = 6^*$. The HOMO energy E_H and LUMO energy E_L of conformations including one solvating IP show major deviations with respect to higher numbers of IPs. With an increasing number of IPs, the resulting energetics do not differ strongly between $3, 6$ and 10 IPs, as the values seem to reach convergence. Interestingly, going from $n = 10$ to 20, a significant gap is observed, especially for E_L and Δ. Considering the molecular structure of **GD2** (Figure 3.32), the butadienemalonic acid group extends far from the molecule's center of mass, which is why this group is not solvated until the 20 ion pair solvent shell. The LUMO is mainly located at this part of the molecule, ensuring a high electron injection rate to the semiconductor in a DSC. This probably explains the discrepancy between $n = 10$ and 20 IP solvation, where E_H seems to be unaffected whereas there is a significant impact on the LUMO energy E_L, and the small band gap follows as a consequence. Therefore, a smart solvation including the explicit solvation of the crucial functional groups of **GD2**, *i.e.*, the central Zn atom, and the malonic acid group, are explicitly solvated with $n = 6^*$ ion pairs (smart solvation indicated with asterisk symbol). Applying this model, E_H and E_L are observed to be higher than in the $n = 20$ case, but the band gap Δ is reproduced very well. As can been from the standard deviations, the HOMO and LUMO levels are not only affected by solvation, but also by the molecules geometry ($n = 0$). The magnitude of the standard deviations does not change very much with the solvent shell size, but the actual HOMO and LUMO levels change, which suggests that the solvation has a very uniform and systematic influence on the energy levels. Furthermore, the overall higher standard deviations of E_L compared

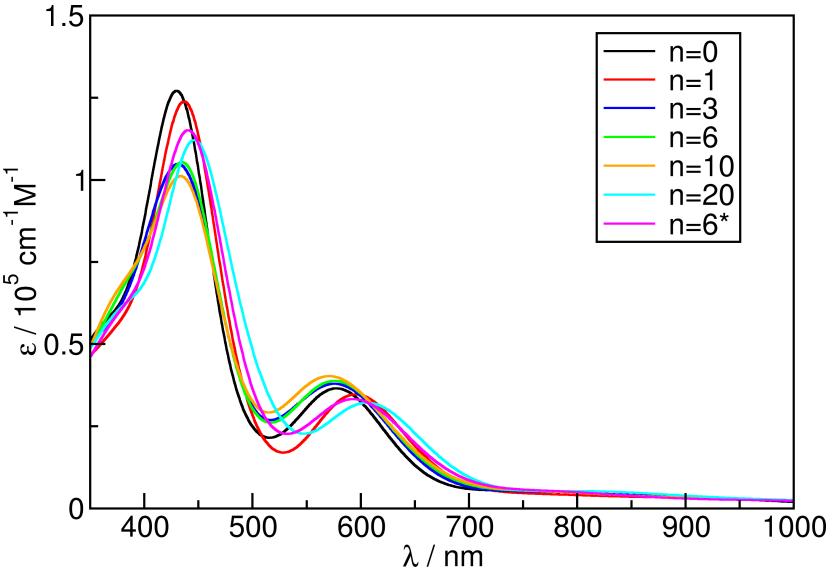

Figure 3.28: Averaged PBE0 sTD-DFT spectra of **GD2** with COSMO model and $[C_2C_1Im][B(CN)_4]$. The number of solvating ion pairs n is varied. Standard (center of mass) solvation of **GD2** is used, except for the $n = 6^*$ (smart solvation), which denotes simultaneous solvation of Zn and the malonic acid group.

to those of E_H show that the LUMO level is more sensitive to changes of solvation and molecular geometry. In order to include as many large solvent shell influences as possible even for smaller numbers of n, special attention should be paid to the solvation of the malonic acid antenna in particular, and to crucial functional groups in general, as already pointed out by Thar et al.[501]

Concerning the spectral properties of **GD2** with respect to the solvent shell size, the respective excitation spectra calculated with sTD-DFT using the PBE0 functional are shown in Figure 3.28. The calculated excitation spectrum of **GD2** with only COSMO embedding ($n = 0$, black line) is slightly broadened and dispersed upon explicit solvation. This effect appears to be pronounced for high wavelengths, *i.e.*, low energy excitations in the visible and near infrared region. The broadening is usually accompanied by a decrease in intensity resulting from the averaging of different spectra. Additionally, approximation of a large solvent shell can be improved by smart solvation ($n = 6^*$), which means including the solvation of functional groups crucial for the excitation spectra, or every other property of interest. However, the size of the solvent shell seems to only have a minor impact on the excitation spectra, and most of the large solvent shell features are already covered by the solvent shell of $n = 3$ IPs. Therefore, a solvent shell size of $n = 3^*$, being an efficient tradeoff between accuracy and computational effort, is used for the upcoming calculations of the solvated dyes.

On the other hand, the number of snapshots and choice of the exchange–correlation functional seems to have a far more crucial effect on the excitation spectra, see Figure 3.29. In the left panel of Figure 3.29, the number of snapshots m is varied from $m = 5, 10, 25$ to $m = 50$. It can can be seen that the spectrum is smoothed the more

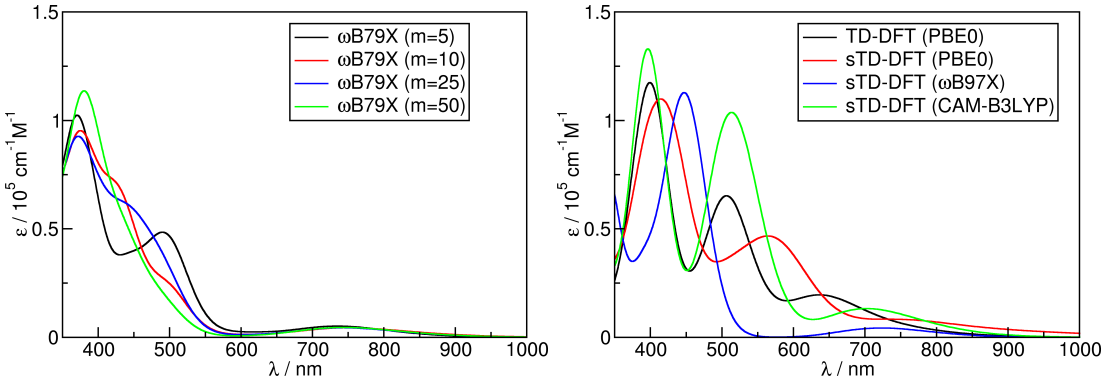

Figure 3.29: Influence of the number of snapshots m and choice of the functional on sTD-DFT spectra in the left panel and comparison between TD-DFT and sTD-DFT spectra in the right panel. Shown are averaged spectra of **GD2** with COSMO model and $[C_2C_1Im][B(CN)_4]$. The number of solvating ion pairs is $n = 6^*$ in the left panel, and $n = 3^*$ in the right panel.

configurations are included. Distinct features, such as the excitation at $\lambda = 500$ nm, are reduced to a broad shoulder of the main excitation in the case of $m = 50$. It can be concluded, that most of the important features are most probably included even for a small number of configurations, but the relative intensity ratios between main absorptions and configuration-dependent features converges slowly. Observing the right panel of Figure 3.29, sTD-DFT spectra calculated with the functionals PBE0, ωB97X-D3, and CAM-B3LYP are compared against the significantly more expensive PBE0 TD-DFT calculation. It can be seen, that the sTD-DFT calculation with the PBE0 functional is redshifted with respect to the TD-DFT calculation, which becomes more pronounced for higher wavelengths. Application of the CAM-B3LYP functional in combination with the efficient sTD-DFT technique however does reproduce peak positions and approximate intensity ratio of the two high-intensity absorptions at $\lambda = 400$ and $\lambda = 520$. Employing the ωB97X-D3 functional, the dominant feature at $\lambda = 500 - 550$ nm is not reproduced. However, the experimental absorption spectrum of **GD2** is characterized by an intense band $\lambda \approx 450$ nm, and a low-intensity tail at higher wavelengths. The ωB97X-D3 functional gives the best result with respect to the experimental spectrum. Therefore, we suggest to use the sTD-DFT technique in combination with the ωB97X-D3 functional for the best reproduction of experimental spectra and investigation of solvated dyes, or the more expensive TD-DFT spectra in special cases where a further characterization is needed.

3.5.3.2 Energetics

Considering now different dye–IL combinations, the dyes **ZnTPP** (Figure 3.30), **GD2** (Figure 3.32), **C218** (Figure 3.33), and **N749** (Figure 3.35) are investigated under the influence of the ILs [B], [N], and [S], respectively. In order to study the IL solvation effect on the dyes, each dye molecule was investigated in the gas phase, with the COSMO

Table 3.15: Ground State HOMO Energy E_H, LUMO Energy E_L and Band Gap Δ for the Dye Molecules in All Systems Investigated and Average Difference Between COSMO and Ionic Liquid Calculations[a]

dye	vacuum	COSMO	$[C_2C_1Im][B(CN)_4]$	$[C_2C_1Im][N(CN)_2]$	$[C_2C_1Im][SCN]$
			E_H / eV		
ZnTPP	-5.47	-5.63	-5.74	-5.58	-5.58
GD2	-5.44	-5.57	-5.62	-5.53	-5.62
C218s	-5.30	-5.26	-5.34	-5.32	-5.30
N749	–	-5.50	-5.78	-5.87	-5.76
difference(COSMO–IL)			-0.13	-0.09	-0.08
			E_L / eV		
ZnTPP	-2.44	-2.64	-2.82	-2.75	-2.73
GD2	-2.80	-3.00	-3.33	-3.05	-3.21
C218s	-2.91	-3.05	-3.09	-3.15	-3.04
N749	–	-3.05	-3.36	-3.37	-3.39
difference(COSMO–IL)			-0.21	-0.14	-0.16
			Δ / eV		
ZnTPP	3.02	2.99	2.92	2.83	2.85
GD2	2.64	2.57	2.30	2.48	2.41
C218s	2.39	2.20	2.25	2.17	2.26
N749	–	2.45	2.43	2.50	2.37
difference(COSMO–IL)			-0.08	-0.06	-0.08

[a]Obtained with the PBE0 functional. Averaged values for systems with explicit solvation.

embedding, and with an explicit IL solvation shell consisting of 3 ion pairs and additional COSMO embedding. For each setup, a geometry optimization was performed and the electronic excitation spectra were calculated at the optimum structure. At least 5 different solvation configurations were optimized for every IL-dye combination, and averaged results are presented. Therefore, the conformations of **GD2** differ from those obtained by AIMD, evaluated in the previous section. Note, that the sampled conformations of **GD2** include explicit solvation of the malonic acid group, as this pattern was found to be crucial for the excitation spectra and energetics.

An overview of selected ground state electronic properties of the systems obtained with the PBE0 functional is given in Table 3.15. Compared to results from calculations with the ωB97X-D3 functional (see supporting information), values, trends, and differences are in qualitative agreement. Therefore, only the results obtained with the PBE0 functional are discussed. It can be seen that the HOMO energies E_H of all dye molecules in vacuum are in the range of ≈ -5.4 eV. When the COSMO model is applied, lower values of E_H are observed for **ZnTPP** and **GD2**, whereas the **C218s** HOMO energy remains unaffected. Explicit solvation of the dye molecules does account for a further lowering of HOMO energies in most cases. An overall lowering of the electronic energy is most likely accomplished by donation of electron density from the dye to the IPs, the suitable acceptor is generally the electron-poor cation. As observed in the case of band level shifts of TiO_2, the anion counteracts this behavior by donating electron density to the dye. For the three investigated ILs, $[B(CN)_4]^-$ is considered weakly coordinating and thus weakly donating, whereas $[N(CN)_2]^-$ as well as $[SCN]^-$ are capable of strong

coordination and electron donation.[502] Hence, on average, observed E_H values are lower in the case of [B] (≈ -0.13 eV versus COSMO energies) solvation, with respect to [N] (≈ -0.09 eV versus COSMO energies) and [S] (≈ -0.08 eV versus COSMO energies) solvation. Differences for the latter both may arise due to specific, directed interactions, which will be discussed in detail later on. Additionally, the observed band shifts are larger for the ruthenium dye **N749** than for the organic dyes.

Turning now to LUMO energies E_L, lower values are observed if the COSMO model is applied with respect to the vacuum calculations (≈ -0.18 eV), in line with lowered E_H values. A further decrease is observed for explicit solvation with [B] (≈ -0.21 eV versus COSMO energies), [N] (≈ -0.14 eV) or [S] (≈ -0.16 eV). A more pronounced effect of IL solvation on the LUMO energies leads to a universal lowering of the dye's band gaps Δ, which amounts overall to ≈ -0.1 eV. The global lowering of the dye's band gaps is expected to cause a redshift in the excitation spectra, which will be discussed in detail and separately for each dye later.

In order to gain more general insight into the electronic structure of the investigated systems, the density of states (DOS) of the frontier orbital region of all compounds was evaluated (see supporting information for graphic representation). It can be seen that the frontier orbital energies are mostly governed by the dye's molecular orbitals, especially from **C218s** and **N749**, as they are the most refined dyes. Further on, the $[SCN]^-$ and $[N(CN)_2]^-$ anions do have occupied states in the frontier region, which possibly interact with the dye's electronic system. The $[B(CN)_4]^-$ anion as well as the imidazolium cation have no notable DOS in the frontier region of -5 to -7 eV.

3.5.3.3 ZnTPP

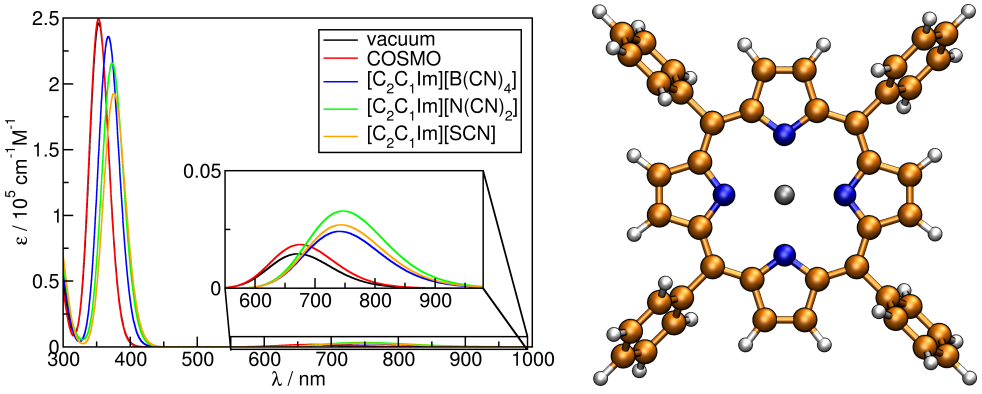

Figure 3.30: Broadened sTD-DFT spectra of **ZnTPP** obtained with the ωB97X-D3 functional with and without implicit and explicit solvation. Boltzmann-weighted spectra in case of IL solvation. **ZnTPP** as ball-and-stick model on the right side, the color coding is H=white, C=orange, N=blue, Zn=gray.

The structure and excitation spectra in vacuum, with implicit, and with explicit solvation of the prototypical porphyrin dye **ZnTPP** are shown in Figure 3.30. The

photoactive part of **ZnTPP** is the extended π system, and so almost all relevant excitations in **ZnTPP** are of $\pi \rightarrow \pi^*$ nature. The experimental spectrum of **ZnTPP** consists of a very high intensity B, or Soret, band around 400 nm, and less intense Q, or α and β, bands between 500 nm and 600 nm.[477] These experimental features are reproduced by the calculated spectra, only the Q bands occur at higher wavelengths in the computed spectra. In the specific case of metalloporphyrins, nucleophile species are able to coordinate the central Zn atom. These axial ligands are known to induce a redshift in the electronic excitation spectra, and change the intensity ratio of the α and β bands.[477]

Comparing the **ZnTPP** vacuum and COSMO spectra, only a minor increase of the Q band intensity in the COSMO spectrum is apparent. However, a significant redshift of the vacuum/COSMO excitation spectra of **ZnTPP** can be observed with respect to explicit solvation in Figure 3.30. Introduction of the explicit IL solvation accounts for a redshift of the most intense B band of ≈ 15 nm in the case of $[C_2C_1Im][B(CN)_4]$, ≈ 20 nm for $[C_2C_1Im][N(CN)_2]$, and ≈ 25 nm for $[C_2C_1Im][SCN]$. Here, the effects of $[N(CN)_2]^-$ and $[SCN]^-$ are stronger, which is in line with the aforementioned coordination strength of the anions.[502] A universal redshift of the Q band excitation wavelength is apparent in the case of IL solvation, but no distinction between the ILs can be seen. With respect to the vacuum excitation, the intensity of the Q bands at ≈ 570 nm is clearly increased upon explicit solvation regardless of the IL, which is also in line with the experimental findings on nucleophile ligands. The increase in absorption intensity most probably arises due to lowered symmetry of the distorted molecule.

Investigation of the optimized structures shows clearly a popular alignment of the IL anions above and below the porphyrin ring plane, enabling coordination of the central Zn atom. Especially the anions $[N(CN)_2]^-$ and $[SCN]^-$ behave as axial ligands, which is illustrated in Figure 3.31. Average Zn–N_t(Anion) distances d in the optimized geometries are $d = 230$ pm for [B], $d = 218$ pm for [N], and $d = 214$ pm for [S], which again confirms the stronger coordination behavior of $[N(CN)_2]^-$ and $[SCN]^-$ with respect to $[B(CN)_4]^-$.

3.5.3.4 GD2

The **GD2** dye seen in Figure 3.32 was synthesized and tested by Grätzel and coworkers as a highly potent porphyrin dye for the use in DSCs.[37] A malonic acid group functioning as the anchor to the TiO_2 surface in a DSC is linked via a π-bridge to the porphyrin ring. This extension of the π-system results in a redshift of B and Q bands with regard to **ZnTPP**, which is nicely reflected in the computed spectra, see Figure 3.30 and Figure 3.32. The intense B band is now observed at $\lambda \approx 400$ nm in the vacuum spectrum, compared to $\lambda \approx 350$ nm for the comparable excitation in **ZnTPP**, and the Q bands are obtained at $\lambda \approx 700$ nm. The calculated vacuum spectrum is in good agreement with the experimental spectrum recorded in DMF, where the maximum

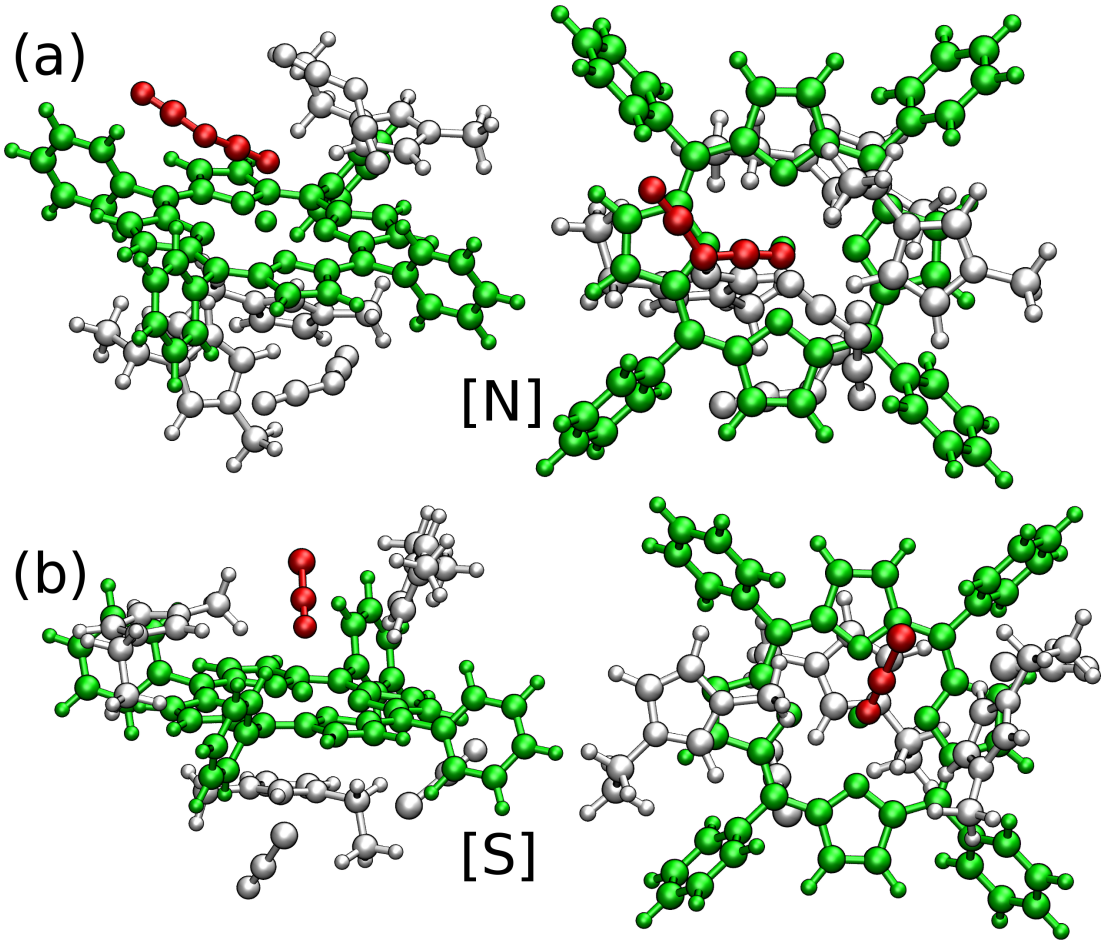

Figure 3.31: (a) Coordination of $[N(CN)_2]^-$ and (b) of $[SCN]^-$, left panels: front view; right panels: top view. **ZnTPP** is colored green, the coordinating axial ligand red, and the remaining non-coordinating ions are shown in light gray.

of the B band is found at $\lambda = 442$ nm, and Q band peak maxima at 532 nm, 570 nm and 610 nm.[37] Again, the Q band calculated with the ωB97X-D3 functional is found at higher wavelengths. Including the COSMO model, a very subtle bathochromic shift is observed, and a slight increase in intensity for the B and Q bands is to be noted.

Changing to explicit IL solvation, a universal redshift of excitation wavelengths with respect to the COSMO solvation is apparent. Interestingly, [B] accounts for the largest impact in that regard, which was different in the case of **ZnTPP**. Turning back to Table 3.15, the HOMO energies were not affected strongly by the IL solvation, but the impact on the LUMO energies was observed to be stronger. In the case of **GD2**, E_L is substantially lowered in case of [B] solvation, resulting in the lowest band gap with respect to [N] or [S] solvation. Consequently, the spectrum of the [B]-solvated **GD2** dye is computed to have the largest redshift. As the LUMO of **GD2** is located mostly at the malonic acid group, the stronger coordination of $[N(CN)_2]^-$ and $[SCN]^-$ at the central Zn atom seems to have a weaker influence on the excitation spectrum compared to the case of **ZnTPP**.

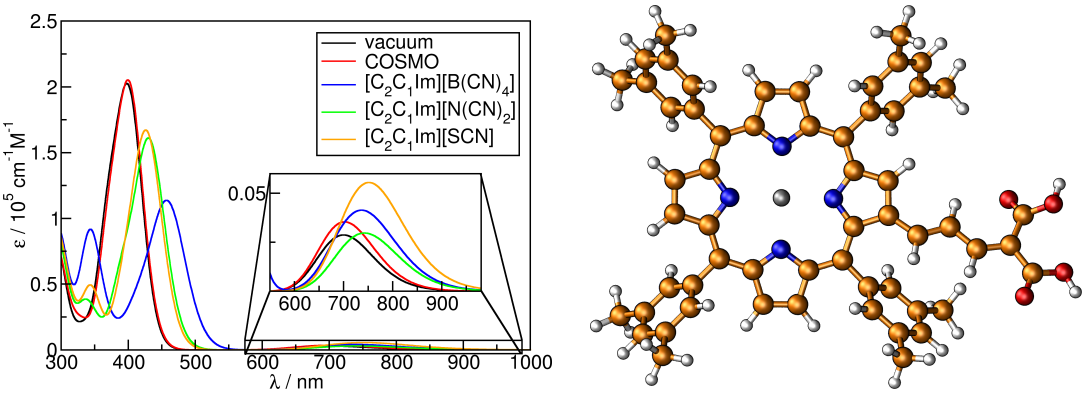

Figure 3.32: Broadened sTD-DFT spectra of **GD2** obtained with the ωB97X-D3 functional with and without implicit and explicit solvation. Boltzmann-weighted spectra in case of IL solvation. **GD2** as ball-and-stick model on the right side, the color coding is H=white, C=orange, N=blue, O=oxygen, Zn=gray.

Further inspecting the individual spectra for different optimized structures, the largest redshifts are obtained when the central Zn atom is coordinated by the anions $[B(CN)_4]^-$, $[N(CN)_2]^-$, and $[SCN]^-$. Coordination of an axial ligand is observed to introduce a redshift of $15 - 30$ nm with respect to conformations where Zn is uncoordinated. The average N_t(Anion)–Zn distances d in the observed geometries are $d = 226$ pm for [B], $d = 217$ pm for [N], and $d = 215$ pm for [S], which are in line with the results obtained for **ZnTPP**, respectively.

3.5.3.5 C218

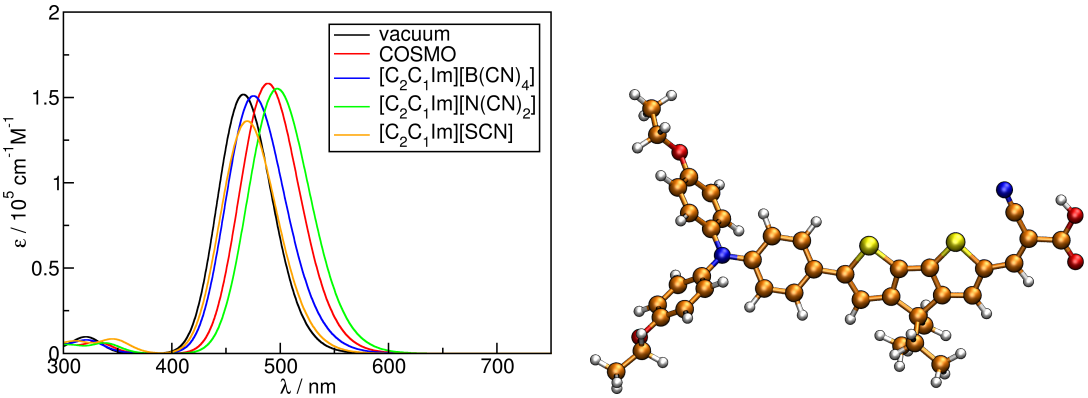

Figure 3.33: Broadened sTD-DFT spectra of **C218s** obtained with the ωB97X-D3 functional with and without implicit and explicit solvation. Boltzmann-weighted spectra in case of IL solvation. **C218s** as ball-and-stick model on the right side, the color coding is H=white, C=orange, N=blue, O=oxygen, S=yellow.

The **C218** dye was engineered recently as a promising organic dye for use in DSCs. [53] The molecular structure of **C218** with shortened alkyl chains (**C218s**) is shown in Figure 3.33, it contains a cyclopentadithiophene unit, which improves properties like an enhanced light absorption and reduced number of surface states with respect to it's

predecessor **D21L6**.[53] For the sake of reducing computational cost, the four hexyl chains of **C218** were reduced to ethyl chains, which has a minor impact on the investigated electronic properties, because the alkyl domains weakly contribute to the frontier orbitals (see supporting information for comparison of **C218** and **C218s** excitation spectra). The experimental spectrum of **C218** in chloroform shows a characteristic absorption band at 555 nm with a very high intensity. A recent study with the semiempirical ZINDO/S method suggests that the main absorption band in the spectrum of **C218** arises from intramolecular charge-transfer transitions, mainly incorporating HOMO-1, HOMO and LUMO MOs. Our calculations with the PBE0 hybrid functional confirm that the very high-intensity absorption is mainly governed by a HOMO $\rightarrow$ LUMO transition, and the second high-intensity absorption at $\approx$ 480 nm involves majorly the HOMO-1 $\rightarrow$ LUMO transition.

Shown in Figure 3.33 are the sTD-DFT spectra calculated with the ωB97X-D3 functional. Application of the COSMO model introduces a significant redshift with respect to the gas phase spectrum, see Figure 3.33, left panel, due to the dielectric effect. Interestingly, explicit solvation does not account for a significant redshift with regard to the COSMO calculations, only with regard to the vacuum calculations. This observation can probably be explained by the lack of distinct interactions like the previously encountered coordination of a central metal ion. In the case of the organic **C218s** dye, interactions are rather uniform based on the dielectric environment provided by either, the COSMO model or the ILs.

Although very similar in shape, the **C218s** spectra with explicit [N] solvation are notably redshifted with respect to [B] or [S] solvation. Again, the HOMO energies are equal among different solvation environments, but the LUMO energy, and consequently the band gap, are distinctly lower in the case of [N] solvation. Recalling the DOS of $[N(CN)_2]^-$ and **C218s**, the occupied frontier orbitals are energetically very close. Furthermore, owing to a flat geometry, the anion is observed to align flatly above the ring plane of **C218s**, which enables orbital interactions of the anion with the extended π system of the dye. The flat geometry and mixing of occupied orbitals is illustrated in Figure 3.34.

Experimentally, the absorption spectra of **C218** were measured in two dummy cells, the first with an acetonitrile/valeronitrile (85/15 v/v) electrolyte, and the second with the [B] ionic liquid electrolyte, both along with different additives (the reader is referred to Ref. 53 for the detailed electrolyte composition). The absorption spectrum of **C218** showed a redshift in the IL electrolyte cell with respect to the organic solvent electrolyte cell. This report shows that the high dielectric character of ILs with respect to organic solvents can cause a bathochromic shift of the dye's absorption spectrum within a DSC.

Furthermore, Zhou et al. tested the **C218** dye in complete DSCs with [B] and [N] containing electrolytes.[160] The authors reported a redshift of the dye's absorption onset wavelength for the [B] containing electrolyte with respect to the [N] containing

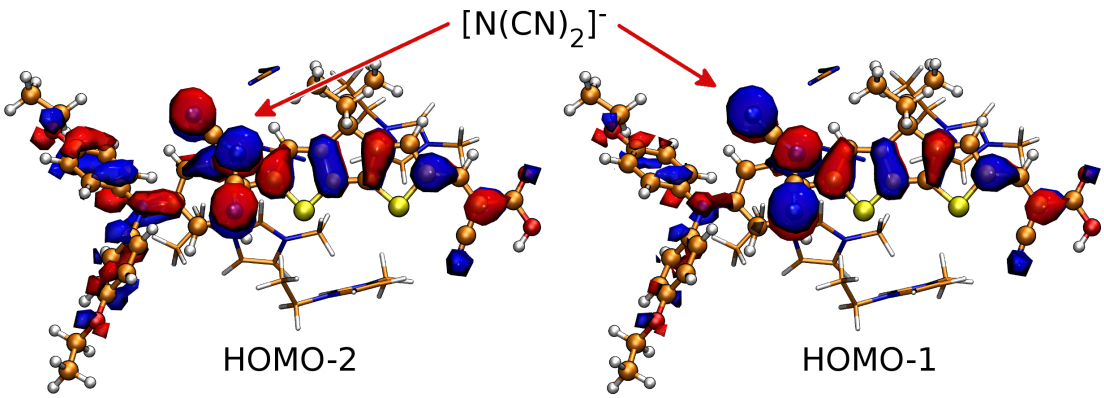

Figure 3.34: Frontier orbitals of **C218s** and $[N(CN)_2]^-$ in an on-top like conformation. Involved molecular compounds in ball-and-stick models, the color coding is H=white, C=orange, N=blue, O=oxygen, S=yellow.

electrolyte. This redshift is not covered by the weighted computed spectra. However, individual **C218s** spectra with explicit [B] solvation show a redshifted adsorption spectrum, but minorly contribute to the weighted spectrum due to a very small Boltzmann weight. Furthermore, the effect of other additives in the electrolyte used in the experiment such as 4-*tert*-butylpyridine is not included in the calculations. Sampling of more configurations, and possibly including other additives with the aid of molecular dynamics simulations might be useful to obtain a more realistic picture. Unfortunately, AIMD simulations for all dye–IL combinations are out of the scope of the present work due to the immense computational cost.

3.5.3.6 N749

N749, or the black dye, was synthesized as successor of N3, a popular ruthenium dye, to have the excitation spectrum shifted toward the near infrared region in order to enhance the light harvesting capability of DSCs.[32] With Ru(II) as the central metal atom, **N749** is anionic, the counterion is usually $[NHEt_3]^+$. The experimental spectrum recorded in ethanol is mainly governed by an intense peak around $\lambda = 620$ nm, attributed to a metal-to-ligand charge transfer (MLCT), whose shoulder stretches out up to 920 nm in the near infrared. Bands at 291 nm and 329 nm with a shoulder at 340 nm in the experimental spectrum are assigned to intraligand $\pi \rightarrow \pi^*$ transitions and additionally, a very dominant peak at $\approx$ 450 nm not described further by the authors is clearly visible from the experimental spectrum. The experimental spectrum in the range of $\lambda > 500$ nm is observed to be very broad, which might be explained by the fact that it was recorded in ethanol, which itself is a decent hydrogen bond donor and acceptor.

The calculated spectra of **N749** along with the dye's molecular structure are shown in Figure 3.35. Unfortunately, due to the negatively charged dye, the pure spectrum

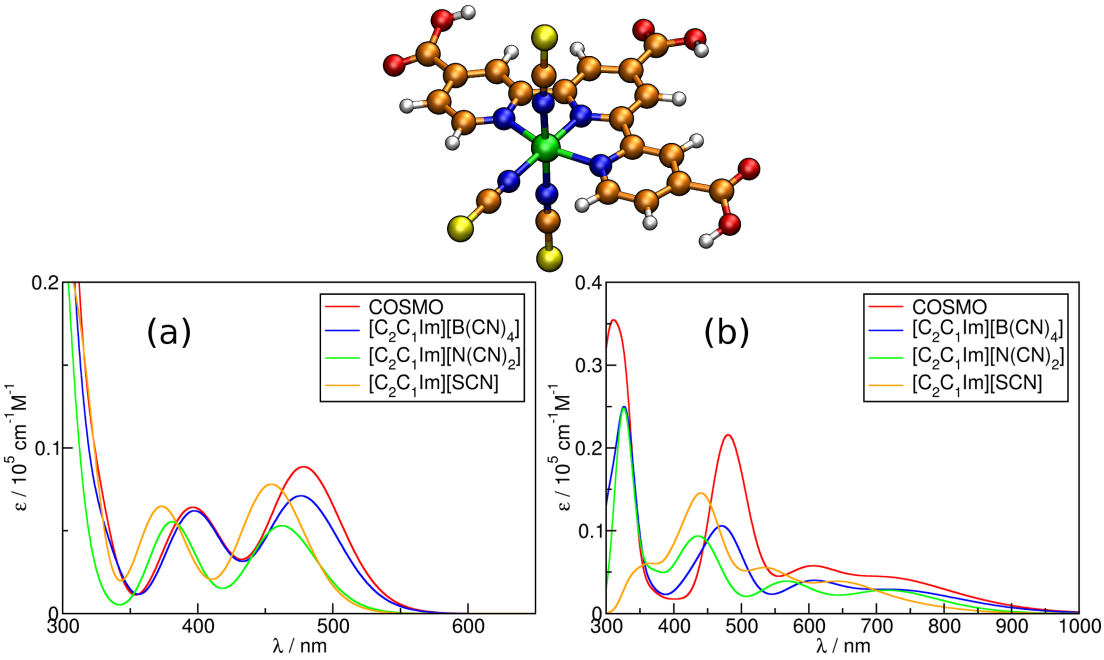

Figure 3.35: Broadened excitation spectra of **N749** with and without implicit and explicit solvation obtained with (a) sTD-DFT and the ωB97X-D3 functional and (b) TD-DFT and the PBE0 functional. Note the different axis scales. Boltzmann-weighted spectra in case of IL solvation. **N749** as ball-and-stick model on top, the color coding is H=white, C=orange, N=blue, O=oxygen, S=yellow, Ru=green.

of **N749** without a counterion in vacuum is not reasonable and therefore omitted with respect to the other dyes. The COSMO model however applies a screening charge and therefore ensures overall charge neutrality, yielding a reasonable spectrum. The calculated ωB97X-D3–sTD-DFT spectrum (Figure 3.35a) appears to be blueshifted with respect to the experimental spectrum. It contains excitations at $\lambda \approx 300$ nm and ≈ 400 nm, which agree with the experiment, but the low-energy excitations at $\lambda > 600$ nm, stretching up to the near infrared are either missing, or alternatively condensed in the strong excitation at 450-550 nm. The high Hartree–Fock exchange, ramping up to 100 %, suppresses artificial charge transfer excitations, but also seems to not reproduce the physically reasonable MLCT excitations at the correct positions. Therefore, the more expensive TD-DFT spectra calculated with the PBE0 functional are shown in addition in Figure 3.35b. Here, the calculated **N749** COSMO spectrum contains all important features of the experimental spectrum, in particular the MLCT peaks at 807 nm, 713 nm, 609 nm and 551 nm, which account for the broad absorption tail extending to the near infrared, and the intense band at 306 nm with shoulders at 323 nm and 280 nm. Visualization of the involved molecular orbitals shows that the peaks at 306 nm and 323 nm could be attributed to mixed transitions including MLCT and intraligand transitions, and the intense band at 280 nm is majorly characterized by an intraligand transition, as suggested by Grätzel and coworkers.[32] Further on, a distinct peak at 480 nm is found in agreement to the response at 450 nm in the

experimental spectrum, which could be identified as mainly MLCT transition.

Introducing explicit solvation, overall charge neutrality was ensured by solvating **N749** with 4 cations and 3 anions of the respective IL. Regardless of the method, the absorption spectrum of **N749** in $[C_2C_1Im][B(CN)_4]$ appears redshifted with regard to the other ILs. With respect to the COSMO model, $[C_2C_1Im][B(CN)_4]$ solvation seems to provide just the same dielectric environment, whereas the stronger coordinating anions $[N(CN)_2]^-$ and $[SCN]^-$ provide a different environment. From the structures, coordination of the anions at the carboxyl groups is visible, which obviously influences the terpyridine's acceptor state energies. In this regard, $[N(CN)_2]^-$ and $[SCN]^-$ are known to be stronger hydrogen bond acceptors than $[B(CN)_4]^-$. Also, compared to **ZnTPP**, the anions now interact with the ligand via hydrogen binding, as opposed to coordination of the central metal ion, which seems to have the opposite effect. The alignment of HOMO and LUMO levels (see Table 3.15) is not sufficient to explain the blueshift upon [N] and [S] solvation. Therefore, the specific interactions of $[N(CN)_2]^-$ and $[SCN]^-$ with the organic ligand are most probably responsible for the observed trends.

3.5.4 Conclusion

The influence of explicit ionic liquid solvation on the excitation spectra of prominent dyes for dye-sensitized solar cells was investigated. It is found that with respect to gas phase spectra, the excitations are generally redshifted. An approximation of the ionic liquid solvation effect is provided by the COSMO solvation model, which was observed to apprehend the bathochromic displacement as well as the elevation of excitation intensities in most cases.

However, the COSMO model alone does not account for specific interactions such as the mentioned coordination at a central metal ion or hydrogen bond like interactions, which cause distinct shifts in the excitation spectra by providing an individual environment around the dye. Therefore, introduction of at least one solvent shell around the important groups is necessary to recognize distinct interactions. The specific interactions introduced require averaging over multiple configurations of explicit solvation, and a weighting of reasonable conformations, for example based on Boltzmann factors is beneficial. Further on, replacement of the organic solvent with an ionic liquid is observed and estimated to lead to a more severe influence on the dye's properties than differences between the very alike cyano-based ionic liquids. Stronger deviations between ionic liquid effects can be expected if very diverse ionic liquids are to be employed, which could be a starting point for future investigations.

Investigation of the solvent shell size influence showed that while solvation with as many solvent molecules as possible is aspired, solvation of the relatively large dye molecules with only three ion pairs of the respective ionic liquid with additional embedding in a continuum model is already sufficient to capture a major portion of the

energetic and spectroscopic properties of the solvated dye. Enhancement of the finite solvent shell size approximation can be gained by consciously solvating functional groups, which are to believed crucial for the property of interest. In the given case, solvation of the central Zn atom in the porphyrin dyes **ZnTPP** and **GD2** was found to be an important pattern, redshifting the excitation spectra for ≈ 20 nm. Differences in the nature of the components, such as coordination strength of the anions, is reflected in the dye's spectrum. In any case, saturation of the hydrogen bond donor and acceptor sites is desirable to achieve an accurate description of the solvation.

These findings will guide experimentalists when choosing an appropriate electrolyte for the use in dye-sensitized solar cells. Upon choice of the solvent, specific interactions can be stimulated, or inhibited, which can drive the process in a favorable fashion. However, it is stressed once again that the ionic liquid–dye interaction cannot be considered separately, as the ionic liquid impacts the semiconductor and other parts of the solar cell simultaneously. Careful testing and further investigations are necessary and will elevate the dye-sensitized solar cell technology to its full potential.

Supporting Information

The supporting information contains the computed energetics with the ωB97X-D3 functional, a graphical representation of the DOS of dyes and ILs, and a comparison of **C218** and **C218s** excitation spectra. The supporting information is attached in Section A.5.

Acknowledgments

This work was financially supported by the DFG project KI-768/12-1 'Materialsynthese nahe Raumtemperatur' and the SFB 813 'Chemie an Spinzentren: Konzepte, Mechanismen, Funktionen'. The support for H.W. by the Fonds der Chemischen Industrie (FCI) is gratefully acknowledged.

4 Conclusion and Final Remarks

In summary, different subsystems of a complete DSC were investigated, always focusing on IL electrolytes. Cyano-based ILs in particular showed to be very promising electrolytes in different experimental studies. Therefore, the three cyano-based ILs $[C_2C_1Im][B(CN)_4]$, $[C_2C_1Im][N(CN)_2]$, and $[C_2C_1Im][SCN]$ were investigated as pure liquids by AIMD. Although they are very similar, distinct differences in structure and dynamics are apparent. Predominantly, the cation–cation π-π stacking is substantially influenced by the anion, which differs mainly in hydrogen bond acceptor capability. Dynamically, the cation's diffusion constant may vary by a factor of up to 4 depending on the anion, which will definitely influence the performance of the IL in a DSC. Generally, slower transport is related to lower short-circuit currents, but all three ILs are still on the lower end of viscosity with respect to other ILs.

By introducing the anatase surface, the bulk IL structure is disturbed, and new interactions at the interface arise. Using *ab initio* methods, detailed insight into the absorption geometry of isolated ions and ion pairs could be gained. It is important to note that the anions mainly interact with unsaturated Ti_{5c} surface titanium atoms, and the electron deficient cations coordinate O_{2c} surface oxygen atoms in a hydrogen bonding manner. With the aid of these detailed *ab initio* calculations, it was possible to combine existing force fields for the involved pure compounds—namely the polarizable PIM FF for TiO_2, and the non-polarizable IL FF—by approximation of the interactions with classical potentials. The derived FF allowed for an extensive simulation of the interfacial systems. Main findings include a cation excess on the titania surface, which depends on the anion and is observed to be higher for the $[C_2C_1Im][SCN]$ IL compared to the $[C_2C_1Im][B(CN)_4]$ IL. The cation excess at the surface translates to alternating layers of cations and anions in the bulk structure, which can extend over several nanometers into the bulk phase. The cation excess influences the titania's DOS, and most likely the recombination behavior of the adsorbed dye. On one hand, this is due to the redox pair, *e.g.*, I^-/I_3^-, being attracted by the positively charged cation surface layer, bringing it in the vicinity of the oxidized dye, but preventing the redox pair from reaching the surface. This kind of blocking layer behavior is beneficial to reduce recombination rates of CB electrons and the redox pair. On the other hand, the multilayered structure might increase the retention time of the redox shuttle in the cation-rich layer. Furthermore, the developed force field is readily applicable to study more realistic systems that include surface defects in form of vacancies (oxygen vacancies are common for real anatase surfaces), kinks, stages, islands, or curved

surfaces. These studies would give an even more realistic insight into the actual electrolyte/semiconductor interactions that play a role in real DSC devices. Moreover, after careful testing, the FF should be expandable to other surface orientations, and even other TiO_2 modifications. The presented method can be used to combine any two existing FFs. The expansion to other semiconductor materials or solvents is straightforward with the described protocol, fitting the missing terms to *ab initio* data.

As discussed, it is known and exploited that the DOS of TiO_2 depends on the adsorbed species at the surface. Therefore, in a broad approach, the influence of 42 different ILs with varying cations and anions on titania's DOS was characterized. With this knowledge, a meaningful preselection of ILs might be possible based on the current energetic situation in a DSC. The IL electrolyte could then be chosen to either upshift or downshift the CB edge of TiO_2, rather than merely be the diffusive medium for the additives. Apart from applicability, the physical origin for this effect was sought after, and a good correlation with the IL's ability to donate or accept electron density was found. Here, the positively charged cation usually accepts electron density from the surface, and the anions donate electron density. As these are competing processes, the nature of the ions and their surface composition—remember the cation excess for condensed systems—then decide the overall outcome.

If an IL is chosen as electrolyte in a DSC, it will interact with all components. Accordingly, the dye/IL system was investigated. Focusing on spectral properties, the excitation spectra of the involved dyes were observed to redshift with respect to the gas phase and therefore, probably also with respect to common unpolar solvents. This results from the IL being a highly dielectric medium, which stabilizes the more polar excited state of a dye better than the respective ground state. Moreover, directed interactions occur, as common IL anions such as thiocyanate have a strongly nucleophilic, and thus coordinating, behavior, which, for example, enables the coordination of metal centers. Besides, hydrogen bonding is a common motif of interaction; the imidazolium cation serves as weak hydrogen bond donor, and many anions serve as hydrogen bond acceptors. The influences of the electrolyte on the spectroscopic properties of the employed dye should be considered upon choice of a suitable IL.

In future works, the subsystem of interest might be extended. For example, it would be possible to investigate the dye/IL/TiO_2 system using a combined QM/MM approach. The adsorbed dye would then constitute the QM region, and the presented TiO_2/IL FF could be used to model the MM (molecular mechanics) region. Moreover, the sTD-DFT method could then be used to determine absorption spectra of the adsorbed dye with the explicit solvent, approaching a more realistic picture.

Furthermore, proceeding research might focus on incorporation of the redox mediator. Whereas the principle redox mechanism is well understood, information of distinct interactions of redox mediator and dye are still rare. Especially the influence of the solvent on the redox mechanism is an interesting target for future research. These stud-

ies might help to understand the fundamental differences of regeneration efficiency in ILs of inner-sphere redox mediators such as I^-/I_3^- versus outer-sphere redox mediatiors based on $Co^{II/III}$ or $Ni^{III/IV}$.

With the accurate description of structure and dynamics of the IL/TiO_2 interface, further studies might focus on the recombination reactions of conduction band electrons with the electrolyte. In that regard, the pure electrolyte might be replaced by a more realistic solution of IL and common additives such as TBP. Investigation of the IL electrolyte influence on electron diffusion in the TiO_2 nanoparticles would give further information and a more complete picture on the overall implications of IL application in DSCs.

While much work was already done in the context of IL electrolytes in DSCs, a complete understanding will definitely require future work and dedication. The DSC itself is a very promising technique and might play a key role in an upcoming energy market focusing on renewable and sustainable energy. In order to make DSCs competitive to established technologies, ILs present a formidable alternative to current organic solvents used in DSCs, and can potentially overcome many of the current problems. For this reason alone, further research and exploration of new materials as well as a deeper understanding of the underlying principles should always be pursued.

A Appendix

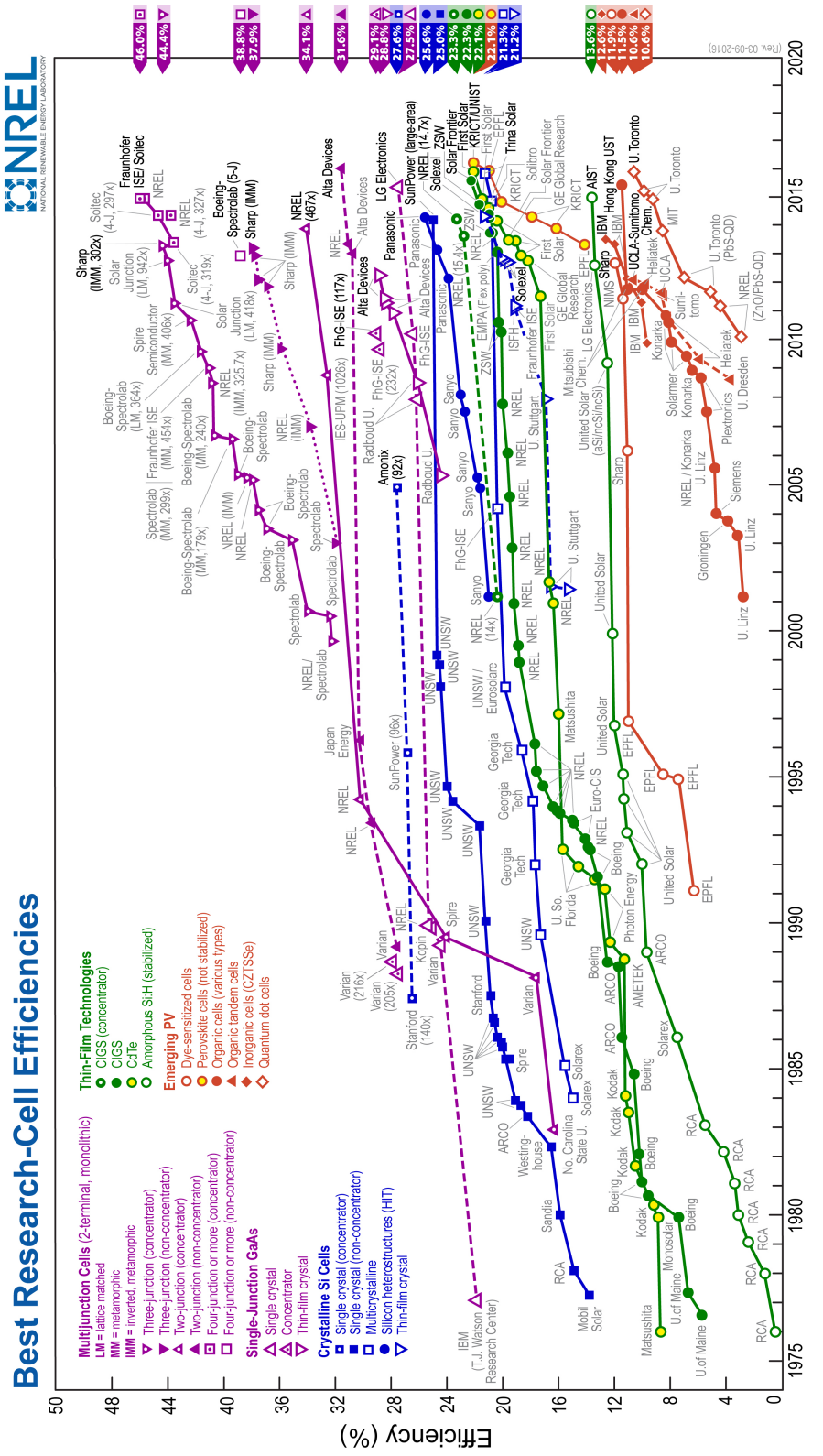

Figure A.1: Summary of progression and current status of various photovoltaics. This plot is courtesy of the National Renewable Energy Laboratory, Golden, CO. [10]

A.1 Supporting Information of: Complex Structural and Dynamical Interplay of Cyano-Based Ionic Liquids

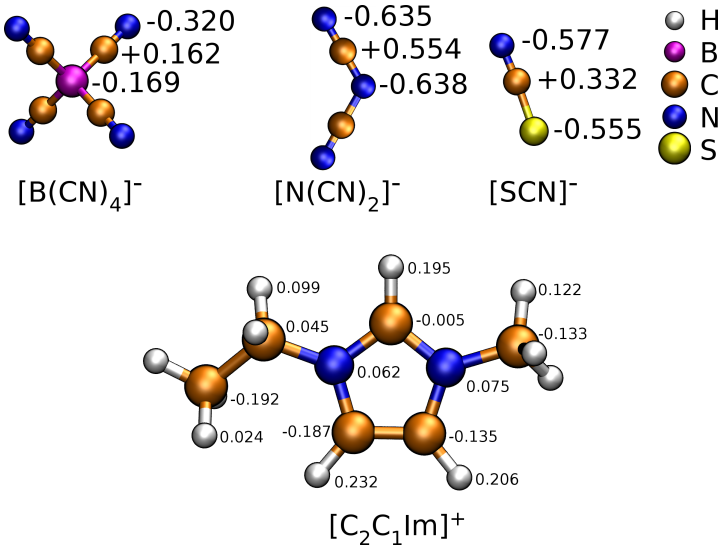

Figure A.2: RESP charges calculated at the Hartree–Fock 6-31++G** level of theory. Labeling of the ILs components: tetracyanoborate $[B(CN)_4]^-$, dicyanamide $[N(CN)_2]^-$, thiocyanate $[SCN]^-$ and 1-ethyl-3-methylimidazolium $[C_2C_1Im]^+$.

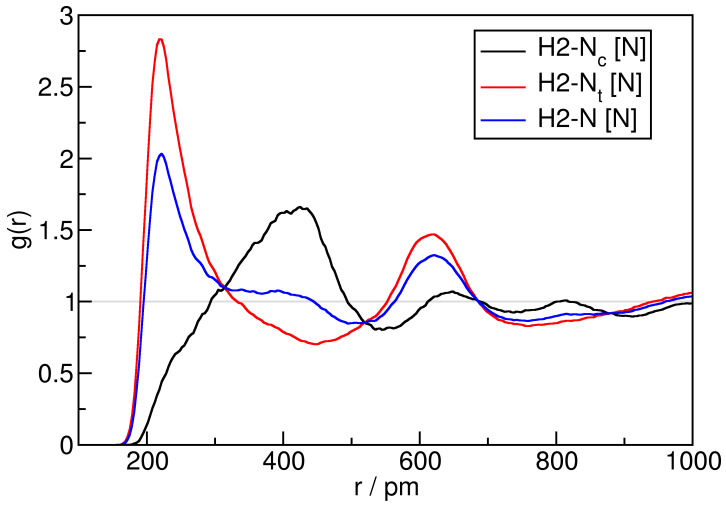

Figure A.3: RDFs of cation–anion interaction in [N], clearly showing weak H2-N_c and strong H2-N_t interaction.

A.2 Supporting Information of: Adsorption Behavior of the 1,3-Dimethylimidazolium Thiocyanate and Tetracyanoborate Ionic Liquids at Anatase (101) Surface

A.2.1 Anatase Bulk and Surface Calculations

Table A.1: Results of Anatase Bulk Calculations[†]

Program	Functional	Basis Set O	Basis Set Ti	a / pm	c / pm
Exp				378.2	950.2
CP2K	PBE–D3, GTH PP	Molopt	Molopt	376.8 (−0.37)	931.1 (−2.06)
Crystal14	PBE–D3	Muscat	Darco	376.4 (−0.48)	981.0 (3.14)
Crystal14	PBE0–D3	Muscat	Darco	372.8 (−1.44)	972.5 (2.29)

[†] a and c denote lattice vectors. Values in parenthesis are deviations from the experimental value [409] in %.

Table A.2: Calculated Surface Energies E_{surf} in Dependence of the Setup and the Slab Thickness

Layers	E_{surf} / J/m^2			
	PBE[a]	PBE0[a]	PBE-D3[b]	PBE0-D3[a]
2	0.632	0.749	0.666	1.097
4	0.666	0.796	0.766	1.202
6	0.725	0.852	0.843	1.272
8	0.747	0.873	0.899	1.298
10	0.753	0.883	0.945	1.308
12	0.757	–	0.985	1.312
14	0.760	–	–	–

[a] Results obtained with Crystal14.

[b] Results obtained with CP2K.

To evaluate the appropriate thickness of the anatase slab, the surface energy E_{surf} was calculated as follows:

$$E_{\text{surf}} = \frac{E_{slab}(n) - nE_{\text{bulk}}}{2A_{\text{surf}}} \tag{A.2.1}$$

With the energy of the slab (E_{slab}) and the bulk (E_{bulk}) calculation, divided by the surface area A_{surf}. Note that the surface area is multiplied by two because of the two exposed surfaces of the slab model. n is the number of formula units of the slab model and the according energy of the slab calculation E_{slab}. To ensure a vanishing dipole moment of the the pure anatase slab in z-direction, only even numbers of stoichiometric layers were considered to study the (101) anatase surface.

For each given computational setup consisting of XC-functional, basis set, and dispersion correction, the elementary crystal cell parameters and atom positions were calculated. As can be seen from A.1, cell parameter a is consistently underestimated, but the relative error is reasonably small with < 2 %. The cell parameter c is overestimated for the calculations employing the Muscat and D'Arco basis sets. This relative

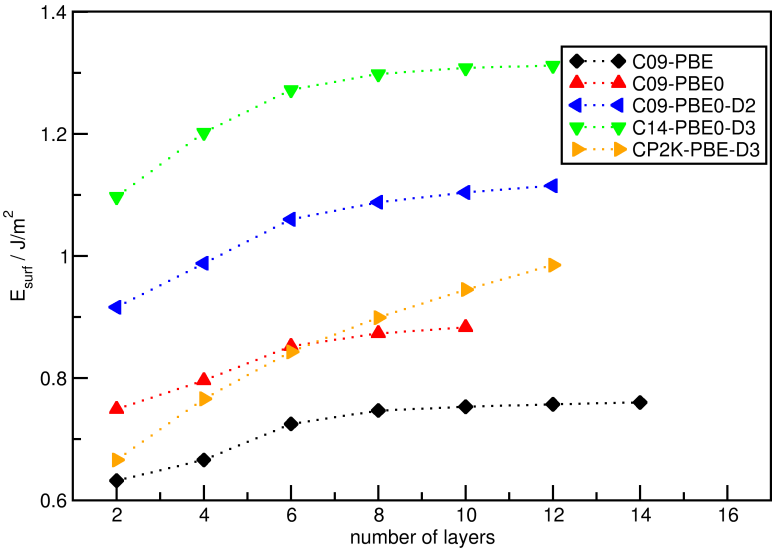

Figure A.4: Surface energy E_{surf} in dependence of slab thickness and setup.

error is lowered when the hybrid functional PBE0 is employed and is further improved by the addition of the D3 dispersion correction. The CP2K calculation with the PBE functional and D3 correction underestimates both cell vectors a and c, but shows a good overall agreement with experimental values. In either case, the inclusion of dispersion correction shortens the cell vectors, as it is a purely attractive correction.

The predominant surface of anatase TiO_2 single crystals is the (101) surface. In order to avoid artificial dipole moments as well as to obtain correct stoichiometry, only specific cut planes and even numbers of layers can be used. To determine the appropriate thickness of the slab models, the convergence behavior of the surface energy was checked, which was calculated according A.2.1 and which is shown in A.4 and A.2. In all CRYSTAL calculations, a satisfactory convergence of E_{surf} is reached at a thickness of 6 to 8 layers, which is in agreement with previous calculations.[333] For the CP2K calculations, to account for the lack of k-point sampling, a surface supercell of the dimensions 4x3 was constructed. Up to a slab thickness of 12 layers, no satisfactory convergence of the surface energy was observed. This is most likely due to the aforementioned lack of k-point sampling and possibly an inadequate size of the CP2K bulk reference and slab models. We therefore decided to use the same thickness as obtained from the CRYSTAL convergence study.

In the previous study of Esch *et al.*[333] the surface energy of anatase (101) was calculated as 0.64 J/m^2 with the PW1PW hybrid functional. In that study, a surface enthalpy H_{surf} of 0.61 J/m^2 was obtained via a phonon calculation using the Γ-approach at 298 K. This value compares to the experimental reference of $H_{\text{surf}}^{\text{exp}} = 0.74 \pm 0.04$ J/m^2.[503] However, the comparison of E_{surf} or H_{surf} is not the aim of this work, these quantities are only a measure to determine an appropriate slab thickness and therefore only the convergence is of interest.

Table A.3: Cell-Size Dependence of the Calculated Interaction Energy of $[C_1C_1Im]^+$ at Anatase (101) at Minimum Position $E_{int,\ min}$, Interaction Energy and Charge Transfer at 1000 pm Distance ($E_{int,\ 1000\ pm}$, $CT_{1000\ pm}$) From Surface. c = 6000 pm, $\alpha = \beta = 90°$, $\gamma = 109.590°$, 6 Layers, Mulliken Charges for CT; CP2K–PBE–D3 Results

supercell	a / pm	b / pm	n(TiO2)	$E_{int,\ min}$ / kJ/mol	$E_{int,\ 1000\ pm}$ / kJ/mol	$CT_{1000\ pm}$ / e
1x1	378.0	563.7	6			
3x2	1134.0	1127.4	36	-242.6	-213.4	0.22138
4x3	1512.0	1691.1	72	-176.2	-86.9	0.09129
6x4	2268.0	2254.8	144	-151.5	-40.4	0.00365
9x6	3402.0	3382.1	324	-149.9	-18.8	0.00001

With satisfactory convergence and to save computational time, a layer thickness of 6 was chosen for the subsequent calculations of the adsorption behavior of the ionic liquids.

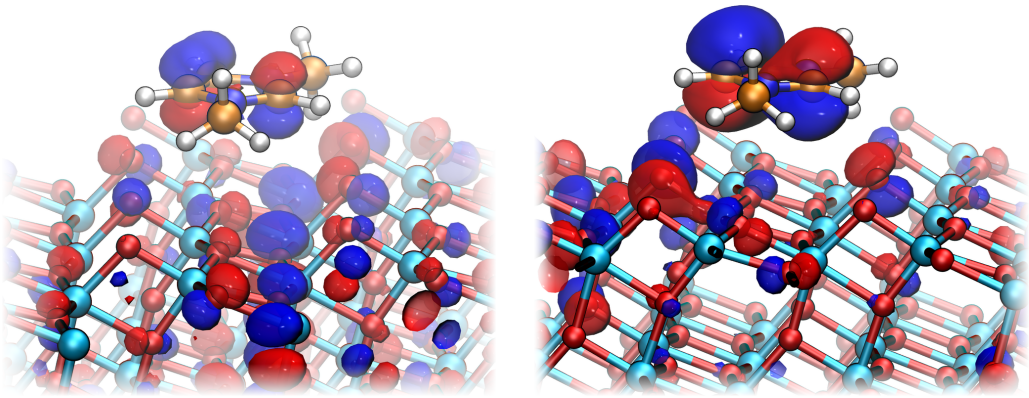

Figure A.5: Molecular Orbitals indicating $p_O \rightarrow \pi_{[C_1C_1Im]^+}$ charge transfer.

A.2.2 Details on classical molecular dynamics simulations

Different starting geometries of the ion pairs on the surface were generated by classical molecular dynamics simulations. The simulations were performed in the N,V,T–ensemble. Temperatures between 300 and 700 K were set by Nosé–Hoover chain thermostats.[297,299,486] The time step was set to τ =0.5 fs. The TiO_2 slab was held fixed during the whole simulations. The ionic liquid was described by the force field of Padua *et al,*[296,504] employing the popular OPLS/AA force field.[247,505,506] Preliminary parameters to describe the ionic liquid – TiO_2 interactions are given in A.4. The functional form of the interaction of particle i with particle j is given by:

$$E_{ij} = \varepsilon_{ij}\left[2\left(\frac{\sigma_{ij}}{r_{ij}}^9\right) - 3\left(\frac{\sigma_{ij}}{r_{ij}}^6\right)\right] \tag{A.2.2}$$

with the energy parameter ε_{ij} and the distance parameter σ_{ij}. See Ref.[507] for further description of the COMPASS force field. RESP partial charges were used for the ionic

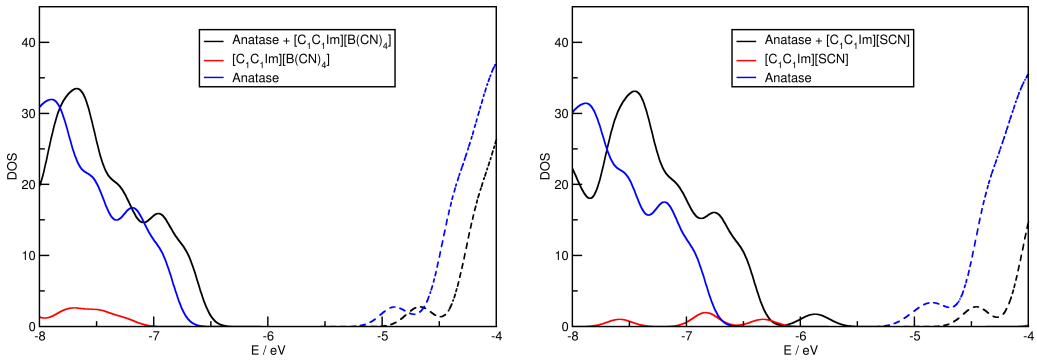

Figure A.6: Density of states of anatase (101) slab and adsorbed IL ion pair, $[C_1C_1Im][B(CN)_4]$ (left), $[C_1C_1Im][SCN]$ (right). PBE-D3-DZVP-MOLOPT level of theory.

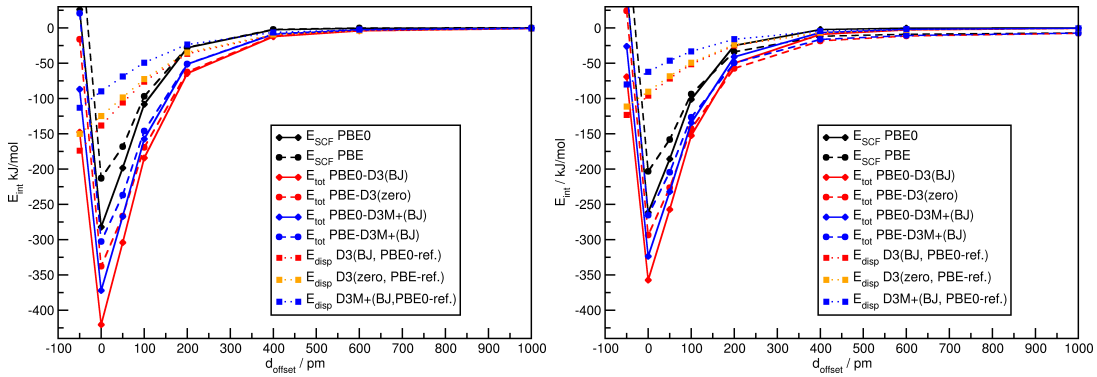

Figure A.7: Detailed interaction energies of a single $[C_1C_1Im][B(CN)_4]$ ion pair (left) and a single $[C_1C_1Im][SCN]$ ion pair (right) with the anatase (101) surface for different methods. d_{offset} depicts the offset of the ion pair from optimized minimum position in z-direction. Energy is split in energy from SCF part of the calculation E_{SCF}, dispersion correction energy E_{disp} and total interaction energy $E_{\mathrm{tot}} = E_{\mathrm{SCF}} + E_{\mathrm{disp}}$.

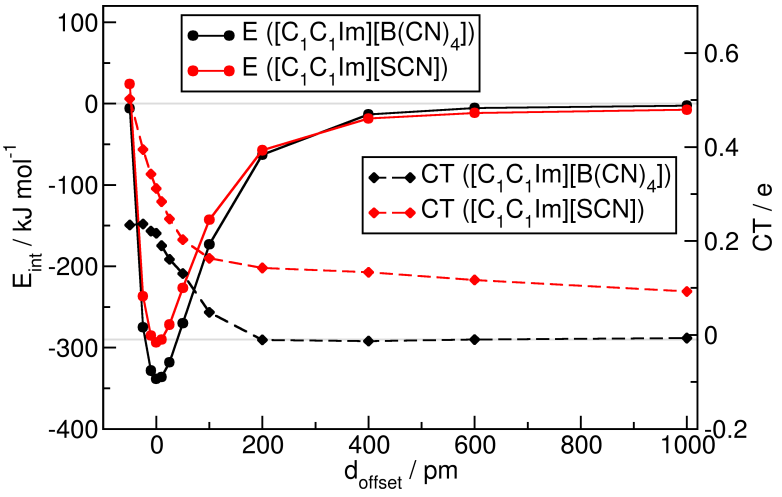

Figure A.8: Interaction energies E_{int} of a single $[C_1C_1Im][B(CN)_4]$ ion pair and a single $[C_1C_1Im][SCN]$ ion pair with the anatase (101) surface at the PBE–D3 level with corresponding charge transfer CT. d_{offset} depicts the offset of the ion pair from optimized minimum position in z-direction.

Table A.4: Parameters Describing the Interaction Between Ionic Liquid and TiO_2 Surface; Labeling According to Reference[296]

i	j	ε_{ij} / kJ mol^{-1}	σ_{ij} / Å
NA	O	0.083	3.74
NA	Ti	0.301	2.41
CR	O	0.191	3.82
CR	Ti	0.005	2.26
C1/CT	O	0.042	3.96
C1/CT	Ti	0.000	5.89
CW	O	0.193	3.83
CW	Ti	0.423	2.53
H1	O	0.047	2.64
H1	Ti	0.000	1.81
HCW	O	0.009	2.59
HCW	Ti	0.071	1.85
HCR	O	0.048	2.60
HCR	Ti	0.000	0.47
N (SCN)	O	1.851	3.04
N (SCN)	Ti	1.564	2.22
C (SCN)	O	0.029	1.97
C (SCN)	Ti	1.838	3.61
S (SCN)	O	0.362	3.33
S (SCN)	Ti	0.034	4.30
B ($B(CN)_4$)	O	0.000	3.96
B ($B(CN)_4$)	Ti	0.899	3.23
C ($B(CN)_4$)	O	0.000	7.05
C ($B(CN)_4$)	Ti	0.488	3.69
N ($B(CN)_4$)	O	0.793	3.21
N ($B(CN)_4$)	Ti	0.391	2.72

liquid,[406] and DDEC/c3 charges for the anatase slab.[508]

A.3 Supporting Information of: Toward an Accurate Modeling of Ionic Liquid–TiO_2 Interfaces

Computational details of the pure bulk ionic liquid simulations: The densities were determined in an NPT simualtion of 2 ns. Subsequently, the viscosities and diffusion coefficients were determined from 10 ns of NVT simulation after another 2 ns of equlibration. Nosé–Hoover chain thermostats ($T = 343.15$ K, $\tau = 100$ fs) and barostat ($P = 1$ bar, $\tau = 1000$ fs) were used with a time step of $\tau = 0.5\ fs$.[297,299,486] Viscosities are determined with the aid of the Green–Kubo equations.[509]

Table A.5: Details of the Molecular Dynamics Simulations Carried Out†

		$[C_2C_1Im][B(CN)_4]$	$[C_2C_1Im][SCN]$
N(IP)		200	256
c / pm		9174.81	8269.69
ρ / kg m^{-3}	experiment	993.6±1.1[510]	1088.4±1.3[510]
	simulation[a]	956.1 (3.8 %)	1047.4 (3.8 %)
η / mPa s	experiment	4.67±0.15[311]	7.773±0.084[511]
	simulation[a]	1.55 (67 %)	2.11 (73 %)
D^a / pm^2 ps^{-1}	cation	270.9	230.0
	anion	200.1	196.6

†N(IP) is the number of ion pairs, c the cell vector in z-direction. The experimental and simulated densities ρ and viscosities η and simulated diffusion coefficients D at 343.15 K are given. Deviation from the experimental values are given in parentheses.

[a] Values taken from IL bulk simulation with the IL FF.

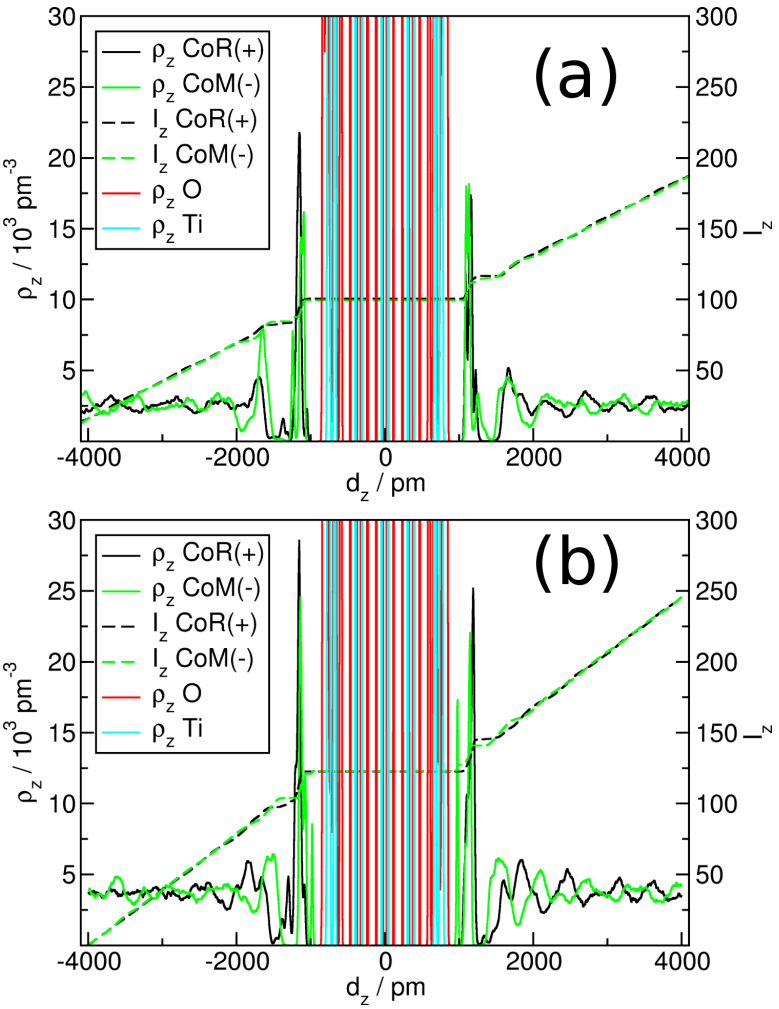

Figure A.9: Density profiles ρ_z and the volume-integrated density I_z yielding the number count with the PIM FF; (a) for $[C_2C_1Im][B(CN)_4]$ and (b) for $[C_2C_1Im][SCN]$. CoR(+) is the center of the imidazolium ring, CoM(-) is the anion's center of mass.

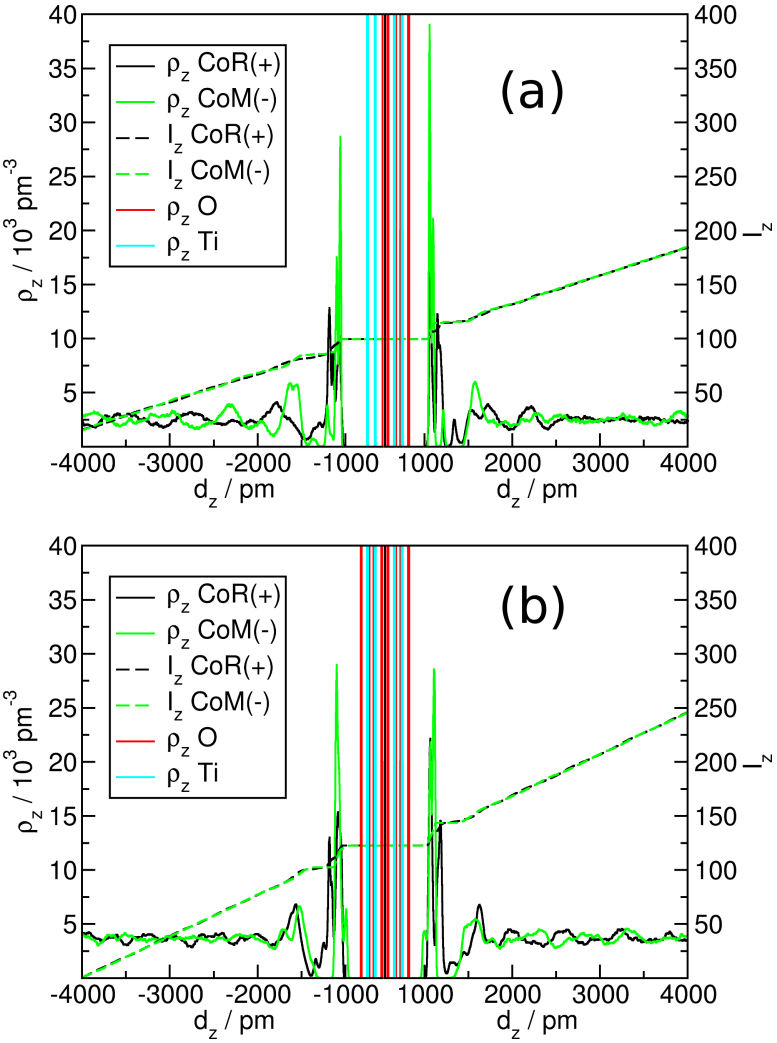

Figure A.10: Density profiles ρ_z and the volume-integrated density I_z yielding the number count with the LJ FF; (a) for $[C_2C_1Im][B(CN)_4]$ and (b) for $[C_2C_1Im][SCN]$. CoR(+) is the center of the imidazolium ring, CoM(-) is the anion's center of mass.

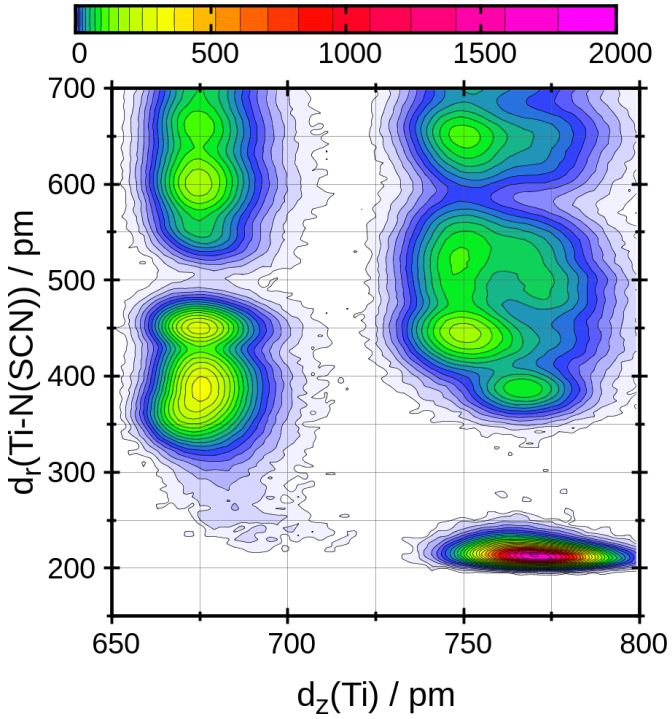

Figure A.11: Combined distance-distance distribution function showing the dependence of the z-position of surface titanium atoms (d_z(Ti)) from the N([SCN]$^-$)-Ti radial distance d_r in the [C_2C_1Im][SCN] system for the PIM FF.

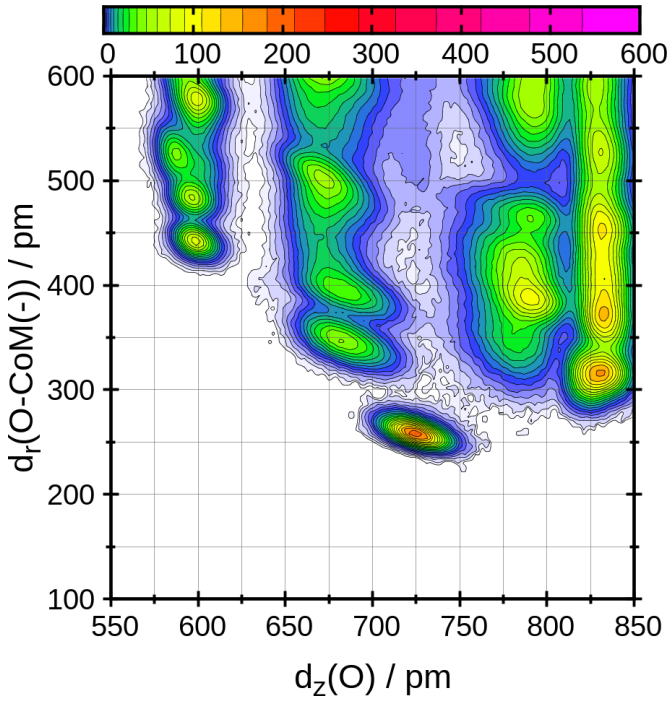

Figure A.12: Combined distance-distance distribution function showing the dependence of the z-position of surface oxygen atoms (d_z(O)) from the anion's center of mass CoM(-)-O radial distance d_r in the [C_2C_1Im][SCN] system for the PIM FF.

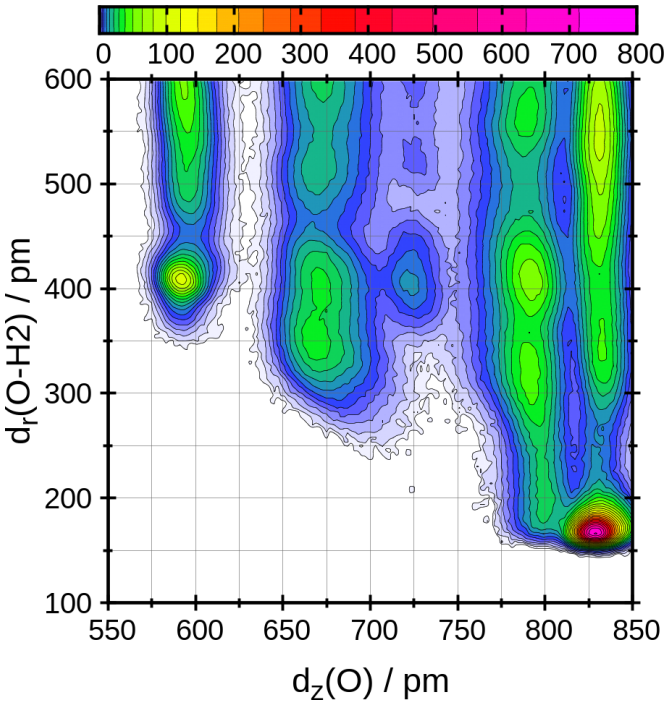

Figure A.13: Combined distance-distance distribution function showing the dependence of the z-position of surface oxygen atoms (d_z(O)) from the H2-O radial distance d_r in the [C_2C_1Im][SCN] system for the PIM FF.

A.4 Supporting Information of: Ionic Liquid induced Band Shift of Titanium Dioxide

Table A.6: Comparison of Iodide Full Core (FC) and Pseudopotential (PP) Calculations for 10 Different Conformations of [C_2C_1Im][I][a]

Conformation	E_H^{FC} / eV	E_H^{PP} / eV	ΔE_H / eV	E_L^{FC} / eV	E_L^{PP} / eV	ΔE_L / eV
1	-7.25	-7.29	0.04	-3.27	-3.28	0.02
2	-7.18	-7.21	0.03	-3.35	-3.37	0.02
3	-7.38	-7.40	0.02	-3.33	-3.35	0.02
4	-7.36	-7.38	0.02	-3.32	-3.34	0.02
5	-7.03	-7.07	0.05	-3.34	-3.36	0.02
6	-7.20	-7.25	0.05	-3.31	-3.33	0.02
7	-6.72	-6.74	0.02	-2.88	-2.90	0.02
8	-7.44	-7.45	0.01	-3.30	-3.32	0.02
9	-7.47	-7.48	0.01	-3.34	-3.37	0.02
10	-7.18	-7.22	0.04	-3.30	-3.33	0.02
Average	-7.22	-7.25	0.03	-3.27	-3.30	0.02

[a] Valence band edge E_H, conduction band edge E_L.

Table A.7: Overview of All Used Ionic Liquid Abbreviations

n	cation	anion	full name
1	$[C_2C_1Im]$	$[B(CN)_4]$	1-ethyl-3-methylimidazolium tetracyanoborate
2	$[C_2C_1Im]$	$[C(CN)_3]$	1-ethyl-3-methylimidazolium tricyanomethanide
3	$[C_2C_1Im]$	$[N(CN)_2]$	1-ethyl-3-methylimidazolium dicyanamide
4	$[C_2C_1Im]$	[SCN]	1-ethyl-3-methylimidazolium thiocyanate
5	$[C_2C_1Im]$	[Cl]	1-ethyl-3-methylimidazolium chloride
6	$[C_2C_1Im]$	[Br]	1-ethyl-3-methylimidazolium bromide
7	$[C_2C_1Im]$	[I]	1-ethyl-3-methylimidazolium iodide
8	$[C_2C_1Im]$	$[BF_4]$	1-ethyl-3-methylimidazolium tetrafluoroborate
9	$[C_2C_1Im]$	$[PF_6]$	1-ethyl-3-methylimidazolium hexafluorophosphate
10	$[C_2C_1Im]$	[FAP]	1-ethyl-3-methylimidazolium tris(pentafluoroethyl)trifluorophosphate
11	$[C_2C_1Im]$	[OTf]	1-ethyl-3-methylimidazolium triflate
12	$[C_2C_1Im]$	$[Tf_2N]$	1-ethyl-3-methylimidazolium bis(trifluoromethylsulfonyl)imide
13	$[C_2C_1Im]$	$[Pf_2N]$	1-ethyl-3-methylimidazolium bis(pentafluoroethylsulfonyl)imide
14	$[C_2C_1Im]$	[OAc]	1-ethyl-3-methylimidazolium acetate
15	$[C_2C_1Im]$	[TFA]	1-ethyl-3-methylimidazolium trifluoroacetate
16	$[C_2C_1Im]$	$[NO_3]$	1-ethyl-3-methylimidazolium nitrate
17	$[C_2C_1Im]$	[DP]	1-ethyl-3-methylimidazolium dihydrogenphosphate
18	$[C_2C_1Im]$	$[EtSO_4]$	1-ethyl-3-methylimidazolium ethylsulfate
19	$[C_1C_1Im]$	$[B(CN)_4]$	1-methyl-3-methylimidazolium tetracyanoborate
20	$[C_3C_1Im]$	$[B(CN)_4]$	1-propyl-3-methylimidazolium tetracyanoborate
21	$[C_4C_1Im]$	$[B(CN)_4]$	1-butyl-3-methylimidazolium tetracyanoborate
22	$[C_6C_1Im]$	$[B(CN)_4]$	1-hexyl-3-methylimidazolium tetracyanoborate
23	$[C_1C_1Im]$	[I]	1-methyl-3-methylimidazolium iodide
24	$[C_3C_1Im]$	[I]	1-propyl-3-methylimidazolium iodide
25	$[C_4C_1Im]$	[I]	1-butyl-3-methylimidazolium iodide
26	$[C_6C_1Im]$	[I]	1-hexyl-3-methylimidazolium iodide
27	$[(C_F)_2C_2C_1Im]$	[I]	1-(3.3-4.4.4-pentafluorobutyl)-3-methylimidazolium iodide
28	$[(C_F)_4C_2C_1Im]$	[I]	1-(3,3-4,4-5,5-6,6,6-nonafluorohexyl)-3-methylimidazolium iodide
29	$[(C_F)_6C_2C_1Im]$	[I]	1-(3,3-4,4-5,5-6,6-7,7-8,8,8-tridecafluorooctyl)-3-methylimidazolium iodide
30	$[(C_F)_2C_2C_1Im]$	$[BF_4]$	1-(3.3-4.4.4-pentafluorobutyl)-3-methylimidazolium tetrafluoroborate
31	$[(C_F)_4C_2C_1Im]$	$[BF_4]$	1-(3,3-4,4-5,5-6,6,6-nonafluorohexyl)-3-methylimidazolium tetrafluoroborate
32	$[(C_F)_6C_2C_1Im]$	$[BF_4]$	1-(3,3-4,4-5,5-6,6-7,7-8,8,8-tridecafluorooctyl)-3-methylimidazolium tetrafluoroborate
33	[Guan]	[I]	guanidinium iodide
34	$[AllylC_1Im]$	[I]	1-allyl-3-methylimidazolium iodide
35	$[C_2C_1C_1Im]$	[I]	1-ethyl-2,3-dimethylimidazolium iodide
36	$[C_4C_1Pyrr]$	[I]	1-butyl-1-methylpyrrolidinium iodide
37	$[C_2Py]$	[I]	1-ethylpyridinium iodide
38	$[C_4Py]$	[I]	1-butylpyridinium iodide
39	$[N_{1111}]$	[I]	tetramethylammonium iodide
40	$[N_{2222}]$	[I]	tetraethylammonium iodide
41	$[N_{4444}]$	[I]	tetrabutylammonium iodide
42	$[N_{4111}]$	[I]	butyl-trimethylammonium iodide

A.5 Supporting Information of: Ionic Liquid Influence on Excitation of Promising Dyes for Dye-Sensitized Solar Cells

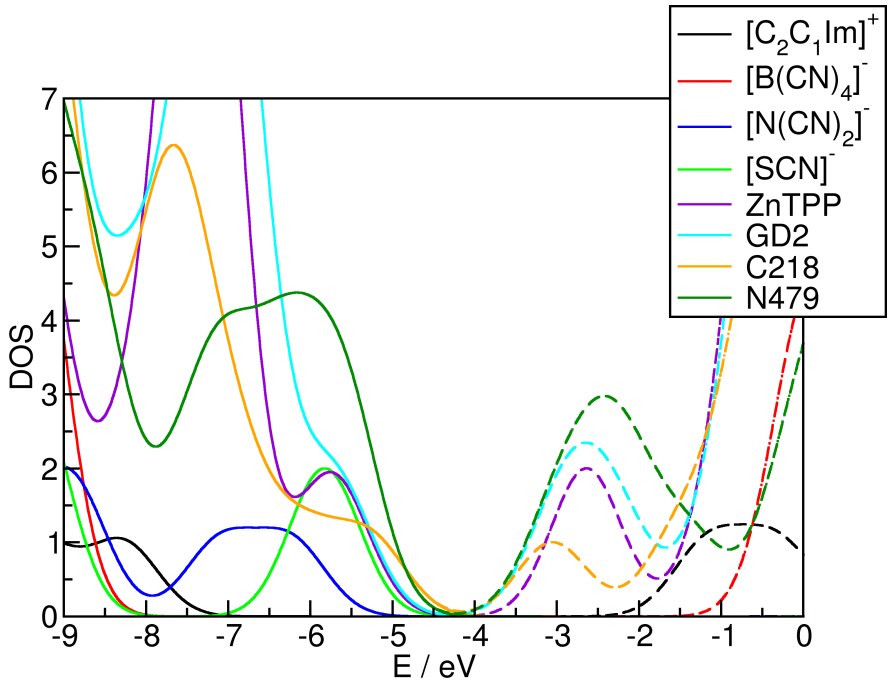

Figure A.14: Calculated density of states of all IL components and dyes. All fragments were embedded with the COSMO model. Straight lines indicate occupied states, the dashed lines indicate unoccupied, or virtual, states.

Table A.8: Ground State HOMO Energy E_H, LUMO Energy E_L and Band Gap Δ for the Dye Molecules in All Systems Investigated and Average Difference Between COSMO and Ionic Liquid Calculations[a]

dye	vacuum	COSMO	$[C_2C_1Im][B(CN)_4]$	$[C_2C_1Im][N(CN)_2]$	$[C_2C_1Im][SCN]$
			E_H / eV		
ZnTPP	-6.84	-7.04	-7.10	-6.94	-6.95
GD2	-6.78	-6.96	-6.97	-6.88	-6.99
C218s	-6.91	-6.85	-6.94	-6.89	-6.91
N749	–	-7.26	-7.26	-7.67	-7.58
difference(COSMO–IL)			-0.04	-0.07	-0.08
			E_L / eV		
ZnTPP	-1.11	-1.34	-1.50	-1.43	-1.42
GD2	-1.42	-1.64	-1.89	-1.66	-1.83
C218s	-1.38	-1.54	-1.56	-1.71	-1.54
N749	–	-1.29	-1.65	-1.70	-1.73
difference(COSMO–IL)			-0.20	-0.18	-0.18
			Δ / eV		
ZnTPP	5.73	5.71	5.60	5.51	5.53
GD2	5.37	5.32	5.08	5.22	5.16
C218s	5.53	5.32	5.38	5.18	5.37
N749	–	5.97	5.85	5.97	5.85
difference(COSMO–IL)			-0.10	-0.11	-0.10

[a]Obtained with the ωB97X-D3 functional. Averaged values for systems with explicit solvation.

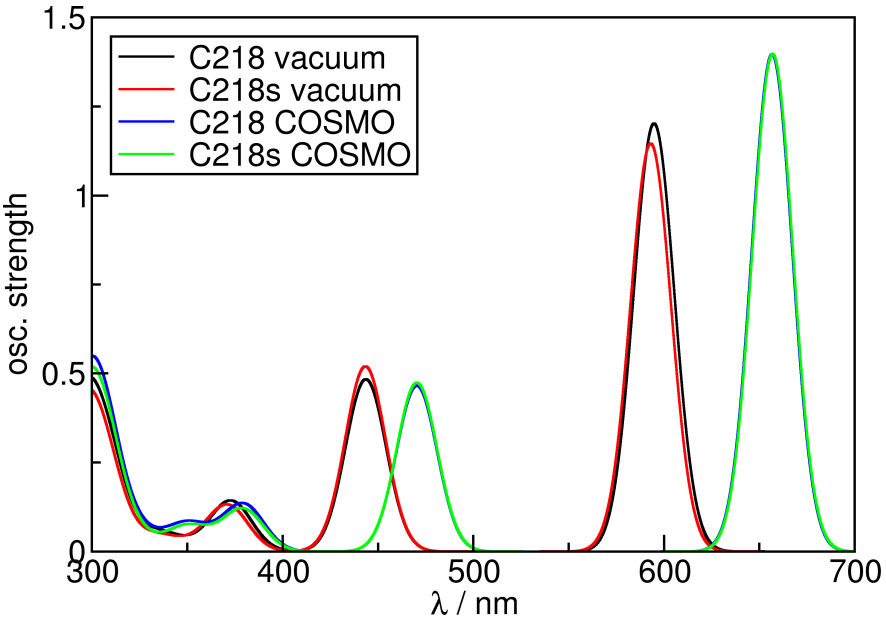

Figure A.15: Comparison of excitation spectra for original C218 dye and the C218s with shortened alkyl chains.

List of Acronyms

Acc	acceptor
ACF	autocorrelation function
AIMD	*ab initio* molecular dynamics
AM	air mass
B88	Becke88
B95	Becke95
B-LYP	Becke–Lee, Yang, Parr
BJ	Becke–Johnson
BMH	Born–Mayer–Huggins
BSSE	basis set superposition error
CAM	Coulomb-attenuating method
CB	conduction band
CE	counter electrode
CP	counterpoise correction
CDF	combined distribution function
CIS	configuration interaction (singles)
CoM	center of mass
CoR	center of ring
COSMO	conductor-like screening model
CSVR	canonical sampling through velocity rescaling
CT	charge transfer
DFT	density functional theory
Do	donor
DOS	density of states
DSC	dye-sensitized solar cell
FF	force field
FTO	fluorine-doped tin oxide
GC	gradient-corrected
GGA	generalized gradient approximation
GTH	Godecker–Teter–Hutter
HB	hydrogen bond
HF	Hartree–Fock
HOMO	highest occupied molecular orbital
IL	ionic liquid

LC	long-range corrected
LDA	local density approximation
LJ	Lennard-Jones
LSDA	local spin density approximation
LR	linear response
LUMO	lowest unoccupied molecular orbital
MD	molecular dynamics
MLCT	metal-to-ligand charge transfer
MM	molecular mechanics
OPV	organic photovoltaics
PBE	Perdew–Burke–Ernzerhof
PIM	polarizable ion model
PSC	perovskite solar cell
QC	quantum chemistry
QM	quantum mechanics
PBC	periodic boundary condition
PDOS	projected density of states
PV	photovoltaic
RDF	radial distribution function
RESP	restrained electrostatic potential
RN	ring normal
SCF	self-consistent field
SDF	spatial distribution function
SI	supporting information
SIE	self-interaction error
SN	surface normal
sTD-DFT	simplified time-dependent density functional theory
sTDA	simplified Tamm–Dancoff Approximation
TBP	4-*tert*-butylpyridine
TD-DFT	time-dependent density functional theory
TDA	Tamm–Dancoff approximation
TPSS	Tao–Perdew–Staroverov–Scuseria
TSIL	task-specific ionic liquid
UV	ultraviolet
UV/VIS	ultraviolet-visible
WE	working electrode
WFN	wavefunction
XC	exchange-correlation

List of Figures

List of Tables

Bibliography

[1] Ellabban, O.; Abu-Rub, H.; Blaabjerg, F. *Renewable Sustainable Energy Rev.* **2014**, *39*, 748–764.

[2] Zhao, J.; Wang, A.; Green, M. A.; Ferrazza, F. *Appl. Phys. Lett.* **1998**, *73*, 1991–1993.

[3] Carlson, D. E.; Wronski, C. R. *Appl. Phys. Lett.* **1976**, *28*, 671–673.

[4] Staebler, D. L.; Wronski, C. R. *Appl. Phys. Lett.* **1977**, *31*, 292–294.

[5] Cusano, D. *Solid-State Electron.* **1963**, *6*, 217–218.

[6] Dimmler, B.; Schock, H. W. *Prog. Photovoltaics Res. Appl.* **1996**, *4*, 425–433.

[7] Alferov, Z. I.; Andreev, V. M.; Kagan, M. B.; Protasov, I. I.; Trofim, V. G. *Sov. Phys. Semicond.* **1971**, *4*, 2047.

[8] Sasaki, K.; Agui, T.; Nakaido, K.; Takahashi, N.; Onitsuka, R.; Takamoto, T. *Proceedings, 9th International Conference on Concentrating Photovoltaics Systems* **2013**, Miyazaki, Japan.

[9] Green, M. A.; Emery, K.; Hishikawa, Y.; Warta, W.; Dunlop, E. D. *Prog. Photovoltaics Res. Appl.* **2016**, *24*, 3–11.

[10] National Center for Photovoltaics, `http://www.nrel.gov/ncpv/`, accessed April 2016.

[11] Abdulrazzaq, O. A.; Saini, V.; Bourdo, S.; Dervishi, E.; Biris, A. S. *Part. Sci. Technol.* **2013**, *31*, 427–442.

[12] Hu, H.; Jiang, K.; Yang, G.; Liu, J.; Li, Z.; Lin, H.; Liu, Y.; Zhao, J.; Zhang, J.; Huang, F.; Qu, Y.; Ma, W.; Yan, H. *J. Am. Chem. Soc.* **2015**, *137*, 14149–14157.

[13] O'Regan, B.; Grätzel, M. *Nature* **1991**, *353*, 737–740.

[14] Halme, J.; Boschloo, G.; Hagfeldt, A.; Lund, P. *J. Phys. Chem. C* **2008**, *112*, 5623–5637.

[15] Jennings, J. R.; Ghicov, A.; Peter, L. M.; Schmuki, P.; Walker, A. B. *J. Am. Chem. Soc.* **2008**, *130*, 13364–13372.

[16] O'Regan, B.; Moser, J.; Anderson, M.; Grätzel, M. *J. Phys. Chem.* **1990**, *94*, 8720–8726.

[17] Södergren, S.; Hagfeldt, A.; Olsson, J.; Lindquist, S.-E. *J. Phys. Chem.* **1994**, *98*, 5552–5556.

[18] Solbrand, A.; Lindström, H.; Rensmo, H.; Hagfeldt, A.; Lindquist, S.-E.; Södergren, S. *J. Phys. Chem. B* **1997**, *101*, 2514–2518.

[19] Nakade, S.; Kanzaki, T.; Kubo, W.; Kitamura, T.; Wada, Y.; Yanagida, S. *J. Phys. Chem. B* **2005**, *109*, 3480–3487.

[20] Boschloo, G.; Fitzmaurice, D. *J. Phys. Chem. B* **1999**, *103*, 2228–2231.

[21] Thompson, T. L.; John T. Yates, J. *Chem. Rev.* **2006**, *106*, 4428–4453.

[22] Westermark, K.; Henningsson, A.; Rensmo, H.; Södergren, S.; Siegbahn, H.; Hagfeldt, A. *Chem. Phys.* **2002**, *285*, 157–165.

[23] Hendry, E.; Koeberg, M.; O'Regan, B.; Bonn, M. *Nano Lett.* **2006**, *6*, 755–759.

[24] Peter, L. *Acc. Chem. Res.* **2009**, *42*, 1839–1847.

[25] Benkstein, K. D.; Kopidakis, N.; van de Lagemaat, J.; Frank, A. J. *J. Phys. Chem. B* **2003**, *107*, 7759–7767.

[26] Moser, J. E.; Grätzel, M. *Chem. Phys.* **1993**, *176*, 493–500.

[27] Kuciauskas, D.; Freund, M. S.; Gray, H. B.; Winkler, J. R.; Lewis, N. S. *J. Phys. Chem. B* **2001**, *105*, 392–403.

[28] Kelly, C. A.; Farzad, F.; Thompson, D. W.; Stipkala, J. M.; Meyer, G. J. *Langmuir* **1999**, *15*, 7047–7054.

[29] Clifford, J. N.; Palomares, E.; Nazeeruddin, M. K.; Grätzel, M.; Nelson, J.; Li, X.; Long, N. J.; Durrant, J. R. *J. Am. Chem. Soc.* **2004**, *126*, 5225–5233.

[30] Yan, S. G.; Prieskorn, J. S.; Kim, Y.; ; Hupp, J. T. *J. Phys. Chem. B* **2000**, *104*, 10871–10877.

[31] Gong, J.; Liang, J.; Sumathy, K. *Renewable Sustainable Energy Rev.* **2012**, *16*, 5848–5860.

[32] K. Nazeeruddin, M.; Pechy, P.; Gratzel, M. *Chem. Commun.* **1997**, 1705–1706.

[33] Hwang, S.; Lee, J. H.; Park, C.; Lee, H.; Kim, C.; Park, C.; Lee, M.-H.; Lee, W.; Park, J.; Kim, K.; Park, N.-G.; Kim, C. *Chem. Commun.* **2007**, 4887–4889.

[34] Mathew, S.; Yella, A.; Gao, P.; Humphry-Baker, R.; Curchod, F. E.; Ashari-Astani, N.; Tavernelli, I.; Rothlisberger, U.; Nazeeruddin, M. K.; Grätzel, M. *Nature Chem.* **2014**, *6*, 242–247.

[35] Nazeeruddin, M. K.; Péchy, P.; Renouard, T.; Zakeeruddin, S. M.; Humphry-Baker, R.; Comte, P.; Liska, P.; Cevey, L.; Costa, E.; Shklover, V.; Spiccia, L.; Deacon, G. B.; Bignozzi, C. A.; Grätzel, M. *J. Am. Chem. Soc.* **2001**, *123*, 1613–1624.

[36] Kay, A.; Grätzel, M. *J. Phys. Chem.* **1993**, *97*, 6272–6277.

[37] Campbell, W. M.; Jolley, K. W.; Wagner, P.; Wagner, K.; Walsh, P. J.; Gordon, K. C.; Schmidt-Mende, L.; Nazeeruddin, M. K.; Wang, Q.; Grätzel, M.; Officer, D. L. *J. Phys. Chem. C* **2007**, *111*, 11760–11762.

[38] Li, L.-L.; Diau, E. W.-G. *Chem. Soc. Rev.* **2013**, *42*, 291–304.

[39] Ma, X.; Hua, J.; Wu, W.; Jin, Y.; Meng, F.; Zhan, W.; Tian, H. *Tetrahedron* **2008**, *64*, 345–350.

[40] Sayama, K.; Tsukagoshi, S.; Mori, T.; Hara, K.; Ohga, Y.; Shinpou, A.; Abe, Y.; Suga, S.; Arakawa, H. *Sol. Energy Mater. Sol. Cells* **2003**, *80*, 47–71.

[41] Sayama, K.; Hara, K.; Mori, N.; Satsuki, M.; Suga, S.; Tsukagoshi, S.; Abe, Y.; Sugihara, H.; Arakawa, H. *Chem. Commun.* **2000**, 1173–1174.

[42] Giribabu, L.; Kumar, C. V.; Reddy, V. G.; Reddy, P. Y.; Rao, C. S.; Jang, S.-R.; Yum, J.-H.; Nazeeruddin, M. K.; Grätzel, M. *Sol. Energy Mater. Sol. Cells* **2007**, *91*, 1611–1617.

[43] Horiuchi, T.; Miura, H.; Uchida, S. *Chem. Commun.* **2003**, 3036–3037.

[44] Hara, K.; Kurashige, M.; Dan-oh, Y.; Kasada, C.; Shinpo, A.; Suga, S.; Sayama, K.; Arakawa, H. *New J. Chem.* **2003**, *27*, 783–785.

[45] Wang, Z.-S.; Sayama, K.; Sugihara, H. *J. Phys. Chem. B* **2005**, *109*, 22449–22455.

[46] Ferrere, S.; Zaban, A.; Gregg, B. A. *J. Phys. Chem. B* **1997**, *101*, 4490–4493.

[47] Li, C.; Yang, X.; Chen, R.; Pan, J.; Tian, H.; Zhu, H.; Wang, X.; Hagfeldt, A.; Sun, L. *Sol. Energy Mater. Sol. Cells* **2007**, *91*, 1863–1871.

[48] Zhao, W.; Hou, Y. J.; Wang, X. S.; Zhang, B. W.; Cao, Y.; Yang, R.; Wang, W. B.; Xiao, X. R. *Sol. Energy Mater. Sol. Cells* **1999**, *58*, 173–183.

[49] Yum, J.-H.; Walter, P.; Huber, S.; Rentsch, D.; Geiger, T.; Nüesch, F.; De Angelis, F.; Grätzel, M.; Nazeeruddin, M. K. *J. Am. Chem. Soc.* **2007**, *129*, 10320–10321.

[50] Yum, J. H.; Moon, S. J.; Humphry-Baker, R.; Walter, P.; Geiger, T.; Nüesch, F.; Grätzel, M.; d K Nazeeruddin, M. *Nanotechnology* **2008**, *19*, 424005.

[51] Liang, M.; Xu, W.; Cai, F.; Chen, P.; Peng, B.; Chen, J.; Li, Z. *J. Phys. Chem. C* **2007**, *111*, 4465–4472.

[52] Tian, H.; Yang, X.; Chen, R.; Zhang, R.; Hagfeldt, A.; Sun, L. *J. Phys. Chem. C* **2008**, *112*, 11023–11033.

[53] Li, R.; Liu, J.; Cai, N.; Zhang, M.; Wang, P. *J. Phys. Chem. B* **2010**, *114*, 4461–4464.

[54] Goncalves, L. M.; de Zea Bermudez, V.; Ribeiro, H. A.; Mendes, A. M. *Energy Environ. Sci.* **2008**, *1*, 655–667.

[55] Kuang, D.; Uchida, S.; Humphry-Baker, R.; Zakeeruddin, S. M.; Grätzel, M. *Angew. Chem. Int. Ed.* **2008**, *47*, 1923–1927.

[56] Bessho, T.; Zakeeruddin, S. M.; Yeh, C.-Y.; Diau, E. W.-G.; Grätzel, M. *Angew. Chem. Int. Ed.* **2010**, *49*, 6646–6649.

[57] Yella, A.; Lee, H.-W.; Tsao, H. N.; Yi, C.; Chandiran, A. K.; Nazeeruddin, M.; Diau, E. W.-G.; Yeh, C.-Y.; Zakeeruddin, S. M.; Grätzel, M. *Science* **2011**, *334*, 629–634.

[58] Lee, J.-J.; Coia, G. M.; Lewis, N. S. *J. Phys. Chem. B* **2004**, *108*, 5269–5281.

[59] Clifford, J. N.; Palomares, E.; Nazeeruddin, M. K.; Grätzel, M.; Durrant, J. R. *J. Phys. Chem. C* **2007**, *111*, 6561–6567.

[60] Montanari, I.; Nelson, J.; Durrant, J. R. *J. Phys. Chem. B* **2002**, *106*, 12203–12210.

[61] Boschloo, G.; Hagfeldt, A. *Acc. Chem. Res.* **2009**, *42*, 1819–1826.

[62] Rowley, J.; Meyer, G. J. *J. Phys. Chem. C* **2009**, *113*, 18444–18447.

[63] Peter, L. M. *J. Phys. Chem. C* **2007**, *111*, 6601–6612.

[64] Papageorgiou, N.; Athanassov, Y.; Armand, M.; Bonhôte, P.; Pettersson, H.; Azam, A.; Grätzel, M. *J. Electrochem. Soc.* **1996**, *143*, 3099–3108.

[65] Kawano, R.; Watanabe, M. *Chem. Commun.* **2005**, 2107–2109.

[66] Boschloo, G.; Gibson, E. A.; Hagfeldt, A. *J. Phys. Chem. Lett.* **2011**, *2*, 3016–3020.

[67] Ondersma, J. W.; Hamann, T. W. *Coord. Chem. Rev.* **2013**, *257*, 1533–1543.

[68] Alebbi, M.; Bignozzi, C. A.; Heimer, T. A.; Hasselmann, G. M.; Meyer, G. J. *J. Phys. Chem. B* **1998**, *102*, 7577–7581.

[69] O'Regan, B. C.; López-Duarte, I.; Martínez-Díaz, M. V.; Forneli, A.; Albero, J.; Palomares, A. M. E.; Torres, T.; Durrant, J. R. *J. Am. Chem. Soc.* **2008**, *130*, 2906–2907.

[70] Splan, K. E.; Massari, A. M.; ; Hupp, J. T. *J. Phys. Chem. B* **2004**, *108*, 4111–4115.

[71] Hara, K.; Horiguchi, T.; Kinoshita, T.; Sayama, K.; Arakawa, H. *Sol. Energy Mater. Sol. Cells* **2001**, *70*, 151–161.

[72] Oskam, G.; Bergeron, B. V.; Meyer, G. J.; Searson, P. C. *J. Phys. Chem. B* **2001**, *105*, 6867–6873.

[73] Bergeron, B. V.; Marton, A.; Oskam, G.; Meyer, G. J. *J. Phys. Chem. B* **2005**, *109*, 937–943.

[74] Wang, P.; Zakeeruddin, S. M.; Moser, J.-E.; Humphry-Baker, R.; Grätzel, M. *J. Am. Chem. Soc.* **2004**, *126*, 7164–7165.

[75] Gregg, B. A.; Pichot, F.; Ferrere, S.; Fields, C. L. *J. Phys. Chem. B* **2001**, *105*, 1422–1429.

[76] Li, T. C.; Spokoyny, A. M.; She, C.; Farha, O. K.; Mirkin, C. A.; Marks, T. J.; Hupp, J. T. *J. Am. Chem. Soc.* **2010**, *132*, 4580–4582.

[77] Hattori, S.; Wada, Y.; Yanagida, S.; Fukuzumi, S. *J. Am. Chem. Soc.* **2005**, *127*, 9648–9654.

[78] Hamann, T. W. *Dalton Trans.* **2012**, *41*, 3111–3115.

[79] Sapp, S. A.; Elliott, C. M.; Contado, C.; Caramori, S.; Bignozzi, C. A. *J. Am. Chem. Soc.* **2002**, *124*, 11215–11222.

[80] Bai, Y.; Zhang, J.; Zhou, D.; Wang, Y.; Zhang, M.; Wang, P. *J. Am. Chem. Soc.* **2011**, *133*, 11442–11445.

[81] Nusbaumer, H.; Moser, J.-E.; Zakeeruddin, S. M.; Nazeeruddin, M. K.; Grätzel, M. *J. Phys. Chem. B* **2001**, *105*, 10461–10464.

[82] Feldt, S. M.; Gibson, E. A.; Gabrielsson, E.; Sun, L.; Boschloo, G.; Hagfeldt, A. *J. Am. Chem. Soc.* **2010**, *132*, 16714–16724.

[83] Nelson, J. J.; Amick, T. J.; Elliott, C. M. *J. Phys. Chem. C* **2008**, *112*, 18255–18263.

[84] Klahr, B. M.; Hamann, T. W. *J. Phys. Chem. C* **2009**, *113*, 14040–14045.

[85] Hagfeldt, A.; Boschloo, G.; Sun, L.; Kloo, L.; Pettersson, H. *Chem. Rev.* **2010**, *110*, 6595–6663.

[86] Hauch, A.; Georg, A. *Electrochim. Acta* **2001**, *46*, 3457–3466.

[87] Papageorgiou, N.; Maier, W. F.; Grätzel, M. *J. Electrochem. Soc.* **1997**, *144*, 876–884.

[88] Pettersson, H.; Gruszecki, T.; Bernhard, R.; Häggman, L.; Gorlov, M.; Boschloo, G.; Edvinsson, T.; Kloo, L.; Hagfeldt, A. *Prog. Photovoltaics Res. Appl.* **2007**, *15*, 113–121.

[89] Kay, A.; Grätzel, M. *Sol. Energy Mater. Sol. Cells* **1996**, *44*, 99–117.

[90] Suzuki, K.; Yamaguchi, M.; Kumagai, M.; Yanagida, S. *Chem. Lett.* **2003**, *32*, 28–29.

[91] Bay, L.; West, K.; Winther-Jensen, B.; Jacobsen, T. *Sol. Energy Mater. Sol. Cells* **2006**, *90*, 341–351.

[92] Saito, Y.; Kitamura, T.; Wada, Y.; Yanagida, S. *Chem. Lett.* **2002**, *31*, 1060–1061.

[93] Saito, Y.; Kubo, W.; Kitamura, T.; Wada, Y.; Yanagida, S. *J. Photochem. Photobiol., A* **2004**, *164*, 153–157.

[94] Wang, M.; Anghel, A. M.; Marsan, B.; Cevey Ha, N.-L.; Pootrakulchote, N.; Zakeeruddin, S. M.; Grätzel, M. *J. Am. Chem. Soc.* **2009**, *131*, 15976–15977.

[95] Wu, J.; Lan, Z.; Lin, J.; Huang, M.; Huang, Y.; Fan, L.; Luo, G. *Chem. Rev.* **2015**, *115*, 2136–2173.

[96] Wu, J.; Lan, Z.; Hao, S.; Li, P.; Lin, J.; Huang, M.; Fang, L.; Huang, Y. *Pure Appl. Chem.* **2008**, *80*, 2241–2258.

[97] Ardo, S.; Meyer, G. J. *Chem. Soc. Rev.* **2009**, *38*, 115–164.

[98] Nogueira, A.; Longo, C.; De Paoli, M.-A. *Coord. Chem. Rev.* **2004**, *248*, 1455–1468.

[99] Yu, Z.; Vlachopoulos, N.; Gorlov, M.; Kloo, L. *Dalton Trans.* **2011**, *40*, 10289–10303.

[100] Gorlov, M.; Kloo, L. *Dalton Trans.* **2008**, 2655–2666.

[101] Nei de Freitas, J.; Nogueira, A. F.; De Paoli, M.-A. *J. Mater. Chem.* **2009**, *19*, 5279–5294.

[102] Li, B.; Wang, L.; Kang, B.; Wang, P.; Qiu, Y. *Sol. Energy Mater. Sol. Cells* **2006**, *90*, 549–573.

[103] Zhang, W.; Cheng, Y.; Yin, X.; Liu, B. *Macromol. Chem. Phys.* **2011**, *212*, 15–23.

[104] Wu, J.; Lan, Z.; Lin, J.; Huang, M.; Hao, S.; Sato, T.; Yin, S. *Adv. Mater.* **2007**, *19*, 4006–4011.

[105] Wu, J.; Hao, S.; Lan, Z.; Lin, J.; Huang, M.; Huang, Y.; Fang, L.; Yin, S.; Sato, T. *Adv. Funct. Mater.* **2007**, *17*, 2645–2652.

[106] Li, D.; Qin, D.; Deng, M.; Luo, Y.; Meng, Q. *Energy Environ. Sci.* **2009**, *2*, 283–291.

[107] Stathatos, E.; Lianos, P.; Lavrencic-Stangar, U.; Orel, B. *Adv. Mater.* **2002**, *14*, 354–357.

[108] Nogueira, A. F.; Durrant, J. R.; De Paoli, M. A. *Adv. Mater.* **2001**, *13*, 826–830.

[109] Wu, J.; Hao, S.; Lan, Z.; Lin, J.; Huang, M.; Huang, Y.; Li, P.; Yin, S.; Sato, T. *J. Am. Chem. Soc.* **2008**, *130*, 11568–11569.

[110] Lowman, G. M.; Hammond, P. T. *Small* **2005**, *1*, 1070–1073.

[111] Meng, Q.-B.; Takahashi, K.; Zhang, X.-T.; Sutanto, I.; Rao, T. N.; Sato, O.; Fujishima, A.; Watanabe, H.; Nakamori, T.; Uragami, M. *Langmuir* **2003**, *19*, 3572–3574.

[112] Saito, Y.; Azechi, T.; Kitamura, T.; Hasegawa, Y.; Wada, Y.; Yanagida, S. *Coord. Chem. Rev.* **2004**, *248*, 1469–1478.

[113] Chung, I.; Lee, B.; He, J.; Chang, R. P. H.; Kanatzidis, M. G. *Nature* **2012**, *485*, 486–489.

[114] Bach, U.; Lupo, D.; Comte, P.; Moser, J.; Weissortel, F.; Salbeck, J.; Spreitzer, H.; Grätzel, M. *Nature* **1998**, *395*, 583–585.

[115] Snaith, H. J.; Moule, A. J.; Klein, C.; Meerholz, K.; Friend, R. H.; Grätzel, M. *Nano Lett.* **2007**, *7*, 3372–3376.

[116] Campbell, W. M.; Burrell, A. K.; Officer, D. L.; Jolley, K. W. *Coord. Chem. Rev.* **2004**, *248*, 1363–1379.

[117] Ito, S.; Nazeeruddin, M. K.; Liska, P.; Comte, P.; Charvet, R.; Péchy, P.; Jirousek, M.; Kay, A.; Zakeeruddin, S. M.; Grätzel, M. *Prog. Photovoltaics Res. Appl.* **2006**, *14*, 589–601.

[118] Wang, P.; Wenger, B.; Humphry-Baker, R.; Moser, J.-E.; Teuscher, J.; Kantlehner, W.; Mezger, J.; Stoyanov, E. V.; Zakeeruddin, S. M.; ; Grätzel, M. *J. Am. Chem. Soc.* **2005**, *127*, 6850–6856.

[119] Wang, P.; Zakeeruddin, S. M.; Humphry-Baker, R.; Grätzel, M. *Chem. Mater.* **2004**, *16*, 2694–2696.

[120] Wang, P.; Zakeeruddin, S. M.; Moser, J.-E.; Grätzel, M. *J. Phys. Chem. B* **2003**, *107*, 13280–13285.

[121] Kuang, D.; Wang, P.; Ito, S.; Zakeeruddin, S. M.; Grätzel, M. *J. Am. Chem. Soc.* **2006**, *128*, 7732–7733.

[122] Wang, P.; Klein, C.; Humphry-Baker, R.; Zakeeruddin, S. M.; Grätzel, M. *Appl. Phys. Lett.* **2005**, *86*, 123508.

[123] Chen, L.-H.; Xue, B.-F.; Liu, X.-Z.; Li, K.-X.; Luo, Y.-H.; Meng, Q.-B.; Wang, R.-L.; Chen, L.-Q. *Chin. Phys. Lett.* **2007**, *24*, 555–558.

[124] Fei, Z.; Kuang, D.; Zhao, D.; Klein, C.; Ang, W. H.; Zakeeruddin, S. M.; Grätzel, M.; Dyson, P. J. *Inorg. Chem.* **2006**, *45*, 10407–10409.

[125] Ito, S.; Zakeeruddin, S.; Humphry-Baker, R.; Liska, P.; Charvet, R.; Comte, P.; Nazeeruddin, M.; Péchy, P.; Takata, M.; Miura, H.; Uchida, S.; Grätzel, M. *Adv. Mater.* **2006**, *18*, 1202–1205.

[126] Fabregat-Santiago, F.; Bisquert, J.; Palomares, E.; Otero, L.; Kuang, D.; Zakeeruddin, S. M.; Grätzel, M. *J. Phys. Chem. C* **2007**, *111*, 6550–6560.

[127] Fan, L.; Kang, S.; Wu, J.; Hao, S.; Lan, Z.; Lin, J. *Energy Sources A* **2010**, *32*, 1559–1568.

[128] Xu, D.; Zhang, H.; Chen, X.; Yan, F. *J. Mater. Chem. A* **2013**, *1*, 11933–11941.

[129] Chen, X.; Xu, D.; Qiu, L.; Li, S.; Zhang, W.; Yan, F. *J. Mater. Chem. A* **2013**, *1*, 8759–8765.

[130] Wang, L.; Zhang, H.; Ge, R.; Wang, C.; Guo, W.; Shi, Y.; Gao, Y.; Ma, T. *RSC Adv.* **2013**, *3*, 12975–12980.

[131] Shi, D.; Pootrakulchote, N.; Li, R.; Guo, J.; Wang, Y.; Zakeeruddin, S. M.; Grätzel, M.; Wang, P. *J. Phys. Chem. C* **2008**, *112*, 17046–17050.

[132] Sauvage, F.; Chhor, S.; Marchioro, A.; Moser, J.-E.; Grätzel, M. *J. Am. Chem. Soc.* **2011**, *133*, 13103–13109.

[133] MacFarlane, D. R.; Tachikawa, N.; Forsyth, M.; Pringle, J. M.; Howlett, P. C.; Elliott, G. D.; Davis, J. H.; Watanabe, M.; Simon, P.; Angell, C. A. *Energy Environ. Sci.* **2014**, *7*, 232–250.

[134] Howlett, P. C.; MacFarlane, D. R.; Hollenkamp, A. F. *Electrochem. Solid-State Lett.* **2004**, *7*, A97–A101.

[135] Garcia, B.; Lavallée, S.; Perron, G.; Michot, C.; Armand, M. *Electrochim. Acta* **2004**, *49*, 4583–4588.

[136] Kim, G.-T.; Jeong, S.; Xue, M.-Z.; Balducci, A.; Winter, M.; Passerini, S.; Alessandrini, F.; Appetecchi, G. *J. Power Sources* **2012**, *199*, 239–246.

[137] Yoon, H.; Lane, G. H.; Shekibi, Y.; Howlett, P. C.; Forsyth, M.; Best, A. S.; MacFarlane, D. R. *Energy Environ. Sci.* **2013**, *6*, 979–986.

[138] Balducci, A.; Jeong, S.; Kim, G.; Passerini, S.; Winter, M.; Schmuck, M.; Appetecchi, G.; Marcilla, R.; Mecerreyes, D.; Barsukov, V.; Khomenko, V.; Cantero, I.; De Meatza, I.; Holzapfel, M.; Tran, N. *J. Power Sources* **2011**, *196*, 9719–9730.

[139] Nikitina, V. A.; Nazet, A.; Sonnleitner, T.; Buchner, R. *J. Chem. Eng. Data* **2012**, *57*, 3019–3025.

[140] Noor, S. A. M.; Howlett, P. C.; MacFarlane, D. R.; Forsyth, M. *Electrochim. Acta* **2013**, *114*, 766–771.

[141] Khoo, T.; Howlett, P. C.; Tsagouria, M.; MacFarlane, D. R.; Forsyth, M. *Electrochim. Acta* **2011**, *58*, 583–588.

[142] Khoo, T.; Somers, A.; Torriero, A. A.; MacFarlane, D. R.; Howlett, P. C.; Forsyth, M. *Electrochim. Acta* **2013**, *87*, 701–708.

[143] Kakibe, T.; ya Hishii, J.; Yoshimoto, N.; Egashira, M.; Morita, M. *J. Power Sources* **2012**, *203*, 195–200.

[144] Simons, T. J.; Howlett, P. C.; Torriero, A. A. J.; MacFarlane, D. R.; Forsyth, M. *J. Phys. Chem. C* **2013**, *117*, 2662–2669.

[145] Rocher, N. M.; Izgorodina, E. I.; Rüther, T.; Forsyth, M.; MacFarlane, D. R.; Rodopoulos, T.; Horne, M. D.; Bond, A. M. *Chem. Eur. J.* **2009**, *15*, 3435–3447.

[146] Sun, J.; Jordan, L.; Forsyth, M.; MacFarlane, D. *Electrochim. Acta* **2001**, *46*, 1703–1708.

[147] Noda, A.; Susan, M. A. B. H.; Kudo, K.; Mitsushima, S.; Hayamizu, K.; Watanabe, M. *J. Phys. Chem. B* **2003**, *107*, 4024–4033.

[148] Angell, C. A.; Xu, W.; Belieres, J.-P.; Yoshizawa, M. U.S. Patent WO2004114445A1, **2004**.

[149] Abraham, T. J.; MacFarlane, D. R.; Pringle, J. M. *Energy Environ. Sci.* **2013**, *6*, 2639–2645.

[150] MacFarlane, D. R.; Forsyth, M.; Howlett, P. C.; Pringle, J. M.; Sun, J.; Annat, G.; Neil, W.; Izgorodina, E. I. *Acc. Chem. Res.* **2007**, *40*, 1165–1173.

[151] Balducci, A.; Dugas, R.; Taberna, P.; Simon, P.; Plée, D.; Mastragostino, M.; Passerini, S. *J. Power Sources* **2007**, *165*, 922–927.

[152] Lin, R.; Taberna, P.; Fantini, S.; Presser, V.; Pérez, C. R.; Malbosc, F.; Rupesinghe, N. L.; Teo, K. B. K.; Gogotsi, Y.; Simon, P. *J. Phys. Chem. Lett.* **2011**, *2*, 2396–2401.

[153] Lu, W.; Fadeev, A. G.; Qi, B.; Smela, E.; Mattes, B. R.; Ding, J.; Spinks, G. M.; Mazurkiewicz, J.; Zhou, D.; Wallace, G. G.; MacFarlane, D. R.; Forsyth, S. A.; Forsyth, M. *Science* **2002**, *297*, 983–987.

[154] Zhou, F.; Izgorodin, A.; Hocking, R. K.; Spiccia, L.; MacFarlane, D. R. *Adv. Energy Mater.* **2012**, *2*, 1013–1021.

[155] Izgorodin, A.; Izgorodina, E.; MacFarlane, D. R. *Energy Environ. Sci.* **2012**, *5*, 9496–9501.

[156] Bates, E. D.; Mayton, R. D.; Ntai, I.; James H. Davis, J. *J. Am. Chem. Soc.* **2002**, *124*, 926–927.

[157] Soutullo, M. D.; Odom, C. I.; Wicker, B. F.; Henderson, C. N.; Stenson, A. C.; James H. Davis, J. *Chem. Mater.* **2007**, *19*, 3581–3583.

[158] Goodrich, B. F.; de la Fuente, J. C.; Gurkan, B. E.; Lopez, Z. K.; Price, E. A.; Huang, Y.; Brennecke, J. F. *J. Phys. Chem. B* **2011**, *115*, 9140–9150.

[159] Firaha, D. S.; Hollóczki, O.; Kirchner, B. *Angew. Chem. Int. Ed.* **2015**, *54*, 7805–7809.

[160] Zhou, D.; Bai, Y.; Zhang, J.; Cai, N.; Su, M.; Wang, Y.; Zhang, M.; Wang, P. *J. Phys. Chem. C* **2011**, *115*, 816–822.

[161] Zhang, M.; Zhang, J.; Bai, Y.; Wang, Y.; Su, M.; Wang, P. *Phys. Chem. Chem. Phys.* **2011**, *13*, 3788–3794.

[162] Bai, Y.; Zhang, J.; Wang, Y.; Zhang, M.; Wang, P. *Langmuir* **2011**, *27*, 4749–4755.

[163] Dai, Q.; Menzies, D. B.; MacFarlane, D. R.; Batten, S. R.; Forsyth, S.; Spiccia, L.; Cheng, Y.-B.; Forsyth, M. *C.R. Chim.* **2006**, *9*, 617–621.

[164] Wachter, P.; Schreiner, C.; Zistler, M.; Gerhard, D.; Wasserscheid, P.; Gores, H. J. *Microchim. Acta* **2008**, *160*, 125–133.

[165] Kawano, R.; Matsui, H.; Matsuyama, C.; Sato, A.; Susan, M. B. H.; Tanabe, N.; Watanabe, M. *J. Photochem. Photobiol., A* **2004**, *164*, 87–92.

[166] Fredin, K.; Gorlov, M.; Pettersson, H.; Hagfeldt, A.; Kloo, L.; Boschloo, G. *J. Phys. Chem. C* **2007**, *111*, 13261–13266.

[167] Bai, Y.; Cao, Y.; Zhang, J.; Wang, M.; Li, R.; Wang, P.; Zakeeruddin, S. M.; Grätzel, M. *Nat. Mater.* **2008**, *7*, 626–630.

[168] Cao, Y.; Zhang, J.; Bai, Y.; Li, R.; Zakeeruddin, S. M.; Grätzel, M.; Wang, P. *J. Phys. Chem. C* **2008**, *112*, 13775–13781.

[169] Zakeeruddin, S. M.; Grätzel, M. *Adv. Funct. Mater.* **2009**, *19*, 2187–2202.

[170] Kambe, S.; Nakade, S.; Kitamura, T.; Wada, Y.; Yanagida, S. *J. Phys. Chem. B* **2002**, *106*, 2967–2972.

[171] Nakade, S.; Saito, Y.; Kubo, W.; Kanzaki, T.; Kitamura, T.; Wada, Y.; Yanagida, S. *Electrochem. Commun.* **2003**, *5*, 804–808.

[172] Shi, C.; Dai, S.; Wang, K.; Pan, X.; Kong, F.; Hu, L. *Vib. Spectrosc.* **2005**, *39*, 99–105.

[173] Nazeeruddin, M. K.; Kay, A.; Rodicio, I.; Humphry-Baker, R.; Mueller, E.; Liska, P.; Vlachopoulos, N.; Grätzel, M. *J. Am. Chem. Soc.* **1993**, *115*, 6382–6390.

[174] Schlichthörl, G.; Huang, S. Y.; Sprague, J.; Frank, A. J. *J. Phys. Chem. B* **1997**, *101*, 8141–8155.

[175] Huang, S. Y.; Schlichthörl, G.; Nozik, A. J.; Grätzel, M.; ; Frank, A. J. *J. Phys. Chem. B* **1997**, *101*, 2576–2582.

[176] Boschloo, G.; Lindström, H.; Magnusson, E.; Holmberg, A.; Hagfeldt, A. *J. Photochem. Photobiol., A* **2002**, *148*, 11–15.

[177] Haque, S.; Palomares, E.; Cho, B.; Green, A.; Hirata, N.; Klug, D.; Durrant, J. *J. Am. Chem. Soc.* **2005**, *127*, 3456–3462.

[178] Boschloo, G.; Häggman, L.; Hagfeldt, A. *J. Phys. Chem. B* **2006**, *110*, 13144–13150.

[179] Liu, Y.; Hagfeldt, A.; Xiao, X.-R.; Lindquist, S.-E. *Sol. Energy Mater. Sol. Cells* **1998**, *55*, 267–281.

[180] Watson, D. F.; Meyer, G. J. *Coord. Chem. Rev.* **2004**, *248*, 1391–1406.

[181] Koops, S. E.; O'Regan, B. C.; Barnes, P. R. F.; Durrant, J. R. *J. Am. Chem. Soc.* **2009**, *131*, 4808–4818.

[182] Jennings, J. R.; Wang, Q. *J. Phys. Chem. C* **2010**, *114*, 1715–1724.

[183] Kopidakis, N.; Neale, N. R.; ; Frank, A. J. *J. Phys. Chem. B* **2006**, *110*, 12485–12489.

[184] Zhang, C.; Huang, Y.; Huo, Z.; Chen, S.; Dai, S. *J. Phys. Chem. C* **2009**, *113*, 21779–21783.

[185] Grätzel, M. *J. Photochem. Photobiol., A* **2004**, *164*, 3–14.

[186] Lewis, N. S. *Science* **2007**, *315*, 798–801.

[187] Wierzbicki, A.; J. H. Davis, J. in *Proceedings of the Symposium on Advances in Solvent Selection and Substitution for Extraction* (AIChE, New York, **2000**).

[188] Casida, M. In *Time-dependent density functional response theory for molecules*; Chong, D., Ed.; Recent Advances in Density Functional Methods, vol. 1, World Scientific: Singapore, 1995; pp 155–192.

[189] Gross, E. K. U.; Dobson, J. F.; Petersilka, M. In *Density Functional Theory II: Relativistic and Time Dependent Extensions*; Nalewajski, R. F., Ed.; Springer: Berlin, Heidelberg, 1996; Chapter Density functional theory of time-dependent phenomena, pp 81–172.

[190] Bauernschmitt, R.; Ahlrichs, R. *Chem. Phys. Lett.* **1996**, *256*, 454–464.

[191] Furche, F. *J. Chem. Phys.* **2001**, *114*, 5982–5992.

[192] Bayliss, S. L.; Cole, J. M.; Waddell, P. G.; McKechnie, S.; Liu, X. *J. Phys. Chem. C* **2014**, *118*, 14082–14090.

[193] Dragoni, D.; Manini, N.; Ballone, P. *ChemPhysChem* **2012**, *13*, 1772–1780.

[194] Brkljača, Z.; Klimczak, M.; Miličević, Z.; Weisser, M.; Taccardi, N.; Wasserscheid, P.; Smith, D. M.; Magerl, A.; Smith, A.-S. *J. Phys. Chem. Lett.* **2015**, *6*, 549–555.

[195] Byrne, A.; English, N. J.; Schwingenschlögl, U.; Coker, D. F. *J. Phys. Chem. C* **2016**, *120*, 21–30.

[196] Schiffmann, F.; VandeVondele, J.; Hutter, J.; Wirz, R.; Urakawa, A.; Baiker, A. *J. Phys. Chem. C* **2010**, *114*, 8398–8404.

[197] De Angelis, F.; Vitillaro, G.; Kavan, L.; Nazeeruddin, M. K.; Grätzel, M. *J. Phys. Chem. C* **2012**, *116*, 18124–18131.

[198] De Angelis, F.; Fantacci, S.; Selloni, A.; Nazeeruddin, M. K.; Grätzel, M. *J. Phys. Chem. C* **2010**, *114*, 6054–6061.

[199] De Angelis, F.; Fantacci, S.; Mosconi, E.; Nazeeruddin, M. K.; Grätzel, M. *J. Phys. Chem. C* **2011**, *115*, 8825–8831.

[200] Mosconi, E.; Selloni, A.; De Angelis, F. *J. Phys. Chem. C* **2012**, *116*, 5932–5940.

[201] Martsinovich, N.; Jones, D. R.; Troisi, A. *J. Phys. Chem. C* **2010**, *114*, 22659–22670.

[202] Rocca, D.; Gebauer, R.; De Angelis, F.; Nazeeruddin, M. K.; Baroni, S. *Chem. Phys. Lett.* **2009**, *475*, 49–53.

[203] De Angelis, F.; Fantacci, S.; Gebauer, R. *J. Phys. Chem. Lett.* **2011**, *2*, 813–817.

[204] Duncan, W. R.; Stier, W. M.; Prezhdo, O. V. *J. Am. Chem. Soc.* **2005**, *127*, 7941–7951.

[205] Huber, R.; Moser, J.-E.; Grätzel, M.; Wachtveitl, J. *J. Phys. Chem. B* **2002**, *106*, 6494–6499.

[206] Tilocca, A.; Selloni, A. *Langmuir* **2004**, *20*, 8379–8384.

[207] Li, W.-K.; Gong, X.-Q.; Lu, G.; Selloni, A. *J. Phys. Chem. C* **2008**, *112*, 6594–6596.

[208] Cheng, H.; Selloni, A. *Langmuir* **2010**, *26*, 11518–11525.

[209] Cheng, J.; Sprik, M. *Phys. Rev. B* **2010**, *82*, 081406.

[210] Schiffmann, F.; Hutter, J.; VandeVondele, J. *J. Phys.: Condens. Matter* **2008**, *20*, 064206.

[211] Sumita, M.; Sodeyama, K.; Han, L.; Tateyama, Y. *J. Phys. Chem. C* **2011**, *115*, 19849–19855.

[212] Hohenberg, P.; Kohn, W. *Phys. Rev.* **1964**, *136*, B864–B871.

[213] Kohn, W.; Sham, L. J. *Phys. Rev.* **1965**, *140*, A1133–A1138.

[214] Becke, A. D. *Phys. Rev. A* **1988**, *38*, 3098–3100.

[215] Lee, C.; Yang, W.; Parr, R. G. *Phys. Rev. B* **1988**, *37*, 785–789.

[216] Perdew, J. P.; Burke, K.; Ernzerhof, M. *Phys. Rev. Lett.* **1996**, *77*, 3865–3868.

[217] Perdew, J. P.; Burke, K.; Ernzerhof, M. *Phys. Rev. Lett.* **1997**, *78*, 1396–1396.

[218] Zhang, Y.; Yang, W. *Phys. Rev. Lett.* **1998**, *80*, 890–890.

[219] Becke, A. D. *J. Chem. Phys.* **1996**, *104*, 1040–1046.

[220] Tao, J.; Perdew, J. P.; Staroverov, V. N.; Scuseria, G. E. *Phys. Rev. Lett.* **2003**, *91*, 146401.

[221] Becke, A. D. *J. Chem. Phys.* **1993**, *98*, 5648–5652.

[222] Adamo, C.; Barone, V. *J. Chem. Phys.* **1999**, *110*, 6158–6170.

[223] Grimme, S. *J. Chem. Phys.* **2006**, *124*, 034108.

[224] Yanai, T.; Tew, D. P.; Handy, N. C. *Chem. Phys. Lett.* **2004**, *393*, 51–57.

[225] Lin, Y.-S.; Li, G.-D.; Mao, S.-P.; Chai, J.-D. *J. Chem. Theory Comput.* **2013**, *9*, 263–272.

[226] Pérez-Jordá, J. M.; Becke, A. *Chem. Phys. Lett.* **1995**, *233*, 134–137.

[227] Kristyán, S.; Pulay, P. *Chem. Phys. Lett.* **1994**, *229*, 175–180.

[228] Hobza, P.; Šponer, J.; Reschel, T. *J. Comput. Chem.* **1995**, *16*, 1315–1325.

[229] Grimme, S. *WIREs Comput. Mol. Sci.* **2011**, *1*, 211–228.

[230] Grimme, S.; Antony, J.; Ehrlich, S.; Krieg, H. *J. Chem. Phys.* **2010**, *132*, 154104.

[231] Runge, E.; Gross, E. K. U. *Phys. Rev. Lett.* **1984**, *52*, 997–1000.

[232] Hirata, S.; Head-Gordon, M. *Chem. Phys. Lett.* **1999**, *314*, 291–299.

[233] Maurice, D.; Head-Gordon, M. *Int. J. Quantum Chem. Symp.* **1995**, *29*, 361–370.

[234] Casida, M. E.; Gutierrez, F.; Guan, J.; Gadea, F.-X.; Salahub, D.; Daudey, J.-P. *J. Chem. Phys.* **2000**, *113*, 7062–7071.

[235] Cordova, F.; Doriol, L. J.; Ipatov, A.; Casida, M. E.; Filippi, C.; Vela, A. *J. Chem. Phys.* **2007**, *127*, 164111.

[236] Tapavicza, E.; Tavernelli, I.; Rothlisberger, U.; Filippi, C.; Casida, M. E. *J. Chem. Phys.* **2008**, *129*, 124108.

[237] Grimme, S. *J. Chem. Phys.* **2013**, *138*, 244104.

[238] Nishimoto, K.; Mataga, N. *Z. Phys. Chem.* **1957**, *12*, 335–338.

[239] Ohno, K. *Theor. Chim. Acta* **1964**, *2*, 219–227.

[240] Klopman, G. *J. Am. Chem. Soc.* **1964**, *86*, 4550–4557.

[241] Löwdin, P.-O. *J. Chem. Phys.* **1950**, *18*, 365–375.

[242] Bannwarth, C.; Grimme, S. *Comput. Theor. Chem.* **2014**, *1040–1041*, 45–53.

[243] Swope, W. C.; Andersen, H. C.; Berens, P. H.; Wilson, K. R. *J. Chem. Phys.* **1982**, *76*, 637–649.

[244] Verlet, L. *Phys. Rev.* **1967**, *159*, 98–103.

[245] Hockney, R. W. *Methods Comput. Phys* **1970**, *9*, 136–211.

[246] Gear, C. W. *Numerical Initial Value Problems in Ordinary Differential Equations*; Englewood Cliff, NJ, Prentice Hall, 1971.

[247] Jorgensen, W. L.; Maxwell, D. S.; Tirado-Rives, J. *J. Am. Chem. Soc.* **1996**, *118*, 11225–11236.

[248] Rappe, A. K.; Goddard III, W. A. *J. Phys. Chem.* **1991**, *95*, 3358–3363.

[249] Rick, S. W.; Stuart, S. J.; Berne, B. J. *J. Chem. Phys.* **1994**, *101*, 6141–6156.

[250] Dang, L. X.; Rice, J. E.; Caldwell, J.; Kollman, P. A. *J. Am. Chem. Soc.* **1991**, *113*, 2481–2486.

[251] Welton, T. In *Ionic Liquids*; Kirchner, B., Ed.; Topics in Current Chemistry; Springer Berlin Heidelberg, 2010; Vol. 290; pp 213–262.

[252] Welton, T. *Mater. Today* **2008**, *11*, 56.

[253] Welton, T. *Green Chem.* **2006**, *8*, 13.

[254] Welton, T. *Proc. R. Soc. London, Ser. A* **2015**, *471*, 20150502.

[255] Kirchner, B. In *Ionic Liquids*; Kirchner, B., Ed.; Topics in Current Chemistry; Springer Berlin Heidelberg, 2010; Vol. 290; pp 213–262.

[256] Kirchner, B.; Hollóczki, O.; Canongia Lopes, J. N.; Pádua, A. A. H. *WIREs Comput. Mol. Sci.* **2015**, *5*, 202–214.

[257] Salanne, M. *Phys. Chem. Chem. Phys.* **2015**, *17*, 14270–14279.

[258] Dommert, F.; Wendler, K.; Berger, R.; Delle Site, L.; Holm, C. *ChemPhysChem* **2012**, *13*, 1625–1637.

[259] Firaha, D. S.; Kirchner, B. *J. Chem. Eng. Data* **2014**, *59*, 3098–3104.

[260] Hollóczki, O.; Firaha, D. S.; Friedrich, J.; Brehm, M.; Cybik, R.; Wild, M.; Stark, A.; Kirchner, B. *J. Phys. Chem. B* **2013**, *117*, 5898–5907.

[261] Zahn, S.; Frank, R.; Hey-Hawkins, E.; Kirchner, B. *Chem. Eur. J.* **2013**, *19*, 1526–1526.

[262] Weber, H.; Bredow, T.; Kirchner, B. *J. Phys. Chem. C* **2015**, *119*, 15137–15149.

[263] Weber, H.; Salanne, M.; Kirchner, B. *J. Phys. Chem. C* **2015**, *119*, 25260–25267.

[264] Deng, M.-J.; Chen, P.-Y.; Leong, T.-I.; Sun, I.-W.; Chang, J.-K.; Tsai, W.-T. *Electrochem. Commun.* **2008**, *10*, 213–216.

[265] Aoyagi, N.; Shinha, Y.; Ikeda-Ohno, A.; Haga, Y.; Shimojo, K.; Brooks, N. R.; Izuoka, A.; Naganawa, H.; Kimura, T.; Binnemans, K. *Cryst. Growth Des.* **2015**, *15*, 1422–1429.

[266] Ren, Z.; Brinzer, T.; Dutta, S.; Garrett-Roe, S. *J. Phys. Chem. B* **2015**, *119*, 4699–4712.

[267] Fumino, K.; Wittler, K.; Ludwig, R. *J. Phys. Chem. B* **2012**, *116*, 9507–9511.

[268] Penna, T. C.; Faria, L. F.; Ribeiro, M. C. *J. Mol. Liq.* **2015**, *209*, 676–682.

[269] Thar, J.; Brehm, M.; Seitsonen, A. P.; Kirchner, B. *J. Phys. Chem. B* **2009**, *113*, 15129–15132.

[270] Pensado, A. S.; Brehm, M.; Thar, J.; Seitsonen, A. P.; Kirchner, B. *ChemPhysChem* **2012**, *13*, 1845–1853.

[271] Kempter, V.; Kirchner, B. *J. Mol. Struct.* **2010**, *972*, 22–34.

[272] Mahurin, S. M.; Lee, J. S.; Baker, G. A.; Luo, H.; Dai, S. *J. Membr. Sci.* **2010**, *353*, 177–183.

[273] Li, P.; Paul, D. R.; Chung, T.-S. *Green Chem.* **2012**, *14*, 1052–1063.

[274] Babarao, R.; Dai, S.; en Jiang, D. *J. Phys. Chem. B* **2011**, *115*, 9789–9794.

[275] Meindersma, G.; De Haan, A. *Sci. China. Chem.* **2012**, *55*, 1488–1499.

[276] Firaha, D. S.; Kavalchuk, M.; Kirchner, B. *J. Solution Chem.* **2015**, *44*, 838–849.

[277] Zeng, S.; Zhang, X.; Gao, H.; He, H.; Zhang, X.; Zhang, S. *Ind. Eng. Chem. Res.* **2015**, *54*, 10854–10862.

[278] García, G.; Atilhan, M.; Aparicio, S. *Phys. Chem. Chem. Phys.* **2015**, *17*, 26875–26891.

[279] García, G.; Atilhan, M.; Aparicio, S. *Phys. Chem. Chem. Phys.* **2015**, *17*, 13559–13574.

[280] Kędra-Królik, K.; Fabrice, M.; Jaubert, J.-N. *Ind. Eng. Chem. Res.* **2011**, *50*, 2296–2306.

[281] Domínguez-Pérez, M.; Tomé, L. I.; Freire, M. G.; Marrucho, I. M.; Cabeza, O.; Coutinho, J. A. *Sep. Purif. Technol.* **2010**, *72*, 85–91.

[282] Fulvio, P. F.; Lee, J. S.; Mayes, R. T.; Wang, X.; Mahurin, S. M.; Dai, S. *Phys. Chem. Chem. Phys.* **2011**, *13*, 13486–13491.

[283] Yang, W.; Fellinger, T.-P.; Antonietti, M. *J. Am. Chem. Soc.* **2011**, *133*, 206–209.

[284] Kamal, A.; Chouhan, G. *Tetrahedron Lett.* **2005**, *46*, 1489–1491.

[285] Yadav, L. D. S.; Patel, R.; Rai, V. K.; Srivastava, V. P. *Tetrahedron Lett.* **2007**, *48*, 7793–7795.

[286] Hutter, J.; Iannuzzi, M.; Schiffmann, F.; VandeVondele, J. *WIREs Comput. Mol. Sci.* **2014**, *4*, 15–25.

[287] VandeVondele, J.; Krack, M.; Mohamed, F.; Parrinello, M.; Chassaing, T.; Hutter, J. *Comput. Phys. Commun.* **2005**, *167*, 103–128.

[288] Zahn, S.; Kirchner, B. *J. Phys. Chem. A* **2008**, *112*, 8430–8435.

[289] Grimme, S.; Hujo, W.; Kirchner, B. *Phys. Chem. Chem. Phys.* **2012**, *14*, 4875–4883.

[290] Fumino, K.; Fossog, V.; Stange, P.; Paschek, D.; Hempelmann, R.; Ludwig, R. *Angew. Chem. Int. Ed.* **2015**, *54*, 2792–2795.

[291] VandeVondele, J.; Hutter, J. *J. Chem. Phys.* **2007**, *127*, 114105.

[292] Goedecker, S.; Teter, M.; Hutter, J. *Phys. Rev. B* **1996**, *54*, 1703–1710.

[293] Hartwigsen, C.; Goedecker, S.; Hutter, J. *Phys. Rev. B* **1998**, *58*, 3641–3662.

[294] Krack, M. *Theor. Chem. Acc.* **2005**, *114*, 145–152.

[295] Plimpton, S. *J. Comput. Phys.* **1995**, *117*, 1–19.

[296] Canongia Lopes, J. N.; Pádua, A. A. H. *J. Phys. Chem. B* **2006**, *110*, 19586–19592.

[297] Nosé, S. *J. Chem. Phys.* **1984**, *81*, 511–519.

[298] Hoover, W. G. *Phys. Rev. A* **1985**, *31*, 1695–1697.

[299] Martyna, G. J.; Klein, M. L.; Tuckerman, M. *J. Chem. Phys.* **1992**, *97*, 2635–2643.

[300] Malberg, F.; Brehm, M.; Hollóczki, O.; Pensado, A. S.; Kirchner, B. *Phys. Chem. Chem. Phys.* **2013**, *15*, 18424–18436.

[301] Brüssel, M.; Brehm, M.; Pensado, A. S.; Malberg, F.; Ramzan, M.; Stark, A.; Kirchner, B. *Phys. Chem. Chem. Phys.* **2012**, *14*, 13204–13215.

[302] Weber, H.; Hollóczki, O.; Pensado, A. S.; Kirchner, B. *J. Chem. Phys.* **2013**, *139*, 084502.

[303] Matthews, R. P.; Welton, T.; Hunt, P. A. *Phys. Chem. Chem. Phys.* **2015**, *17*, 14437–14453.

[304] Bochyński, Z.; Drozdowski, H. *Acta Phys. Slovaca* **1999**, *49*, 409–418.

[305] Neves, C. M. S. S.; Kurnia, K. A.; Coutinho, J. A. P.; Marrucho, I. M.; Canongia Lopes, J. N.; Freire, M. G.; Rebelo, L. P. N. *J. Phys. Chem. B* **2013**, *117*, 10271–10283.

[306] Lehmann, S. B. C.; Roatsch, M.; Schöppke, M.; Kirchner, B. *Phys. Chem. Chem. Phys.* **2010**, *12*, 7473–7486.

[307] Hunt, P. A.; Kirchner, B.; Welton, T. *Chem. Eur. J.* **2006**, *12*, 6762–6775.

[308] Brüssel, M.; Brehm, M.; Voigt, T.; Kirchner, B. *Phys. Chem. Chem. Phys.* **2011**, *13*, 13617–13620.

[309] Batista, M. L. S.; Kurnia, K. A.; ao P. Pinho, S.; Gomes, J. R. B.; Coutinho, J. A. P. *J. Phys. Chem. B* **2015**, *119*, 1567–1578.

[310] Brehm, M.; Weber, H.; Thomas, M.; Hollóczki, O.; Kirchner, B. *ChemPhysChem* **2015**, *16*, 3271–3277.

[311] Koller, T.; Rausch, M. H.; Schulz, P. S.; Berger, M.; Wasserscheid, P.; Economou, I. G.; Leipertz, A.; Fröba, A. P. *J. Chem. Eng. Data* **2012**, *57*, 828–835.

[312] Noda, A.; Hayamizu, K.; Watanabe, M. *J. Phys. Chem. B* **2001**, *105*, 4603–4610.

[313] Alcalde, R.; García, G.; Atilhan, M.; Aparicio, S. *Ind. Eng. Chem. Res.* **2015**, *54*, 10918–10924.

[314] Zahn, S.; Bruns, G.; Thar, J.; Kirchner, B. *Phys. Chem. Chem. Phys.* **2008**, *10*, 6921–6924.

[315] Kohagen, M.; Brehm, M.; Lingscheid, Y.; Giernoth, R.; Sangoro, J.; Kremer, F.; Naumov, S.; Iacob, C.; Kärger, J.; Valiullin, R.; Kirchner, B. *J. Phys. Chem. B* **2011**, *115*, 15280–15288.

[316] Kohagen, M.; Brehm, M.; Thar, J.; Zhao, W.; Müller-Plathe, F.; Kirchner, B. *J. Phys. Chem. B* **2011**, *115*, 693–702.

[317] Zhang, Y.; Maginn, E. J. *J. Phys. Chem. Lett.* **2015**, *6*, 700–705.

[318] Kirchner, B.; Malberg, F.; Firaha, D. S.; Hollóczki, O. *J. Phys.: Condens. Matter* **2015**, *27*, 463002.

[319] Hollóczki, O.; Malberg, F.; Welton, T.; Kirchner, B. *Phys. Chem. Chem. Phys.* **2014**, *16*, 16880–16890.

[320] Chen, X.; Selloni, A. *Chem. Rev.* **2014**, *114*, 9281–9282.

[321] Diebold, U. *Surf. Sci. Rep.* **2003**, *48*, 53–229.

[322] De Angelis, F.; Di Valentin, C.; Fantacci, S.; Vittadini, A.; Selloni, A. *Chem. Rev.* **2014**, *114*, 9708–9753.

[323] Schneider, J.; Matsuoka, M.; Takeuchi, M.; Zhang, J.; Horiuchi, Y.; Anpo, M.; Bahnemann, D. W. *Chem. Rev.* **2014**, *114*, 9919–9986.

[324] Kapilashrami, M.; Zhang, Y.; Liu, Y.-S.; Hagfeldt, A.; Guo, J. *Chem. Rev.* **2014**, *114*, 9662–9707.

[325] Ma, Y.; Wang, X.; Jia, Y.; Chen, X.; Han, H.; Li, C. *Chem. Rev.* **2014**, *114*, 9987–10043.

[326] Bai, Y.; Mora-Seró, I.; De Angelis, F.; Bisquert, J.; Wang, P. *Chem. Rev.* **2014**, *114*, 10095–10130.

[327] Bai, J.; Zhou, B. *Chem. Rev.* **2014**, *114*, 10131–10176.

[328] Rajh, T.; Dimitrijevic, N. M.; Bissonnette, M.; Koritarov, T.; Konda, V. *Chem. Rev.* **2014**, *114*, 10177–10216.

[329] Bourikas, K.; Kordulis, C.; Lycourghiotis, A. *Chem. Rev.* **2014**, *114*, 9754–9823.

[330] Zhang, H.; Banfield, J. F. *J. Phys. Chem. B* **2000**, *104*, 3481–3487.

[331] Zhang, H.; Banfield, J. F. *J. Mater. Chem.* **1998**, *8*, 2073–2076.

[332] Feldhoff, A.; Mendive, C.; Bredow, T.; Bahnemann, D. *ChemPhysChem* **2007**, *8*, 805–809.

[333] Esch, T. R.; Gadaczek, I.; Bredow, T. *Appl. Surf. Sci.* **2014**, *288*, 275–287.

[334] Kumara, G. R. A.; Kaneko, S.; Okuya, M.; Tennakone, K. *Langmuir* **2002**, *18*, 10493–10495.

[335] Bandara, J.; Yasomanee, J. P. *Semicond. Sci. Technol.* **2007**, *22*, 20–24.

[336] Krüger, J.; Plass, R.; Cevey, L.; Piccirelli, M.; Grätzel, M.; Bach, U. *Appl. Phys. Lett.* **2001**, *79*, 2085–2087.

[337] Chen, D.; Zhang, Q.; Wang, G.; Zhang, H.; Li, J. *Electrochem. Commun.* **2007**, *9*, 2755–2759.

[338] Shen, X.; Xu, W.; Xu, J.; Liang, G.; Yang, H.; Yao, M. *Solid State Ionics* **2008**, *179*, 2027–2030.

[339] Armel, V.; Pringle, J. M.; Forsyth, M.; MacFarlane, D. R.; Officer, D. L.; Wagner, P. *Chem. Commun.* **2010**, *46*, 3146–3148.

[340] Armel, V.; Pringle, J. M.; Wagner, P.; Forsyth, M.; Officer, D.; MacFarlane, D. R. *Chem. Commun.* **2011**, *47*, 9327–9329.

[341] Brandenburg, J. G.; Grimme, S. In *Prediction and Calculation of Crystal Structures*; Atahan-Evrenk, S., Aspuru-Guzik, A., Eds.; Topics in Current Chemistry; Springer International Publishing, 2014; Vol. 345; pp 1–23.

[342] Malberg, F.; Pensado, A. S.; Kirchner, B. *Phys. Chem. Chem. Phys.* **2012**, *14*, 12079–12082.

[343] Brehm, M.; Weber, H.; Pensado, A. S.; Stark, A.; Kirchner, B. *Phys. Chem. Chem. Phys.* **2012**, *14*, 5030–5044.

[344] Stark, A.; Brehm, M.; Brüssel, M.; Lehmann, S. B.; Pensado, A. S.; Schöppke, M.; Kirchner, B. In *Electronic Effects in Organic Chemistry*; Kirchner, B., Ed.; Topics in Current Chemistry; Springer Berlin Heidelberg, 2014; Vol. 351; pp 149–187.

[345] Zahn, S.; Brehm, M.; Brüssel, M.; Hollóczki, O.; Kohagen, M.; Lehmann, S.; Malberg, F.; Pensado, A. S.; Schöppke, M.; Weber, H.; Kirchner, B. *J. Mol. Liq.* **2014**, *192*, 71–76.

[346] Pensado, A. S.; Malberg, F.; Costa Gomes, M. F.; Pádua, A. A. H.; Fernández, J.; Kirchner, B. *RSC Adv.* **2014**, *4*, 18017–18024.

[347] Grimme, S.; Ehrlich, S.; Goerigk, L. *J. Comput. Chem.* **2011**, *32*, 1456–1465.

[348] Ehrlich, S.; Moellmann, J.; Reckien, W.; Bredow, T.; Grimme, S. *ChemPhysChem* **2011**, *12*, 3414–3420.

[349] Moellmann, J.; Ehrlich, S.; Tonner, R.; Grimme, S. *J. Phys.: Condens. Matter* **2012**, *24*, 424206.

[350] Jug, K.; Bredow, T. *J. Comput. Chem.* **2004**, *25*, 1551–1567.

[351] Martyna, G. J.; Tuckerman, M. E. *J. Chem. Phys.* **1999**, *110*, 2810–2821.

[352] Dovesi, R.; Orlando, R.; Erba, A.; Zicovich-Wilson, C. M.; Civalleri, B.; Casassa, S.; Maschio, L.; Ferrabone, M.; De La Pierre, M.; D'Arco, P.; Noël, Y.; Causá, M.; Rérat, M.; Kirtman, B. *Int. J. Quantum Chem.* **2014**, *114*, 1287–1317.

[353] Bredow, T.; Heitjans, P.; Wilkening, M. *Phys. Rev. B* **2004**, *70*, 115111.

[354] Cora, F. *Mol. Phys.* **2005**, *103*, 2483–2496.

[355] Muscat, J. PhD Thesis, University of Manchester, 1999.

[356] Kusama, H.; Orita, H.; Sugihara, H. *Sol. Energy Mater. Sol. Cells* **2008**, *92*, 84–87.

[357] Kusama, H.; Orita, H.; Sugihara, H. *Langmuir* **2008**, *24*, 4411–4419.

[358] Szieberth, D.; Maria Ferrari, A.; Dong, X. *Phys. Chem. Chem. Phys.* **2010**, *12*, 11033–11040.

[359] Ballenegger, V.; Arnold, A.; Cerdá, J. J. *J. Chem. Phys.* **2009**, *131*, 094107.

[360] Mulliken, R. S. *J. Chem. Phys.* **1955**, *23*, 1833–1840.

[361] Blöchl, P. E. *J. Chem. Phys.* **1995**, *103*, 7422–7428.

[362] Boys, S.; Bernardi, F. *Mol. Phys.* **1970**, *19*, 553–566.

[363] Pisani, C.; Aprá, E.; Causá, M. *Int. J. Quantum Chem.* **1990**, *38*, 395–417.

[364] Pisani, C.; Aprá, E.; Causá, M.; Orlando, R. *Int. J. Quantum Chem.* **1990**, *38*, 419–433.

[365] Humphrey, W.; Dalke, A.; Schulten, K. *J. Mol. Graphics* **1996**, *14*, 33–38.

[366] Grace development team. `http://plasma-gate.weizmann.ac.il/Grace/`.

[367] Cohen, A. J.; Mori-Sánchez, P.; Yang, W. *Science* **2008**, *321*, 792–794.

[368] Toher, C.; Filippetti, A.; Sanvito, S.; Burke, K. *Phys. Rev. Lett.* **2005**, *95*, 146402.

[369] Ke, S.-H.; Baranger, H. U.; Yang, W. *J. Chem. Phys.* **2007**, *126*, 201102.

[370] Johnson, E. R.; Mori-Sánchez, P.; Cohen, A. J.; Yang, W. *J. Chem. Phys.* **2008**, *129*, 204112.

[371] Cohen, A. J.; Mori-Sánchez, P.; Yang, W. *J. Chem. Phys.* **2007**, *126*, 191109.

[372] Perdew, J. P.; Zunger, A. *Phys. Rev. B* **1981**, *23*, 5048–5079.

[373] d'Avezac, M.; Calandra, M.; Mauri, F. *Phys. Rev. B* **2005**, *71*, 205210.

[374] VandeVondele, J.; Sprik, M. *Phys. Chem. Chem. Phys.* **2005**, *7*, 1363–1367.

[375] Makov, G.; Payne, M. C. *Phys. Rev. B* **1995**, *51*, 4014–4022.

[376] Marx, D.; Hutter, J. *Ab Initio Molecular Dynamics*; Cambridge University Press, 2009.

[377] Kirchner, B.; Dio, P.; Hutter, J. In *Multiscale Molecular Methods in Applied Chemistry*; Kirchner, B., Vrabec, J., Eds.; Topics in Current Chemistry; Springer Berlin Heidelberg, 2012; Vol. 307; pp 109–153.

[378] Epling, W. S.; Peden, C. H.; Henderson, M. A.; Diebold, U. *Surf. Sci.* **1998**, *412–413*, 333–343.

[379] Diebold, U.; Madey, T. E. *J. Vac. Sci. Technol. A* **1992**, *10*, 2327–2335.

[380] Román, E.; de Segovia, J. *Surf. Sci.* **1991**, *251-252*, 742–746.

[381] Román, E. L.; de Segovia, J.; Kurtz, R. L.; Stockbauer, R.; Madey, T. E. *Surf. Sci.* **1992**, *273*, 40–46.

[382] Sakamaki, K.; Matsunaga, S.; Itoh, K.; Fujishima, A.; Gohshi, Y. *Surf. Sci.* **1989**, *219*, L531–L536.

[383] Suzuki, S.; Yamaguchi, Y.; Onishi, H.; Sasaki, T.; Fukui, K.-i.; Yasuhiro, I. *J. Chem. Soc., Faraday Trans.* **1998**, *94*, 161–166.

[384] Herman, G. S.; Dohnálek, Z.; Ruzycki, N.; Diebold, U. *J. Phys. Chem. B* **2003**, *107*, 2788–2795.

[385] Tonner, R.; Heydenrych, G.; Frenking, G. *Chem. Asian J.* **2007**, *2*, 1555–1567.

[386] Hollóczki, O.; Nyulászi, L. *Org. Biomol. Chem.* **2011**, *9*, 2634–2640.

[387] Thomas, M.; Brehm, M.; Hollóczki, O.; Kirchner, B. *Chem. Eur. J.* **2014**, *20*, 1622–1629.

[388] Labat, F.; Baranek, P.; Adamo, C. *J. Chem. Theory Comput.* **2008**, *4*, 341–352.

[389] Grätzel, M. *Nature* **2001**, *414*, 338–344.

[390] Giantomassi, M.; Stankovski, M.; Shaltaf, R.; Grüning, M.; Bruneval, F.; Rinke, P.; Rignanese, G.-M. *Phys. Status Solidi B* **2011**, *248*, 275–289.

[391] Perdew, J. P.; Parr, R. G.; Levy, M.; Balduz, J. L. *Phys. Rev. Lett.* **1982**, *49*, 1691–1694.

[392] Hayes, R.; Warr, G. G.; Atkin, R. *Chem. Rev.* **2015**, *115*, 6357–6426.

[393] Plechkova, N. V.; Seddon, K. R. *Chem. Soc. Rev.* **2008**, *37*, 123–150.

[394] Ohno, H., Ed. *Electrochemical Aspects of Ionic Liquids*, 2nd ed.; John Wiley & Sons, Inc., 2011.

[395] Rana, U. A.; Forsyth, M.; MacFarlane, D. R.; Pringle, J. M. *Electrochim. Acta* **2012**, *84*, 213–222.

[396] Yasuda, T.; Watanabe, M. *MRS Bull.* **2013**, *38*, 560–566.

[397] Urahata, S. M.; Ribeiro, M. C. C. *J. Chem. Phys.* **2004**, *120*, 1855–1863.

[398] Merlet, C.; Rotenberg, B.; Madden, P. A.; Salanne, M. *Phys. Chem. Chem. Phys.* **2013**, *15*, 15781–15792.

[399] Kornyshev, A. A.; Qiao, R. *J. Phys. Chem. C* **2014**, *118*, 18285–18290.

[400] Smith, A. M.; Lovelock, K. R. J.; Gosvami, N. N.; Licence, P.; Dolan, A.; Welton, T.; Perkin, S. *J. Phys. Chem. Lett.* **2013**, *4*, 378–382.

[401] Salanne, M.; Rotenberg, B.; Jahn, S.; Vuilleumier, R.; Simon, C.; Madden, P. *Theor. Chem. Acc.* **2012**, *131*, 1143.

[402] Corradini, D.; Dambournet, D.; Salanne, M. *Sci. Rep.* **2015**, *5*, 11553.

[403] Fumi, F.; Tosi, M. *J. Phys. Chem. Solids* **1964**, *25*, 31–43.

[404] Tosi, M.; Fumi, F. *J. Phys. Chem. Solids* **1964**, *25*, 45–52.

[405] Tang, K. T.; Toennies, J. P. *J. Chem. Phys.* **1984**, *80*, 3726–3741.

[406] Singh, U. C.; Kollman, P. A. *J. Comput. Chem.* **1984**, *5*, 129–145.

[407] Hehre, W. J.; Ditchfield, R.; Pople, J. A. *J. Chem. Phys.* **1972**, *56*, 2257–2261.

[408] Francl, M. M.; Pietro, W. J.; Hehre, W. J.; Binkley, J. S.; Gordon, M. S.; DeFrees, D. J.; Pople, J. A. *J. Chem. Phys.* **1982**, *77*, 3654–3665.

[409] Burdett, J. K.; Hughbanks, T.; Miller, G. J.; Richardson, J. W.; Smith, J. V. *J. Am. Chem. Soc.* **1987**, *109*, 3639–3646.

[410] Bussi, G.; Donadio, D.; Parrinello, M. *J. Chem. Phys.* **2007**, *126*, 014101.

[411] Martínez, L.; Andrade, R.; Birgin, E. G.; Martínez, J. M. *J. Comput. Chem.* **2009**, *30*, 2157–2164.

[412] Brehm, M.; Kirchner, B. *J. Chem. Inf. Model.* **2011**, *51*, 2007–2023.

[413] CN/ASD Group, *MINUIT — Users Guide, nProgram Library D506*, CERN, 1993.

[414] James, F.; Winkler, M. `http://www.cern.ch/minuit`, CERN, April 2015.

[415] Koßmann, S.; Thar, J.; Kirchner, B.; Hunt, P. A.; Welton, T. *J. Chem. Phys.* **2006**, *124*, 174506.

[416] Kirchner, B. *J. Chem. Phys.* **2005**, *123*, 204116.

[417] Salanne, M.; Madden, P. A. *Mol. Phys.* **2011**, *109*, 2299–2315.

[418] Zhao, Y.; Boström, T. *Curr. Org. Chem.* **2015**, *19*, 556–566.

[419] Ramdin, M.; de Loos, T. W.; Vlugt, T. J. *Ind. Eng. Chem. Res.* **2012**, *51*, 8149–8177.

[420] Zhang, L.; Chen, J.; Lv, J. X.; Wang, S. F.; Cui, Y. *Asian J. Chem.* **2013**, *25*, 2355–2358.

[421] Zhang, X.; Zhang, X.; Dong, H.; Zhao, Z.; Zhang, S.; Huang, Y. *Energy Environ. Sci.* **2012**, *5*, 6668–6681.

[422] Otaka, H.; Kira, M.; Yano, K.; Ito, S.; Mitekura, H.; Kawata, T.; Matsui, F. *J. Photochem. Photobiol., A* **2004**, *164*, 67–73.

[423] Grätzel, M. *J. Photochem. Photobiol., C* **2003**, *4*, 145–153.

[424] Hardin, B. E.; Snaith, H. J.; McGehee, M. D. *Nat. Photonics* **2012**, *6*, 162–169.

[425] Furube, A.; Katoh, R.; Hara, K. *Surf. Sci. Rep.* **2014**, *69*, 389–441.

[426] Marinado, T.; Hagberg, D. P.; Hedlund, M.; Edvinsson, T.; Johansson, E. M. J.; Boschloo, G.; Rensmo, H.; Brinck, T.; Sun, L.; Hagfeldt, A. *Phys. Chem. Chem. Phys.* **2009**, *11*, 133–141.

[427] Furube, A.; Katoh, R.; Hara, K.; Sato, T.; Murata, S.; Arakawa, H.; Tachiya, M. *J. Phys. Chem. B* **2005**, *109*, 16406–16414.

[428] McLean, B.; Li, H.; Stefanovic, R.; Wood, R. J.; Webber, G. B.; Ueno, K.; Watanabe, M.; Warr, G. G.; Page, A.; Atkin, R. *Phys. Chem. Chem. Phys.* **2015**, *17*, 325–333.

[429] Thomas, M.; Brehm, M.; Kirchner, B. *Phys. Chem. Chem. Phys.* **2015**, *17*, 3207–3213.

[430] Wannier, G. H. *Phys. Rev.* **1937**, *52*, 191–197.

[431] Mantina, M.; Chamberlin, A. C.; Valero, R.; Cramer, C. J.; Truhlar, D. G. *J. Phys. Chem. A* **2009**, *113*, 5806–5812.

[432] Slater, J. C. *J. Chem. Phys.* **1964**, *41*, 3199–3204.

[433] Clementi, E.; Raimondi, D. L.; Reinhardt, W. P. *J. Chem. Phys.* **1967**, *47*, 1300–1307.

[434] Gatti, C.; Saunders, V. R.; Roetti, C. *J. Chem. Phys.* **1994**, *101*, 10686–10696.

[435] Krishnan, R.; Binkley, J. S.; Seeger, R.; Pople, J. A. *J. Chem. Phys.* **1980**, *72*, 650–654.

[436] Hariharan, P.; Pople, J. *Theoret. Chim. Acta* **1973**, *28*, 213–222.

[437] Lichanot, A.; Aprá, E.; Dovesi, R. *Phys. Status Solidi B* **1993**, *177*, 157–163.

[438] Aprá, E.; Causá, M.; Prencipe, M.; Dovesi, R.; Saunders, V. R. *J. Phys.: Condens. Matter* **1993**, *5*, 2969–2976.

[439] Rassolov, V. A.; Ratner, M. A.; Pople, J. A.; Redfern, P. C.; Curtiss, L. A. *J. Comput. Chem.* **2001**, *22*, 976–984.

[440] Doll, K.; Stoll, H. *Phys. Rev. B* **1998**, *57*, 4327–4331.

[441] Glukhovtsev, M. N.; Pross, A.; McGrath, M. P.; Radom, L. *J. Chem. Phys.* **1995**, *103*, 1878–1885.

[442] Lee, H.-J.; Lee, J.-K.; Kim, M.-R.; Shin, W. S.; Jin, S.-H.; Kim, K.-H.; Park, D.-W.; Park, S.-W. *Mol. Cryst. Liq. Cryst.* **2007**, *462*, 75–81.

[443] Kubo, W.; Kitamura, T.; Hanabusa, K.; Wada, Y.; Yanagida, S. *Chem. Commun.* **2002**, 374–375.

[444] Abate, A.; Petrozza, A.; Roiati, V.; Guarnera, S.; Snaith, H.; Matteucci, F.; Lanzani, G.; Metrangolo, P.; Resnati, G. *Org. Electron.* **2012**, *13*, 2474–2478.

[445] Xia, J.; Masaki, N.; Jiang, K.; Wada, Y.; Yanagida, S. *Chem. Lett.* **2006**, *35*, 252–253.

[446] Wang, P.; Zakeeruddin, S.; Grätzel, M.; Kantlehner, W.; Mezger, J.; Stoyanov, E.; Scherr, O. *Appl. Phys. A* **2004**, *79*, 73–77.

[447] Wang, P.; Dai, Q.; Zakeeruddin, S. M.; Forsyth, M.; MacFarlane, D. R.; ; Grätzel, M. *J. Am. Chem. Soc.* **2004**, *126*, 13590–13591.

[448] Santa-Nokki, H.; Busi, S.; Kallioinen, J.; Lahtinen, M.; Korppi-Tommola, J. *J. Photochem. Photobiol., A* **2007**, *186*, 29–33.

[449] Rühle, S.; Greenshtein, M.; Chen, S.-G.; Merson, A.; Pizem, H.; Sukenik, C. S.; Cahen, D.; Zaban, A. *J. Phys. Chem. B* **2005**, *109*, 18907–18913.

[450] Ronca, E.; Pastore, M.; Belpassi, L.; Tarantelli, F.; De Angelis, F. *Energy Environ. Sci.* **2013**, *6*, 183–193.

[451] Merrigan, T. L.; Bates, E. D.; Dorman, S. C.; Davis Jr., J. H. *Chem. Commun.* **2000**, 2051–2052.

[452] Russina, O.; Lo Celso, F.; Di Michiel, M.; Passerini, S.; Appetecchi, G. B.; Castiglione, F.; Mele, A.; Caminiti, R.; Triolo, A. *Faraday Discuss.* **2013**, *167*, 499–513.

[453] Hollóczki, O.; Macchiagodena, M.; Weber, H.; Thomas, M.; Brehm, M.; Stark, A.; Russina, O.; Triolo, A.; Kirchner, B. *ChemPhysChem* **2015**, *16*, 3325–3333.

[454] Cremer, T.; Kolbeck, C.; Lovelock, K. R. J.; Paape, N.; Wölfel, R.; Schulz, P. S.; Wasserscheid, P.; Weber, H.; Thar, J.; Kirchner, B.; Maier, F.; Steinrück, H.-P. *Chem. Eur. J.* **2010**, *16*, 9018–9033.

[455] Higashino, T.; Imahori, H. *Dalton Trans.* **2015**, *44*, 448–463.

[456] Weber, H.; Kirchner, B. **2016**, in preparation.

[457] Gorlov, M.; Pettersson, H.; Hagfeldt, A.; Kloo, L. *Inorg. Chem.* **2007**, *46*, 3566–3575.

[458] Fabian, J. *Theor. Chem. Acc.* **2001**, *106*, 199–217.

[459] Ridley, J.; Zerner, M. *Theor. Chim. Acta* **1973**, *32*, 111–134.

[460] McDouall, J. J.; Peasley, K.; Robb, M. A. *Chem. Phys. Lett.* **1988**, *148*, 183–189.

[461] Buenker, R. J.; Peyerimhoff, S. D.; Butscher, W. *Mol. Phys.* **1978**, *35*, 771–791.

[462] Christiansen, O.; Koch, H.; Jørgensen, P. *Chem. Phys. Lett.* **1995**, *243*, 409–418.

[463] Grimme, S. *J. Chem. Phys.* **2003**, *118*, 9095–9102.

[464] Perdew, J. P.; Ruzsinszky, A.; Tao, J.; Staroverov, V. N.; Scuseria, G. E.; Csonka, G. I. *J. Chem. Phys.* **2005**, *123*, 062201.

[465] Goerigk, L.; Moellmann, J.; Grimme, S. *Phys. Chem. Chem. Phys.* **2009**, *11*, 4611–4620.

[466] Goerigk, L.; Grimme, S. *J. Chem. Phys.* **2010**, *132*, 184103.

[467] Jacquemin, D.; Planchat, A.; Adamo, C.; Mennucci, B. *J. Chem. Theory Comput.* **2012**, *8*, 2359–2372.

[468] Schreiber, M.; Silva-Junior, M. R.; Sauer, S. P. A.; Thiel, W. *J. Chem. Phys.* **2008**, *128*, 134110.

[469] Petit, L.; Maldivi, P.; Adamo, C. *J. Chem. Theory Comput.* **2005**, *1*, 953–962.

[470] Tomasi, J.; Mennucci, B.; Cammi, R. *Chem. Rev.* **2005**, *105*, 2999–3094.

[471] Scalmani, G.; Frisch, M. J.; Mennucci, B.; Tomasi, J.; Cammi, R.; Barone, V. *J. Chem. Phys.* **2006**, *124*, 094107.

[472] Santoro, F.; Improta, R.; Lami, A.; Bloino, J.; Barone, V. *J. Chem. Phys.* **2007**, *126*, 084509.

[473] Santoro, F.; Lami, A.; Improta, R.; Barone, V. *J. Chem. Phys.* **2007**, *126*, 184102.

[474] Santoro, F.; Lami, A.; Improta, R.; Bloino, J.; Barone, V. *J. Chem. Phys.* **2008**, *128*, 224311.

[475] Improta, R.; Barone, V. *J. Mol. Struct. THEOCHEM* **2009**, *914*, 87–93.

[476] Ferrer, F. J. A.; Improta, R.; Santoro, F.; Barone, V. *Phys. Chem. Chem. Phys.* **2011**, *13*, 17007–17012.

[477] Nappa, M.; Valentine, J. S. *J. Am. Chem. Soc.* **1978**, *100*, 5075–5080.

[478] Ahlrichs, R.; Bär, M.; Häser, M.; Horn, H.; Kölmel, C. *Chem. Phys. Lett.* **1989**, *162*, 165–169.

[479] Schäfer, A.; Huber, C.; Ahlrichs, R. *J. Chem. Phys.* **1994**, *100*, 5829–5835.

[480] Weigend, F.; Ahlrichs, R. *Phys. Chem. Chem. Phys.* **2005**, *7*, 3297–3305.

[481] Risthaus, T.; Hansen, A.; Grimme, S. *Phys. Chem. Chem. Phys.* **2014**, *16*, 14408–14419.

[482] Neese, F. *WIREs Comput. Mol. Sci.* **2012**, *2*, 73–78.

[483] Klamt, A.; Schüürmann, G. *J. Chem. Soc., Perkin Trans. 2* **1993**, 799–805.

[484] Hermansson, K.; Knuts, S.; Lindgren, J. *J. Chem. Phys.* **1991**, *95*, 7486–7496.

[485] Eggenberger, R.; Gerber, S.; Huber, H.; Searles, D.; Welker, M. *J. Chem. Phys.* **1992**, *97*, 5898–5904.

[486] Nosé, S. *Mol. Phys.* **1984**, *52*, 255–268.

[487] Grimme, S. *Chem. Eur. J.* **2012**, *18*, 9955–9964.

[488] Zhao, Y.; Truhlar, D. G. *J. Phys. Chem. A* **2005**, *109*, 5656–5667.

[489] Weigend, F.; Furche, F.; Ahlrichs, R. *J. Chem. Phys.* **2003**, *119*, 12753–12762.

[490] Goerigk, L.; Grimme, S. *Phys. Chem. Chem. Phys.* **2011**, *13*, 6670–6688.

[491] Klamt, A. *J. Phys. Chem.* **1995**, *99*, 2224–2235.

[492] F. Eckert and A. Klamt, COSMOtherm, Version C3.0, Release 16.01; COSMOlogic GmbH & Co. KG, http://www.cosmologic.de.

[493] Perdew, J. P. *Phys. Rev. B* **1986**, *33*, 8822–8824.

[494] Sure, R.; Grimme, S. *J. Comput. Chem.* **2013**, *34*, 1672–1685.

[495] Neugebauer, J.; Reiher, M.; Kind, C.; Hess, B. A. *J. Comput. Chem.* **2002**, *23*, 895–910.

[496] Vahtras, O.; Almlöf, J.; Feyereisen, M. W. *Chem. Phys. Lett.* **1993**, *213*, 514–518.

[497] Eichkorn, K.; Treutler, O.; Öhm, H.; Häser, M.; Ahlrichs, R. *Chem. Phys. Lett.* **1995**, *240*, 283–289.

[498] Eichkorn, K.; Weigend, F.; Treutler, O.; Ahlrichs, R. *Theor. Chem. Acc.* **1997**, *97*, 119–124.

[499] Weigend, F. *Phys. Chem. Chem. Phys.* **2006**, *8*, 1057–1065.

[500] Bannwarth, C.; Grimme, S. *J. Phys. Chem. A* **2015**, *119*, 3653–3662.

[501] Thar, J.; Zahn, S.; ; Kirchner, B. *J. Phys. Chem. B* **2008**, *112*, 1456–1464.

[502] Weber, H.; Kirchner, B. *J. Phys. Chem. B* **2016**, *120*, 2471–2483.

[503] Navrotsky, A. *ChemPhysChem* **2011**, *12*, 2207–2215.

[504] Canongia Lopes, J. N.; Deschamps, J.; Pádua, A. A. H. *J. Phys. Chem. B* **2004**, *108*, 2038–2047.

[505] Kaminski, G.; Jorgensen, W. L. *J. Phys. Chem.* **1996**, *100*, 18010–18013.

[506] McDonald, N. A.; Jorgensen, W. L. *J. Phys. Chem. B* **1998**, *102*, 8049–8059.

[507] Sun, H. *J. Phys. Chem. B* **1998**, *102*, 7338–7364.

[508] Manz, T. A.; Sholl, D. S. *Journal of Chemical Theory and Computation* **2012**, *8*, 2844–2867.

[509] Zwanzig, R. *J. Chem. Phys.* **1966**, *45*, 1858.

[510] Seki, S.; Tsuzuki, S.; Hayamizu, K.; Umebayashi, Y.; Serizawa, N.; Takei, K.; Miyashiro, H. *J. Chem. Eng. Data* **2012**, *57*, 2211–2216.

[511] Freire, M. G.; Teles, A. R. R.; Rocha, M. A. A.; Schröder, B.; Neves, C. M. S. S.; Carvalho, P. J.; Evtuguin, D. V.; Santos, L. M. N. B. F.; Coutinho, J. A. P. *J. Chem. Eng. Data* **2011**, *56*, 4813–4822.

Acknowledgment

I would like to thank Prof. Dr. Barbara Kirchner for the opportunity of working on this topic and for the supervision of the whole thesis. I would also like to thank Prof. Dr. Thomas Bredow, Prof. Dr. Helmut Baltruschat and Prof. Dr. Andreas Bartels for reviewing the thesis and completing the doctoral committee. Financial support by the Fonds der Chemischen Industrie as well as by the Deutsche Forschungsgemeinschaft is gratefully acknowledged.

I am especially thankful to my friends and colleagues Dr. Martin Thomas, Dr. Friedrich Malberg and Joseph Wladkowski for proofreading, suggestions and fruitful discussions. Moreover, I thank all members of the group of Prof. Kirchner for a friendly and pleasant working atmosphere. Furthermore, I am deeply thankful for the ongoing and unlimited support of my family and especially of Katharina Roßberg.

Eidesstattliche Erklärung

Hiermit erkläre ich, Henry Weber, dass ich der einzige Autor der vorgelegten Arbeit bin. Die vorgelegte Arbeit wurde persönlich, selbständig und ohne Benutzung anderer Hilfsmittel, abgesehen von den ausdrücklich bezeichneten Hilfsmitteln, angefertigt. Die aus anderen Quellen direkt oder indirekt übernommenen Daten und Konzepte sind unter Angabe der Quelle kenntlich gemacht. Die vorgelegte Arbeit oder ähnliche Arbeiten sind nicht bereits anderweitig als Dissertation eingereicht worden. Es wurden keine vorherigen Promotionsversuche unternommen. Für die Erstellung der vorgelegten Arbeit wurde keine fremde Hilfe, insbesondere keine entgeltliche Hilfe von Vermittlungs- bzw. Beratungsdiensten in Anspruch genommen.

Bonn, October 31, 2016

Henry Weber

List of Publications

Used in this thesis:

[1] Weber, H.; Kirchner, B. Complex Structural and Dynamical Interplay of Cyano-Based Ionic Liquids. *J. Phys. Chem. B* **2016**, *120*, 2471–2483.

[2] Weber, H.; Bredow, T.; Kirchner, B. Adsorption Behavior of the 1,3-Dimethylimidazolium Thiocyanate and Tetracyanoborate Ionic Liquids at Anatase (101) Surface. *J. Phys. Chem. C* **2015**, *119*, 15137–15149.

[3] Weber, H.; Salanne, M.; Kirchner, B. Toward an Accurate Modeling of Ionic Liquid–TiO_2 Interfaces. *J. Phys. Chem. C* **2015**, *119*, 25260–25267.

[4] Weber, H.; Kirchner, B. Ionic Liquid Induced Band Shift of Titanium Dioxide. *ChemSusChem* **2016**, *9*, 2505–2514.

[5] Weber, H.; Bannwarth, C.; Grimme, S.; Kirchner, B. Ionic Liquid Influence on Excitation of Promising Dyes for Dye-Sensitized Solar Cells. *Manuscript in preparation.*

Not used in this thesis:

[6] Cremer, T.; Kolbeck, C.; Lovelock, K. R. J.; Paape, N.; Wölfel, R.; Schulz, P. S.; Wasserscheid, P.; Weber, H.; Thar, J.; Kirchner, B.; Maier F.; Steinrück, H.-P. Towards a Molecular Understanding of Cation-Anion Interactions-Probing the Electronic Structure of Imidazolium Ionic Liquids by NMR Spectroscopy, X-ray Photoelectron Spectroscopy and Theoretical Calculations. *Chem. Eur. J.* **2010**, *16*, 9018–9033.

[7] Brehm, M.; Weber, H.; Pensado, A. S.; Stark, A.; Kirchner, B. Proton Transfer and Polarity Changes in Ionic Liquid-Water Mixtures: A Perspective on Hydrogen Bonds from Ab Initio Molecular Dynamics at the Example of 1-Ethyl-3-methylimidazolium Acetate-Water Mixtures. Part 1. *Phys. Chem. Chem. Phys.* **2012**, *14*, 5030–5044.

[8] Brehm, M.; Weber, H.; Pensado, A. S.; Stark, A.; Kirchner, B. Liquid Structure and Cluster Formation in Ionic Liquid/Water Mixtures - An Extensive ab initio Molecular Dynamics Study on 1-Ethyl-3-Methylimidazolium Acetate/Water Mixtures - Part2. *Z. Phys. Chem.* **2013**, *227*, 177–203.

[9] Weber, H.; Hollóczki, O.; Pensado, A. S.; Kirchner, B. Side Chain Fluorination and Anion Effect on the Structure of 1-Butyl-3-methylimidazolium Ionic Liquids. *J. Chem. Phys.* **2013**, *139*, 084502.

[10] Zahn, S.; Brehm, M.; Brüssel, M.; Hollóczki, O.; Kohagen, M.; Lehmann, S. B. C.; Malberg, F.; Pensado, A. S.; Schöppke, M.; Weber, H.; Kirchner, B. Understanding Ionic Liquids from Theoretical Methods. *J. Mol. Liq.* **2014**, *192*, 71–76.

[11] Brehm, M.; Weber, H.; Thomas, M.; Hollóczki, O.; Kirchner, B. Domain Analysis in Nanostructured Liquids: A Post-Molecular Dynamics Study at the Example of Ionic Liquids. *ChemPhysChem* **2015**, *16*, 3271–3277.

[12] Hollóczki, O.; Macchiagodena, M.; Weber, H.; Thomas, M.; Brehm, M.; Stark, A.; Russina, O.; Triolo, A.; Kirchner, B. Triphilic Ionic-Liquid Mixtures: Fluorinated and Nonfluorinated Aprotic Ionic-Liquid Mixtures. *ChemPhysChem* **2015**, *16*, 3325–3333.

[13] Kiefer, J.; Noack, K.; Penna, T. C.; Ribeiro, M. C. C.; Weber, H.; Kirchner, B. Vibrational Signatures of Anionic Cyano Groups in Imidazolium Ionic Liquids. *Vib. Spectrosc.* **2016**, *doi:10.1016/j.vibspec.2016.05.004*.